A DVD-ROM based high-throughput cantilever sensing platform

Bosco, Filippo

Publication date:
2012

Document Version
Publisher's PDF, also known as Version of record

A DVD-ROM based high-throughput cantilever sensing platform

Filippo Giacomo Bosco
Ph.D. Thesis

October 28, 2011

DTU Nanotech - Department of Micro and Nanotechnology
Technical University of Denmark
Building 345 East
2800 Kgs. Lyngby
DENMARK

To my uncle Guido, to my family, my girlfriend and my friends

Acknowledgments

First, I want to acknowledge the persons that made possible the accomplishment of the work presented in this thesis. My advisor, Prof. Anja Boisen, the best supervisor (and project manager) I could imagine, for constantly backing my ideas and for the determination she always put in project development strategies. My co-supervisor, Stephan Keller, for the great support and constant encouragement across the three years of PhD program. Michael Bache, a good friend and a great biochemist, who made possible the biological sensing achievement reported here.

A special thanks goes to En-Te Hwu (Edwin for friends), the most brilliant micro-engineer I ever met (and that probably I will ever meet), able to design, manufacture and test new brilliant technologies with uncommon ease.
Ching-Hsiu Chen (Albert for friends) deserves a special thanks, too. A software engineer with impressive programming skills, he revealed to be a talented programmer as well as a precious friend, to who I wish the best for his newcoming baby daughter.

Thanks to my mum, my dad and my brother Edo, without who I would never reached this point in my life. Thanks to my grandmothers, my aunts and my uncles, for the endless support they always gave me during the past 28 years. Thanks to Olga, my girlfriend, for being with me for the past three years, for tolerating me, supporting me and helping me in the difficult moments.

Thanks to the whole Nanoprobes group, which have ceaselessly provided a fantastic environment for personal growth, scientifically and personally. Thanks in particular to Dr. Fisher, Dr. Noeth, and Dr. Schmid for their knowledge (and beers) sharing policy, to Dr. Cagliani for being a great friend and a precious colleague, and for the all nice party nights I had the luck to share with. Thanks to Dr. Schmidt for his pungent irony (nice company during the long experiments days) and to Dr. Kenneth Olsen, for all the help he gave me in the first year of PhD.
Out of Nanoprobes, special thanks go to Dr Booth, for a long series of reasons that range from excellent scientific discussions to crazy trips around the north pole. Thanks to Silja Senkbeil, a friend and a great polymer lab company, and to Jan Kafka and Josiane Lafleur for interesting discussions about lab-on-a-chip devices fabrications and uses.

About friends/colleagues in the Copenhagen area, I have to thank Dr. Alberti, Dr. Nunes, Dr. Donolato and Mr. Sottini for 3 years of exciting academic life lived on the edges between university and night clubs. Thanks to Dr. Godino, Dr. Rodriguez-Trujllo, Mr. Sasso, Mr. Fragiacomo (both soon doctors) and to Mr. Tanzi for the nice time spent together and for the (too many) smoking breaks at DTU Nanotech. Thanks to Elisa especially for all the dinners, lunches and merendas she provided to me. Thanks to Yannis (Dr. Margaris) for the endless discussions about life, economy and politics, and thanks to Agis for being the best flatmate I ever had (together with Oscar, over more than 20 persons). Thanks to Stine, Magny, Jacob, Laerke, Drude, Rella e Martinelli for the nice time spent in the house.

Besides the Copenhagen environment, I cannot ignore the importance that my "old" life's friends had in the overall quality of my life in the last three years. Within this context, I have to thank my friends in Milan, who always gave me the feeling of being home, every time I was back. Thanks to Jacopo (Reppi, Zio, Lozi), Valerio (Ciccio, Valuz, Ciciu), Filo (Raul, Bovaz, PM, Gomez), Alessandro (Torn, Hornets, Hornessio, Hombressio, Herbert, Alesändro, Raptor, Na-na-na-naa-na, Tornessio), Paolo (Panino, Panatta, Moneglia, Grappeggia, Monatti, Granaglia, Stucchi veneziani), Paolo (Antulini, Ciccio, Fragolo), Lorenzo (Mister, Il biondo, Biondezza), Giancarlo (Giovanni, Lulini), Alessandra (Ale, Cipo, Cipolla, Smiquiuz, Merlaz, Sminquiulini), Cristina (Cri, Kriki, Fristicchi, Cristicchi), Francesca (La Sgubbi), Barbara (Barby), Eleonora (Elly), Emanuele (Spinotto, Ema), Marco (Tenente), Marco (Lilly, Willy), Vincenzo (Vincio, Pit Lynch) and thanks also to all the ones that I forgot.

Locations have also been supporting my scientific and private life. Among them, primary role had the offices at Zeropuntozero Srl, in Milan. It offered me a stimulating environment for working, writing, chatting, relaxing and having fun for the past 8 years. Christiania deserves a special thanks too. Its unique characteristics have allowed me to fully exploit the features of my way of thinking and being. Thanks to the New York Public library too, which provided the desks and the internet connection where most of this thesis has been written on.

Abstract

This thesis has been written as a partial fulfillment of the requirements for obtaining the PhD degree at DTU Nanotech. The project has been carried out at the Technical University of Denmark (DTU) at the department of Micro- and Nanotechnology, in the three-years period between November 2008 and October 2011. The project was part of the Xsense research network, funded by the Strategic Danish Research Council, and supervised by Prof. Anja Boisen.

The goal of the Xsense project is to design and fabricate a compact and cheap device for explosive sensing in air and liquid. Four different technologies (Cantilevers, Calorimetric, Colorimetric and Raman) were to be integrated into a single portable platform. My PhD project has been focusing on the cantilever technology part. Furthermore, I have been addressing the issue of designing and fabricating the overall sensing platform, which is going to integrate the four different sensors. The platform was developed specifically for cantilever sensor applications Preliminary tests on Raman-based device integration has been carried out. The inclusion of the other two sensing techniques is currently under development.

This thesis reports on the demonstration of a high-throughput label-free sensor platform utilizing cantilever based sensors. These sensors have often been acclaimed to facilitate highly parallelized operation. Unfortunately, so far no concept has been presented which offers large data sets as well as easy liquid sample handling. We use optics and mechanics from a DVD player to handle liquid samples and to read-out cantilever deflection and resonant frequency. In a few minutes, several liquid samples can be analyzed in parallel, measuring over several hundreds of individual cantilevers.
Three generations of systems have been developed and tested during the three years. These devices have been used for sensing of proteins, antibodies and explosives. Different rotating platforms, specifically designed for gas and liquid measurements, have also been designed, fabricated and tested. The resulting platform represents a completely novel and powerful tool for analyzing biochemical reactions through cantilever sensors, where the reliability of the measurements is ensured by statistical analysis and by parallel characterization of cantilevers.

Dansk Resume

Denne afhandling repræsenterer en del af kravet for at opnå Ph.D. graden ved DTU Nanotech. Projektet er udført på Danmarks Tekniske Universitet, Danmark (DTU) ved Institut for Micro og Nanoteknologi i perioden fra november 2008 til oktober 2011. Projektet er en del af X-sense forskningsnetværk, finansieret af det Danske strategiske Forskningsråd. Projektet er vejledt af Professor Anja Boisen.
Målet med projektet er at designe og fabrikere en kompakt og billig måleenhed til detektion af eksplosive stoffer i luft og væske. Målet er at integrere fire forskellige detektions principper (Cantilever overflade stress, kalorimetrisk, kemisk farveskift og RAMAN) i en enkelt bærbar platform. Mit Ph.D. projekt har primært fokuseret på udviklingen af Cantilever overflade stress sensoren. Sekundært beskrives designet og produktionen af den centrale sensor platform hvori de fire detektions principper skal integreres. Denne platform er udviklet med fokus på Cantilever sensoren. De indledende test af RAMAN sensoren er medtaget. Den kalorimetriske og kemisk farveskift sensor er stadig under udvikling og derfor ikke medtaget.
Denne afhandling beskriver en High-Throughput Label-free sensor som udnytter overflade stress skift af en Cantilever sensor. Disse sensorer er ofte blevet tillagt evnen til at kunne udføre multiple parallelle målinger, men der er endnu ikke bygget et system der kan producere en så stor simultan datamængde med et simpelt fluid system. I dette system bruges optik og mekanikken fra en DVD disk aflæser til håndtering af de fluide prøver og til aflæsning af Cantilever afbøjning og resonans frekvens. Systemet muliggør en simultan parallel måling af fluide prøver ved brug af mange hundrede individuelle Cantilever i løbet af få minutter.
Tre separate generationer af systemer er udviklet og testet i løbet af projektets tre år. Hvert system er brugt til at detektere proteiner, antistoffer og eksplosive stoffer. Diverse rotations platforme til gas og fluide målinger er desuden udviklet, produceret og testet. Den nuværende platform repræsenter et nyt og effektiv værktøj til at analysere biokemiske reaktioner ved hjælp af en Cantilever sensor, hvor målesikkerheden er valideret gennem statistisk analyse og gennem den simultane karakterisering af hver Cantilever.

Contributions

The results reported in this thesis were achieved through a collaboration network between different institutes. Several people have actively worked on different aspects of the project, whose integration has been a key point for the overall progress of the system development. These persons are listed in the following table, linked to the field which they contributed to develop.

Researcher	Position	Institute	Contribution
A. Boisen	Professor	DTU Nanotech	Project management
			Ideas & PhD supervision
S. S. Keller	Assistant professor	DTU Nanotech	PhD co-supervision
			SU-8 fabrication
M. Bache	Postdoc	DTU Nanotech	Biochemistry
			Functionalization protocols
E.-T. Hwu	Assistant professor	IPAS	PUH Opto-electronics
			CAD design
			Systems assembly
C.-H. Chen	Software engineer	IPAS	Software development
			Labview implementation
C. Werner	Electronic engineer	IPAS	Electronics
K. A. Nielsen	PhD student	University of Southern Denmark	TTF synthesis
J. O. Jeppesen	Professor	University of Southern Denmark	TTF synthesis
J. Yang	PhD student	Columbia University	Aptamer protocols
T. S. Alstrom	PhD student	DTU Informatics	Matlab code optimization
D. Dupont	Postdoc	Aarhus University	uPA/PAI-1 aptamers synthesis

Contents

List of Acronyms

ASE Advanced Silicon Etching

BAM 2,6-Dichlorobenzamide

BNC Bayonet NeillConcelman

BSA Bovine Serum Albumin

CAD Computer-Aided Design

CD-ROM Compact Disc Read Only Memory

CNC Computer Numerical Control

COP Cyclic Olefin Polymer

DAQ Data Acquisition

DAT 2,4-Diaminotoluene

DIEA N-Ethyldiisopropylamine

DMF Dimethylformamide

DMSO Dimethylsulfoxide

DNA Deoxyribonucleic acid

DNT 2,4-Dinitrotoluene

DTU Technical University of Denamrk

DVD-ROM Digital Versatile Disc Read Only Memory

EDM Electrical Discharge Machining

EDTA Ethylenediaminetetraacetic acid

ELISA Enzyme Linked Immunosorbent Assay

FES Focus Error Signal

FFC Flat Flexible Connector

FFT Fast Fourier Transform

HDMI High Definition Multimedia Interface

HEPES 4-(2-hydroxyethyl)-1-piperazineethanesulfonic acid

HMDS Hexamethyldisilazane

IPA Isopropanol

IPAS Institute of Physiscs Academia Sinica

MMT MicroMotive

MVD Molecular Vapor Deposition

NA Numerical Aperture

OVA Ovalbumin

PBS Phosphate buffered saline

PC Personal Computer

PCI Peripheral Component Interconnect

PCR Polymerase Chain Reaction

PDGF Plateret Derived Growth Factor

PDIC Photo Detector Integrated Circuit

PDMS Polydimethylsiloxane

PGMEA propylene glycol methyl ether acetate

PMMA Poly(methyl methacrylate)

PUH Pickup Head

RIE Reactive Ion Etching

RMS Root Mean Square

RNA Ribonucleic acid

SELEX Systematic Evolution of Ligands by Exponential Enrichment

SNR Signal to Noise Ratio

TNB 1,3,5-Trinitrobenzene

TNT 2,4,6-trinitrotoluene

TTF Tetrathiafulvalene

VCM Voice Coil Motor

XPS X-ray Photoelectron Spectroscopy

Chapter 1

Introduction

This chapter aims at providing the background and motivations for the work presented in this thesis. Section 1.1 introduces the project framework and funding, while Section 1.2 provides information on working principle and applications of cantilever sensors. After a brief description of state of the art of cantilever readout technologies, a short analysis of their limitations and of the challenges that upcoming technologies have to face is presented. Section 1.3 presents the motivations that drove the technological development of this project. Technology features are also briefly described. Section 1.4 introduces the thesis structure.

1.1 The Xsense project

This PhD project was part of a strategic research network named Xsense, whose goal is to fabricate a miniaturized sensors for explosive detection in air and liquid. The targeted device is a multi sensor platform which integrates different analysis principles into a single compact platform [1–3]. The project, funded by the Danish Strategic Research Council, started in 2008 and will run until the end of 2012, employing 4 Ph.D. students and 3 post doctoral researchers.
The overall goal of the project is the detection of TNT and other military explosives (DNT, RDX, PETN, HMX, etc.) at parts per billion concentrations. The integration of the different sensors is believed to reduce the rate of false positive to less than 0.1%. A brief description of three of the four sensing techniques is presented in the following paragraphs. The fourth sening principle, the cantilever-based sensing, will be the main topic of this thesis.

Colorimetric arrays

The colorimetric sensing technique is based on chemical dyes immobilized on a silica support [1]. The dyes are arranged in an array and each dye is addressed for its selectivity towards specific analytes.
When the array is exposed to an analyte in liquid or vapor phase, the dyes change color.

Analyzing the color map before and after the exposure to a sample, a signature of the analyte can be obtained. This map represents a unique fingerprint of specific explosive compounds, like DNT, HMX, RDX and TATP.

Calorimetric sensors

This type of sensor has been extensively investigated in the Nanoprobes group in the past 5 years [4–6].
Calorimetry is the determination of heat generated or absorbed from chemical reaction, ideal for measuring the exothermal output of an energetic material like explosives. Through device miniaturization, the sensitivity can get to the sub-nanogram level [7, 8]. The device consists of a narrow bridge-like structure composed by heating tracks and measuring tracks. Increasing the heating rate, deflagration of explosive compounds can be initiated. The exothermal response is used to determine the presence of deflagrating material.
A key feature of the calorimetry approach is that each explosive gives a unique response to a fast heat ramp. This is due to different deflagration properties of the different compounds. This type of sensor can thus detect different explosives and also determine the type of compounds.

Surface Enhanced Raman Scattering sensors

Using Raman spectroscopy the vibrational modes of explosive compounds can be investigated. When a molecule is exposed to the incident laser light, inelastic scattering and consequently a shift frequency of the scattered light occurs.
The frequency shift is due to vibrational states of the molecules, which are specific for each analyte. Enhancement of the Raman signal can be obtained through modification of the surface that host the molecules to be detected. In this project the surface is modified growing nanopillars on a silicon substrate, and coating them with Au or Ag. Large enhancement was demonstrated for explosive molecules, reaching up to two orders of magnitude larger enhancement for commercially available substrates [9, 10].

1.2 Cantilever-based biosensing

Cantilevers are micrometer sized free-standing beams anchored at only one end. Cantilevers are commonly fabricated from Si, SiN or polymers. Typical cantilever lengths range from few μm up to few mm, with thicknesses varying from few hundred nm up to few μm.
Micrometer and even nanometer sized cantilevers-based sensors have since the mid-1990s emerged as a promising label free detection technique, which has been used for high precision mass detection and bio-molecular recognition [11–21].
Typically, one cantilever surface is chemically functionalized with probe molecules designed to specifically bind certain target molecules in solution.

1.2.1 Operating modes

Cantilever sensing capabilities have been investigated mainly in two working modes, the static and the dynamic mode, schematically illustrated in Figure 1.1. In static mode, a cantilever functionalized with receptor molecules on one cantilever surface binds target molecules. This binding induces difference in surface stress between the two sides of the cantilever [22–27]. This change of surface stress causes the cantilever to bend (Figure 1.1a). Measuring the free-end displacement, it is possible to determine the differential stress between the two sides of the cantilever.

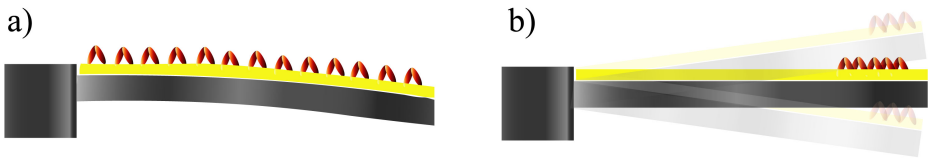

Figure 1.1: Illustration of the static and dynamic operating modes of cantilever-based sensors. a) Molecules binding on one of the cantilever surfaces induce surface stress change which causes bending of the cantilever. b) Mass change is monitored through changes in the resonant frequency of the cantilever.

When a cantilever sensor operates in dynamic mode, the resonance frequency of the cantilever is monitored as the cantilever is exposed to the target molecules. As mass adsorb onto the structure, the resonance frequency, which is inversely proportional to the added mass, decreases [28–32] (Figure 1.1b).
Cantilever sensors have been employed for sensing in both gas and liquid. Typically the cantilevers are inserted into a sensing chamber which is exposed to gas flow (in case of vapor detection) or to continuous liquid flow (in case of biological analyte sensing). The measurements carried out in liquid have some disadvantages compared to the ones performed in air. The most crucial is the damping generated by the liquid surrounding the cantilever, which generally limits the possibility of measuring in dynamic mode.
A way to circumvent this limitation is to perform liquid phase reactions which are monitored in dry phase. That is, the cantilever characteristics are measured in air before and after exposure to liquid samples, highly reducing the complexity of the measurements. Similar approach has previously been used for i.e. bacteria detection [33]. In this thesis this working mode is refereed as "wet & dry".

1.2.2 Applications

Cantilever-based sensing has been used for a wide range of biochemical detection applications, from single DNA strands [34,35] to whole bacteria cells [36–38]. These label-free sensors have been widely employed for proteins detection [39–44], glucose detection [45], pesticide detection [46, 47] and heavy metal ions detection [48, 49]. Furthermore, cantilever sensors have been employed in measurement of pH [50] and for sensing of different

vapor compounds [51–55].
The use of cantilever sensors for explosive detection has been also widely demonstrated and investigated in the past years [56–59].

1.2.3 Functionalization

To employ cantilever-based sensors in specific analyte detection, one of the cantilever surfaces needs to be coated with specific receptor molecules. For surface stress measurements it is crucial that only one side of the cantilever is functionalized, since equal surface stress change on both surfaces would result in null deflection of the cantilever. On the other hand, when dynamic mode is investigated, double side functionalization would enhance the sensitivity of the detection, allowing more target molecules to contribute to the overall cantilever mass change.

Several functionalization techniques have been developed during the past years. Probably the most common one involves the use of thiol-based chemistry for treating Au coated surfaces [60, 61]. In case of Si surfaces, silane-based chemistry is often employed [62], while for polymer cantilevers different methods have been investigated, for example binding to the epoxy groups on SU-8 surfaces [63].

Functionalization layers are applied through a set of different methodologies. Immersion chemistry is often preferred (immersing the cantilevers into the functionalization solution) due to its simplicity. Microspotting technology can also be used, where commercial devices for this purpose are now available [64]. Alternatively, capillaries can be used as single functionalization units for individual cantilevers [65].
In this project standard beaker-based functionalization was the preferred coating method. Microspotting on single cantilevers was also employed for pesticide detection experiments.

1.2.4 Cantilever readout technologies

Nowadays, the prevalent method of monitoring vibrational amplitudes and cantilever deflection is based on the optical leverage technique [66] widely used in atomic force microscopy [67]. A laser beam is focused on a cantilever which reflects the beam onto a position-sensitive detector (PSD). The distance between the cantilever and the PSD magnifies the deflection of the cantilever. With this technique sub-nanometric deflections can be resolved. For research purposes several optical leverage based read-out systems have been developed [68, 69]. The optical lever technique needs a tedious and time consuming alignment process before measuring bending of each cantilever. Therefore, this method may not be an optimum solution for new technological tasks such as fast or simultaneous detection on large cantilever arrays.
Alternatively, a CCD camera has been used for monitoring cantilever deflection and hereby large 2-dimensional cantilever arrays can be read simultaneously [70]. However, all cantilevers have to be in the same focal plane which is extremely difficult to achieve

in practice.
These two techniques only apply to micrometer sized cantilevers. In optical leverage the laser spot size is typically 20 μm or above and in the CCD system the amount of reflected light is too low for smaller devices.
Integrated read-out has been suggested by several groups. For example, cantilevers with piezoresistive [53, 71], piezoelectric [72, 73] and MOSFET-based [74, 75] read-out have been developed and applied for molecular recognition. Generally, these cantilevers have to be carefully insulated in order to be operated in liquid and the devices require significantly more packaging due to electrical interconnections.

Read-out method	Measurement	Company/Institute	Country	Device Price
Optical lever	Static, dynamic	Veeco [76]	US	n.a.
		Concentris [65]	CH	$\sim$ 100.000 €
		Mecwins [77]	ES	$\sim$ 100.000 €
		Uni Basel [78]	CH	$\sim$ 80.000 €
		Protiveris[1]	US	n.a.
Piezoresistive	Static, dynamic	Cantion/Nanonord [79]	DK	$\sim$ 80.000 €
		Seiko Instruments [80]	JP	n.a.
Piezoelectric	Static, dynamic	Intelligent Microsystem Center [81]	KR	n.a.
Capacitive	Dynamic	Graviton Inc[1]	US	n.a.
Hard contact	Dynamic	Nanoprobes, DTU [32]	DK	n.a.
CCD camera	Static	Nano Engineering Lab, Berkeley [44]	US	n.a.

[1]Company and product info not available

Table 1.1: List of cantilever readout technologies and corresponding commercially available products.

In the past 20 years several readout devices based of the cited technologies have been commercialized. These products are often research-oriented, with high prices and low measurement throughput. These issues are believed to highly affect the proper breakthrough of the cantilever-based technology into the out-of-the-lab sensors market. Table 1.1 lists the commercially available cantilever readout products, the manufacturing companies and the estimated prices per instrument.

1.3 Motivation

Most of the cantilever sensing platforms (e.g. the ones listed in Table 1.1) normally measure few cantilevers at a time. Because of primarily the instrumentation, few papers on cantilever-based sensing present statistically analyzed data sets. Moreover, the laser spot size in most commercially available optical lever systems is several micrometers, making difficult to measure on sub-micrometer sized structures.
Present optical readout setups typically perform measurements on single chips, generating doubts on the reliability of the measurements when critical sensing tasks have to be performed, as in case of diagnostic or homeland security.

This thesis presents an innovative approach to detect the deflection and vibrational frequency of the cantilevers employing the same light, compact, portable and high throughput optical device.
This device, based on DVD-ROM technology, significantly reduces the aforementioned obstacles and challenges in cantilever based sensing. The concept is highly scalable and at this stage serial measurements of multiple samples over hundreds of cantilevers has been demonstrated. Also, the simultaneous monitoring of multiple physical parameters (deflection, resonant frequency and optical roughness) is believed to highly increase the reliability of the output data.
In this work we have extensively tested the capabilities of our sensing platform to perform static and dynamic measurements in gas flow, liquid flow and wet & dry.

1.3.1 DVD-ROM based readout principle

The idea of developing a high-throughput DVD-ROM-based readout mechanism for cantilever sensors was born through a strong collaboration between DTU Nanotech and the Institutes of Physics (IPAS), Academia Sinica, in Taiwan. IPAS's experience in measuring resonance of cantilever beams (primarily for AFM application), together with their ability to deal with optoelectronic components of the DVD-ROM optical heads, matched well with the strong knowhow in cantilever-based sensing developed at the Nanoprobes group, at DTU Nanotech.

High-throughput readout system

A CD-shaped disc is used to mount several cantilever chips along circular "sensing tracks" patterned in concentric rings on the disc surface (see Figure 1.2a).
The cantilever chips are clicked into individual reservoirs patterned into the disc-like substrate with radial symmetry. Approximately 1 mm below the disc, DVD-ROM optical pickup heads provide the read-out system. The disc is spun and cantilevers are illuminated by the DVD laser beam. The laser spot diameter is only 565 nm (Full Width Half Maximum).
The laser scans from the bottom, passes through a glass substrate and focuses on the cantilever surface. The deflection profiles are measured using the astigmatic detection

mechanism embedded in the DVD-ROM system. In this work, silicon cantilevers with a length of 500 μm, width of 100 μm and a thickness of 1 μm were mostly used.

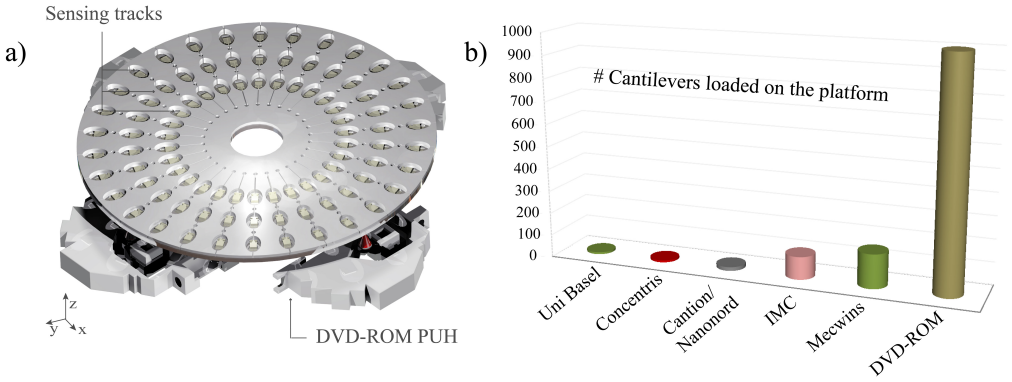

Figure 1.2: a) Layout of the CD-like platform which can hold 720 cantilevers aligned along three sensing tracks. b) Estimated amount of cantilevers which can be simultaneously monitored by the commercially available readout technologies. The DVD-ROM platform offers the possibility of measuring up to 1000 cantilevers mounted on the same sensing disc.

We have proven the possibility of measuring cantilever deflections at rotating velocities up to 200 rpm (comparable to the rotation of CDs when scanning the outer tracks). A disc loaded with 200 cantilevers would then give a readout speed of more than 500 cantilevers per second.
Furthermore, by combining cantilever scans at sequential radial positions it is possible to construct a 3D image of the cantilever surfaces. Few other commercially available setup offer the possibility of measuring surface reconstruction of the cantilevers. The measured surface reconstruction can for example be used to evaluate the distribution of biomolecules on the cantilever surface.
Finally, the system can measure changes in the resonant frequency of the cantilever using the thermal noise peaks of the cantilevers.

Figure 1.2b illustrates the estimated amount of cantilevers which can be simultaneously monitored by the commercially available readout technologies. Defining the "throughput cost" as the cost per cantilever measured in a single experiment, present systems charge an average price of 2000 €per measured cantilever (see Table 1.1).
Our device aims at a "throughput cost" reduction of at least two orders of magnitudes. We believe that our platform, once optimized, could bring the cantilever technology into the applied sensors market.

1.3.2 Centrifugal microfluidics

Another advantage of the CD-like format is the possibility to integrate centrifugal microfluidics. The DVD disc format has in the past 10 years been widely used for liquid handling [82–84]. The centrifugal forces generated by spinning the disc can be used to

move liquid from the center of the disc towards the edges [85, 86].

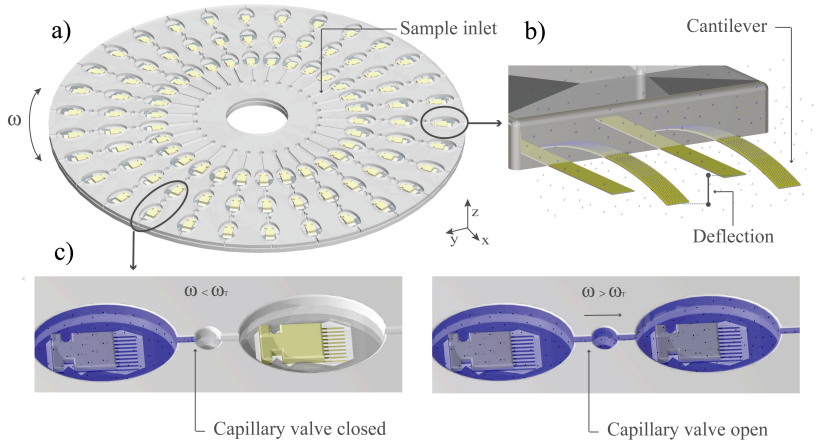

Figure 1.3: a) Schematic model of the DVD-ROM platform mounted over four DVD-ROM Pickup Heads. b) the chips are composed by arrays of eight cantilevers. c) The sample is driven across the microfluidic channels through rotation of the disc.

The design of dedicated passive valves allows the manipulation of the fluid through the tuning of the rotational frequency of the disc. These valves, often referred as capillary burst microvalves, offer an easy method to regulate microliquid flow in rotational stages [87–89].
Furthermore, the absence of pumps strongly reduces the amount of external noise. The centrifugal forces generated by spinning the disc are used to drive the sample from the inlets towards serial sensing chambers and, after reaction has occurred, to wash the reservoirs for optional dry phase measurements.
Figure 1.3a-b illustrates a layout of microfluidic channels connecting the chip reservoirs. Each liquid sample is delivered to three reservoirs placed in series, starting at the center and ending at the outer rim of the disc. Figure 1.3c shows the liquid front moving between two adjacent chambers. The liquid moves when the disc rotational speed generates enough pressure to overcome the pressure barrier at the capillary valve [90, 91].

1.4 Outline

Chapter 2 presents in details the technology development across three generations of sensing setups (*Systems*). Chapter 3 describes the different versions of rotating platforms (*Discs*) which were tested in connection with the *System* versions. The *Discs* fabrication processes are described in Chapter 4. Chapter 5 presents a detailed description of data analysis and processing. Application in explosive detection and biosensing leads to the results reported in Chapter 6. Chapter 7 summarizes the conclusions.

Chapter 2

The System

This chapter describes the technology employed for building the three generations of the high-throughput DVD-ROM based cantilever platform. First, an introduction to the DVD optical head and its components is presented in Section 2.1. Then, Section 2.2 presents the first measurement tests which proved the capability of the DVD-ROM based readout to perform deflection and thermal noise measurement of microcantilevers. Sections 2.3, 2.4 and 2.5 illustrate in details the three generations of the system that were developed during the project.

2.1 The DVD-ROM pickup head

Optical storage systems (CDs, DVDs, Blue Rays) usually consist of a drive unit with a spinning disc, an optical readout system, and some electronics for the control of the automation.
The most important part of these systems is the optical path, placed in the Pickup Head (PUH), usually consisting of a semiconductor laser, a lens system for guiding the laser beam, and a photodiodes array for detecting the light reflected from the disc surface.
Considering that the readout signal that contains the serial data stream of a DVD is typically in the high MHz or even in the GHz range, PUHs embed optical receivers and amplifiers with a high bandwidth.
A commercially available DVD-ROM (Digital Versatile Disk Read-Only Memory) PUH contains the following components: laser diode, grating, polarization beam splitter and $\lambda/4$ plate, four-quadrant Photodetector Integrated Circuit (PDIC), objective lens and voice coil motor (VCM). Using advanced packaging technology to combine these components results in a very useful tool for the purpose of optical measurements. In Figure 2.1 a CAD model of a PUH is shown.
The modern DVD discs contain high-density data (thus very small pitch size), therefore high quality laser spot is required for accurately acquiring the data stored on the fast-spinning disc. In order to perform correctly in such high-density data environment, the laser beam of PUH must have very stable power and a small spot size.

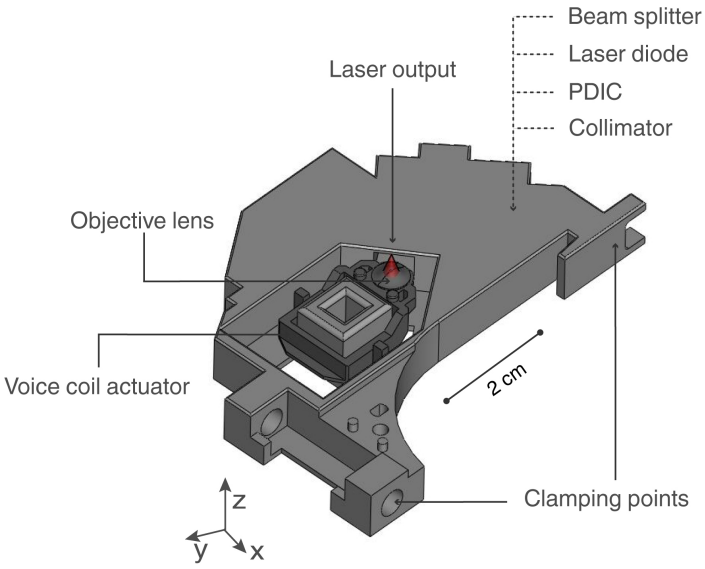

Figure 2.1: PUH CAD model. The DVD PUHs used in this project were purchased from Topray Technologies (TOP 1100S-slim type).

Assuming that the laser beam emitted from laser diode has an intensity distribution across the beam which is in the form of a Gaussian, the size of the focal spot (D) depends on the wavelength (λ) and the numerical aperture (NA) of the lens as:

$$D = 0.52\frac{\lambda}{NA} \tag{2.1}$$

The numerical aperture, the dimensionless number that characterizes the range of angles over which the system can accept or emit light, is itself related to the optical properties of the lens. The relation can be expressed as:

$$NA = n \sin\theta \tag{2.2}$$

where n is the index of refraction of the medium in which the lens is working, and θ is the half-angle of the maximum cone of light that can enter or exit the lens.
The standard objective lens of a DVD PUH has NA of 0.6, a free working distance of 1.28 mm [92] and emits laser light at the wavelengths of 655 nm (red). According to Eq. 2.1, a standard DVD-ROM PUH emits laser light whit a spot size of 568 nm, when perfectly focused.
The spot size, as well as several other parameters, depend on the NA of the lens employed on the PUH. Modifications to the objective lenses has revealed extremely interesting feasibility in customizing the performance of the optical devices, as will be explained in Section 2.5.2 in more detail.

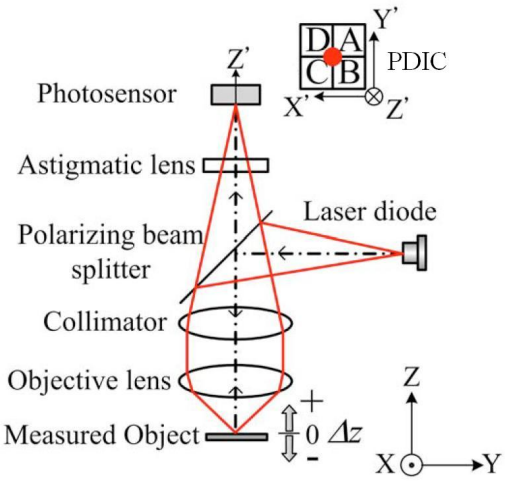

Figure 2.2: Schematic diagram of a typical astigmatism-based optical system [93].

2.1.1 The astigmatic method

Astigmatism is an optical aberration that occurs when an optical system is not symmetric about the optical axis, as in the case of the cylindrical lenses embedded in the PUH. The astigmatic method is the technique employed by DVD-ROM PUHs to precisely evaluate vertical and angular deviations of the optical discs from the correct focusing distance. This technique, which is a standard feature of a DVD PUH, offers the possibility to measure displacements of surfaces with very high precision.
Figure 2.2 illustrates a typical astigmatic optical path that can be found in many CD/DVD heads. Inside the DVD PUH, the laser light emitted from the laser diode is collimated and focused onto the measured object by a collimator and an objective lens. The laser light reflected passes through a polarizing beam splitter plate and an astigmatic shaping device composed by a cylindrical lenses. It then impinges onto a PDIC.
The PDIC has four quadrant photo elements (A-D) with a current preamplifier for each of them. When the laser spot is focused onto the PDIC, the focus error signal (FES) is defined as:

$$FES = (S_A + S_C) - (S_B + S_D) \tag{2.3}$$

where S_A, S_B, S_C and S_D are signals generated by the photo sensors A, B, C and D of the PDIC module.
When the laser beam is perfectly focused on the object's surface, the laser spot onto the PDIC is circular as shown in Figure 2.3c. When the reflective surface is slightly deviated from the optimal focus distance, the spot on the PDIC appears more elongated, as illustrated in Figures 2.3a and 2.3b. The shape change of the laser spot on the photodetectors is then translated into the corresponding FES value. For a circular laser spot, FES=0.

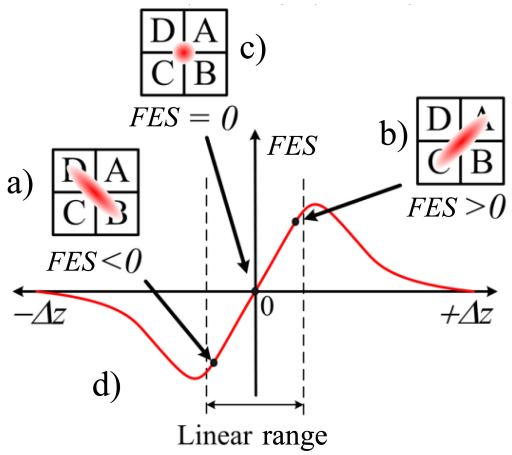

Figure 2.3: a-c) Laser spot shapes projected onto the photodetector in different defocusing positions. d) Focus error signal Vs displacement illustrates the well-known S-curve.

Figure 2.3d shows the S-curve that relates the FES to the vertical displacement of the reflective surface ΔZ [94]. Within this range, changes in the vertical distance are linearly converted into an output voltage signal, generated through the relation given by Eq. 2.3. A standard DVD-ROM PUH has a linear range voltage output from -10 V to +10 V. The linear working range of the optical system is about 6 μm, resulting in a vertical displacement sensitivity in air of about 0.3 nm/mV, where typical RMS noise values of preamplifiers range between 2-5 mV. The resolution of the system was thus calculated to vary between 0.6 and 1.5 nm, depending on the electronic circuit employed.
Modifications applied to the NA of the objective lens will induce dramatic changes in the optical properties of the system, both in the linear range and in the overall detection resolution. In Section 2.5.2 the analysis of the optical properties of PUH in air and liquid under different NA values, together with the determination of their linear ranges and resolutions, are presented.
Additionally, the PDIC module has a very high working bandwidth that is capable of measuring signals up to 80 MHz. This feature makes the PUH a suitable device for dynamic measurements of micromechanical resonators.

2.1.2 The Voice Coil Motor

The VCM of a DVD-ROM PUH is an electromechanical device that belongs to the category of Voice Coil Actuators. These are limited motion devices that use a permanent magnetic field and a coil to produce a force proportional to the current applied to the coil itself.
The electromechanical conversion is governed by the Lorentz force principle, stating that if a current-carrying conductor is placed in a magnetic field, a force will act upon it.
In DVD-ROM optical heads, the VCM is composed by the objective lens, the bobbin

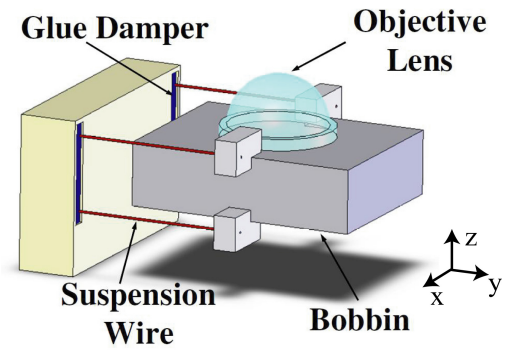

Figure 2.4: Schematics of a VCM for DVD-ROM PUHs [95].

and the suspension wires. A schematic view of the VCM is shown in Figure 2.4.
In operation, when the distance between the reflective surface (the DVD, for example) and the optical system varies, the displacement is detected by the PUH, which generates a corresponding output voltage signal (the FES).
The FES is then used to evaluate the current necessary to drive the VCM in such a way that the objective lens' focal point falls again upon the measured surface.
The VCM can move in two directions, with degrees of freedom along the Z and X axes (see Figure 2.4). These movements are used in standard DVD-ROM reading to compensate the vertical (Z) and radial (X) misalignment of the disc during its spinning (auto-focusing). The minimum vertical movement that can be generated by the coil is in the order of tens of nanometers, while overall distance range is up to 1 mm in both direction.
The capability of moving along the Z-axis was used in this project to implement an auto-tracking system, presented in Section 2.3.3, similar in concept to the one used in standard DVD reading applications. On the other hand the VCM X-axis spanning was used to perform surface reconstruction of the measured microcantilever sensors (see Section 2.2.1).

The employment of PUH and VCM for non-standard applications (everything but reading a DVD) has been widely investigated by several research groups in the past decade [96–98].
Several examples are given on how a PUH can be used to measure distances with [96] and without auto-tracking [99]. Also, dynamic analysis of microsystems has been performed using such a device [98]. Optical profilometers based on the astigmatic method have found widespread applications for precision profile and surface roughness measurements [100–103]. Quericioli et al. [104] were the first to use a CD PUH as the measuring device for cantilevers in an AFM [105–107].

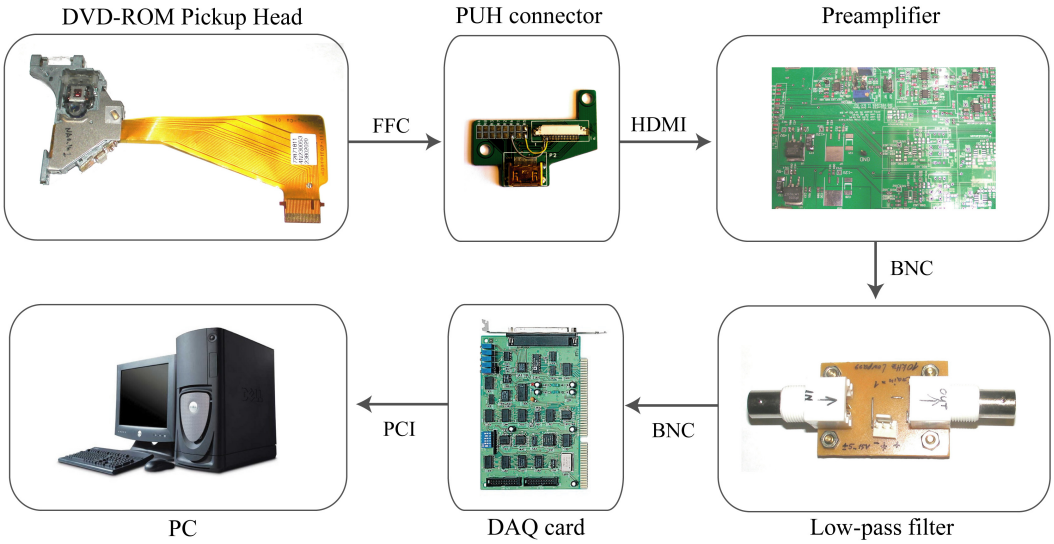

Figure 2.5: Schematic block diagram of the PUH interfacing system. The PUH is connected through flat flexible connector (FFC) to the electronic block, composed by a connector, a preamplifier and a low-pass filter. The data are then sent to a DAQ card that directly interfaces with the computer.

2.1.3 Interfacing the DVD-ROM PUH

Some of the most critical knowhow in dealing with a DVD-ROM PUH is its interfacing procedure. In order to acquire the voltage output from the PDIC (the FES, in this case), dedicated electronics has been developed at IPAS.
The main barrier for using the PUH for purposes different than reading a DVD is the complexity of the electronic interface to the PUH itself. 26 pins are embedded in Flat Flexible Connector (FFC), and the right pin assignment is critical for controlling the PUH features. Datasheets are typically not available to end users, and strong collaboration with manufacturing companies is required to access information about the correct pin assignment.
11 out of 26 pins are used to drive the PUH tools for cantilever sensing, each of them addressing a specific task. In the following the used pin are listed:

- Pin 1-4: output - PDIC quadrants signal
- Pin 5-6: input - VCM coils (X and Z)
- Pin 7-8: input - VCM coils grounds
- Pin 9: input - Laser powering voltage
- Pin 10: input - Reference voltage
- Pin 11: input - Ground

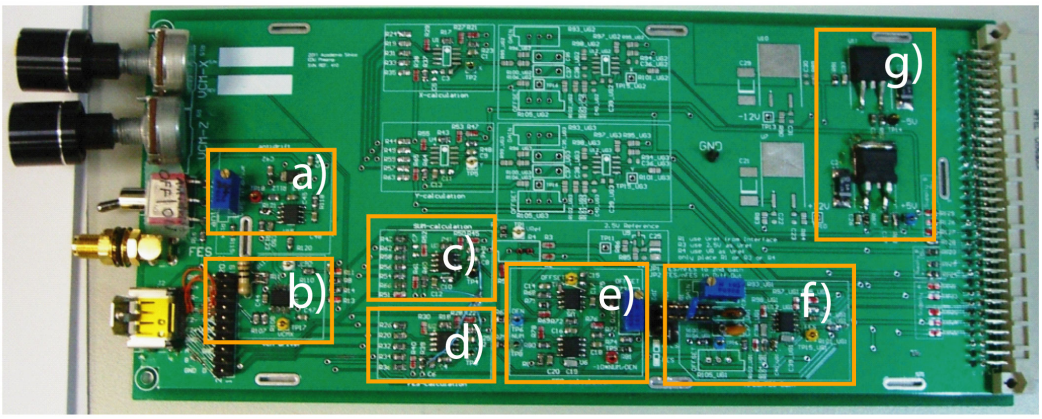

Figure 2.6: Picture of the preamplifier circuit. The marked circuits correspond to to the following functions: a) auto-tracking, b) VCM driver, c) sum function, d) FES acquisition, e) normalization function, f) gain stage and g) power supply line.

The FFC is plugged into a specifically designed connector. The output is carried through a High-Definition Multimedia Interface (HDMI) cable to the electronic block. The use of HDMI interface is particularly convenient, since this type of cable has 19 lines embedded. It is thus possible to assign each pin to a specific line. The internal lines are coaxially shielded leading to a cross-talk-free data transmission block, very suitable for applications where low-noise transmission is required.

The signal is then transfered to the main electronic block, the preamplifier. Figure 2.6 shows the circuit and its main circuit blocks. The design of the circuit has been developed over several years of experiments at IPAS. The preamplifier allows to interface data acquisition systems with the PUH. It allows access to the PDIC quadrants signals (FES) and to control the movement of the VCM. It also allows access to the auto-tracking process. Furthermore it includes a FES normalizing function, which normalizes the FES over the total intensity.
The normalization function divides the FES by the total intensity reflected on the PDIC. Since both signals are proportional to the reflectivity of the measured surface, this technique eliminate signal variations due to reflectivity differences of measured surfaces. As an example, cantilevers with different optical reflectivity would, without normalization, give different voltage responses to the same deflection change. Normalizing the FES is hence a procedure that significantly reduces risks of miscalibration of the detection processes.

Finally, after passing through a low-pass filter (cutoff frequency for cantilever readout system set at 10 kHz), the signal is sent through a DAQ card that interacts with the PC. Coaxial cables and standard Bayonet NeillConcelman (BNC) connectors are employed

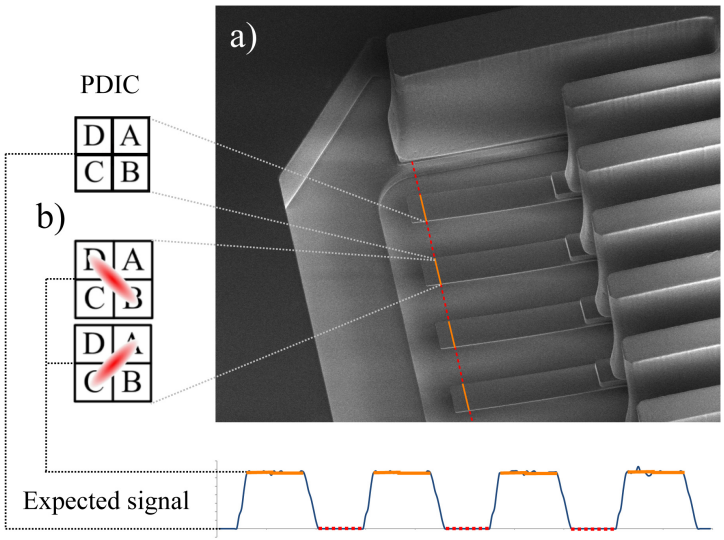

Figure 2.7: Schematic view of the profile measurement process.

for the data transmission between the preamplifier and the DAQ card.
The card used in this project is a high-speed 14-Bit DAQ card (PCI-9820, ADLINK Technology Inc, TW) with a sampling rate up to 130 MHz. Through the Peripheral Component Interconnect (PCI) bus, the digital data are finally analyzed by a custom designed Labview (National Instruments Corporation, US) program, which also acts as the operational interface for parameter-setting.

2.2 Preliminary tests

This section illustrates the working principles of the measurements methods investigated during the project. Section 2.2.1 introduces the measurement capabilities of the DVD-ROM based readout system, while proof of concept of deflection and thermal noise measurements are presented, respectively, in Section 2.2.2 and 2.2.3.

2.2.1 Measurement principle

The astigmatic detection method described in Section 2.1.1 was applied to fast scanning of cantilever sensors mounted onto a rotating stage. The working principle of this DVD-ROM based readout is illustrated in Figure 2.7.
A cantilever chip is mounted on a glass substrate keeping the cantilever suspended over a glass window. The laser beam is positioned at a distance from the cantilever apexes that falls inside the linear range of the PUH.
When the disc is spinning, the laser scans the beams acquiring the FES generated by the laser spot shape on the PDIC (Figure 2.7b).

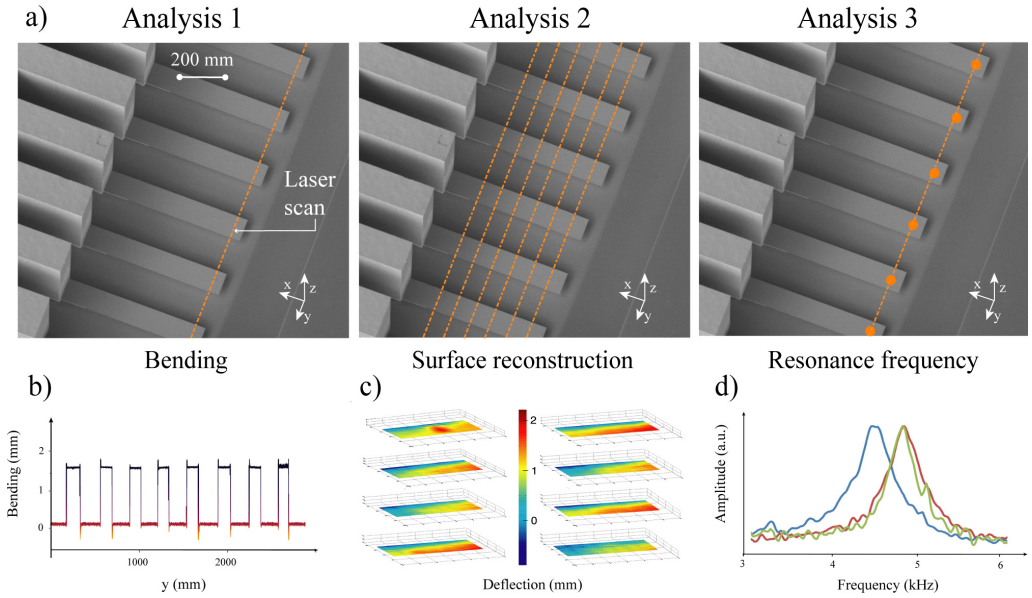

Figure 2.8: Illustration of the multiple analysis concept. The laser movement and the resulting data are shown for three different data acquisition modes: (left) deflection, (middle) surface roughness, and (right) resonant frequency.

When the laser path crosses the gap between cantilevers (red lines), no signal is acquired due to the lack of reflective material. On the other hand, when the light shines onto the cantilevers the FES is measured and the cantilever profile is acquired (orange lines).
The expected signal is thus an array of profiles spaced by null signal. Each point of the profile represents the distance between the PUH and the local position of the reflective surface.
The average of these points gives information on the absolute distance between the PUH and the cantilever, while the profile shapes give indication on the orientation (tilting) and on the surface topography (roughness).
The number of points acquired along the cantilever width varies depending on the data acquisition speed and the scanning velocity. Measuring these values continuously makes it possible to evaluate the changes of the cantilevers, e.g. change of deflection, torsional orientation or surface roughness.

Another interesting feature of the astigmatic detection system is the capability of measuring small oscillations of the intensity of the laser illuminating the PDIC. Through Fast Fourier Transform (FFT) processing it is possible to determine the resonance frequency of vibrating surfaces measuring the periodic oscillations of the FES that they generate. The PUH is able to detect oscillation in the sub-nanometer level, allowing to measure the cantilevers vibrational frequencies even in absence of external actuation [108].

The system was designed taking into account a possible simultaneous application of

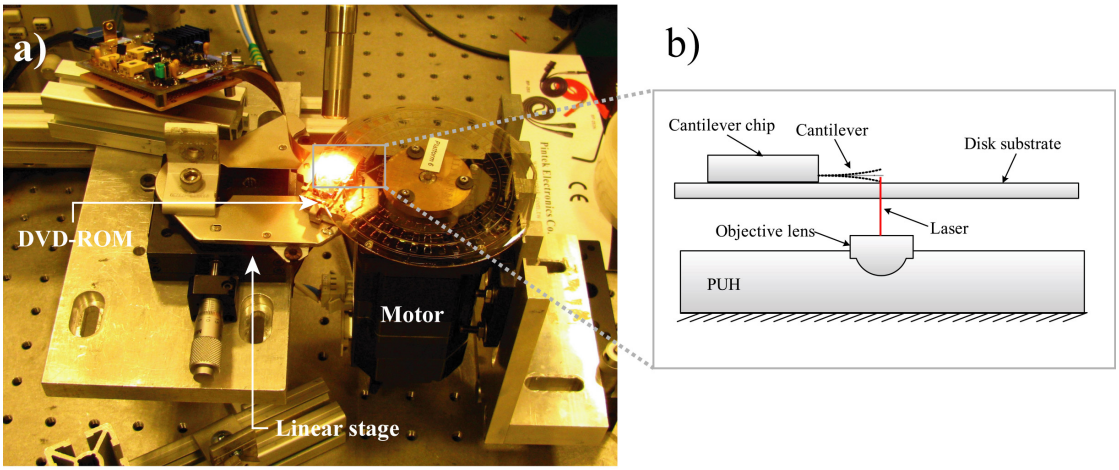

Figure 2.9: a) Picture of the assembly used for the first signal acquisition demonstration. b) Schematics sideview of the system.

the above mentioned measurement techniques. Figure 2.8 illustrates the three working principle as they were planned at the first stage of this project. A disc fabricated in glass and SU-8 is loaded with several cantilever chips, and multiple PUH placed under the substrate perform the different acquisition processes: b) deflection, c) surface roughness and d) resonant frequency. Each working principle was evaluated with preliminary tests as discussed in the following sections.

2.2.2 Cantilever deflection measurements

At the beginning of the project several tests were carried out as proof of concept. In order to obtain information on the capabilities of the system, first cantilever measurement tests were performed simply by placing a DVD-ROM head below the disc. The laser was focused on the cantilever apexes and signal were recorded. The VCM of the PUH was used to move the objective lens along the Z axis to focus the laser beam on the back plane of the cantilevers. A schematic of this detection platform is illustrated in Figure 2.9b, while Figure 2.9a shows a picture of the first test version of the system. The DVD-ROM block is mounted on a linear stage for rough alignment on the cantilever tracks. The disc was spun at very low speed (0.5 rpm) and the FES was acquired from the PUH.
Figure 2.10b shows the profile measurement of an SU-8 cantilever chip composed by 8 cantilevers. Each microcantilever is 500 μm long, 100 μm wide and 5.2 μm thick (20 nm of gold coating). At the sides of the chip two protection bars are present (see Figure 2.10a)
The cantilevers are seen to have an initial non-uniformity deflection, where the central cantilevers are bent more than the ones at the sides. The negative value of the signal indicates that the cantilevers are measured in the negative part of the PUH linear range,

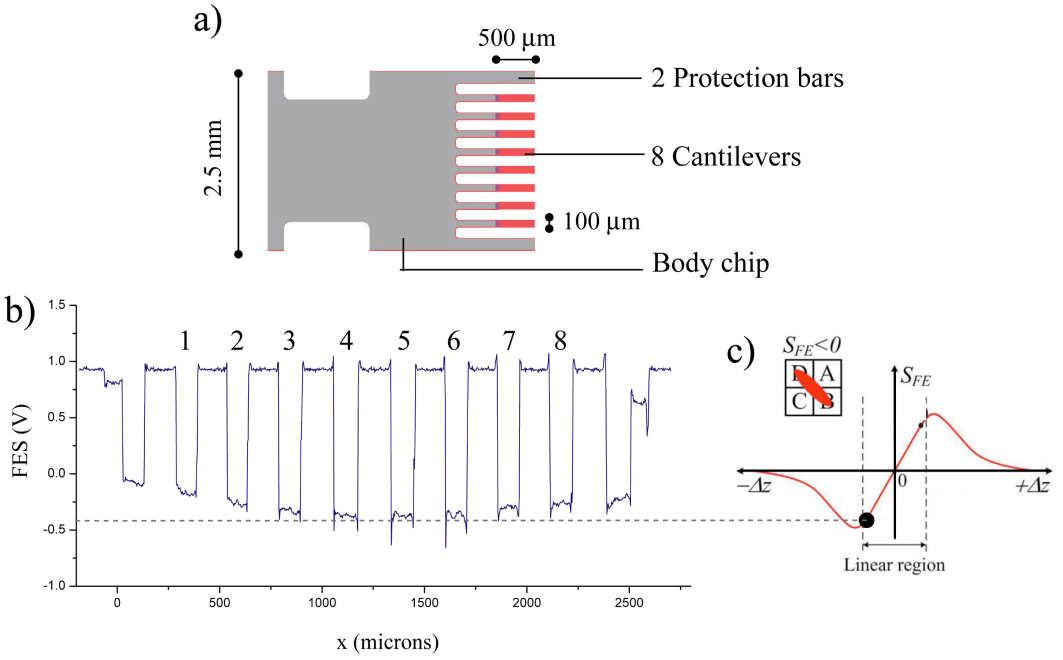

Figure 2.10: a) Mask layout of the IBM chips with eight cantilevers and two protection bars. b) Scanning profile measurement for a single SU-8 cantilever chip and c) its corresponding FES.

as illustrated in Figure 2.10c.
Spikes seem to occur at the edges of the profiles due to the reflected light from the corners of the cantilevers. The signal obtained from the outer cantilevers is around 0.4 V less than the one obtained from the central ones, indicating a initial bending difference of about 120 nm.

2.2.3 Cantilever thermal noise measurements

In this section the capability of the DVD-ROM technology to measure thermal noise of microcantilevers is reported. The test experiments were carried out using the setup illustrated in Figure 2.9. No spinning of the disc was applied, in order to give the laser sufficient time to dwell on the cantilever tip and allow the system to measure enough counts for the FFT process. It was later proved that, depending on the experimental conditions, a time between 100 ms and 1 s is sufficient for accurate resonance peak identification.
For working in dynamic mode, the FFT algorithm transforms the time-domain FES into the frequency domain. The thermal noise of the cantilever can be measured by the PDIC system even without external excitation. The signal to noise ratio (SNR) is related to the reflectivity of the cantilever surface. If the cantilever has low reflectivity, the amplitude of the resonance peak is low and might be comparable with the noise level of the system.

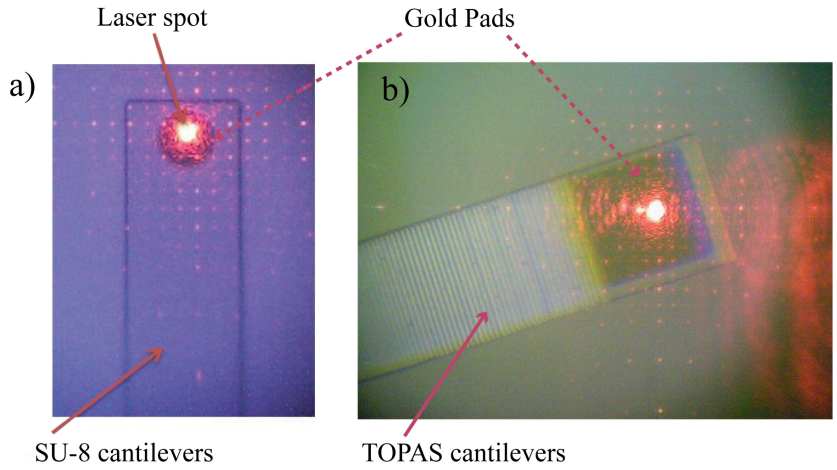

Figure 2.11: Optical microscope pictures of the laser spot focused on the gold pad embedded in a a) SU-8 and b) TOPAS cantilever.

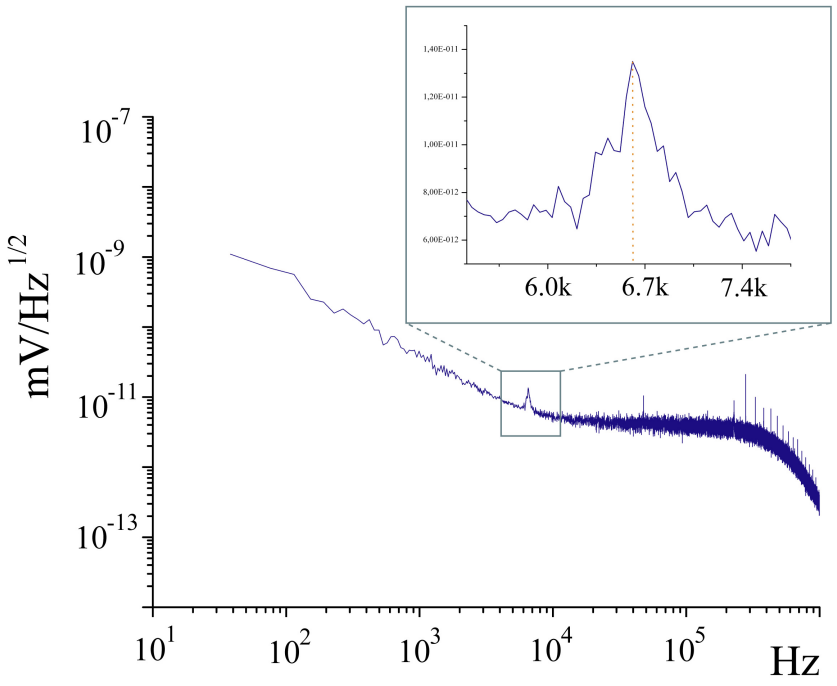

Figure 2.12: Resonant frequency peak at 6.671 kHz measured for a gold coated SU-8 cantilever.

Cantilever	length (μm)	width (μm)	thickness (μm)	f (kHz)	Q factor
SU-8	500	100	5.5	6.641	16
TOPAS	500	100	4.5	4.774	10

Table 2.1: Geometrical parameters, resonant frequency and Q factor for SU-8 and TOPAS cantilevers measured in air.

As initial tests, resonant frequency measurements were performed on SU-8 [109,110] and TOPAS [55] cantilevers. Gold pads were patterned on the surface of the cantilevers to provide higher reflectivity and increase the SNR (see Figure 2.11). In Figure 2.12 the resonant frequency measurement of a SU-8 cantilever having length of 500 μm, width of 100 μm and thickness of 5.2 μm is shown. The measurements were acquired in air. Similar measurements were done for TOPAS cantilevers, and in both cases the intensity of the reflected light was sufficient for the resonant peaks to be detected.
Table 2.1 summarizes the measured frequencies and corresponding Q factors.

Conclusions on system requirements

At this stage it was proved that the system was able to acquire signals from micro-cantilevers and, together with deflection measurement and profile analysis, to perform sequential thermal noise measurements over several cantilevers. Compared with the optical lever technology, the laser alignment process of the PUH was extremely simplified. However a series of technological issues were to be faced:

- Mechanics: a stable mechanical system was needed. PUH performances were expected to be highly influenced by external mechanical noise sources. The rotating stage was to be embedded in a stiff structure connected to the PUH plane. the DVD-ROM heads had to be positioned precisely along the cantilever tracks, with the need of rough and fine positioning options.

- Data acquisition and processing: a software support was necessary to acquire and store the data sent to the DAQ card. The issue of the data size was critical, considering each scan of one chip was giving around 20 Mb of raw data. With this initial acquisition protocol, a single experiment of the ones reported in Chapter 6 would have lead to more than 10 Gb of text files.

- Automation: a motor and PUH mutual interface was necessary to perform automated measurements. The software was needed to control the different input (FES, motor position) and output (VCM coils, motor controller) simultaneously and through the same program.

According to the limitations of the configuration illustrated in Figure 2.9, the first version of the system was assembled.

2.3 *System V1*

System V1 was fabricated after the preliminary tests presented in Section 2.2 were completed. This first version of the full system was designed to approach solutions for solving problems that were identified as priority issues: system robustness enhancement, wobbling compensation, data acquisition and automation development. Particular attention was given to the development of wobbling reduction strategies.

2.3.1 Mechanical assembly

Figure 2.13 schematically illustrates the assembly process of *System V1*. Even though the approach to the mechanical design was basic, several tests were able to be carried out with this system.
The use of multiple optical heads in this preliminary version was implemented for several reasons. (i) Multiple PUHs could be employed simultaneously to perform monitoring of bending, surface roughness and resonance frequency. (ii) The PUHs could be arranged at different radius positions and employed for measuring simultaneously chips placed at various distances from the center of the disc. (iii) One or more PUHs could be dedicated to wobbling compensation purposes.

2.3.2 System wobbling compensation

Several tests were aimed at determining the intrinsic wobbling of the shaft-disc system illustrated in Figure 2.13. To this purpose a dedicated disc fabricated in SU-8 and coated with a reflecting layer of aluminum was used. The PUH was focused on the metal ring and the system was spun at very low speed. The monitoring of the FES during the spinning gave information about the deviation of the disc surface from the focal point during the rotation.

The distance between laser and cantilever apex was found to vary during disc revolution due to inhomogeneities in the disc and in the motor-shaft assembly. Deviations up to 600 μm in the Z direction were measured during the experimental tests. Considering the short linear range of the PUH (6 μm), an automated protocol that employed an auto-tracking PUH was required to keep the lasers continuously focused on the reflective surface.

The role of the auto-tracking PUH is illustrated in Figure 2.14. The feedback loop of the FES was used to readjust the Z-position of the laser spot through the vertical movement of the VCM (see Section 2.1.2). Focusing PUH 1 onto the reflective coating, the feedback loop measured the voltage cycle needed to keep the laser focused at a constant distance from the disc surface. This signal is then superimposed phase-shifted to the voltages input driving PUHs 2, 3 and 4. The real-time approach in the auto-tracking process ensured that any variation of the disc-PUH relative distance was instantaneously

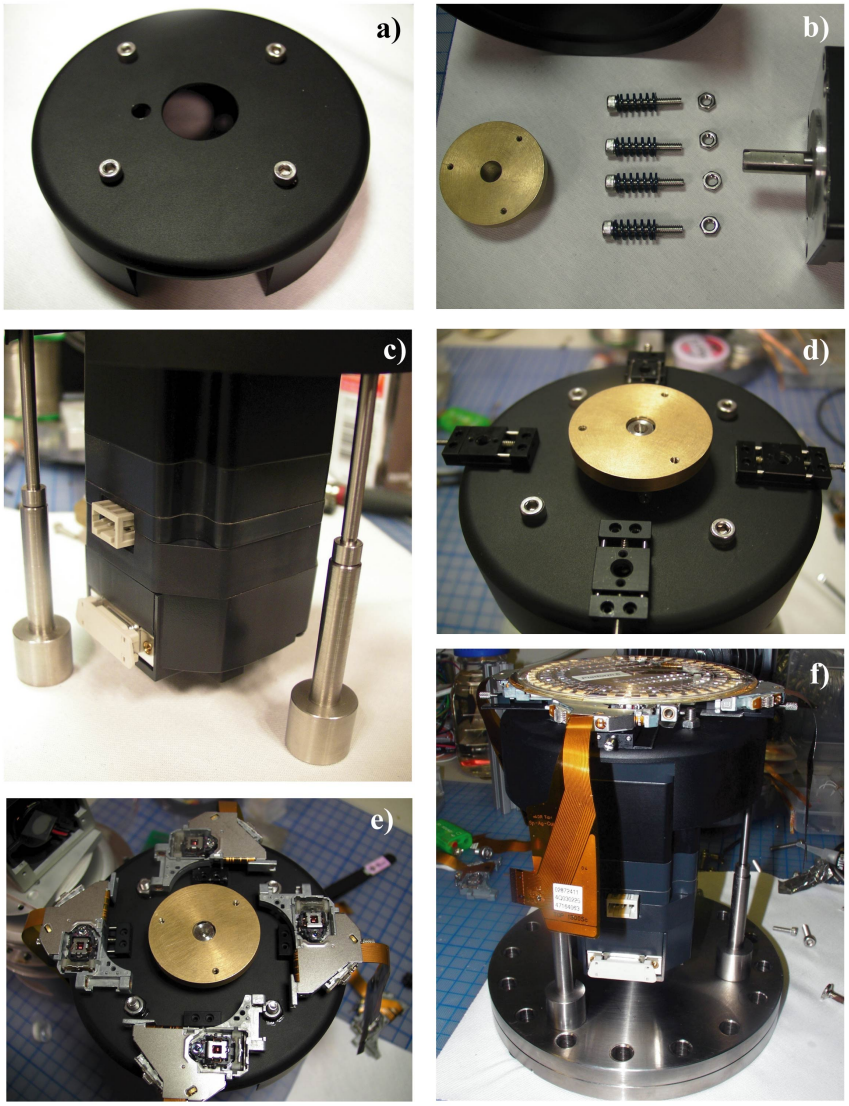

Figure 2.13: Assembly process for the first version of the system. a) A central hole was cut onto a metal support. b) Four spring-loaded screws were used to clamp the motor on the support and c) four steel bars were used to keep the motor suspended. d) Four 10 mm range linear stages oriented toward the center of rotation were glued on the support, and e) four PUHs were mounted on the stages. f) Complete system with a disc mounted on the rotating shaft.

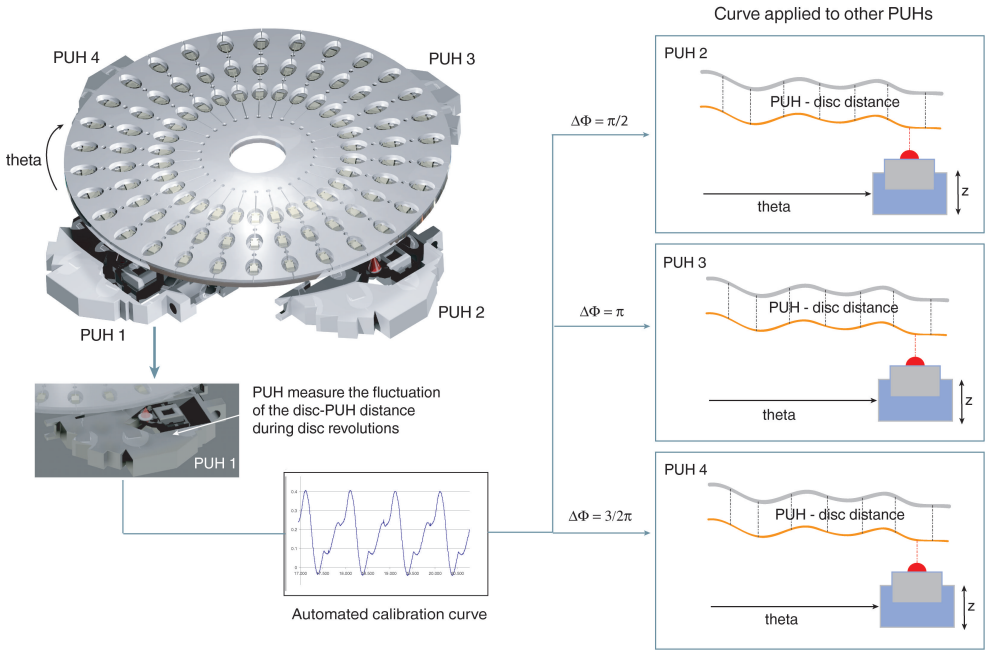

Figure 2.14: Scheme of the 4-PUHs auto-tracking approach.

recorded and the VCM position of the sensing PUH corrected.

Auto-tracking system limitations

The main problem of the auto-tracking method was due to the different responses of the VCMs to the same current signal applied to their coils.
Each PUH was in fact found to move along the Z direction slightly differently for same values of input current.
In Figure 2.15 the VCM autofocusing movement for two PUHs is plotted. In this experiment 2 PUHs were used for auto-tracking, and their response were compared to evaluate the congruence of the two signals.
After phase shifting one of the curves, it was observed that the signals were similar but not fully coincident. While the disc was spinning, PUH 1 measured the "wobbling voltage" slightly differently than PUH 2.
These small differences in the output voltage correspond to several tens of microns in vertical deviation, compromising the possibility of applying the auto-tracking method to high precision measurements.
Furthermore, the acquisition speed was found to affect the auto-tracking process. During the tests it was possible to apply this method at relatively low speed (below 10 rpm), while at higher values the method suffered the time delay of the auto-tracking data process, leading to small misalignments of the sensing PUHs.
On top of this, a slight cross-talk between the currents applied in the Z and in the X

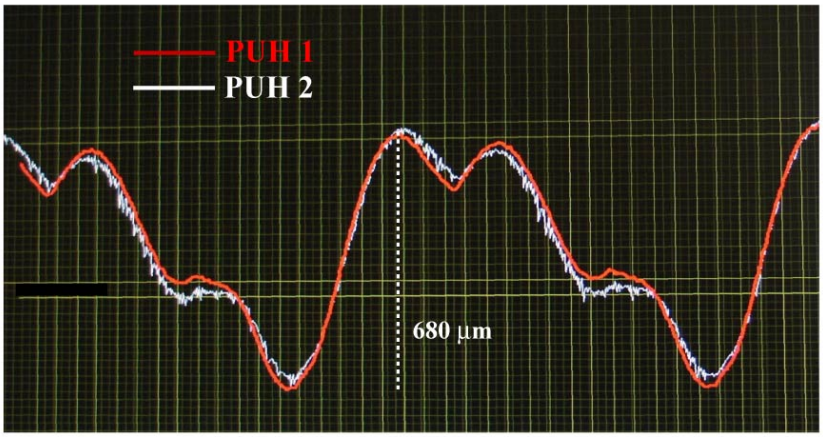

Figure 2.15: Auto-tracking curves acquired using 2 different PUHs. The signal acquired from PUH 1 (red) slightly differs from the one measured with PUH 2 (white). The measured wobbling was, in its maximum, almost 600 μm.

direction was observed. This cross-talk induces a small tilting of the lens when current is applied to one of the coils, affecting the accuracy of the measurements.

Eventually, optical corrections of the lenses and mechanical optimization of the rotating stage were found more convenient solutions than the elegant but technologically challenging auto-tracking method.
The experience gained trying to apply a auto-tracking system was anyway found very useful for future development of the platform.

2.3.3 High-throughput measurements - proof of concept

In order to circumvent some of the limitations imposed by the wobbling, a lens with lower NA was used to carry out the first high-throughput measurements. A plastic lens with NA=0.16 was mounted on the PUH and its optical response was characterized. It was found that the characteristic S-curve (Figure 2.3d) consisted in a very long linear range, measured to be around 350 μm. The sensitivity of the detection was however reduced, dropping from 0.3 nm/mV to 30 nm/mV. The overall resolution hence was estimated to be around 60 nm.
Employing this new optical system the first high-speed tests were performed.

Figure 2.16 shows the system interfaced to its external components. The sensing platform (a) is connected to a 4-channels preamplifier (b), where each channel corresponds to one PUH, and is interfaced to the PC through the DAQ card (c). The motor controller (d) allows the setting of the rotational parameters (speed, acceleration, spinning direction) through its commercial software. The data were constantly monitored using a standard

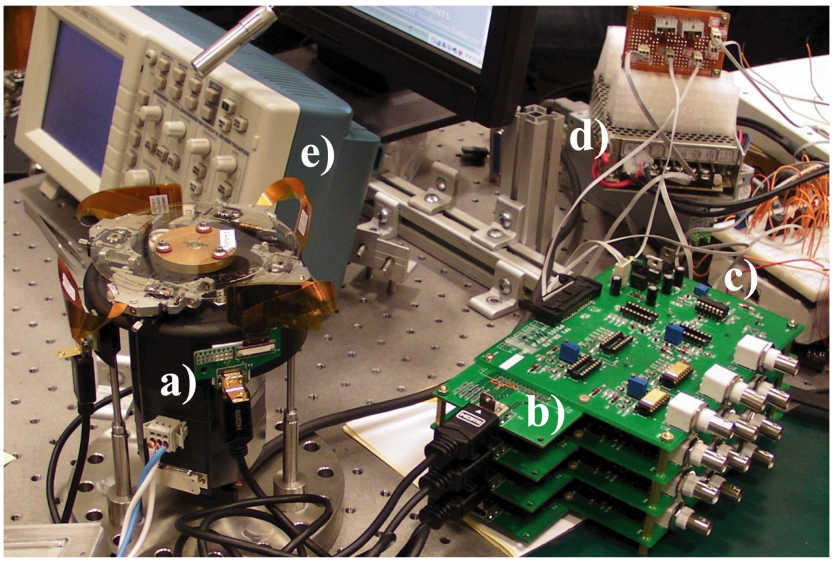

Figure 2.16: Picture of the first version of the system a) connected to its external components: b) the preamplifier, c) the DAQ card, d) the motor controller and e) the oscilloscope.

oscilloscope (e) (TPS2000B, Tektronix Inc, US).
To perform high-density data measurement tests, a disc track was loaded with 39 SU-8 chips and one silicon one, resulting in a total of 320 microcantilever beams.
When spinning the disc, the 600 μm system wobbling caused the loss of almost 25% of the cantilevers, whose focal points were lying outside the linear range of the PUH ($\sim$350 μm). However, more than 200 cantilevers were able to be read from the DVD-ROM. As reference baseline we used the focal point of a silicon cantilever. The data measured on the SU-8 ones were then referenced to this measurement point. Figure 2.17 shows a zoom of the disc containing the SU-8 chips.
During the tests the cantilevers profiles were acquired scanning the laser at different velocities.
Raw cantilever deflection signals acquired during one revolution of the disc at 60 rpm is shown in Figure 2.18a. The plot is composed of around 1.000.000 data points. Each distinguishable peak represents a chip with 8 cantilevers. Zooming in on Figure 2.18a we can extract the individual cantilever profiles, as seen in Fig 2.18b. Figure 2.18c reports the distribution of the acquired signals. The distribution has an average of 0.49 V, corresponding to 14.7 μm. The standard deviation is 0.39 V, corresponding to 11.7 μm. Assuming that the silicon cantilevers are ideally flat (datasheet from the company claim an initial deflection less than 1 μm), these variations are in agreement with initial bending measurements previously performed on batches of SU-8 chips.

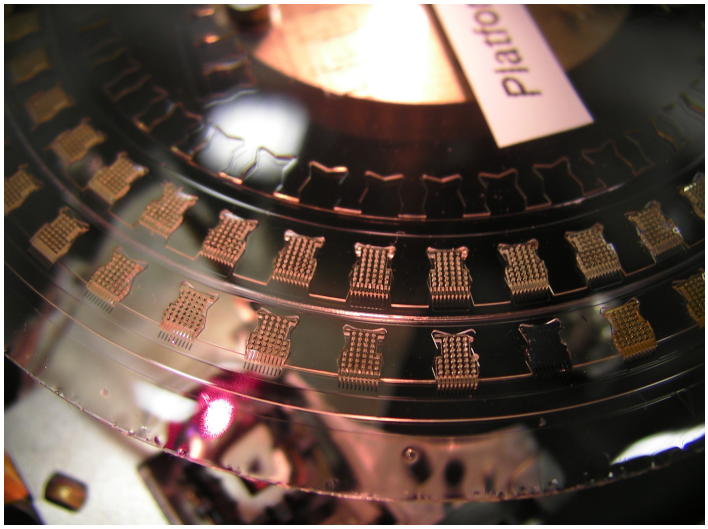

Figure 2.17: SU-8 disc loaded with 80 chips (640 cantilevers) on two different tracks. A DVD-ROM PUH with NA=0.16 lens was employed to make the first high-throughput tests.

2.3.4 System outlook

*System V*1 was used for testing high-throughput and high-resolution capabilities of the DVD-ROM based readout method. Using lenses with NA=0.16 hundreds of cantilevers could be scanned at high speed. Using lenses with NA=0.6, preliminary sensing of proteins and antibodies have also been tested (see Chapter 6). The system was also used for proof of concept of the three different measurements analyses presented in Section 2.2.1: bending, thermal noise and surface reconstruction.
Profile acquisition while spinning the disc up to 60 rpm was demonstrated. Data acquisition speed limited the actual measurement throughput. However, the analog signal observed with the oscilloscope identified cantilever profiles even when spinning the disc at 600 rpm. Software improvements are believed to allow actual measurements at very high rotational speeds.

Towards *SystemV*2

*System V*1 was extensively used for almost one year to test several discs design, software algorithms and data analysis processes.
In the following are listed the main technology limitations that brought the project in designing and fabricating the second generation of the sensing system.

- Mechanical parts: the mechanical components needed to be re-designed: the *System V*1 overall stiffness of the system was found to be insufficient for absorbing the vibrations generated by the motor. The noise level (measured by focusing the laser onto a cantilever and monitoring the RMS of the signal) shifted from 5 mV to 20 mV when the disc was rotating.

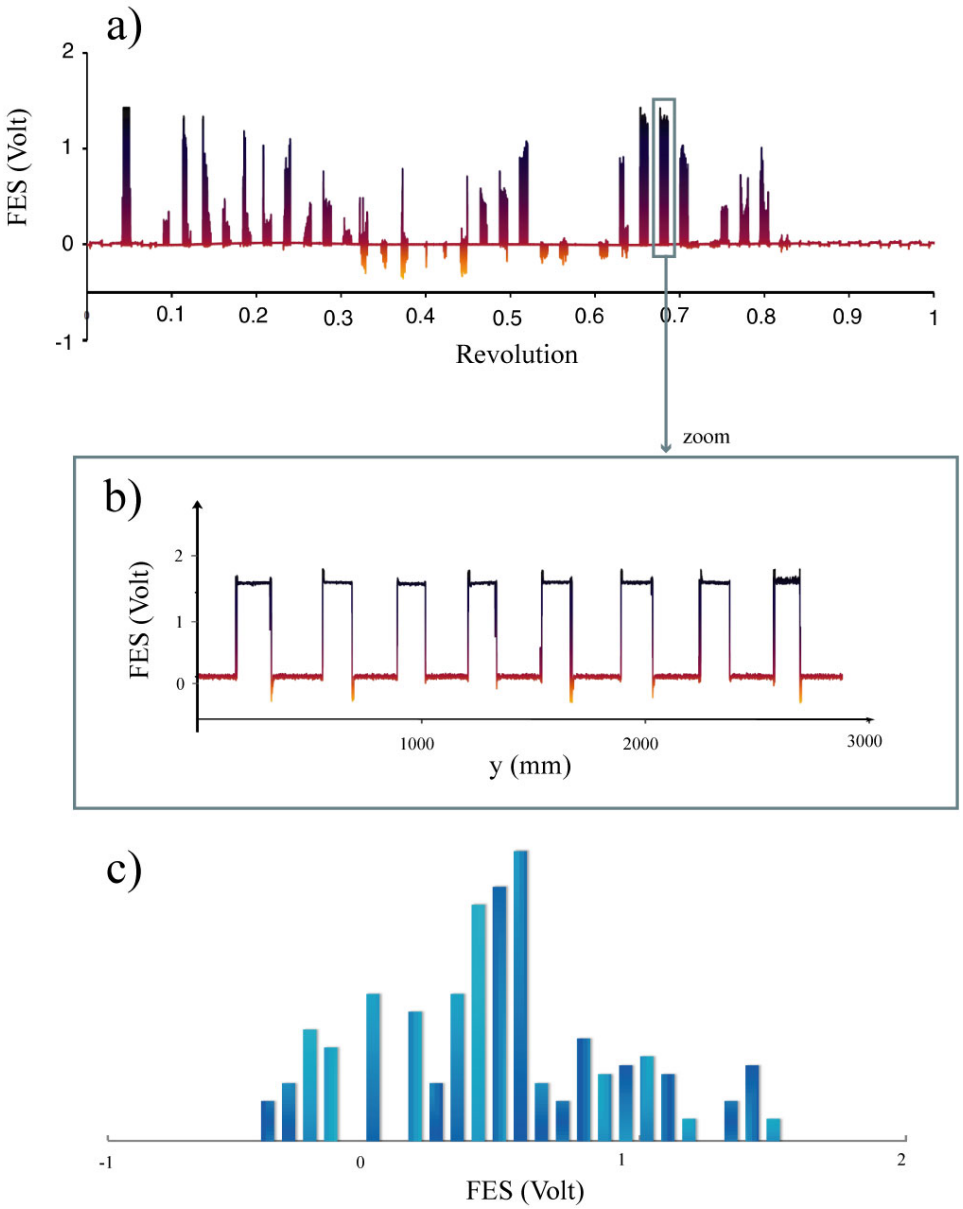

Figure 2.18: Demonstration of parallel data acquisition. a) Raw data from one revolution of the DVD. Each peak corresponds to one cantilever chip. b) The obtained profiles from a single cantilever chip. c) Distribution of the measured initial bending of in total 240 cantilevers.

The linear stages were inappropriate for fully exploit the capabilities of the system. Longer range movement was required in order to scan the entire surface of the disc, and a Z-direction stage for rough alignment was found to be necessary if different NA lenses were to be employed.
The disc has to be shielded from external environmental changes (e.g. temperature, air flow, acoustic waves, etc...), thus requiring a closed chamber design.

- Rotating stage: the wobbling of the rotating disc had to be highly reduced, if high-throughput and high-resolution should be achieved. Within this context, the mechanical shaft had to be re-designed. Furthermore the motor used in *System V1* was overheating very fast, inducing temperature gradients around the PUHs. These thermal fluctuations were later found to highly affect the performance of the DVD-ROM PUHs.

- Microfluidics: at this stage the no microfluidics has been integrated. The reservoirs were manually filled with the sample by using pipettes. The design of centripetal-microfluidics-based discs was only partially tested with the *System V1* which did not include tools for liquid handling. It was clear a needing of a plug-and-play inlet system, as well as an appropriate waste sample handling system. Furthermore neither the PUHs nor their electrical connections were protected from liquid leakages. When spinning fast to empty the sensing reservoir, the PUH had to be protected by the user with lab tissues.

2.4 *System V2*

In order to address the limitations listed in the previous section, a new version of the system was designed and fabricated with improvements to the electronics and to the mechanics. The electronic modifications were oriented mainly to enhance the signal to noise ratio and to reduce the overall size of the external components of the system (preamplifier, PUH connectors, motor controller and various cables).
The main improvements were focusing on mechanical components design/configuration, on rotational stage's optimization, and on integration of microfluidics tools for liquid dispensing.
System V2 was used to perform first tests of continuous flow measurements (e.g. for DNT detection and PDGF sensing).

2.4.1 System design and mechanical parts

Contrary to *System V1* which was built by assembling existing components, this improved version was designed using CAD software (SolidWorks 2008, Dassault Systmes SolidWorks Corp., US) before being manufactured and assembled (Figure 2.19).
The new platform was mounted onto a thick aluminum base, 26 cm wide and 1 cm thick, which provided high mechanical stability to the whole system.
Four L-shaped platform supports were screwed to the base of the platform. Long X-Z

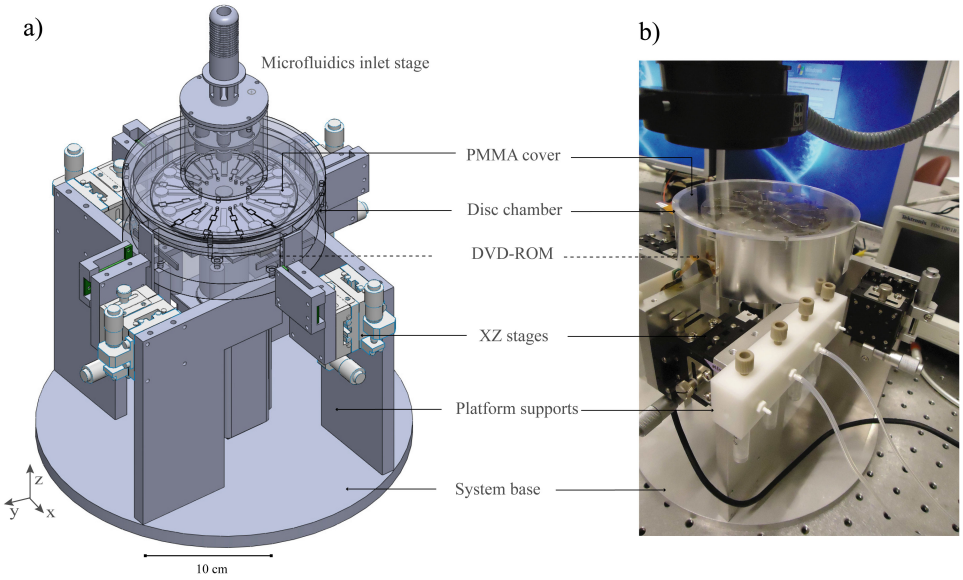

Figure 2.19: a) CAD model of *System V*2. b) Picture of the setup.

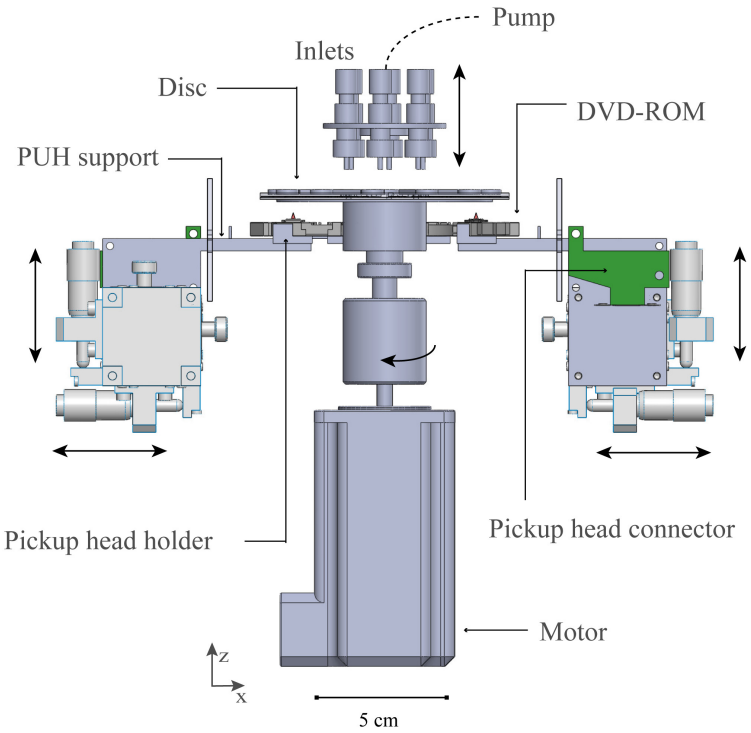

Figure 2.20: Section view of the CAD model. The arrows indicate the degrees of freedom of the PUH supports movement (X and Z).

stages (Misumi XYCRS40, Misumi Corporation, JP) were mounted on each support, providing 1 cm of linear movement in both direction. On each X-Z stage a cantilever-shaped aluminum support for the PUH were mounted. These beam structures (5 mm thick) were free to move inside the chamber (See Figures 2.20 and 2.21) along the stages direction, providing long-range multiple direction adjustment for the DVD-ROM PUHs.

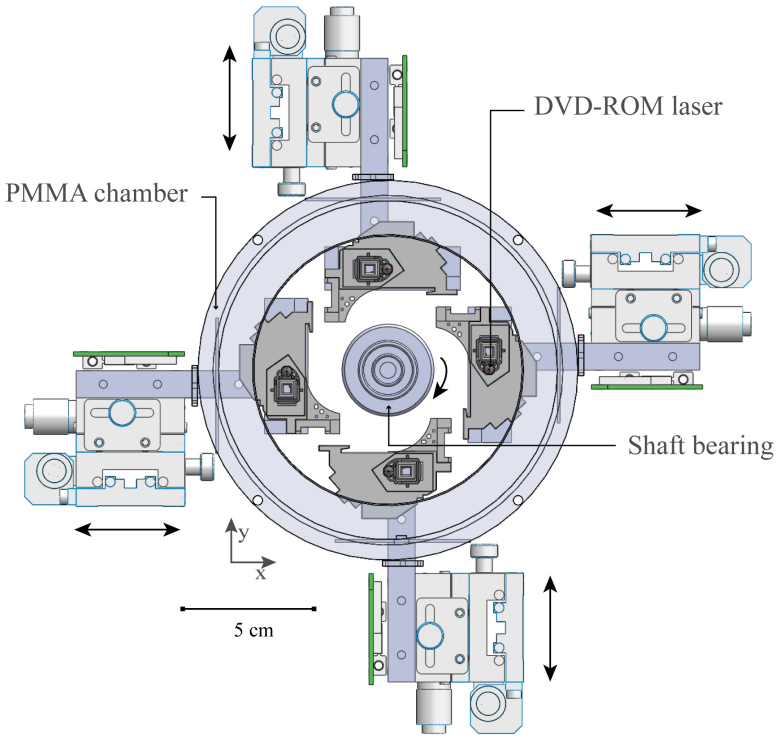

Figure 2.21: Top view of the CAD model. The four PUHs are mounted over their supports which can move towards the center of rotation. A bearing is mounted on the shaft head for wobbling reduction.

The electronics connectors, plugged to the PUHs through the FFC, were mounted directly on these supporting structures. All the mechanical components were built in aluminum.
A 12 cm diameter aluminum chamber was built on top of the system. The chamber, visible from the top in Figure 2.21, had 4 open features for the PUH supports. The chamber was closed with a PMMA cover to ensure sealing from external air flow.
The arrows in Figures 2.20 and 2.21 illustrate the movable parts of the system. In Figure 2.20 the section view of the system shows the PUH supports linear movement in the X-direction (toward the center of rotation for focusing on the cantilever apexes), and in the Z-direction (for focus distance adjustment). A set of movable inlets for the sample

injection can move along the Z-direction on the top of the disc.
In Figure 2.21 is possible to see the sensing chamber and the configuration of the PUHs below the rotating disc.

A new stepper motor (Fastech Ezi-STEP-PR-35S, Fastech Corp., KR) with higher precision and less thermal heating was used for this setup. This device had the possibility of rotating with a resolution of 20.000 steps per revolution. This angular resolution (0.018°) was enough to allow the focusing of the laser on the individual cantilevers, important feature for automatic thermal noise measurements. Scanning along the width (100 μm) of cantilevers positioned at 3.5 cm from the center of rotation implied a rotation of the disc of 0.16°. With this new motor it was thus possible to automatically position the laser spot onto 8 different points along the width of one single cantilever.
Heat exchangers were also mounted on the motor's base in order to further reduce the overall heating of the system.
The design of the new motor shaft was aimed at reducing the wobbling of the rotating stage. Several high-precision bearings were employed as connection between the rotating shaft and the loading head. Strong pre-load was applied to the system in order to minimize the effects of the intrinsic fluctuation of the manufacturing of the shaft head. The total wobbling (at the cantilever track radius) was measured to be around 250 μm in the Z-direction, roughly half the value measured on *System V*1.

2.4.2 Microfluidics integration

One of the main achievements of *System V*2 was the integration of a microfluidics system for automatic handling of the samples.
A pressure-driven pump (Fluigent MSC-8-1000, Fluigent, FR) was connected to 1 ml containers positioned at the sides of the system (See Figure 2.19b). The Fluigent device is a fully automated multi-channels pump which interfaces through Labview programs with the PC. Each channel can be controlled independently with pressures ranging from 0 to 1000 mbar. This instrument was found to be extremely useful for injecting multiple samples with high speed and precision in the channels patterned on the sensing disc (where on the other side had some disadvantages when working in continuous flow).
A six-nozzle system was designed and built into a circular PMMA frame. Magnet-assisted clamping of the nozzles to the microfluidics disc was found to be an extremely efficient way of building a plug-and-play injection system.
The working principle is illustrated in Figure 2.22a. Six inlets (tip diameter 1.8 mm) are encapsulated into a circular PMMA structure to fit their relative holes in the microfluidics disc. The sensing disc is positioned above a 1 mm thick iron disc, clamped to the motor shaft. Rare earth magnets (Supermagnete, Webcraft GmbH Corp, DE) are glued to the center of the PMMA frame, and the magnetic force generated from the iron disc is used to seal the inlets. Several tests were performed at different pressures without observing leakage problems.

The overall rotating structure is thus composed motor shaft, iron disc (clamped to

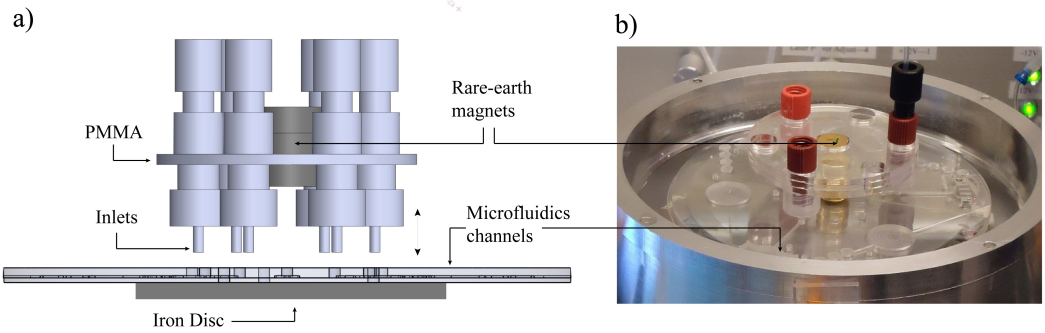

Figure 2.22: a) Schematic view of the magnet-based microfluidic clamping. The attractive force between the magnets and the iron plate under the disc keeps the six nozzles tightly connected to the corresponding microfluidic inlets. b) Picture of a polymer disc connected to 3 nozzles through 5 rare earth magnets.

the shaft), sensing disc and microfluidics inlets. When performing measurements in wet & dry, the inlets are clamped to the structure, the liquid dispensed, and then they are released to leave the disc free to rotate without tubing. On the other hand, when continuous flow measurements are carried out, the microfluidics inlets are left connected to the rotating stage and the entire structure is spinning. This configuration does not allow rotate the disc for several revolutions as tubes will wrap and eventually snap. To avoid this situation the disc is spun clock-wise (e.g. for 1 revolution) and counter-clock-wise. The cantilevers are thus measured within the same time frame and speed, however this method avoids problems related to the tube presence and allow continuous flow measurements to be performed under the same high-throughput conditions.
In order to clamp and release the inlets in a fast way, the PMMA frame is connected to a handle bar that can be manually pushed toward the disc, and then pulled back.

2.4.3 System outlook

Experiments in gas and liquid phase on explosive samples (see Section 6.4) were performed using this setup, as well as some of the preliminary experiments done on aptamer-functionalized cantilevers reported in Section 6.5.
The main limitation of this version was given by its sensitivity (hence resolution and detection limit) in liquid phase. The sensitivity of the device was the same as in the previous version, since the PUH settings were basically unchanged. Using NA=0.16 it was possible to scan the whole disc and measure hundreds of cantilevers simultaneously, however remaining with optical sensitivity of 30 nm/mV in air, and 100 nm/mV in liquid. These values were found sufficient to carry high-concentration measurements (for example in the μM range of Streptavidin measured in wet & dry), but were not optimized for lower concentrations detection, in particular in liquid flow.

Towards *SystemV3*

The following list summarizes the main issues that brought the project to move towards the third generation of the platform.

- Optics and resolution: In order to achieve resolutions comparable with existing technologies, vertical sensitivities in the nm/mV range were necessary. These values were already obtained for measurements in air but not in liquid. The sensitivity of the NA=0.16 lens was found to be poor for nM concentration measurements (where cantilevers deflect in the orders of tens to hundreds of nm).

- Rotating stage: even if the wobbling of the rotating disc was highly reduced in the *System V*2, the rotating stage had to be re-designed to allow the cantilever apexes to fall within the linear range of higher resolution lenses. NA=0.2 or NA=0.45 were good candidates, having vertical displacement sensitivity in liquid of, respectively, $\sim$ 25 nm/mV and $\sim$ 5 nm/mV (once optimized). Their working range was measured to fall between 40 μm and 120 μm. In order to implement this huge reduction of the wobbling, a new approach to the rotating stage was then necessary.

- Weight and size: Once the overall stiffness of the system was sufficient for mechanical noise reduction, options for reducing the size of the system were investigated. The motor was too bulky in the vision of commercializing the system, however the resolution of stepper motors is generally proportional to their size and weight. New strategies had to be implemented to overcome such difficulty.

2.5 *System V3*

*System V*3 was built during the last months of the PhD project. Its purpose was to create a stable wobble-free platform for high-resolution continuous flow measurements in liquid medium. This system was specifically designed to integrate the high-throughput concept, proved with *System V*1, with high-resolution measurements, demonstrated through the use of NA=0.6 lenses in connection with *Systems V*1 and *V*2.
Furthermore, first attempts to miniaturize the platform were carried out. In the next sections the main design improvements are presented.

2.5.1 System design and mechanical parts

The design of the mechanical components was specifically aimed at reducing the mechanical wobbling. As introduced in Section 2.3.2, VCM driven wobbling compensation approaches were found non trivial to be implemented. A mechanical approach was found more feasible and easier to apply.
In order to eliminate the main source of wobbling (the motor shaft and the clamping metal head), a smaller motor was connected to a high-precision rotating bearing through a pulley belt. The rotating bearing (Reali-slim Type X, Kaydon Corporation Inc, US) is composed by steel spheres that allow the structure to float above the spheres. The

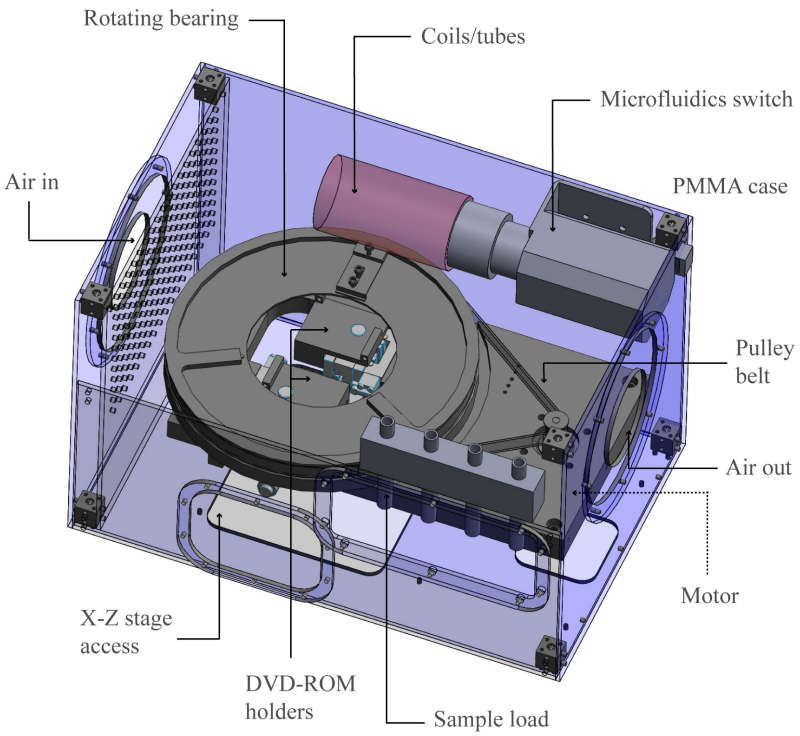

Figure 2.23: CAD model of *System V*3. The PMMA case keeps the system isolated from external environmental noise. Several open-close accesses are available for manual adjustments of the stages and for sample loading.

wobbling of the stage thus relies on the precision of the dimensions of the spheres.
The rotating bearing and the motor are mounted over an aluminum support. Two X-Z linear stages (same as the ones employed in *System V*2) hold the PUH under the rotating bearing.
Figure 2.23 shows the CAD model of the complete system. The design reveals several new functionalities, compared to version 2:

- New pulley belt system: the rotating stage is now composed by a big high-precision ring bearing that is driven by a belt, allowing the rotating stage precision to rely on the bearing instead of on the motor shaft. The bearing has X-Y plane precision of about 5 micron (from datasheet specs). Wobbling is thus in this way highly reduced.

- New motor: the new motor (Fastech Ezi-42S-B, Fastech Corp., KR) is considerably smaller than the one mounted on *V*2, with lower precision in terms of steps/revolution. However the pulley belt system magnifies the angular resolution by a factor equal to the ratio between the rotating stage diameter (188 mm) and

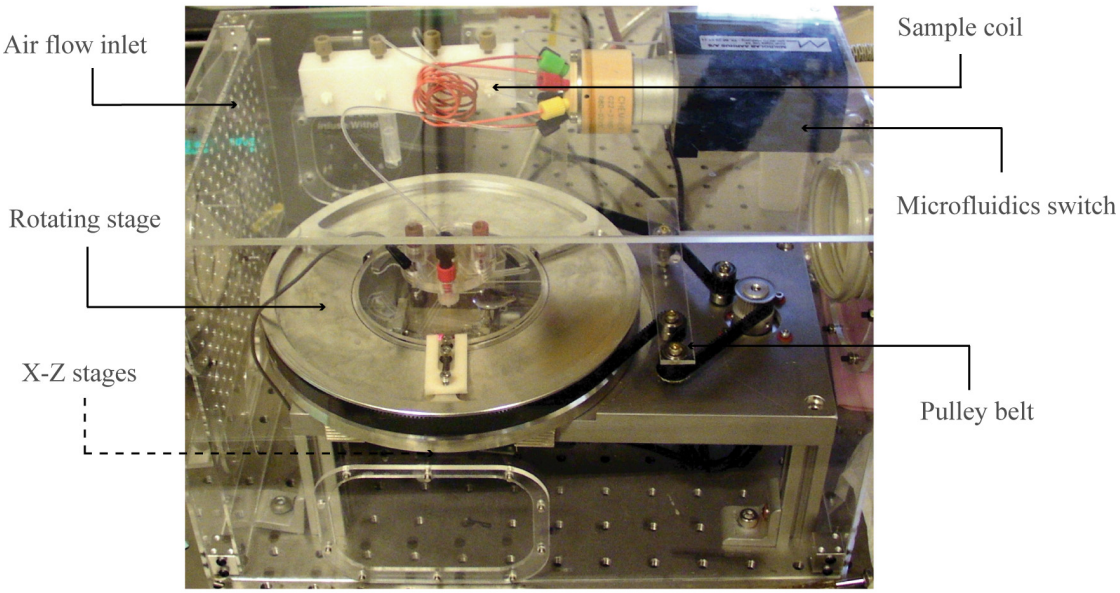

Figure 2.24: Picture of *System V3* at present status.

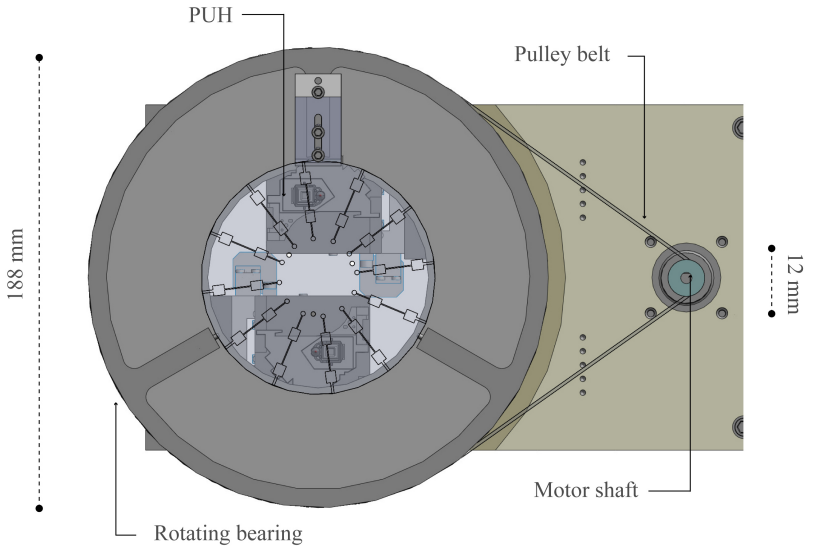

Figure 2.25: Top-view of the CAD drawing of *System V3*. The ratio between the pulley shaft (12 mm) and the rotating bearing (188) magnifies the angular resolution of a factor of 15. Under the disc, two PUHs are aligned along the sensing tracks.

the pulley shaft diameter (12 mm). The angular resolution is thus enhanced by a factor of 15 (See Figure 2.25), resulting in a overall angular resolution about twice the one *System V2* had.

- New preamplifier: a new electronics block developed at IPAS for AFM measurements was implemented on the system. The preamplifier allows magnification of the FES signal output.

- Integrated microfluidics: the switch, the coils, the tubes, the inlet and outlets, the waste and the sample loading reservoir were all positioned within the PMMA external frame. The PMMA case keeps the temperature of the overall microfluidics path at constant temperature. The sample can be loaded in the coils directly from the system. Two tubes connect the system to the external pump (e.g. a syringe pump).

- Environmental shielding: The PMMA case is covering completely the system. Several access points (open-close configuration through magnetic clamping) are used for stage adjustments, sample loading and replacing. A flow controller device (Airthermz-ATX, Mestek, Inc., US) is used for keeping the temperature constant via controlled heating of air flow throughout the camber.

- Higher resolution lenses: different lenses with higher resolution performances were tested and integrated in the system.

2.5.2 Optics characterization

One of the key technologies implemented in the system development was the modification of the optical path of the DVD-ROM PUHs. The parameters defining the S-curve illustrated in Figure 2.3d (linear range and sensitivity) could be tuned through adjustments of the NA of the lens and through magnification of the output signal.
The combinations of these two methods made it possible to make very fine adjustments of the optical properties of the sensing system.

Lens modification

Using commercial PUHs without modification it was found impossible to perform high-throughput analysis, due to the intrinsic incompatibility between the initial bending of the cantilever sensors (from ± 1 μm to ± 10 μm), the mechanical wobbling of rotating stages (from ± 20 μm to ± 500 μm), and the short linear range of commercially available optical heads (from 2 μm to 6 μm).
Without lenses modifications it was also difficult to perform measurements in liquid. The cantilever apexes were placed 1.5 mm from the bottom surface of the glass disc, while the DVD-ROM has working distance of just 1.28 mm.
Using lenses whose NA varies from 0.6 to 0.1 it was indeed possible to tune the working distance range of the PUH, and to modulate the FES linear range from few μm up to

Objective lens		0.6	0.45	0.3	0.2	0.16
Working distance	(mm)	1.28	2.3	4.2	10	18
Linear range (air)	(μm)	6	20	60	$\sim$ 140	$\sim$ 350
Linear range (liquid)	(μm)	n.a.	40	150	$\sim$ 380	$\sim$ 500
Sensitivity (air)	(nm/mV)	0.3	5	15	$\sim$25	$\sim$30
Sensitivity (liquid)	(nm/mV)	n.a.	$\sim$10	$\sim$40	$\sim$80	$\sim$ 100

Table 2.2: Optical properties of PUH with different NA lenses without signal amplification (zero gain).

350 μm.
Controlling the focus distance and the sensitivity of the detection, it was possible to monitor the deflection, the surface roughness, and the thermal noise of multiple cantilevers with improved resolutions. In liquid, sensitivities of the order of few nm/mV when measuring hundreds of cantilevers could be achieved.
Table 2.2 reports the measured values of sensitivity and linear range in liquid and in air for the 5 types of lenses employed in the project.
Figure 2.26 schematically illustrates the relation between NA and resulting FES linear range.

FES amplification

Another strategy to enhance the sensitivity of the FES detection involve the magnification of the output signal. At a cost of a reduced linear range, the sensitivity could be improved up to one order of magnitude.
In order to characterize the response to signal magnification, several lenses were calibrated, in air and in liquid, applying different magnifications to the FES. Measuring the output voltage at different vertical displacements it was possible to derive the characteristic S-curve. Through the linear range it was immediate to evaluate the sensitivity
Figure 2.27 illustrates the results obtained through calibration, in air and in liquid, of a NA=0.2 lens at different amplifications (gain values). It is clear that the higher the gain value, the shorter is the linear range and the higher is the sensitivity (slope of the curve). The same is valid both for calibration in air and in liquid.

Many tests were carried out on four lenses magnified at different gains. Figure 2.28 reports the measured values of sensitivity as a function of the linear range, in liquid and in air. With the combination of lens modification and gain implementation it is possible to use PUHs whose linear range varies from 2 μm to 500 μm, and whose sensitivity range from 0.5 nm/mV to 100 nm/mV.

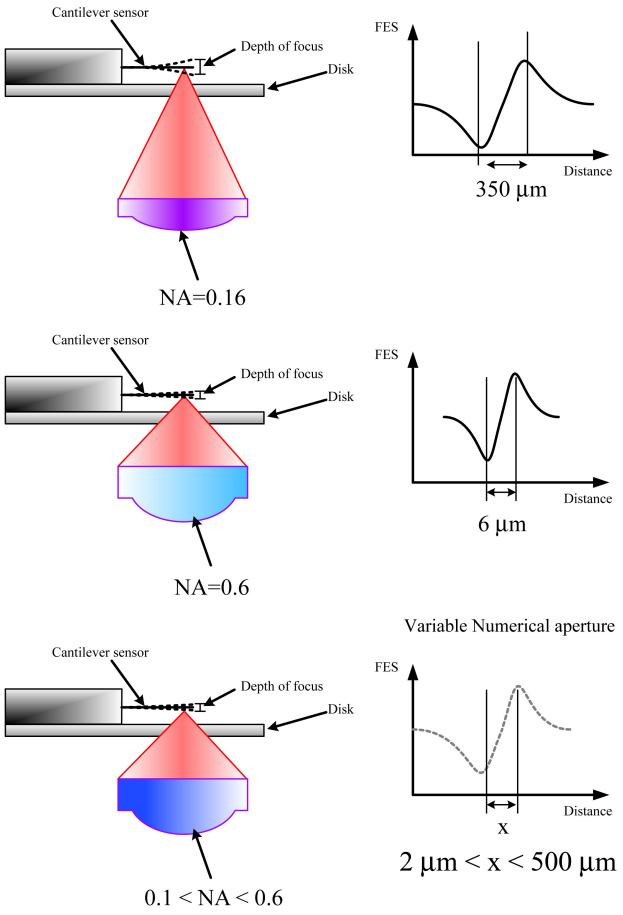

Figure 2.26: Example of different Numerical Aperture lenses modification. (top) NA=0.16 give linear range of the FES of about 350 m. (center) The built-in lens with NA=0.6 gives very small linear range (6 μm), impossible to use for high-throughput measurements or for liquid measurements. (bottom) Different NA are mounted on the PUH for tuning the FES range to the specific sensing process.

2.6 Conclusions

The DVD platform offers a number of advantages over traditional cantilever sensing. It readily supplies large amount of data for statistical analysis facilitating the onset of statistical cantilever based sensing. Moreover, the platform allows for simultaneous measurements of deflection, vibrational amplitude and surface roughness increasing the amount of information to be achieved and consequently the reliability of data.
Finally, the platform allows the integration of simple and well established method of controlling liquids by centrifugal forces. Three generations of systems have been design, built and tested. Each of them contributed to the improvement of the platform in terms of resolution, measurement speed and system robustness. In the last version of the system integration of microfluidics components has been implemented, and new optics

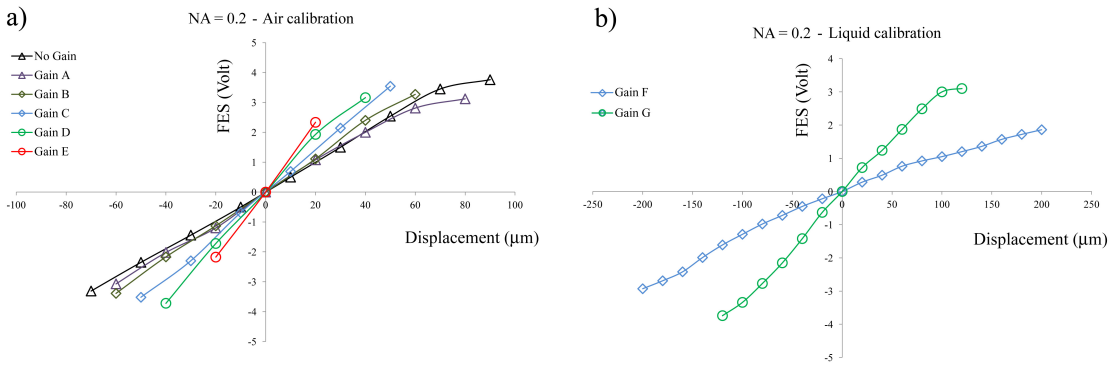

Figure 2.27: Manual calibration measurements for NA=0.2 lens, a) in air and b) in liquid. Gain values are increasing with the letter order. At increasing gain the characteristic S-curves reduce their linear ranges but enhance the sensitivity.

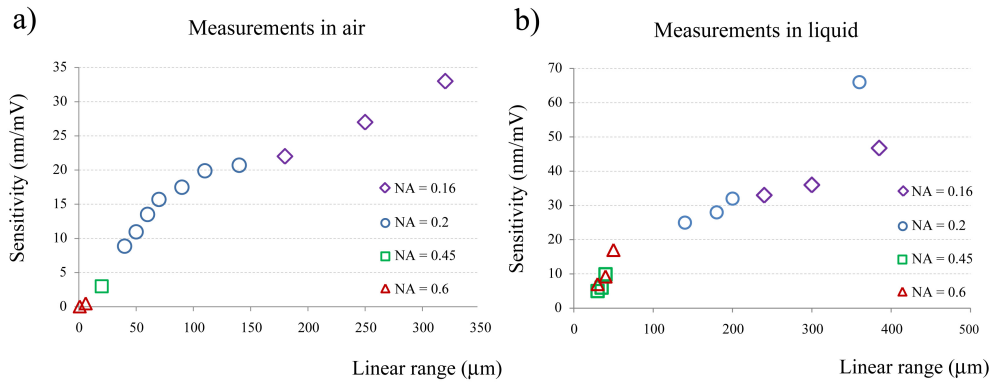

Figure 2.28: Sensitivity Vs linear range for four lenses amplified at different gains, a) in air and b) in liquid. As observed in Figure 2.27 the values of sensitivity increase (gets worse) with the linear range.

have been optimized for measurement in liquid flow.
The best optical sensitivity achieved with *System V3* range between 4 nm/mV and 8 nm/mV. Even though tens of nanometers of resolution is still far from state of the art optical lever techniques, it is believed that subnanometric resolutions can be soon achieved through further optimization of the platform.

Chapter 3

The Disc

During the three years of system development more than a dozen of disc designs were fabricated and tested. Seven designs from different fabrication processes have been chosen to be presented in this report. The disc designs can be sorted into three main categories, whose key features generally followed the progress and requirements of the corresponding system versions:

- *Disc* $V1$: Disc fabricated in SU-8 without integrated microfluidics. Mainly two designs were used with *System* $V1$ for proving high-throughput measurements. These discs, named $V1$-A and $V1$-B, are described in Section 3.2. One of them has auto-tracking patterns that were used for X-direction and Z-direction wobbling compensation.

- *Disc* $V2$: Discs fabricated in SU-8 with integrated microfluidics. Three main designs ($V2$-A, $V2$-B and $V2$-C, presented in Section 3.3) were tested and widely employed for first sensing measurements with *System* $V2$. The experience obtained through tests on *Discs* $V2$-A and $V2$-B led to the design of the last optimized SU-8 based disc, $V2$-C.

- *Disc* $V3$: Discs fabricated entirely in PMMA with integrated microfluidics. These platforms ($V3$-A and $V3$-B) were used for continuous flow measurements in connection with *System* $V3$.

Table 3.1 summarizes the main features of the disc designs that are presented in this Chapter.

3.1 Design considerations

3.1.1 Platform geometry

The idea of using a disc-like substrate design to carry out the experiments was found to be a simple and powerful concept for the development of the project.
This design has in fact several advantages: (i) the rotational symmetry of the DVD-like

Disc Version	Metal coating	Tracks	# chips	Material	Microfluidics	Used in System
$V1$-A	-	3	132	SU-8	No	$V1$
$V1$-B	Ti+Al	3	90	SU-8	No	$V1$,$V2$
$V2$-A	-	1	30	SU-8	Yes	$V1$,$V2$
$V2$-B	Ti+Al	2	24	SU-8	Yes	$V2$
$V2$-C	Ti+Al	1	36	SU-8	Yes	$V2$
$V3$-A	-	1	18	PMMA	Yes	$V2$,$V3$
$V3$-B	-	1	30	PMMA	Yes	$V3$

Table 3.1: Disc designs features.

platform allows very fast scanning of the sensors without applying torsional forces on the cantilever beams. Similar speeds would never be achievable by linear scanning. (ii) High precision handling of fluids at the microliter scale is possible by simply tuning the rotational speed of the disc itself. (iii) Several hundreds of sensors can be radially placed along defined "tracks" and read continuously. (iv) Moving the DVD-ROM PUH along the X-axis (the radial direction toward the center, see Figure 2.8) the pick-up head allows scanning of the entire cantilever surfaces, where 3D reconstruction of the beams is then obtained.

The materials used for fabrication of the different disc versions were basically three: Glass, SU-8 and PMMA. Commercially available glass wafers and PMMA plates have diameter of 10 cm (glass wafer has diameter of 10.16 cm). The overall dimensions of the discs have been kept constant along the different designs.

3.1.2 Sensing tracks geometry

The first considerations were aimed at defining the best way of placing the cantilevers on the rotating disc.
The orientation of the cantilevers could be either orthogonal or parallel to the scanning path of the laser beam. The two configurations are schematically illustrated in Figure 3.1. If the chips were to be place parallel to the scanning laser path (Figure 3.1b) the main advantage was given by the ability to measure along the entire length of the cantilever during rotation of the disc. The PUH could then be moved along the radial direction and the next cantilever could then be measured. However, the main concern was the centripetal force that the cantilevers would experience if spinning the disc at high velocities. Furthermore, the VCM-driven fine adjustment along the X direction of the PUH (for measuring the different cantilevers) was, as presented in Section 2.3.2, not trivial to apply. It was believed that the configuration illustrated in Figure 3.1a would

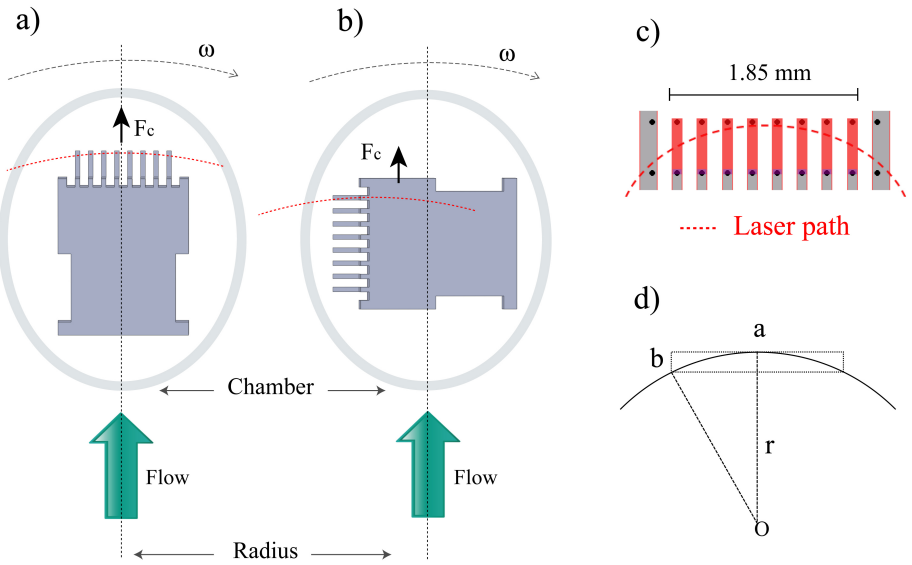

Figure 3.1: a-b) Possible cantilever orientations with respect to the laser path. c-d) Schematic illustration the curved laser scanning path along the cantilevers apexes.

bring less problems to the system development.
In this configuration the cantilevers are oriented orthogonal to the laser path, and only their apexes are scanned by the laser beam. The centripetal force would, in this configuration, act on the cantilevers along their length. This orientation was expected to reduce possible torsional behaviors of the cantilevers under fast spinning.

The laser path is circular while the cantilever apexes are distributed along a line. The radius at which the chip is placed on the disc thus affects the overall cantilever scanning process.
Figures 3.1c and 3.1d schematically illustrates this point. The entire chip width (a) is 1.85 mm. The portion of the cantilevers lengths scanned by the laser (b) depends on the distance between the cantilevers and the center of the disc (r) through the geometrical relation:

$$b = r - \sqrt{r^2 - \frac{a^2}{4}} \tag{3.1}$$

In order to be able to measure cantilevers with, for example, 20 μm long Au pads at their apexes, the chips have to be positioned at a radius of at least 2.1 cm (see Figure 3.2). A low value of b ensures that the cantilevers will be always scanned at a very similar distance from their apexes. Typically, the cantilever tracks are placed at 3.4 cm from the center, corresponding to a b value of 8 μm.

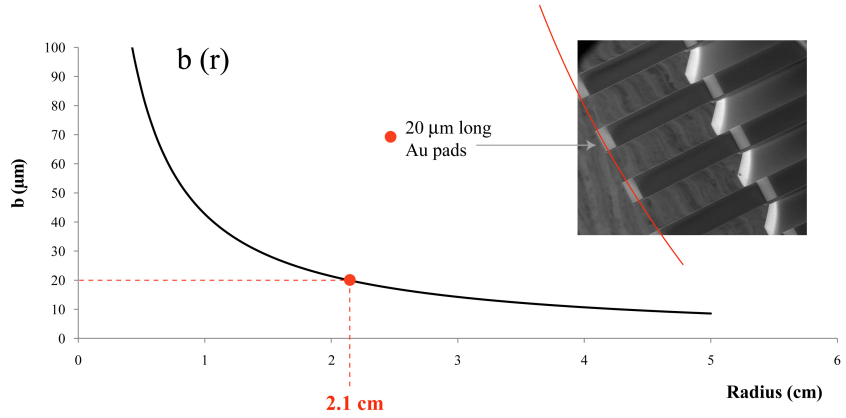

Figure 3.2: Curve shows the relation between the maximum difference between acquisition points along the cantilevers lengths (b), and the radius at which the cantilevers are placed (r). In order to keep the laser beam scanning along the Au pads (20 μm long) the minimum radius should be 2.1 cm.

3.1.3 Chip clamping

The cantilever chips should be tightly clamped on the X-Y plane of the disc but at the same time easy to move in the Z direction, e.g. for replacement of the chips. Furthermore, the cantilevers need to be suspended in order to be free to deflect and vibrate.

The cantilever suspending configuration was at first obtained by spin-coating and structuring two layers of SU-8 on a transparent Pyrex wafer (see Figure 3.3). The Pyrex aperture, patterned under the cantilevers for the bottom-up laser reading, was obtained developing a 50 μm thick SU-8 layer. On top of this, a 350 μm thick layer of SU-8 was structured for the chip clamping (the "footprint" layer). Figure 3.3b shows gold coated SU-8 cantilevers suspended over a 50 μm deep pool.
Several footprint shapes were fabricated in order to optimize the holding properties for different cantilever chip: clamping of SU-8, silicon and TOPAS chips was proven. The cantilever chips were placed by tweezers on the substrate.
It was observed that the substrate-chip holding efficiency (empirically evaluated through consecutive placement and removal of the chip from the footprint) was highly increased when moving from the traditional holder structure, where the body chip is encapsulated into a square footprint (edge-edge clamping), to configurations where the chip corners were clamped by the footprint walls (corner-edge clamping) or where the chip sides were clamped by concave footprint structures (edge-corner clamping). An example of efficient clamping structure is shown in Figure 3.4b. It integrates both edge-corner (round markers) and corner-edge (square markers) clamping points.
These geometries allowed the best fixation of the SU-8 chips. SU-8 chips show intrinsic

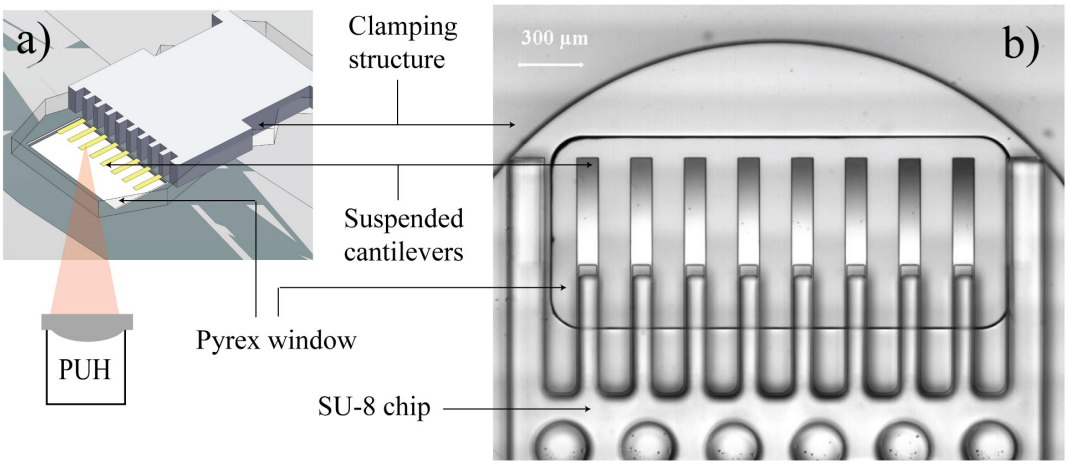

Figure 3.3: a) Schematic view of the cantilevers suspended over a glass window. b) Eight-cantilever chip fabricated in SU-8. The 500 μm long and 100 μm wide gold coated cantilevers are suspended over the 50 μm deep pool

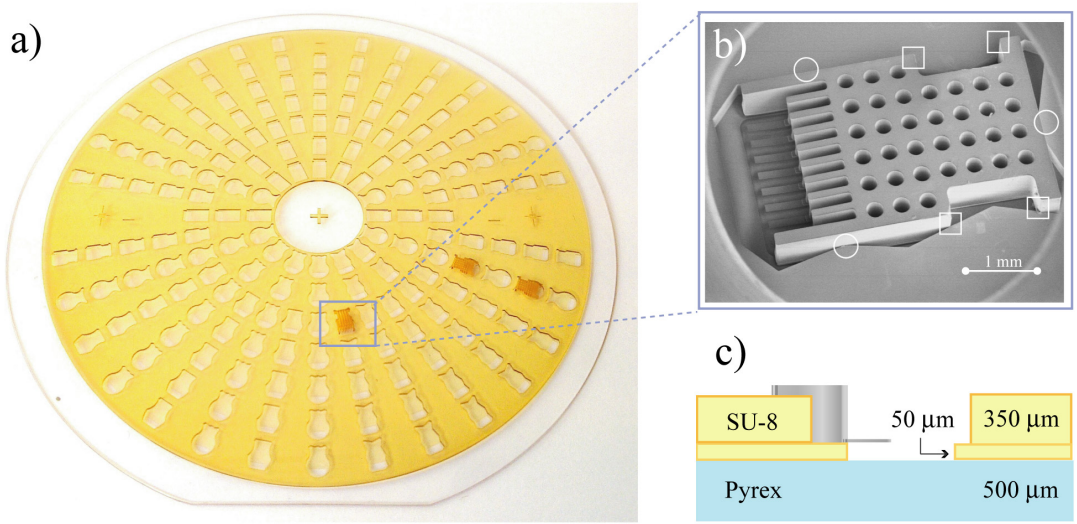

Figure 3.4: a) Picture of first disc fabricated in SU-8. More than 20 different footprint shapes were patterned in the thick SU-8 layer. b) SEM picture of the footprint configuration for SU-8 chips with best holding properties. It integrates both edge/corner (round markers) and corner/edge (square markers) clamping points. c) Cross-section view of the fabricated structures.

fluctuations of the body chip dimensions due to the photolithographic process (up to 40 μm). SU-8 corners were brittle enough to be deformed. Hereby it was possible to fit chips fabricated with different resolutions in the same footprint. Configurations like the one illustrated in Figure 3.4 were also found to allow an easy and efficient replacement of the chips, without showing significant damages of the body chip structure or of the holding structure walls. This type of clamping structure has been extensively used during the whole project.

3.2 *Disc V*1 - Proof of concept

3.2.1 High-throughput measurements

*Disc V*1-*A* was the first disc to be used for cantilever test measurements. It was used for the proof of concept of bending and thermal noise measurements (Section 2.2) and for first demonstration of high-throughput profile acquisition (Section 2.3.3).

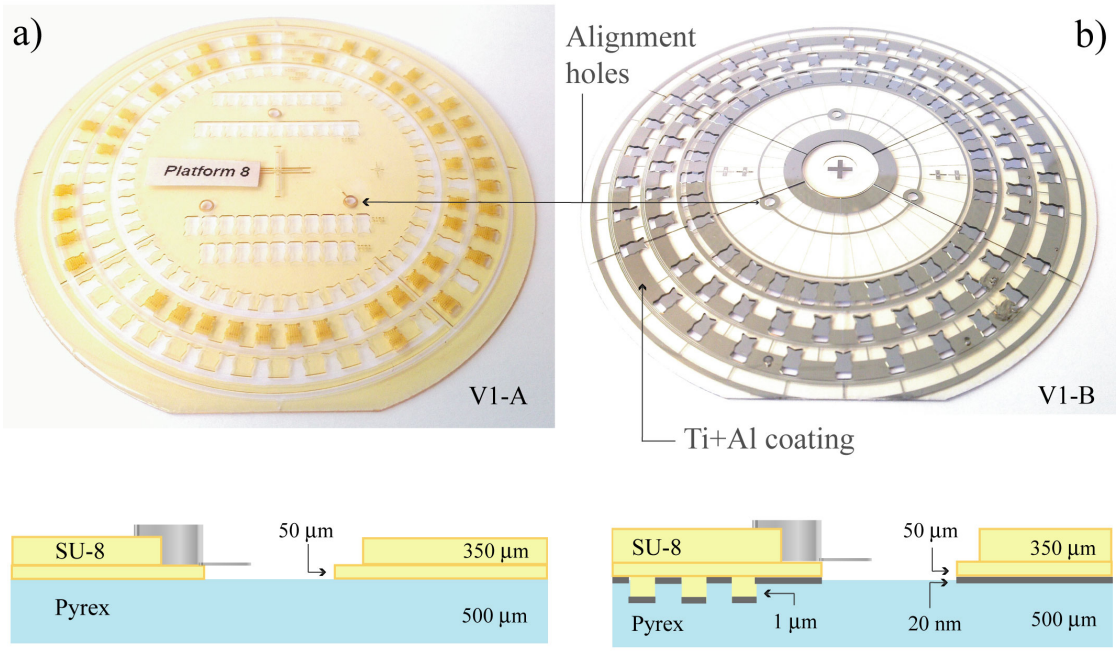

Figure 3.5: a) Picture of *Disc V*1-*A*. The disc is composed of two layers of SU-8. b) *Disc V*1-*B* includes a regular 1 μm deep pattern for X-direction tracking, etched in the fused silica wafer. The wafer is coated with 20 nm of Ti and 100 nm of Al before structuring the two layers of SU-8.

The disc, shown in Figure 3.5a can hold 132 chips on three sensing tracks, resulting in a

total of 1056 individual cantilevers loaded on the disc. The disc was fabricated in SU-8 on a Pyrex wafer.
Figure 3.5a also shows a section view of the disc: a 50 μm thick layer of SU-8 is spin-coated and patterned over the Pyrex wafer. This layer defines the pool above which the cantilevers are suspended. Thanks to this thin layer the cantilevers are free to bend or to vibrate and can be read through the Pyrex aperture. The second SU-8 layer is 350 μm thick and is used for the body chip clamping. The clamping geometry is the one illustrated in Figure 3.4b.

Disc V1-A was the first tool employed for accurate system wobbling characterization. During rotation of the disc two types of wobbling were observed. The first was the "standard" Z-direction wobbling described in Section 2.3.2. The second was an in-plane deviation of the disc rotation due to a small mismatch (ΔO) between the disc geometrical center and the motor center of rotation. ΔO was generated by misalignments between the motor shaft head and the alignment holes drilled into the disc.

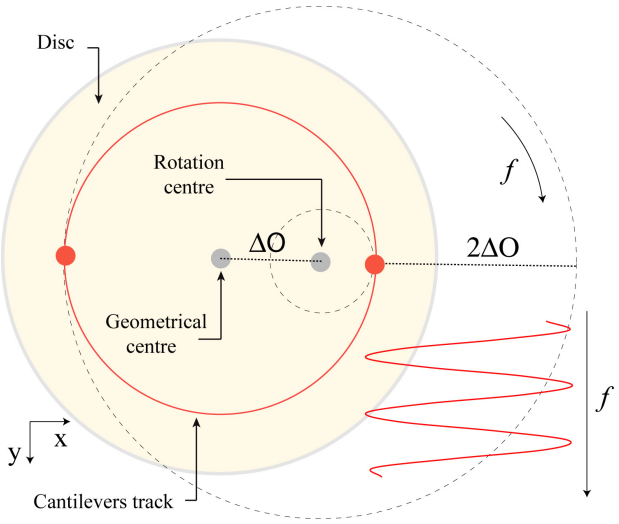

Figure 3.6: Geometrical drawing illustrating the sinusoidal path that cantilevers tracks project onto the X-Z plane. The total amplitude of the curve (i.e. the total X-wobbling variation) equals two times the mismatch (ΔO) between the geometrical center and the center of rotation.

Since the basis of the disc is made of glass, sandblasting was the only option to drill holes into the substrate. The precision of the sandblasting process (small nozzle shooting a beam of fine sand) is generally poor, being the operation carried manually. Even with alignment pattern on the disc, the misalignment between disc and rotating stage was found to reach up to few millimeters.
To perform high-throughput measurements the laser beam should scan the cantilevers with an X-direction resolution of few μm (see Figure 3.2). The issue of X-wobbling compensation was then found to be as critical as for the Z-direction.
When seen from the PUH, ΔO induces a sinusoidal-shaped oscillation in the X-direction

with amplitude twice the centers mismatch (ΔO) and with period π. Figure 3.6 illustrates how the X-wobbling is generated. To compensate this in-plane wobbling the VCM needs to follow this oscillation. This could be obtained applying to the VCM X-coil a signal, $V_{VCM-x}(f)$ defined by:

$$V_{VCM-x}(f) = 2V_{\Delta O} \sin(2\pi f) \tag{3.2}$$

Where f is the rotation frequency of the disc and $V_{\Delta O}$ the voltage required for moving the VCM of a distance ΔO, equal to the mismatch between the geometrical center and the rotation center.

3.2.2 Auto-tracking pattern

Superimposition of adjustment signal to the VCM X-coil was however found insufficient to properly compensate the wobbling. In fact cross-talk between the Z-wobbling and the X-wobbling added external fluctuations with a projection on the X-Y plane that slightly differs from the curve expressed in Eq. 3.2.
Off-line X-wobbling compensation (measure the value and superimpose the signal to the VCM coil) was then found inappropriate for high resolution adjustments of the PUH. In order to address this problem, a new set of discs ($V1$-B) was fabricated to integrate wobbling compensation into an on-line system.

The *Disc* $V1$-B, shown in Figure 3.5b, was fabricated with the same SU-8 procedure as used in $V1$-A. Under the SU-8 layers however, auto-tracking patterns designed to solve the X-wobbling were etched by Reactive Ion Etching (RIE) and coated with 20 nm Ti + 100 nm Al.
The pattern consists of a series of adjacent triangular steps (50 μm long, 40 μm wide at the base and 1 μm deep) aligned along the cantilevers track. When the laser scans the triangular pattern, the acquired signal varies depending on the position of the laser spot along the radial direction (see Figure 3.7c). When it is centered in the triangular track (red line) the signal is composed by an array of equally spaced steps. When it scans too close or too far from the rotational center, the gap between steps varies. The center of the triangular pattern is aligned with the cantilever free-ends, positioned 3.4 cm from the geometrical center of the disc.
Integrating the signal it is possible to feedback the VCM X-coil and to center the beam again, with a closed-loop approach similar to the one employed for Z-wobbling compensation (Figure 3.7a).
When the laser beam approaches the cantilever apexes it passes through a pattern (a grid with 5 μm period) which acts as acquisition trigger. The auto-tracking stops and the cantilever profiles are acquired. The same approach was implemented for the Z-direction auto-tracking.

System $V1$ (and *Discs* $V1$) were used for proof of concept and on-line X- and Z-direction wobbling compensation was successfully demonstrated. However, the technological challenges that this on-line approach added to the overall system complexity caused the next

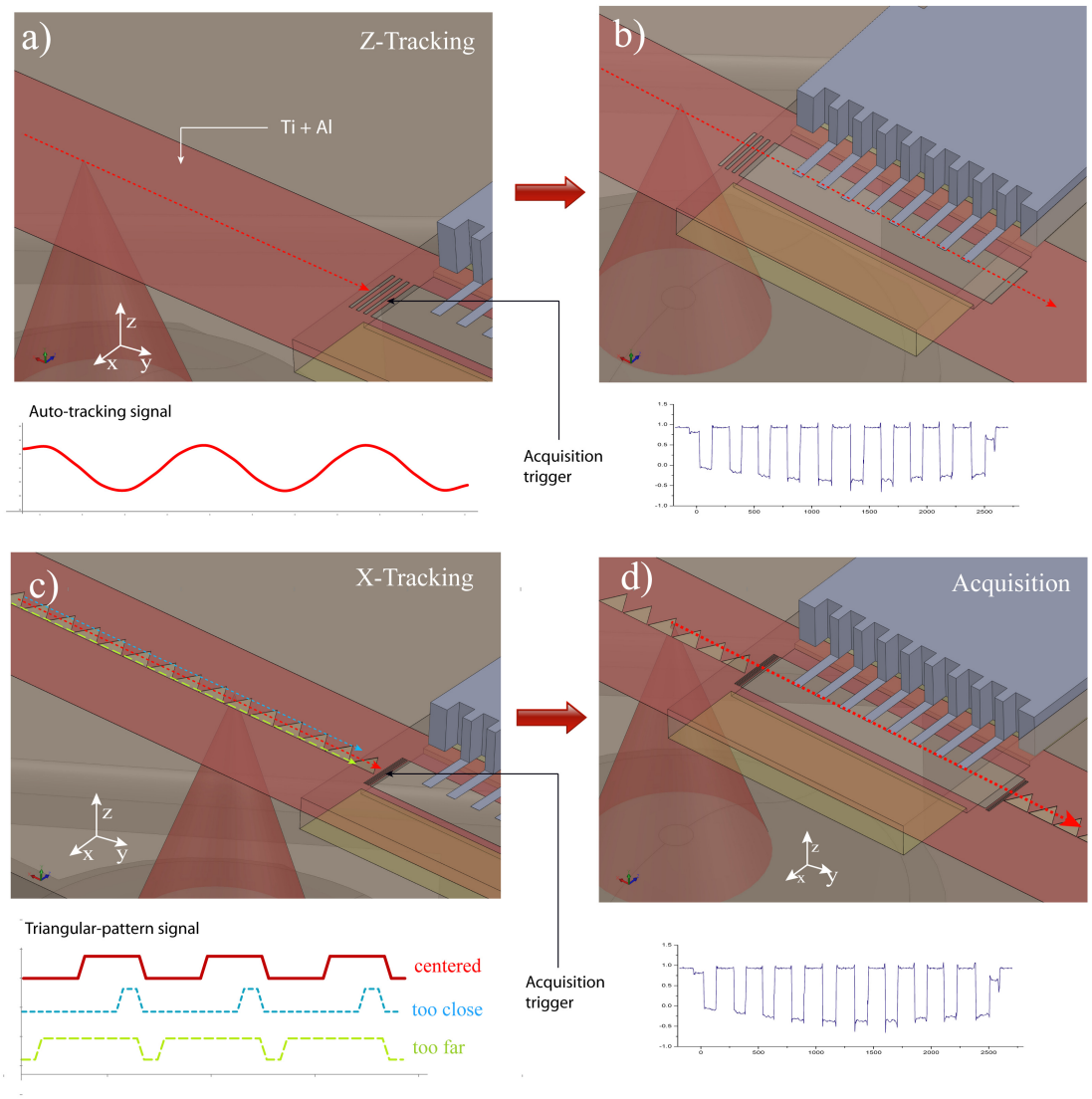

Figure 3.7: Schematics of the auto-tracking patterns for Z- and X-direction. a) The laser beam scans along a ring of reflective material (Al) and compensate the wobbling measuring the auto-tracking curve (Section 2.3.2). b) Before reaching the cantilevers the laser beam passes on a grid that acts as acquisition trigger. The auto-tracking stops and the cantilever profiles are acquired. c) The in-plane wobbling is compensated moving the VCM along direction toward the center of rotation. When the laser scans along the triangular pattern, the acquired signal varies depending on the position of the laser spot. When it is centered in the track (red line) the signal is composed of an array of steps equally spaced. When the laser scans too close to the center of rotation the signal looks like the blue curve (middle one), while when it scans too far from the center it looks like the green curve (bottom one). Integrating the signal it is possible to feedback the VCM X-direction coil and center the beam again. d) the cantilevers are then measured after the laser beam scans an acquisition trigger pattern.

generation discs to rely on simpler methods for misalignment compensation. In a similar way to the Z-wobbling compensation, also the X-direction one was later approached by mechanical improvements of the rotating stage. This simple approach allowed to focus on other disc performance improvements (e.g. microfluidics integration).
Furthermore, scanning of specific sectors of the cantilevers tracks (e.g. scanning 5 chips instead of 30) considerably reduced the effects of the X-wobbling, allowing the precise scanning of the cantilever apexes even in absence of VCM-driven auto-tracking systems.

3.3 *Disc V2* - Integrated microfluidics

The disc designs presented in this section were developed around the same time *System V2* was started to be tested. The main difference between *Discs V1* and *V2* is the integration of microfluidic channels and reservoirs.

Several discs containing different channel designs were fabricated and tested. In this section three of them are reported: (i) Disc *V2-A* had one single sensing track which could load 30 chips. This disc was used for preliminary microfluidics tests and did not include reflective material. (ii) *Disc V2-B* could hold 24 chips placed on two sensing tracks. The sensing chambers were serially connected by 200 μm channels, and Ti+Al coated rings were embedded for auto-tracking implementation. First, continuous flow measurements were carried out using this platform. (iii) *Disc V2-C* contained 36 chips placed on a single track and included reflective coating patterns. This design was the first to include multiple chips within the same sensing chamber.

3.3.1 Integrated SU-8 channels

Discs V2-A and *V2*-B were designed and fabricated at the same time. The fabrication processes and the overall disc designs were similar, and their use in the project determined a starting point for the integration of microfluidic systems into the platform. After the patterning of two SU-8 layers similar to the ones structured on *Disc V1*, a third SU-8 layer was spincoated and structured on top of them. This 350 μm thick layer (mask layout shown in Figure 3.9) defined the path for the sample to move from the inlets to the waste reservoirs. The designs were made in order to allow the manipulation of fluid simply by rotation of the platform. Capillary valves were found to be an excellent and simple method to drive the liquid along the channels without the need of external pumps [91].

Disc V2-A

Disc V2-A (illustrated in Figure 3.8a) was the first disc designed to include channels inside the SU-8 structures and to be used for preliminary tests of fluid manipulation.
The liquid was applied through inlet holes positioned close to the center of the disc. 30

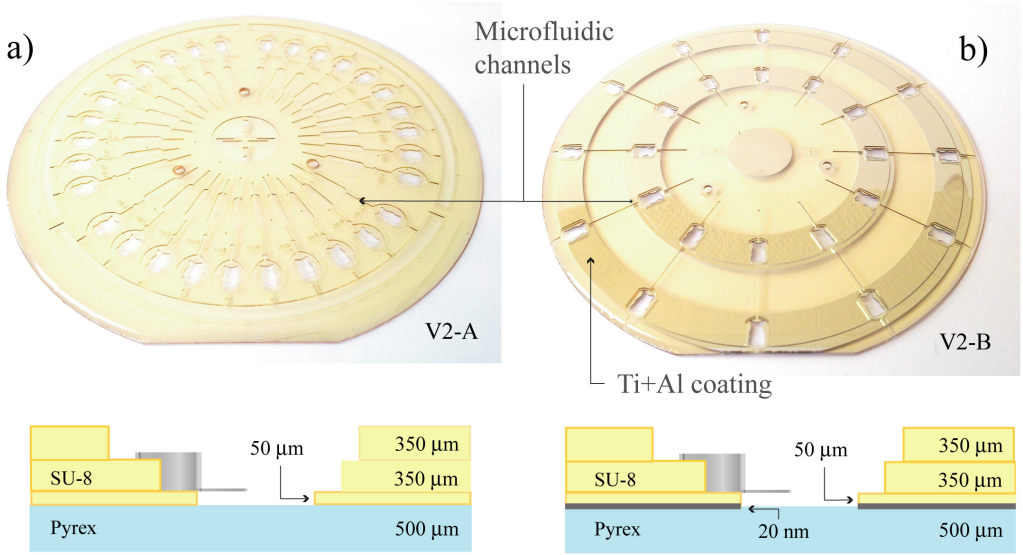

Figure 3.8: a) Picture of *Disc V2-A*. The disc is composed of three layers of SU-8. The thin one is used to keep the cantilever suspended, while the two thick ones are, respectively, for chip clamping and for microfluidic channels b) *Disc V2-B* is coated with 4 nm of Ti and 20 nm of Al before structuring the three layers of SU-8.

channels were running from the center of the disc toward the sensing chambers (see Figure 3.9). The liquid was passing to a pre-incubation chamber which provided damping of the pumping noise and allowed possible alternative testing of the fluid (e.g. SERS or microscopy-based analysis). The liquid then passed through a channel into a capillary valve ($ValveA$) at which it stopped until further pressure was provided [87]. The cross section of $ValveA$ was varying from 80 μm to 150 μm, depending on the design of the channel. The corresponding frequencies at which the valves opened were ranging from 120 rpm to 220 rpm.
When sufficient pressure was applied (rotating the disk above a certain frequency threshold such that the pressure provided by the centrifugal force is larger than the capillary pressure of the valve), the sample was moving inside the sensing chamber where the cantilever chip was clamped. After the reaction time had passed (typically around 10 min) the disc was spun at high speed in order to open $Valve\ B$ (burst frequency between 180 rpm and 250 rpm) and move the sample inside the waste chamber. Figure 3.9 shows the mask layout of the top SU-8 layer defining the microfluidic channels and valves.
Capillary valves capability of holding liquid during spinning of the disc was widely employed in the project. In the experiments, often just $Valve\ B$ was used. The sample was immediately introduced through the whole microfluidic channels to the cantilever sensors, and the liquid stopped once the the sensing chamber was completely filled. In this context $Valve\ B$ was used for emptying the sensing chamber. Typically rotational frequencies above 300 rpm were used for this purpose.

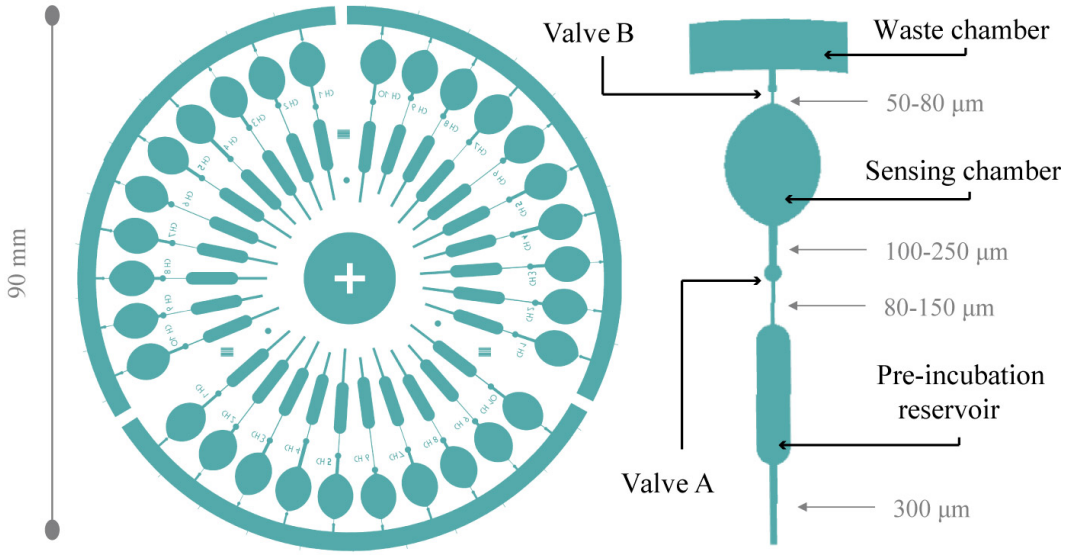

Figure 3.9: Mask layout for the SU-8 layer defining the microfluidic channels of *Disc V2*-A. The channels are connected to the chambers through capillary valves (abrupt changes in the cross section of the channel).

Operations with liquid required sealing of the top of the channels. A PMMA plate covered with microfluidic tape was initially used. This pressure-activated hydrophilic tape bonds to materials when enough pressure is applied to the tape-platform. A bonding press was used to seal the system, applying forces in the range of few kN for 10 minutes.

Disc V2-B

Disc V2-B was very similar to *V2*-A in terms of fabrication and layers structure. It included a Ti+Al coating for auto-tracking purposes, and the channels where separated by a second sensing chamber positioned at 2.1 cm from the center of the disc. Figure 3.8b shows the disc and its cross-section view. This disc, designed without capillary valves, was used for the first tests of continuous flow measurements. In this context, a pressure-driven pump was connected to one of the inlet hole and the liquid was injected at constant pressure. The liquid was moved along the channels and chambers while the disc was rotating and the DVD-ROM was scanning the cantilevers through the glass substrate. The disc was rotating 180° back and forth to avoid tubing wrapping.
The channel width was designed to be constant along the radial direction (200 μm). Similarly to *Disc V2-A*, a thin PMMA plate sealed with microfluidic tape was used as lid for the channels and reservoirs.

3.3.2 Optimized SU-8 disc design

Disc V2-C was the last SU-8 based disc that was designed and fabricated during the project. Its design includes several of the features tested with the previous disc generations, plus a few new characteristics:

- Two thick SU-8 layers. Instead of patterning the thin layer of SU-8 for keeping the cantilevers suspended, the thick layer (350 μm) defining the clamping structures was directly built over the Pyrex surface (see Figure 3.10a). The cantilever chips were then clamped upside-down, allowing the cantilevers to be still suspended and free to vibrate. The second layer (also 350 μm thick) was then patterned to define the microfluidic components.

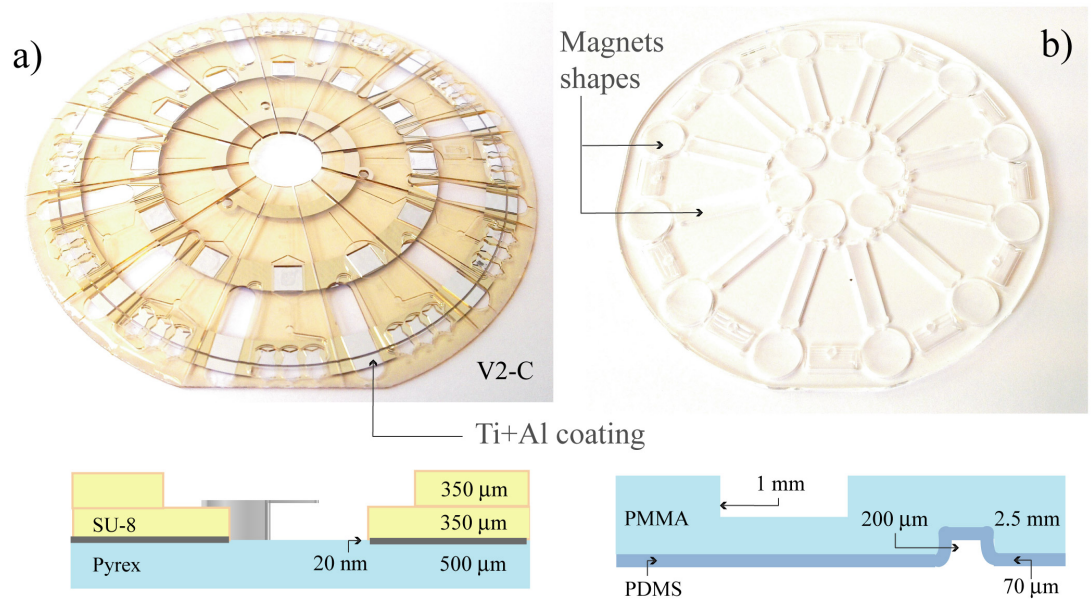

Figure 3.10: a) Picture and cross-section view of the *Disc V2-C*. The SU-8 microfluidic layer is structured to include three chips each chamber. Ti+Al coating is used for Z-wobbling compensation and X-wobbling evaluation. b) Photo and section schematic of the PMMA microfluidic lid. The bottom surface of the lid is coated with 70 μm PDMS layer.

- Multiple chips chambers. In this design the cantilever chips were mounted along the sensing track in groups of three. The microfluidics structured on the top of the clamping layer was designed to contain the three chips, i.e. 24 cantilevers, within the same sensing chamber (see Figure 3.11b). Different functionalized chips could then be exposed to the same sample.

- Z- and X-wobbling patters. A 4nm Ti + 20 nm Al coating was applied to the disc. This metal coating was structured in concentric rings in order to be employed

as Z-wobbling evaluation pattern (as illustrated in Figure 3.7a). The X-wobbling compensation pattern shown in Figure 3.7c was actually not implemented. Instead, thin gaps were left between the concentric rings. Focusing the laser beam through these narrow gaps and spinning the disc, it was possible to measure the X-wobbling simply by monitoring if the laser beam was lying within the gaps for the entire disc revolution. Several gaps were patterned, from 5 μm to 500 μm wide. This method allowed precise evaluation of the X-wobbling that could be compensated through subsequent mechanical adjustments of the rotating stage.

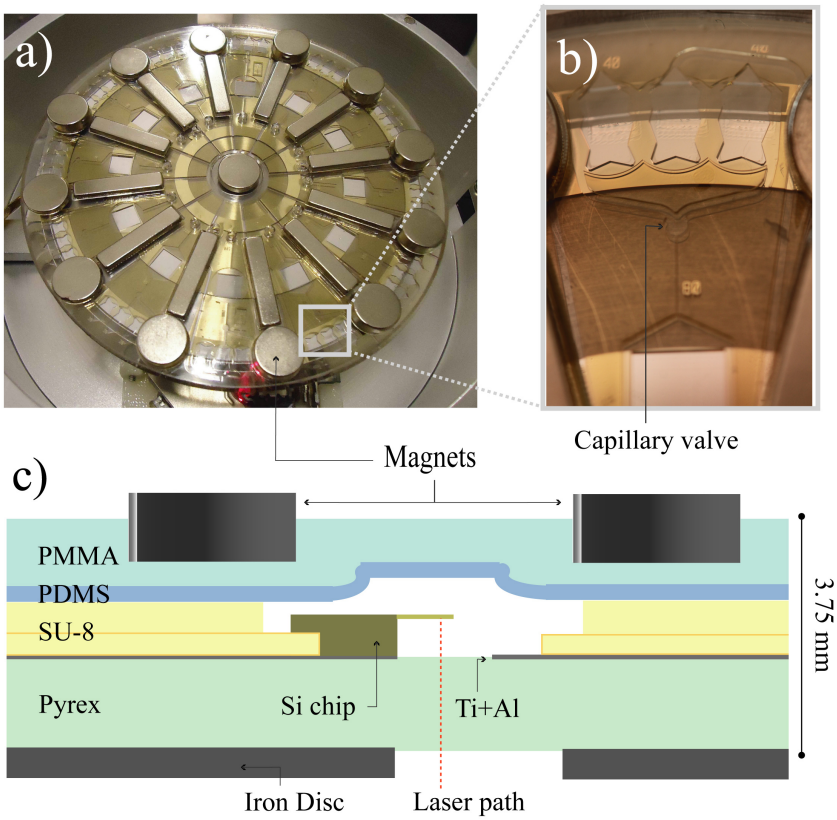

Figure 3.11: a) Photo of the complete *Disc V2-C* mounted on *System V2*. b) zoom of the microfluidic channels. A capillary valve and three footprints for chip clamping are visible. c) Cross-section view of the disc assembly. Magnetic force between rare-earth magnets and an iron disc is used for sealing the chamber. The iron disc includes holes in correspondence with the chip chambers, allowing the laser to pass through the glass and shine onto the cantilever apexes.

- Capillary valves. Valves similar to the one illustrated in Figure 3.9 were structured on the second thick SU-8 layer and placed few mm before the sensing chamber (after the pre-incubation reservoir). These valves were designed to open at frequencies of the order of 150 rpm. After the sensing chamber, narrow channels were acting

as high-pressure barrier valves, which were opened (i.e. emptying the chamber) when spinning the disc above 300 rpm.

- Magnet-based microfluidic sealing: an open-close method for magnet-assisted channel sealing was implemented in this platform. The PMMA lid was structured to clamp rare-earth magnets, whose attraction force towards an iron disc placed below the disc sealed the microchannels.

As illustrated in Figure 3.10, the design of *Disc V2-C* consisted of to separate parts, namely, the platform and the microfluidic lid. The platform consisted in a Pyrex wafer coated with a thin metal layer and covered with two thick layers of SU-8. The microfluidic lid was a wafer-shaped 2 mm thick PMMA substrate machined through micromilling technology or CO_2 laser technology. Figure 3.11 shows the picture of the complete disc, the close view of the microfluidic channels and the section schematics of the assembly.

On the bottom side of the lid, 200 μm deep indents were carved (Fig. 3.11c) directly above the cantilever chips in order to maintain a sufficient gap between the cantilevers and the lid. On the same side of the PMMA lid, a 70 μm layer of Polydimethylsiloxane (PDMS) was spincoated and cured. PDMS is a hydrophobic silicone compound widely used to seal microfluidic channels and chambers. On the top side of the PMMA lid, 25 clamping structures for magnets were cut out. These magnets were distributed on the PMMA lid in order to apply uniform force on the SU-8 substrate and thus seal the channels. The magnetic force was acting toward a 1 mm thick iron disc positioned below the Pyrex wafer (see Figure 3.11c).
The liquid to be tested was applied through an inlet hole close to the center of the disk. From this point it passed to a pre-incubation reservoir before entering the sensing chamber containing three chips.

The magnet configuration shown in Figure 3.11a was found to successfully clamp together the two parts of the disc and to close the channels and reservoirs. Small leakage was however observed at the edges of the wafer, due to intrinsic curvatures of the thick SU-8 layers in proximity of the wafer edges. Vertical sidewalls at the wafer's edge were extremely difficult to be obtained through standard SU-8 fabrication processes (due to the edge bead obtained during spincoating), compromising the future use of these disc designs for high-precision fluid handling.
The design of discs machined entirely in PMMA, presented in the next Section, was specifically oriented to solve this leaking issue.

3.4 *Disc V3* - Continuous flow measurements

In this Section the disc designs that were fabricated for continuous flow measurements in connection with *System V3* are presented. These platforms were fabricated entirely in PMMA without cleanroom facilities. Two designs are described in this Section, namely *V3-A* and *V3-B*, which are very similar in terms of microfluidics geometry, materials and

fabrication. *Disc V3-B* differs from its previous version mostly in terms of technology optimization details.

3.4.1 New chip clamping

In order to provide sealed microfluidics for steady-flow conditions, the discs were fabricated in PMMA with micromilling technology. The use of mask-free fabrication techniques allowed the investigation of several channel geometries and clamping methods, thanks to the very flexible fast-prototyping capabilities of this fabrication process.

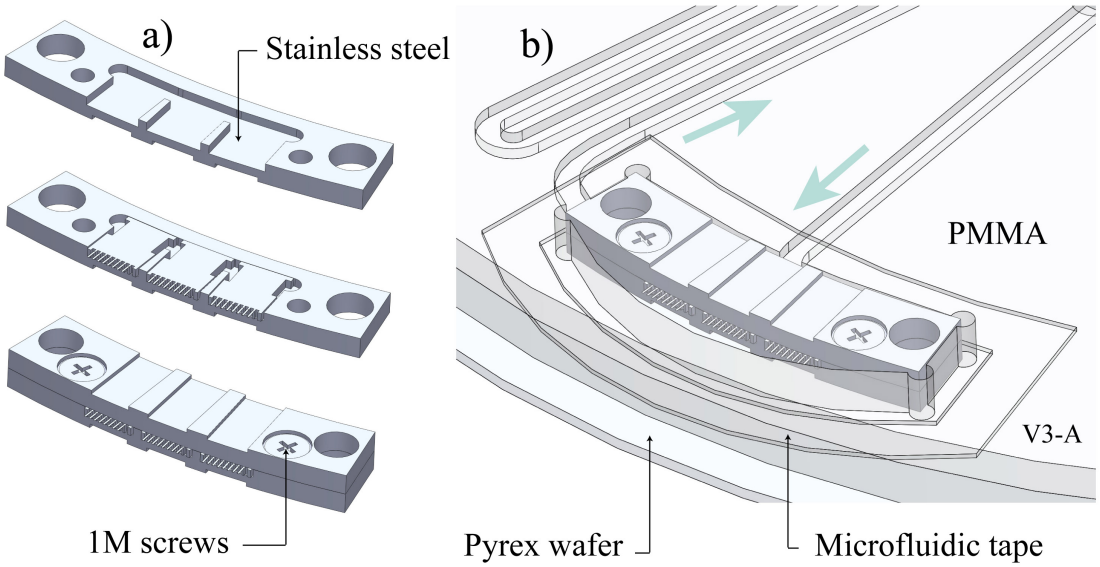

Figure 3.12: a) Schematics of chip clamping on stainless steel holder. The sandwich-like structure is then clamped with 1 mm screws. b) The holder encapsulated in its sensing chamber. The sealing of the chamber is done throughout the use of double-side microfluidic tape.

Several structures were milled in the PMMA plates in order to test clamping methods to fix the silicon chips directly on the polymer substrate. Machining of structures similar to the ones used with SU-8 based discs (Figure 3.4) was tested but found inappropriate for proper clamping of chips. Roughness of the machined surfaces, together with small deviation of the structures dimensions from the nominal value, led to situations where the chips were slightly "loose" inside their clamping footprints.

In order to solve these problems a new clamping approach based on stainless steel bulk holders was implemented. These holders were designed to precisely clamp three silicon chips within a sandwich-like structure. Figure 3.12a illustrates the working principle of the holders.

Three chips were placed on the bottom part of the holder, machined to precisely fix the body chips on the X-Y plane. The top part was then secured with two 1 mm screws which provide very tight clamping in the Z direction. The whole structure is 10 mm x 2 mm x 2 mm and includes three chips that can be functionalized separately. The holder was then placed inside a microfluidic pattern (machined with micromilling on the PMMA substrate), which includes sensing chamber and microchannels for dispensing the sample. The stainless steel holders were much easier to handle than single chips.

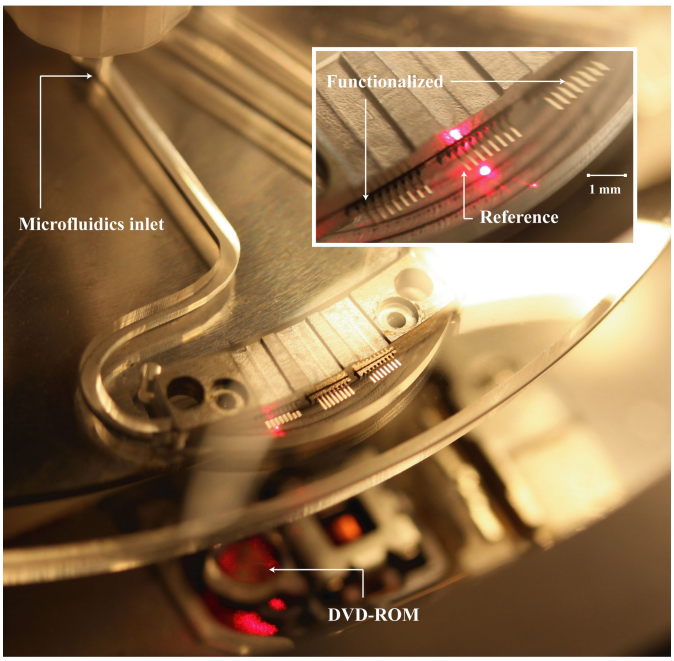

Figure 3.13: Close view of the sensing chamber of *Disc V3-A* loaded with steel holder and three silicon chips. The outer chips were functionalized while the central one was used as reference. The disc is mounted on *System V2*.

Figure 3.12b shows an example of microfluidics design that embeds the stainless steel holder. The liquid enters the chamber from the backside of the holder, carved with trenches that allow the sample to flow through the holder itself. Once the sample fills the chamber, it moves towards the outlet positioned at the edge of the reservoir. Several inlets and outlets configurations were tested thanks to the high flexibility of the micromilling fabrication processes. In Figure 3.13 a picture of *Disc V3-A* loaded on *System V2* is shown.

3.4.2 Microfluidics sealing

Sealing of *Disc V3* was challenging. Standard irreversible bonding techniques (thermal, laser assisted) were inappropriate. The system needed to be an open-close device, where chips could be easily replaced. Furthermore, bonding that involved high-temperatures

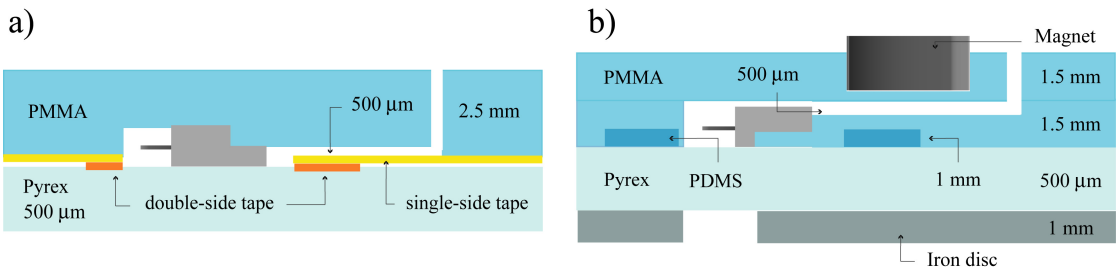

Figure 3.14: a) Cross-section scheme of *Disc V3-A*. The channels patterned on the PMMA plate are sealed with single-side tape leaving the sensing chamber open. The substrate is then clamped to a Pyrex wafer using small fragments of double-side microfluidic tape, that seal the chambers and allow the laser to shine on the cantilevers. b) Cross-section scheme of *Disc V3-B*. The substrate is composed by two thermally bonded PMMA plates. A PDMS ring is used for sealing of the chamber and magnets are used to apply force between the PMMA substrate and the Pyrex wafer.

around the cantilevers should be avoided since this could damage the functionalization and induce strong bending due to bi-morph effects on bi-material cantilevers.

Disc V3-A

In order to test the microfluidic properties of *Disc V3*, simple approaches were initially employed. One of the simplest and most successful methods is schematically presented in Figure 3.14a. A single PMMA plate was structured with channels, chambers, inlets and outlets. The whole PMMA disc was then covered with single-side microfluidic tape which was patterned by laser micromachining. The tape was patterned with holes corresponding to the sensing reservoirs, thus sealing the entire sets of channels except for the chambers, which were left open. Around the sensing reservoir a small piece of double-side tape was attached, and the entire PMMA plate was pressed onto a Pyrex wafer. The tape segment (visible in Figure 3.12b) was acting as "o-ring" for the sensing chamber, sealing the sample path and leaving plain Pyrex surface below the cantilevers for bottom-up laser scanning.
This tape-based method was very useful for characterizing the microfluidics. Several channels dimensions were fabricated and tested in order to find the optimal configuration for bubbles-free flow measurements. The design shown in Figure 3.13 (1 mm wide channels, inlet and outlet positioned at the sides of the holder) was found to work well in continuous flow conditions. The liquid was injected at relatively high flow-rate (around 200 μl/min) from the side of the holder. The sample rapidly filled the chamber and moved toward the outlet. At this point the flow rate was reduced to the desired value for the sensing process (typically 20 μl/min) before actual cantilever measurements started.
Injecting liquid at high flow-rate was found to be a very convenient way of avoiding air bubbles in the chamber. If the liquid was infused directly at 20 μl/min, the hydrophilicity of the steel holder caused the liquid to flow along the metal towards the outlet, without completely filling the chamber. In this situations air bubbles were trapped around the

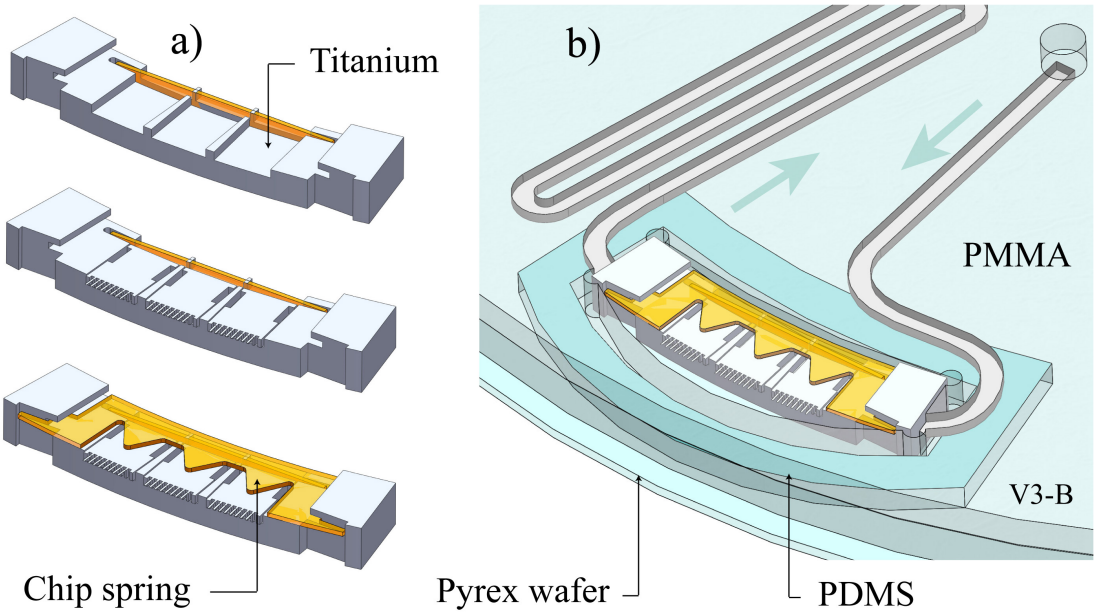

Figure 3.15: a) Schematic of the new chip holder preparation. The chips are placed on the bulk Titanium holder and then clamped through specifically designed springs. b) The whole structure is inserted into the microfluidic system.

cantilever chips making measurements impossible.
The use of microfluidic tape for channel sealing had some disadvantages. The Pyrex substrate was in fact glued to the PMMA disc, making it difficult to release the disc for substitution of cantilever chips. It was not uncommon that the glass wafer broke during the release process. Furthermore, the thin double-side tape (20 μm) was sometimes generating small leakages on the sides of the sensing reservoir, affecting the reliability of the steady-flow condition.

Disc V3-B

In order to address these issues a new sealing approach was implemented. This method could be considered as a combination between the magnet-assisted sealing approach illustrated in Figure 3.11c and the tape-based one shown in Figure 3.12b.
The discs fabricated with this approach are called *V3-B*, and the section scheme is presented in Figure 3.14b. The microfluidic lid was fabricated via bonding of two 1.5 mm thick PMMA plates . One plate was patterned with channels and chambers, the second was used as sealing layer in a similar fashion as the single-side tape used in *Disc V3-A*. Instead of using a tape-based "o-ring" to close the chamber, a 1 mm deep square pool was patterned on the PMMA plate around the chamber. This pool was then filled with PDMS. Magnets were encapsulated in the top side of the PMMA lid, and the at-

tractive force toward the iron disc placed below the Pyrex wafer was used to seal the whole structure. Figure 3.15b shows the schematic view of the PDMS "o-ring" structure.

Furthermore, new holders were employed in *Disc V3-B*. There were several reasons for designing the new holders illustrated in Figure 3.15a: (i) the stainless steel holders had some geometrical deviations from the nominal values. Some of the holders were slightly tilted and thus induced focusing issues for cantilever scanning. (ii) the stainless steel holders were specifically designed for 400 μm thick body chips. If chips with other dimensions were inserted in the holders, they would be too loose (if slightly thinner) or would not fit (if slightly thicker), limiting the variety of sensors that could be employed on the disc. (iii) the 1 mm screws used for fixing the two parts of the holders were found to rust when in contact with buffer solutions for prolonged time. Screws-free approaches were therefore preferred.

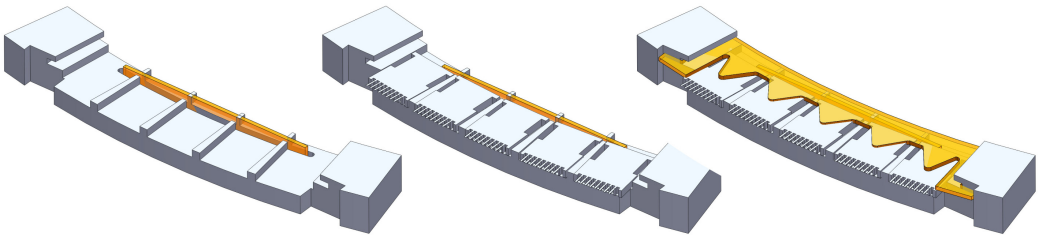

Figure 3.16: Layout of 5-chips holder designed and fabricated at the end of the project. The clamping method is the same of the holders illustrated in Figure 3.15a

To address these issues, a new set of holders fabricated in Ti was built through Electrical Discharge Machining (EDM). The clamping layer (the top one) is replaced by new titanium-made chip springs. These flexible structures (500 μm thick) provided a very efficient clamping of the chips independently of their thickness. The working principle is illustrated in Figure 3.15a. The thin Ti springs included triangular-shaped springs that applied force on the top side of the body chips, tightly clamping them to the bulk Ti holder. The springs were placed inside threads patterned at the edges of the holder in order to be firmly fixed to the whole structure. The holder was then inserted inside the microfluidics in a similar way as the previous steel versions.

At the end of the project titanium holders which could hold five chips were also fabricated. These holders were tested in connection with *Disc V3-B* and *System V3*. The overall reduction of wobbling, together with the employment of optimized optics, allowed the precise scanning of 40 cantilevers (5 chips) which could all fit inside the linear range of the optical detector.

3.5 Conclusions

Of the dozen of discs designed and tested during the project, seven of them were presented in this chapter. The overall development of the disc technology generally followed the progresses of the system and software development. *Disc V*1 was in fact addressing issues such as the need for high-throughput measurements, as well as embedding features for compensating X- and Z-direction wobbling of the rotating system. The applicability to integrate these features into the disc was demonstrated.
In version $V2$, the development of discs with integrated microfluidics evidenced the possibility of handling liquid by simple rotation of the disc.
The last versions ($V3$) were developed to be compatible with the properties of *System V*3. The use of steady-flow conditions was necessary in order to perform more accurate sensing experiments. In general, the latest designs that embed PMMA substrates for microfluidics were found to give better flow conditions than the SU-8 based ones. The fabrication process was less tedious, and full-polymer discs are more suitable for mass production technologies (e.g. via injection molding).

Chapter 4

Disc Fabrication

4.1 Introduction

This Chapter presents the processes utilized for fabrication of the discs described in Chapter 3. The chapter is divided in two main sections which describe the fabrication, respectively, with cleanroom facilities and with general laboratory facilities. Section 4.2 illustrates the microfabrication of SU-8 based discs and of silicon masters used for polymer embossing, while Section 4.3 focuses on polymer micromachining processes (milling, laser-assisted machining and hot embossing). These processes were mostly used for lids fabrication.
For the different generations of the discs, mostly three polymers were used: SU-8, PMMA and PDMS. Alternative tests included the use of TOPAS and Polycarbonate, as presented in Section 4.3.2. Apart from these processes, few alternative methods have been tested during the project. These processes were typically found inappropriate (as in case of hot embossing), however they gave useful information on future possible large-scale disc production.

Materials

- SU-8: SU-8 is a commonly used epoxy-based negative photoresist developed in the 1980s and widely employed in microfluidics and microfabrication since the 1990s [111]. The photosensitivity of SU-8 is 300-400 nm, a region accessible with conventional photolithography equipment. When exposed, its monomers cross-link causing solidification of the material. Also, because of the highly cross-linked matrix in the exposed material, it is thermally (up to 200°C) and chemically stable after development. [112]. It is now mainly used in fabrication of microfluidics systems [113], mainly via soft lithography, but also via other techniques such as nanoimprint lithography [114].

- PDMS: Polydimethylsiloxane (PDMS) belongs to a group of polymeric organosilicon compounds that are commonly referred to as silicones. PDMS is since almost

two decades the most widely used silicon-based organic polymer, and it is particularly known for its unusual rheological (or flow) properties [115]. PDMS is viscoelastic and is commonly used as a stamp resin in the procedure of soft lithography, making it one of the most common materials used for microfluidics chips fabrication [116–119].

- PMMA: Poly(methyl-methacrylate) is a transparent, strong and lightweight polymer with good impact strength. It transmits up to 92% of visible light (3 mm thickness), and gives a reflection of about 4% from each of its surfaces. Its optical properties and clarity however are not as good as Polycarbonate or Cyclic olefin copolymer (COC). PMMA furthermore swells and dissolves in many organic solvents, with poor resistance to many other chemicals. PMMA is widely employed for microfluidics applications [120]. It is typically machined through laser processes [121, 122], or via Computer Numerical Control (CNC) milling machining [123]. In this project both methods were extensively employed.

SU-8 was chosen as the initial fabrication material for several reasons: (i) High aspect ratio structures could be obtained. (ii) combination between thin and thick structures (e.g. pools and footprint patterns) could be easily achieved spincoating different SU-8 thicknesses on top of each other. (iii) High precision microfabrication resolution was achievable even with very thick structures (e.g. for the 350 μm thick footprint layer). (iv) the transparency of the polymer was thought to allow the laser beam to pass through thin SU-8 layers for cantilevers readout. (v) Chemical stability and resistance to solvents was envisioned as useful features for biochemical analysis and regeneration of the channels and surfaces.
Furthermore, fabrication of SU-8 stress-free processes were already optimized for cantilever chip fabrication in the DTU-Danchip facility [124].

4.2 Cleanroom fabrication

In this section the processes run for the fabrication of *Discs* $V1$ and $V2$ are presented. All the SU-8 based discs were fabricated at DTU-Danchip.
Standard recipes were used for metal deposition and AZ-photolithography, while optimized processes for low-stress thin and thick SU-8 structures [110] were used and adjusted during the years.
Four different material processes are described in this section: metal deposition and patterning, SU-8 lithography, glass microfabrication and silicon masters production. The silicon masters were use for embossing tests of TOPAS and Polycarbonate, presented in Section 4.3.2. Pyrex wafers (4") with thickness of 1 mm and 0.5 mm were used as substrates during the project. The different thicknesses were tested in order to determine the thickness' influence on the ability to withstand the stresses produced by the thick SU-8 layers patterned on the wafers.

The three-layer-SU-8 fabrication process presented in this section refers to the layout of *Disc V2-B*, shown in Figure 3.8b. This disc included reflective material coating, one thin and two thick SU-8 layers structured on the top of the Pyrex wafer. Except for the auto-tracking pattern of *Disc V1-B* (etched in the glass and described in Section 4.2.3), the fabrication of all the SU-8 based platforms were carried out using combinations of the steps presented here. The individual fabrication process details are reported in Appendix B.

4.2.1 Metal deposition

The wafer was first cleaned and prepared for the adhesion of photoresist. This was done by using an adhesion promoter such as Hexamethyldisilazane (HMDS), which ensured firm adhesion of AZ photoresist on the glass surface [125].

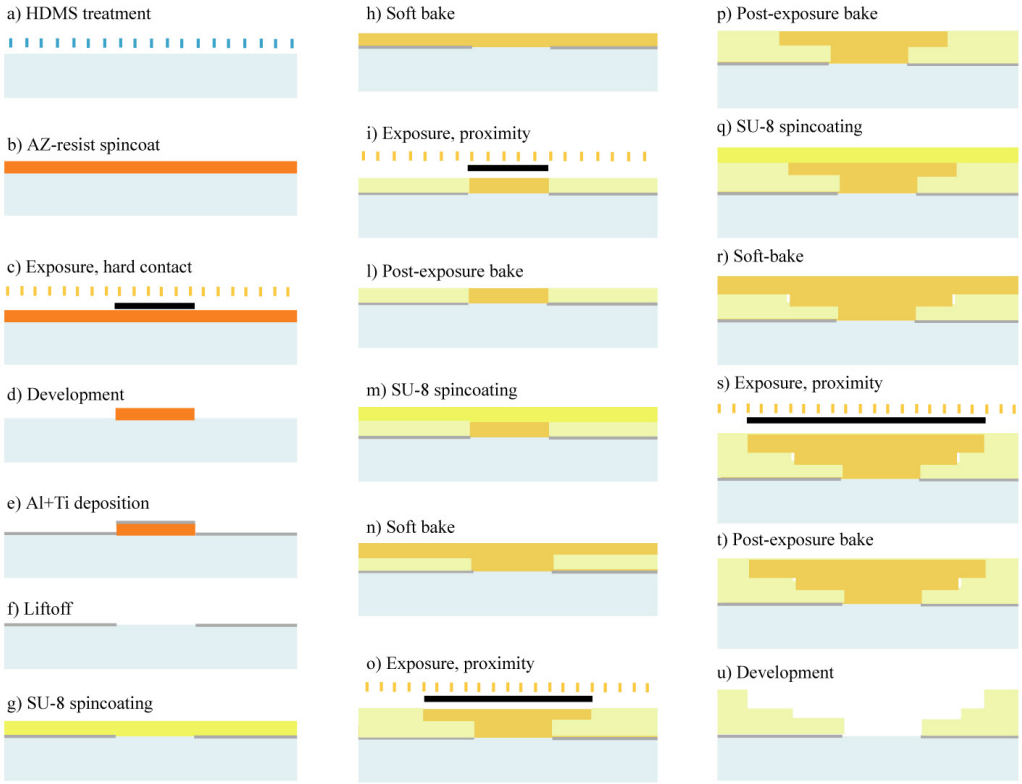

Figure 4.1: Schematics of the *Disc V2-B* four masks fabrication process.

In this process the contact angle is increased, obtaining low surface energy which highly improve adhesion.

After HMDS pre-treatment (Figure 4.1a), photoresist was spincoated onto the wafers with a target thickness of 2.2 μm (Figure 4.1b). Using a UV aligner (Karl Suss Aligner,

	Step 1			Step 2			
	Speed (rpm)	Acc (rpm/s)	Time (s)	Speed (rpm)	Acc (rpm/s)	Time (s)	Thickness (μm)
SU-8 2075	1000	100	30	2500	100	60	50
SU-8 2075	1000	200	30	3000	400	120	34
SU-8 2075	1000	200	30	5000	500	120	20
SU-8 2150	500	100	30	1250	100	60	350
SU-8 2150	500	100	30	1150	100	60	380

Table 4.1: Spinner parameters for obtaining different thin SU-8 layer thicknesses.

SUSS MicroTec AG, Germany) the resist was exposed in hard contact mode with a dose of 70 mJ/cm^2 (Figure 4.1c). The exposed resist was developed in an AZ-developer solution for 100 seconds (Figure 4.1d).
Two metal layers were deposited onto the wafer through E-beam deposition. First 20 nm of Ti and afterwards 80 nm of Al were evaporated at a deposition rate of 10 Å/s (Figure 4.1e). The Ti layer acted as adhesion layer for the Al coating. The reflective metal layer was patterned using AZ liftoff bath for 1 hour in a pulsed ultrasound bath (Figure 4.1f).

4.2.2 SU-8 photolitography

After the reflective metal layer was patterned on the Pyrex wafer, the first thin SU-8 layer was spincoated. This layer was fabricated with SU-8 2075, stored in syringes prepared a couple of days in advance to avoid bubbles in the solution. Three processes were used for spincoating this thin layer (Figure 4.1g), with target thicknesses of 20 μm, 34 μm and 50 μm. Table 4.1 reports the acceleration and speed parameters for the spinner (Karl Suss Spinner, SUSS MicroTec AG, Germany) and the resulting thicknesses. Mostly, 50 μm thick layers were used in the discs fabrication.

After spinning, the wafers were softbaked for 4 hours (2 h for 34 μm and 1 h for 20 μm thick layers) at 50°C on a hot plate with ramping temperature of 2°C/min (Figure 4.1h). Each wafer was then exposed twice to 250 mJ/cm^2 (proximity) in order to define the apertures for the suspended cantilevers (Figure 4.1i). The wafers were baked for 6 h at 50°C (Figure 4.1l), ramped up at 2°C/min.

On top of the thin SU-8 layer, two thick layers were structured. The first one was obtained by spincoating SU-8 2150 over the mostly cross-linked SU-8 2075 surface with a target thickness of 350 μm (Figure 4.1m). Table 4.1 includes the spinner setting for spincoating the thick layers. The wafers were then softbaked at at 50°C for 14 h (Figure 4.1n). The SU-8 surface was exposed four times to 250 mJ/cm^2 through the mask designed for the clamping structures (Figure 4.1o) and later baked for 12 h at 50°C (Figure 4.1p).

The same process was repeated for the patterning of the third layer which defined the microfluidics. The spincoating, exposure and baking processes (Figures 4.1q-t) were performed using the same parameters as the second layer. The uncross-linked SU-8 was then removed in an propylene-glycol-methyl-ether-acetate (PGMEA) solution for 80 minutes (Figure 4.1u).

4.2.3 Glass microfabrication

The fabrication of auto-tracking patterns like the ones embedded in *Disc V1-B* (see Figure 3.5b) was performed through Reactive Ion Etching (RIE) of the glass surfaces. This process involves the use of a chemically reactive plasma which removes material from the wafer surface. High-energy ions from the plasma generated under vacuum by an electromagnetic field attack the wafer surface and react with it [126].

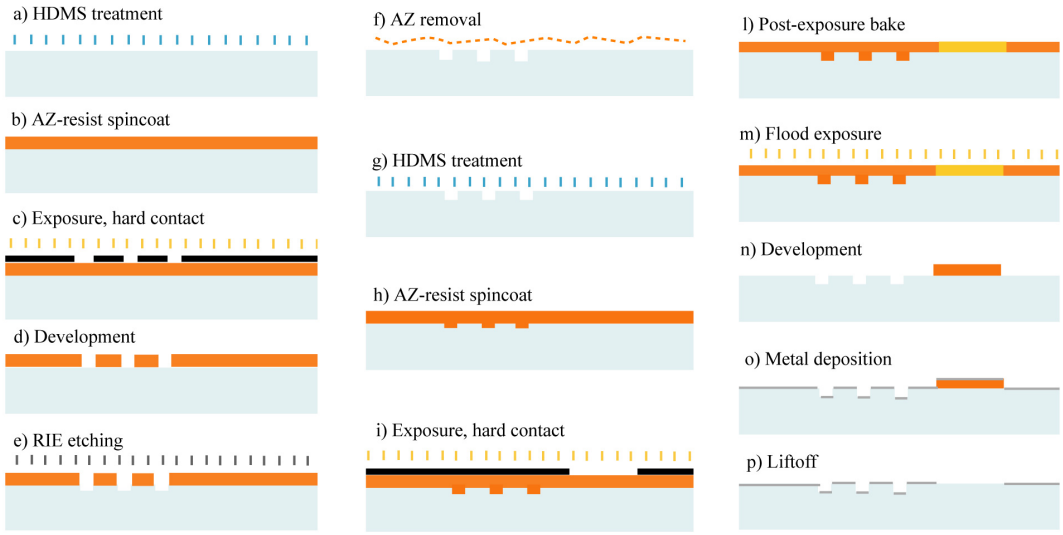

Figure 4.2: Fabrication steps for etching of shallow structures in glass.

A 4" fused silica wafer was pretreated with HMDS before 2.2 μm thick AZ-resist was spincoated onto its surface (Figures 4.2a-b). The resist was exposed in hard contact mode to a dose of 70 mJ/cm^2 and the exposed resist was developed by 100 seconds shaking in an AZ-developer bath (Figure 4.2c-d).
The wafer was then loaded into the RIE chamber and etched. A standard recipe for glass etching, developed at the DTU-Danchip, was used for etching depths in the range between 200 nm and 1000 nm. Tuning the etching time, different depths were obtained. Figure 4.3 illustrates the linear dependency of the etched depth as a function of the etching time, characterized through profilometry measurements (Dektak 8 stylus profiler, Veeco, US). The targeted depths for the auto-tracking pattern embedded in *Disc V1-B* were 500 nm and 1 μm.
After repeating the HMDS pre-treatment, a new 4.2 μm thick AZ-resist was spincoated

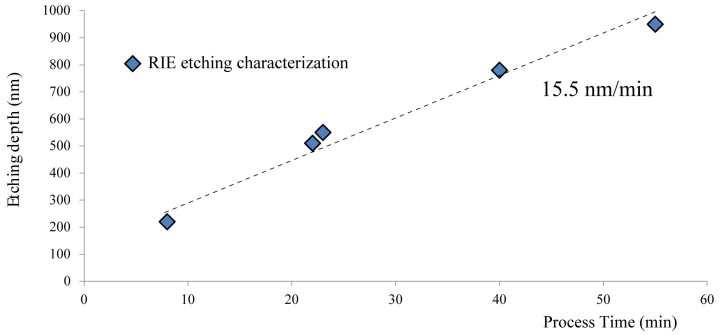

Figure 4.3: Linear relation of the etching depth in function of etching time for RIE process with fixed parameters. A etch rate of 15 nm/min was measured through profilometry.

on the wafer (Figure 4.2g-h). Standard negative photolithographic steps were then applied to the AZ-resist layer: (i) 35 mJ/cm^2 exposure in hard contact; (ii) 110 seconds of post-exposure bake at 120 °C; (iii) 210 mJ/cm^2 flood exposure; (iv) 100 seconds development in AZ-developer. These steps are illustrated in Figures 4.2i-n.
The metal deposition and liftoff processes were run under the same conditions as described in Section 4.2.1.
After the glass fabrication process was completed, SU-8 structures were fabricated according to the steps illustrated in Figure 4.1g-u. The fabrication of *Disc V*1-*B* consisted of 23 individual steps.

4.2.4 Silicon masters fabrication

In order to test the capabilities of fabricating the discs and their microfluidic lids in high optical quality polymers (e.g. TOPAS or polycarbonate), silicon masters were fabricated to be used as molds. The process aimed at fabricating a negative mold of the layout illustrated in Figure 3.5. This negative replica would then consist of positive structures extruded from the silicon wafer. The first block would define the footprints for chips clamping while the second, protruding from the top of the first, would define the pools for the suspensions of the cantilevers.
Figure 4.4 illustrates the fabrication steps for this type of silicon master.
The wafer was first immersed in HF buffer bath for 30 seconds to remove native oxide and enhance the adhesion of AZ-resist on the silicon surface [127], before 1.5 μm thick AZ-resist was spincoated on the wafer surface (Figure 4.4a-b). Positive lithography was performed using the same parameters as the process illustrated in Figures 4.1, before the etching of the silicon was processed.
A standard deep etching program in the Advanced Silicon Etching machine (ICP Advanced Silicon Etcher, SPTS Technologies Inc., UK) was used for the definition of the master structures. ASE consists in alternating two process steps: the fast etch rates

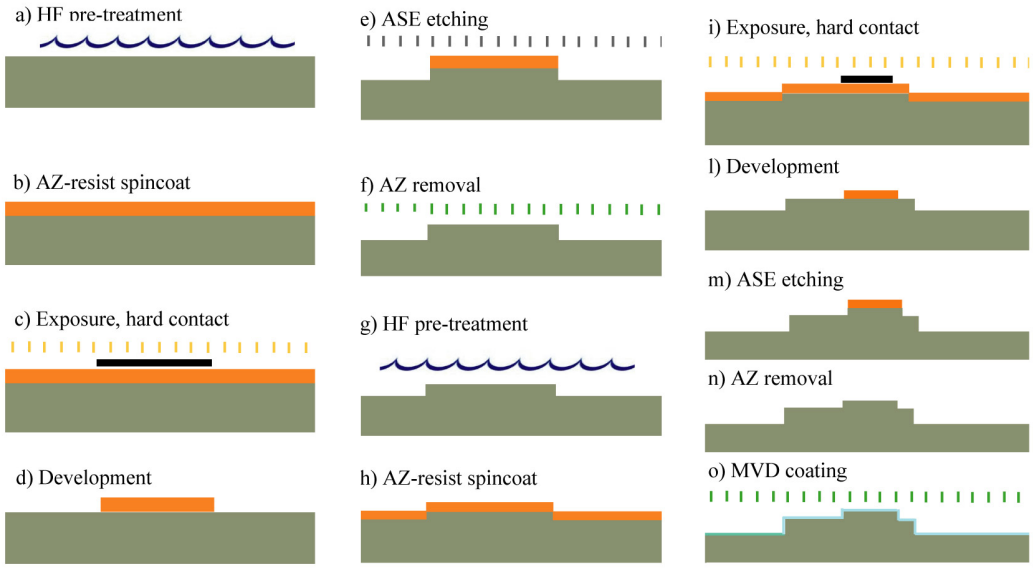

Figure 4.4: Process details for the silicon master fabrication.

achieved in an isotropic Si etch (typically through the use SF_6 plasma) and the passivation processes which utilize $C4F_8$ plasma. ASE provides an anisotropic Si etch. The vertical sidewalls obtained throughout this process are suitable for applications like masters fabrication. Depths of 50 μm to 200 μm were obtained by varying the etching rate of the process (Figure 4.1e).
After AZ removal and HF-pretreatment of the etched surface (Figure 4.1f-g), the same processes were repeated: (i) spincoating, (ii) exposure, (iii) development, (iv) etching and (v) AZ-removal (Figure 4.1h-n).

Once the structures were completed, an anti-adhesion layer was deposited by Molecular Vapor Deposition (MVD 100, Applied Microstructures Inc.). MVD is widely used for deposition of a monolayer-thick fluorocarbon film for producing extremely hydrophobic surfaces, used for example in anti-sticking layers for embossing and nanoimprinting [128]. This coating acts as anti-sticking layer, facilitating the release of the embossed polymer from the master during the detachment of the stamp.

4.3 Polymer lab fabrication

In this section the techniques used for microfabrication of polymer platforms are presented. Section 4.3.1 describes the use of CO_2 laser micro-machining on PMMA plates and introduces a PDMS casting technique. Section 4.3.2 illustrates hot embossing processes performed on TOPAS and polycarbonate plates using silicon masters. Finally, Section 4.3.3 introduces the use of micromilling technology.

Speed/ Power	20	25	30	40	50	70
200	-	D	D	D	D	D
240	-	D	D	D	D	D
250	-	-	D	D	D	D
260	-	-	D	D	D	D
280	-	-	-	D	D	D
300	-	-	-	D	D	D
380	-	-	-	-	-	D

Table 4.2: Laser powers and velocities tested on PMMA plate. The "D" indicates deformation of the PMMA features at the pattern's edges.

4.3.1 CO_2 laser micro-machining

The principle of CO_2 laser micro-machining of PMMA is based on thermal ablation of the molecules of the surface of the polymer plate. Infrared light (10.6 μm wavelength) is irradiated from the system and is focused on the PMMA plate. Due to the low absorption of PMMA above 300 nm [129], photochemical breaking of polymer bonds is neglectable compared to heat-induced bond breaking. The material then quickly melts, decomposes and vaporizes from the surface due to the fast rising of the temperature as the laser passes [130].

A commercial CO_2 laser system (Mukilteo, Synrad Inc., USA) was used. Designs were prepared with CAD program that can interface with the machine. This program allows the users to define variables for the overall machining process: (i) laser beam speed, (ii) laser power, (iii) number of laser passes and (iv) time interval between passes.
The CO_2 machine at DTU Nanotech has maximum laser power of 65 W and a focal length of 189 mm. The feature size resolutions is not excellent, lying in the hundreds of μm range. However, the vertical ablation can be tuned to reach depth of the order of few μm, when optimized. The in-plane resolution is often limited by melting of material on the side of the beam path. The cross-section of the features assumes the shape of the Gaussian profile of the laser intensity [131].

PMMA Disc fabrication

The CO_2 laser was mostly used to structure the PMMA microfluidic lid of $V2$-C, shown in Figure 3.10. Laser-assisted machining was also employed for microfluidic tape shaping and for thick PMMA components fabrication (e.g. the covers of the *System* $V2$ chamber). Tape cutting and component fabrication did not require much optimization of the laser parameters. For tape cutting, a laser power of 2-3 % power and speed of 380 mm/s were found to be exellent settings. For carving out thick pieces of PMMA plates (2-3 mm), 70-80% power at the same speed were found to be good settings. Only the wait time between laser passes waas adjusted. Typically 10-15 laser passes were

Power (%)	Speed (mm/s)	Depth (nm)	Roughness (nm)
3	250	10968	845
5	250	30009	1079
6	250	61770	1565
8	250	88084	2296
3	300	2747	990
5	300	N/A	992
6	300	47501	1128
8	300	80752	1343

Table 4.3: Depth and roughness measurements for laser powers between 3% and 8% at laser speeds of 250 mm/s and 300 mm/s on PMMA plates.

required to cut a 2.5 mm thick PMMA plate, and 15 sec wait time between them was found necessary to avoid excessive melting of the polymer. If too much melting occurs, the trenches machined in PMMA will close and the overall cutting process efficiency is reduced.

The PMMA substrate used as microfluidic lid for *Disc V2-C* was machined on both sides. The top side was structured with 1 mm deep structures for magnets clamping, while the bottom side was patterned with shallow chambers (200 μm deep, see Figure 3.10).

First, the CO_2 laser parameters (power, speed and number of passes) were optimized for both ablation processes (deep and shallow). A grid of square areas 5 mm x 5 mm was designed in CAD and each square was assigned a different combination of laser power and laser speed. The number of passes was set to 1 and kept constant. The depth of features ablated with power ranging from 3% to 70% and speed varying from 200 mm/s to 380 mm/s was investigated. For the magnets clamping structures, power range from 20% to 50% and speed range from 240 mm/s to 300 mm/s were first analyzed. For the chip chambers power range from 3% to 15% and a speed range from 200 mm/s to 380 mm/s were selected.

The results on higher power ablation (see Table 4.2) showed that the sidewalls of the trenches dug in PMMA are deformed when ablating at high power and at low speed. Powers above 30% led to edges deformation and speeds higher than 280/mm significantly reduced the depth of the ablation step. The optimal parameters for the magnets clamping structures were chosen to be the ones that gave the highest depth per pass, without deformation of feature edges. At laser power of 25% and speed of 260 mm/s were found to comply the requirements. The depth per pass was measured to be 95 μm, requiring 10 steps for the fabrication of the structures for magnets clamping. A wit time of 10 s was implemented.

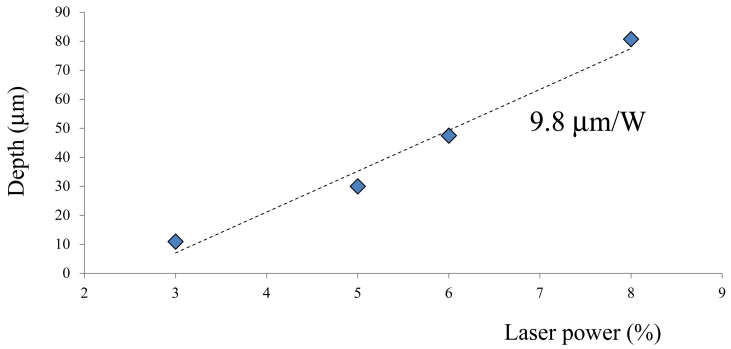

Figure 4.5: Laser power Vs depth for laser speed of 250 mm/s. The linear trend has a slope of 9.8 μm/W.

In Table 4.3 depth and roughness measurements on the shallow chamber are presented. Powers between 3% and 8% and speed of 250 mm/s and 300 mm/s were used.
The roughness of the machined surface was seen to increase when powers higher than 3% were used. The higher the power, the rougher the surface.
In *System V*2, an optical microscope was positioned over the cantilevers pools, thus requiring the carved shallow chamber surfaces to be as smooth as possible (see Figure 3.11). Powers below 3% were however difficult to characterize, since only a few microns were actually carved per pass. A large number of passes would have been required to reach the targeted depth of 200 μm.
Therefore a compromise between depth and roughness had to be defined. These values show a linear relation between laser power and obtained depth per pass. Figure 4.5 illustrates this behavior at fixed speed of 250 mm/s. The parameters used to carve the chip chambers were 5% power and 250 mm/s speed. These values provided enough low roughness and a reasonable depth. Seven passes were needed to reach a total depth of 200 μm.

PDMS spin-coating

PDMS was used for cover the bottom side of the microfluidic lid of *Disc V*2-*C* and to fill the o-ring-like structure patterned on the bottom side of *Disc V*3-*B*.
The PDMS was prepared by mixing in a 10:1 ratio silicone elastomer and its curing agent. The compound was left in a vacuum chamber for 15 minutes in order to eliminated bobbles in the elastomer. In case of *Disc V*2-*C*, the PDMS was poured on the PMMA disc clamped onto a spinner. Different spinning programs which targeted different thicknesses were used. The sealing properties of the lid were found optimal when 70-100 μm thick layer was spincoated and cured on the PMMA lid.
This thicknesses were obtained using the following spinner parameters:

- Step 1. 10 s at 400 rpm (acceleration of 200 rpm/s)
- Step 2a. 40 s at 1100 rpm (PDMS thickness 110 μm)

- Step 2b. 40 s at 1400 rpm (PDMS thickness 85 μm)
- Step 2c. 40 s at 1500 rpm (PDMS thickness 70 μm)

After spinning, the discs were left in an oven for 15 min at 90°C.
When used for filling the structures in *Disc V3-B*, the PDMS was prepared and loaded into syringes before being placed inside the vacuum chamber. Using a large needle (1 mm diameter) the PDMS was poured inside the cavities and cured in the oven.

4.3.2 Hot embossing

During the project the possibility of fabricating discs via hot embossing technology was investigated. The idea was to fabricate a fully polymeric platform, i.e. eliminating the Pyrex wafer that each of the disc version included as a support. The optical properties and the rigidity of glass were in fact very suitable for the application, and its use as microfluidics support (e.g. Discs *V3-A* and *V3-B*) was not too problematic. However, in the future vision of low cost disc manufacturing, different polymers with good optical properties were tested.

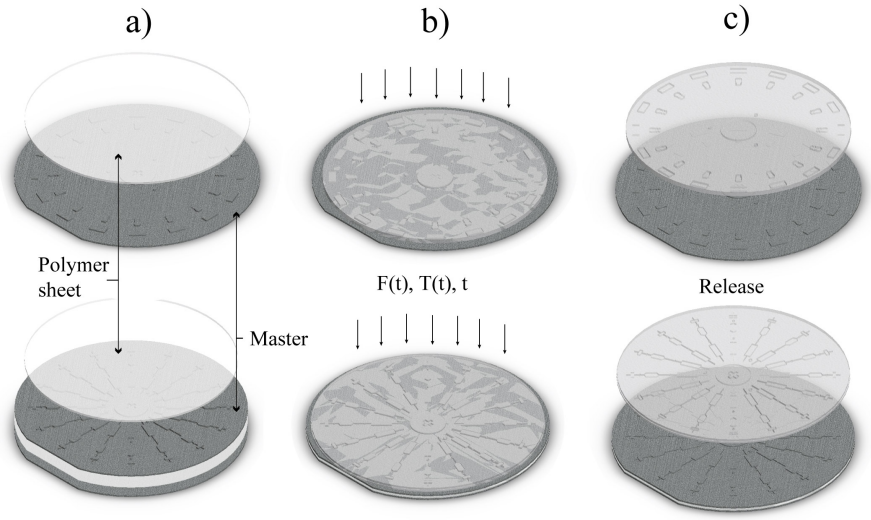

Figure 4.6: Schematics of the embossing process. a) A polymer sheet is brought in contact with the silicon master. b) A certain force $F(t)$ and temperature $T(t)$ are applied for a time interval t. c) The polymer sheet is released from the master.

Hot embossing is a well know microfabrication technique for lab-on-a-chip devices, widely employed for replication of structures patterned in silicon masters [132]. Embossing of PMMA [133], polycarbonate [132] and Cyclic Olefin Polymers (COP) [134] has been demonstrated and used to fabricate chips for a variety of applications.
TOPAS is a type of COP, a class of polymers based on cyclic olefin monomers and

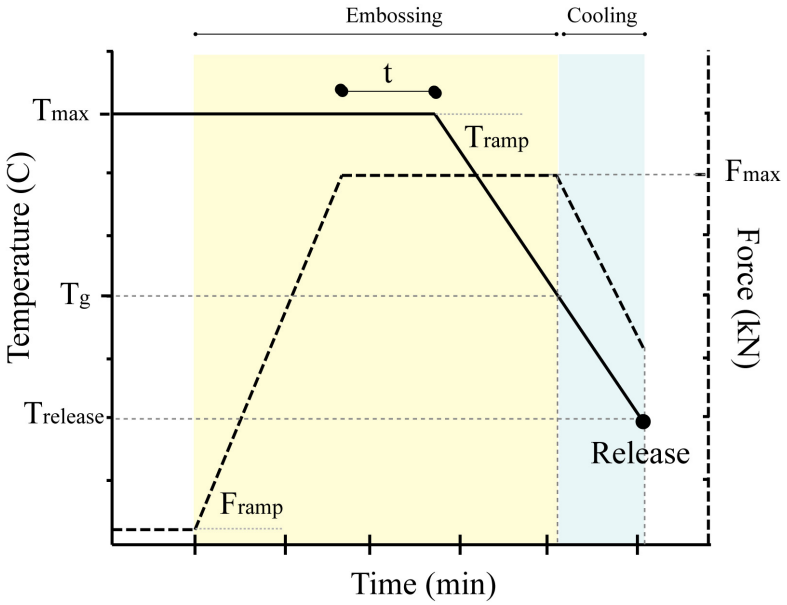

Figure 4.7: Force and Temperature applied to the sandwich structure plotted versus time. The master is released at a certain temperature $T_{release}$, below the glass transition temperature of the polymer (T_g).

ethene [135]. COPs have high-transparency properties in the visible and near ultraviolet, making these materials particularly suitable for applications requiring glass-like clarity. Polycarbonate is also known for its application in optics. CD and DVD are currently made out of polycarbonate.
First, polymer sheets were disc-shaped and sandwiched between the silicon master and a second silicon wafer. The sandwich was then loaded between the plates of a bonding press (Tempress, Germany). Often the bottom of the silicon master was glued to another wafer to increase the stiffness of the entire structure. In this way the risk of breaking the master during the release process was highly reduced.
The plates were heated above the glass transition temperature of the polymer and

Material	T_g (°C)	T_{max} (°C)	T_{ramp} (°C/min)	$T_{release}$ (°C)	F_{max} (kN)	F_{ramp} (kN/min)	t (min)	depth (μm)
TOPAS AS8007S-04	78	123	-3	45	20	3	3	85
TOPAS 5013S-04	134	175	-3	75	20	2	5	65
Polycarbonate	150	175	-3	85	20	3	5	65

Table 4.4: Values of T_g, T_{max}, $T_{release}$, F_{max}, F_{ramp} and t for the optimized embossing processes for TOPAS and polycarbonate. The ramping down (T_{ramp} depends on the cooling system of the bonding press. The measured cooling ramp was 3°C/min.

brought into contact with a controlled force, typically of the order of tens of kN for few minutes. The force, the embossing time and the temperature varied depending on the polymer used.

The force in the bonding press is applied with a ramp (F_{ramp}) on the order of few kN/min (see Figure 4.7). When the maximum force (F_{max}) is reached, the sandwich is kept under constant conditions for a time interval, t. After that, while keeping the embossing force constant, the sandwich is cooled to a release temperature ($T_{release}$) below the glass transition temperature of the polymer (T_g). Demoulding of the polymer from the master was performed manually releasing the wafers from the embossed surface .
Table 4.4 reports the values of T_g, T_{max}, $T_{release}$, F_{max}, F_{ramp} and t for the optimized embossing processes for TOPAS and polycarbonate.

Figure 4.8 shows pictures of test structures and capillary valves embossed, respectively, in TOPAS and in Polycarbonate. The structures are 50 μm deep.

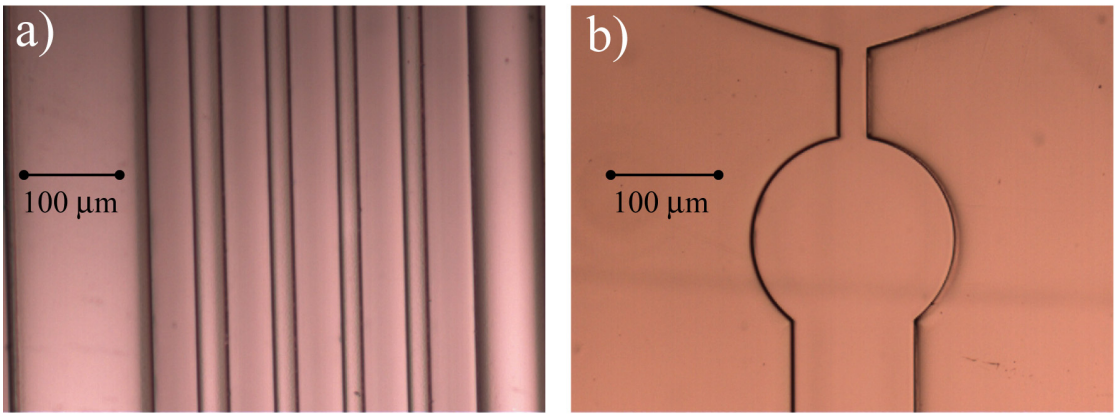

Figure 4.8: Pictures of embossed structures in a) TOPAS and b) Polycarbonate. The depth of the features is 50 μm.

The test grid embossed in TOPAS AS8007S-04 (Figure 4.8a) reveals good resolution of the pattern transfer for features dimension in the range between 20 μm and 100 μm. In a similar way, 30 μm wide channels embossed in Polycarbonate (Figure 4.8b) show the capability of reproducing the microstructures etched in the silicon master.
On the other hand, the embossing quality was found to vary across the area of the wafer. Typically, just a small portion of the embossed polymer was properly structured, while at the edges of the sheet the features were not completely shaped. Generally speaking, the lack of uniformity in the embossing process compromised the use of the technique for discs fabrication. However clamping tests for cantilever chips and microfluidic tests on embossed capillary valves were run, giving positive perspectives on a future employment of full-polymer discs.

4.3.3 Micromilling

CO_2 laser machine and micromilling technology were employed for PMMA microfabrication. Micromilling is a well established microfabrication technology for patterning microfluidic in polymeric materials [136–139]. *Discs* $V3$-A and $V3$-A were entirely fabricated with this technology.
A computer controlled 3-axis milling machine (Minitech Machining Corporation, US) was used. The machine embeds spindle motor which holds the milling tools and rotates along the Z-axis with defined speed. While the tool moves vertically, the table which holds the polymer plate moves along the X-Z plane. The nominal movement resolution of the X-Y stages is 0.1 μm.
The disc were fabricated clamping the PMMA plates on the X-Y stage, loading the CNC program and running a process with appropriate tools. Typically, 2 mm drill tools were used to make holes, while flat end mills (400 μm, 800 μm, 1 mm and 2 mm) were employed for patterning of channels and for pocketing of reservoirs.

Chapter 5

Data Analysis

This chapter describes the mathematical analysis of the data generated by the systems and introduces the software tools employed to acquire and store the data themself. Section 5.1 illustrates the statistical models used for data analysis and treatment of the huge amount of data generated during the experiments. Section 5.2 gives an overview on the Labview based program that interfaces the sensing device with a computer.

5.1 Signal processing

This Section illustrates how the cantilever profiles acquired through the DVD-ROM PUH are stored, averaged and post-processed. A brief introduction to the data analysis process is described in Sections 5.1.1 and 5.1.2, while Sections 5.1.3 and 5.1.4 illustrate how the cantilever profiles are acquired and stored. The statistical models employed for data treatment are described in detail in Section 5.1.5.
All the codes for data analysis were written in Matlab (Matlab 2009, Mathworks, US).

5.1.1 Introduction

The data process is composed by three steps: a characterization block (Block 1), a sensing block (Block 2) and a post-processing block (Block 3). In the characterization and sensing blocks, the signals are acquired, separated and stored in the computer's Random Access Memory (RAM). The data are pre-processed and assigned to specific variables that are saved on the computer hard drive in form of, for example, text files. After the experiments have been completed, post-processing is performed. It consists of statistical analysis of the stored variables and graphical output generation. Figure 5.1 illustrates the work-flow for the overall data processing.

The platform performs statistical characterization of a set of M cantilevers over N measurements rounds (revolutions), before the sample to be analyzed is actually dispensed to the sensing reservoirs. During this characterization process M measurements were thus acquired at each n^{th} revolution of the disc.

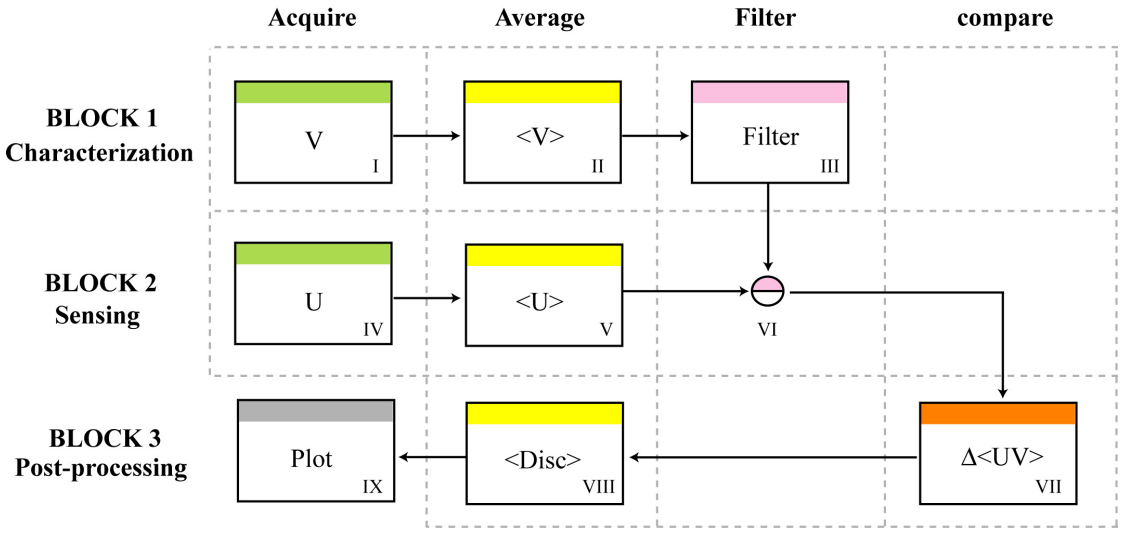

Figure 5.1: Workflow for the data acquisition, treatment and processing. In Block 1 the characterization profiles and resonance curves are acquired, pre-processed and stored on the hard drive. Block 2 includes the same operations for the sensing data. Block 3 operates the post-processing and produces output data plots.

After the characterization has been completed, the sensing data is acquired. It consists of MN' independent measurements on the same set of cantilevers, where N' is the number of sensing revolutions. The total amount of measurements is thus $M(N+N')$. In the experiments performed with *System V*3, typical values of M ranged from 24 to 72, while N and N' were generally set to 50. Within this context, around 5.000 measurements are typically performed in a single experiments. Considering that a single bending measurements is composed by approximatively 3000 points, a single roughness measurements by 20.000 points, and every resonance frequency measurement by 10.000 points, the overall "raw data" generated from one experiment exceeds 50.000.000 of single measurement points (i.e. float numbers on the computer memory).
Performing simple pre-processing before storing the data on the hard drive reduces the amount of points with almost two orders of magnitudes.

5.1.2 Data labeling

An important issue to be addressed for implementing analysis of this amount of data is to define a robust labeling method for the cantilever profiles (and resonance frequency peaks) acquired during the laser scan. Each profile can then be easily addressed and used for mathematical operations. Figure 5.2 shows the variable assignment principle implemented in this project.

When multiple cantilever chips are scanned by the DVD-ROM laser, a set of profiles spaced by null signal is generated. After the individual profiles are cut and saved in the RAM, a set of variables is assigned to each profile: the index number of the cantilever

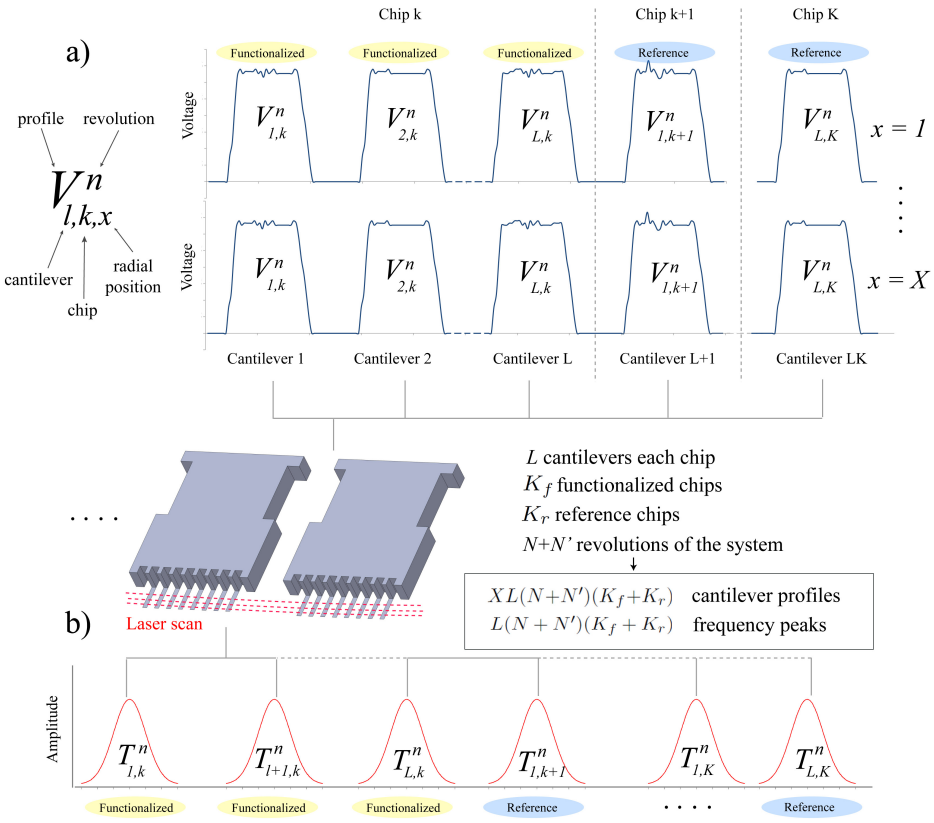

Figure 5.2: Schematics of the generation of raw signal. The cantilevers are scanned and their a) profile and b) resonance curves are acquired and stored in the RAM in temporary variables.

(l), the index number of the chip (k), the number of the revolutions at which the profile is acquired (n), and the position along the cantilever at which the profile is acquired (x). Setting L as the total number of cantilevers per chip, K_f as the total number of functionalized chips, K_r as the total number of reference chips, X as the total number of radial positions at which the cantilever surfaces are scanned, and N and N' as the total number of characterization and sensing revolutions, $XL(N+N')(K_f+K_r)$ single profiles are acquired in one experiments. Simultaneously, the PUH measures the vibrational spectra of the cantilevers. These spectra are generated from each cantilever at every laser pass (revolution). $L(N+N')(K_f+K_r)$ individual peaks are then obtained in one experiments.

Defining the single spatial measurement point as p, a profile consists of P voltage values measured along points of the cantilever width, $V(p)$, where $p \in [1, P]$. According to the variables listed in Figure 5.2, a generic cantilever profile is univocally identified as $V^n_{l,k,x}(p)$, and its resonance frequency measurement is labeled as $T^n_{l,k}$.

While L, K and X are kept constant during the whole experiment (i.e. during char-

acterization and sensing), the number of revolutions performed during Block 1 could differ from the ones used in Block 2. Two different revolution variables are then set: n for characterization and n' for sensing. N is then the total number of characterization revolutions while N' is the total number of sensing revolutions. Profiles acquired during Block 1 are labeled as $V^n(p)$ while the ones obtained in Block 2 are written as $U^{n'}(p)$. The same is valid for resonance frequency spectra, set as T^n for Block 1 and $J^{n'}$ for Block 2.
In this way every single profile or frequency plot can be univocally labeled and stored in the RAM, from where it can be recalled for mathematical operations. Table 5.1 reports the variable names and definitions.

Symbol	Variable	Unit	Domain
n	# Characterization revolutions	-	$n \in Z[1, N]$
n'	# Sensing revolutions	-	$n' \in Z[1, N']$
l	Cantilever number	-	$l \in Z[1, L]$
k	Chip number	-	$k \in Z[1, K]$
x	radial position number	-	$x \in Z[1, X]$
p	Acquisition point	-	$p \in Z[1, P]$
$V^n_{l,k,x}(p)$	Characterization profile	(Volt)	$(PX1)$ array
$U^{n'}_{l,k,x}(p)$	Sensing profile	(Volt)	$(PX1)$ array
$T^n_{l,k}$	Characterization peak	(Hz)	$T \in Q$
$J^{n'}_{l,k}$	Sensing peak	(Hz)	$Y \in Q$

Table 5.1: List of variables for labeling of the acquired data.

The next Sections describes the three Blocks individually. Sections 5.1.3 and 5.1.4 introduce the pre-processing operations performed on respectively, characterization and sensing data. Section 5.1.5 presents the methods employed to generate the statistical output.

5.1.3 Block 1 - Characterization

This Block consists of measuring the "characterization signal" of the cantilevers at every revolution n. Profiles and resonance peaks are acquired, pre-processed and saved on the PC hard drive in form of text files (.txt).
For simplicity, in this report the value of x will be kept constant and equal to 1 (i.e. referring to the radial acquisition point closer to the free-end of the cantilevers). The whole statistical approach remains the same, and inclusion of the radial position can be done by simply introducing the variable into the equations.

In most of the experiments, the cantilevers are measured along their width in both directions. This is due to the fact that most of the experiments are performed over a circular sector of the disc, typically including 3-9 chips (i.e. 24-72 cantilevers). Changing the rotation direction and scanning the cantilevers clockwise and counter-clockwise thus increases the measurement throughput, compared to the situation where the disc makes complete revolutions.
Furthermore, small differences between measurements run in the two directions were observed. This behavior could be attributed to a dependency of the rotational stage alignment on the rotation direction. Noise at the edges of the cantilevers is also believed to affect the equality of the two profiles.
Each measured profile is then overlapped and averaged to its counterpart, further reducing the risk of artifact measurements. $V^n_{l,k}(p)$ is then actually composed by two terms:

$$V^n_{l,k}(p) = \frac{1}{2}\left[V^n_{l,k}(p)_{CCW} + V^n_{l,k}(P-p)_{CW}\right] \tag{5.1}$$

The averaging of clock-wise and counter-clockwise measurements is the first mathematical operation run in Block 1.

Four more variables are generated at the end of the acquisition process. $\bar{V}^n_{l,k}$ evaluates the average voltage value across the width of a cantilever at a given revolution, with standard deviation $\sigma^n_{V(l,k)}$. $\bar{V}_{l,k}(p)$ is an array of measurement points obtained by averaging the N profiles of a given cantilever. The standard deviation values are stored in $\sigma_{V(l,k)}(p)$. Table 5.2 lists the name of the variables and their analytical expressions.

Variable	Symbol	Analytical expression	
Profile average	$\bar{V}^n_{l,k}$	$\bar{V}^n_{l,k} = \frac{1}{P}\sum_{p=1}^{P} V^n_{l,k}(p)$	(5.2)
Profile stdev	$\sigma^n_{V(l,k)}$	$\sigma^n_{V(l,k)} = \sqrt{\frac{1}{P}\sum_{p=1}^{P}\left(V^n_{l,k}(p) - \bar{V}^n_{l,k}\right)^2}$	(5.3)
Point average	$\bar{V}_{l,k}(p)$	$\bar{V_{l,k}}(p) = \frac{1}{N}\sum_{n=1}^{N} V^n_{l,k}(p)$	(5.4)
Point stdev	$\sigma_{V(l,k)}(p)$	$\sigma_{V(l,k)}(p) = \sqrt{\frac{1}{N}\sum_{n=1}^{N}\left(V^n_{l,k}(p) - \bar{V_{l,k}}(p)\right)^2}$	(5.5)

Table 5.2: List of variables calculated at the end of the acquisition process in Block 1.

The calculated profile averages ($\bar{V}^n_{l,k}$) are then filtered from the noise present at the edges of the cantilevers. When the laser spot (0.5 μm to 30 μm diameter, depending on the NA) is not fully projected on the cantilever surface, the noise is higher at the outer 10-15 μm (100-150 points) of the cantilever profile. The filtering procedure aims at selecting the useful part (P^*) of the measured cantilevers profiles. The range in which

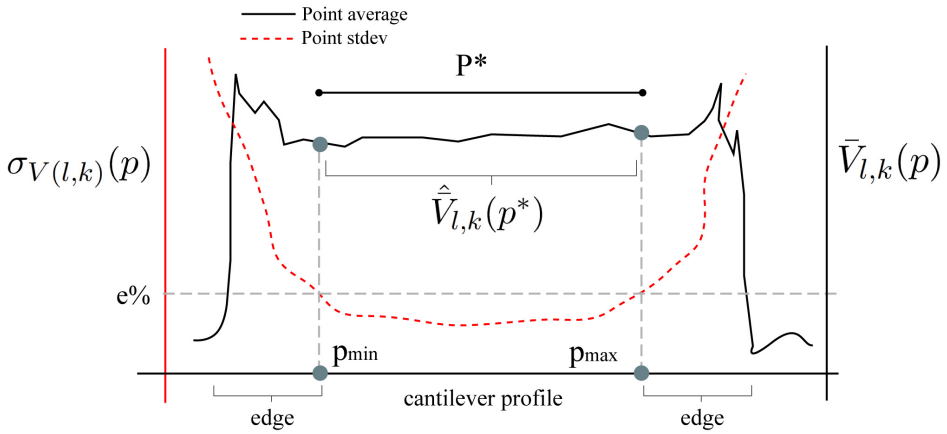

Figure 5.3: Schematic illustration of the filter process. The new profiles, $\hat{V}^n_{l,k}(p^*)$, are obtained sectioning the raw profiles in the range (p_{min}, p_{max}) in which $\sigma_{V(l,k)}(p) < e\%$.

the profile standard deviation of a given cantilever ($\sigma_{V(l,k)}(p)$) is less than a defined percentage ($e\%$) defines the highly reproducible profile portion of the signal (p_{min},p_{max}). In formulas, this is described as:

$$\hat{V}^n_{l,k}(p^*) = V^n_{l,k}(p)_{|\sigma_{V(l,k)}(p)<e\%|} \tag{5.6}$$

$$P^* = p_{max} - p_{min} \tag{5.7}$$

Figure 5.3 schematically illustrates how the cantilever profiles are cut. This process

Variable	Symbol	Analytical expression	
Filtered profile average	$\hat{\bar{V}}^n_{l,k}$	$\hat{\bar{V}}^n_{l,k} = \frac{1}{P^*}\sum_{p=p_{min}}^{p_{max}} V^n_{l,k}(p)$	(5.8)
Filtered profile stdev	$\hat{\sigma}^n_{\hat{V}(l,k)}$	$\hat{\sigma}^n_{\hat{V}(l,k)} = \sigma^n_{V(l,k)\|p\in[p_{min},p_{max}]\|}$	(5.9)
Filtered point average	$\hat{\bar{V}}_{l,k}(p^*)$	$\hat{\bar{V}}_{l,k}(p^*) = \frac{1}{N}\sum_{n=1}^{N} \hat{V}^n_{l,k}(p^*)$	(5.10)
Filtered point stdev	$\hat{\sigma}_{\hat{V}(l,k)}(p^*)$	$\hat{\sigma}_{\hat{V}(l,k)}(p^*) = \sigma_{V(l,k)}(p)_{\|p\in[p_{min},p_{max}]\|}$	(5.11)

Table 5.3: Characterization variables defined after filtering operation is performed.

generates a new set of variables, with new measurement points domain defined by Eqs. 5.6 and 5.7. Table 5.3 lists the new filtered variables and their analytical expression.

In case of dynamic mode analysis, the FFT plot (see Figure 2.12) is cut within values close to the expected resonance frequency of the cantilever (between 1 kHz and 10 kHz, in case of a Si cantilever's first mode). The measured resonance curve is then fitted with

a Lorentzian function and the resonance frequency (ω_r) is extracted. The Q factor is calculated by dividing the resonance frequency with the bandwidth at -3 dB (so-called 3dB method):

$$Q = \frac{\omega_r}{\Delta\omega_{-3dB}} \tag{5.12}$$

The values of ω_r and Q are then stored in a new set of variables, $T^n_{l,k}$. The average and standard deviation of the resonance frequency over N revolutions of a given cantilever are then calculated as

$$T_{l,k} = \frac{1}{N}\sum_{n=1}^{N} T^n_{l,k} \tag{5.13}$$

$$\sigma_{T(l,k)} = \sqrt{\frac{1}{N}\sum_{n=1}^{N}\left(T^n_{l,k} - \bar{T}_{l,k}\right)^2} \tag{5.14}$$

5.1.4 Block 2 - Sensing

During the sensing Block, the cantilevers are measured after exposure to a sample. The profiles are acquired, treated and stored in the same way as Block 1.
The profiles are filtered according to the domain (P^*) defined during the characterization block. The new variables are then generated and saved on the PC hard drive. Table 5.4 lists the variable names and formulas used to compute them.

Variable	Symbol	Analytical expression	
Profile average	$\hat{\bar{U}}^{n'}_{l,k}$	$\hat{\bar{U}}^{n'}_{l,k} = \frac{1}{P^*}\sum_{p^*=1}^{P^*} U^{n'}_{l,k}(p^*)$	(5.15)
Profile stdev	$\hat{\sigma}^{n'}_{\hat{U}(l,k)}$	$\hat{\sigma}^{n'}_{\hat{U}(l,k)} = \sqrt{\frac{1}{P^*}\sum_{p^*=1}^{P^*}\left(\hat{U}^{n'}_{l,k}(p^*) - \hat{\bar{U}}^{n'}_{l,k}\right)^2}$	(5.16)
Point average	$\hat{\bar{U}}_{l,k}(p^*)$	$\hat{\bar{U}}_{l,k}(p^*) = \frac{1}{N'}\sum_{n'=1}^{N'} \hat{U}^{n'}_{l,k}(p^*)$	(5.17)
Point stdev	$\hat{\sigma}_{\hat{U}(l,k)}(p^*)$	$\hat{\sigma}_{\hat{U}(l,k)}(p^*) = \sqrt{\frac{1}{N'}\sum_{n'=1}^{N'}\left(\hat{U}^{n'}_{l,k}(p^*) - \hat{\bar{U}}_{l,k}(p^*)\right)^2}$	(5.18)

Table 5.4: List of variables calculated after the acquisition process in Block 2.

The same approach used in Block 1 is then applied to the resonance measurements performed during the sensing block. The frequencies are identified and located in the $J^{n'}_{l,k}$ variables. The average and standard deviation of the resonance frequency over N' revolutions of a given cantilever are then calculated as

$$J_{l,k} = \frac{1}{N'}\sum_{n'=1}^{N'} J^{n'}_{l,k} \tag{5.19}$$

$$\sigma_{J(l,k)} = \sqrt{\frac{1}{N'}\sum_{n=1}^{N'}\left(J_{l,k}^{N'} - \bar{J}_{l,k}\right)^2} \tag{5.20}$$

5.1.5 Block 3 - Post processing

After the sensing acquisition is completed, the information stored in the variables listed in the previous sections are processed.
The post-processing functions generate the statistical output for the analysis of bending, surface roughness and thermal noise.

Drift compensation

Before the actual post-processing is run, the filtered profiles obtained through Eq. 1.8 and 1.15 are treated in order to eliminate artifacts due to signal drifting. Several reasons cause drift of the voltage signal read from the electronics. Among these, the most relevant identified factors are: (i) temperature gradients around the PUHs, (ii) uncontrolled air flow around the system, (iii) mechanical expansion of the PUH due to temperature rising, (iv) laser intensity decay, (v) electronics oscillations, (vi) data acquisition program clock delay, (vii) radio-frequency environmental noise and (viii) intrinsic micromechanical drift of the cantilevers.

A drift-compensation signal ($S(t)$) is thus subtracted from the profiles in order to avoid artifact results from the mentioned drift sources.

$$\hat{\tilde{V}}^S(t) = \hat{\tilde{V}}(t) - S(t) \tag{5.21}$$

The choice of $S(t)$ is not trivial. Initially it was set as a linear function, since most of the drift sources vary linearly during time. However, it was found that the drift is actually composed by superimposition of linear and non-linear factors. The analytical evaluation of this drift is very difficult, being affected by several parameters not easily computable. An on-line drift measurement system was then implemented.
A fixed structure was positioned next to the cantilever chips. A body of the cantilever chips was found to be an excellent drift-compensation tool. The body chip was clamped inside the footprint areas rotated 180° on the X-Y plane. The laser then scans the bulk silicon block (positioned at the same Z level of the cantilevers) and record the values of the FES obtained from scanning the profile of the body chip. The voltage signal variation of the body-chip profile during the discs revolutions is actually an on-line measurement of the drift, since the bulk silicon piece is unable to bend. Defining this signal as $S(n)$, the drift-free characterization profile at a given revolution n is expressed by:

$$\hat{\tilde{V}}_{l,k}^{Sn} = \hat{\tilde{V}}_{l,k}^{n} - S(n) \tag{5.22}$$

The drift is measured continuously also during the sensing acquisition, namely $S(n')$.

The same operation is then applied to the profiles acquired during the sensing block:

$$\hat{\tilde{U}}_{l,k}^{Sn'} = \hat{\tilde{U}}_{l,k}^{n'} - S(n' + N) \tag{5.23}$$

$\hat{\tilde{V}}_{l,k}^{Sn}$ and $\hat{\tilde{U}}_{l,k}^{Sn'}$ then represent the filtered and un-drifted profiles of the individual cantilevers.

Bending analysis - Continuous flow

Assuming that the l cantilevers of the chip k are equally treated (e.g. all functionalized or all reference), the individual profiles belonging to the same chip are averaged:

$$\hat{\tilde{V}}_{k}^{Sn} = \frac{1}{L} \sum_{l=1}^{L} \hat{\tilde{V}}_{l,k}^{Sn} \tag{5.24}$$

Then, different chips equally treated are averaged again, obtaining the averaged profile of all the characterized cantilevers of the same type at a given revolution n:

$$\hat{\tilde{V}}_{f}^{Sn} = \tfrac{1}{K_f} \textstyle\sum_{k=1}^{K_f} \hat{\tilde{V}}_{k}^{Sn} \qquad \hat{\tilde{V}}_{r}^{Sn} = \tfrac{1}{K_r} \textstyle\sum_{k=1}^{K_r} \hat{\tilde{V}}_{k}^{Sn} \tag{5.25}$$

Where K_f is the total number of functionalized chips and K_r the total number of reference chips.

It has to be noticed that the domain of Eqs. 5.24 and 5.25 generally differ from the total number of functionalized cantilevers (LK_f) and reference cantilevers (LK_r). This is due to loss of signal from some cantilevers, either due to measurement issues (software, mainly) or due to odd behaviors of individual cantilevers. Data loss occurs also when the initial difference in deflection between the cantilevers exceeds the DVD-ROM optics linear working range. The actual statistically useful domain is then typically 10%-30% smaller than the total number of cantilevers employed in the experiements. At the moment an automatic selection of the "useful" cantilevers has not been implemented yet. The selection is then performed manually before the actual post-processing is run.
Eqs. 5.24 and 5.25 are then applied to the sensing profiles in accordance to the cantilevers that actually gave signal during the characterization. These operations return the averaged sensing profiles of cantilevers of the same type at a given revolution n':

$$\hat{\tilde{U}}_{k}^{Sn'} = \frac{1}{L} \sum_{l=1}^{L} \hat{\tilde{U}}_{l,k}^{Sn'} \tag{5.26}$$

$$\hat{\tilde{U}}_{f}^{Sn'} = \tfrac{1}{K_f} \textstyle\sum_{k=1}^{K_f} \hat{\tilde{U}}_{k}^{Sn'} \qquad \hat{\tilde{U}}_{r}^{Sn'} = \tfrac{1}{K_r} \textstyle\sum_{k=1}^{K_r} \hat{\tilde{U}}_{k}^{Sn'} \tag{5.27}$$

$\hat{\tilde{V}}_{f}^{Sn}$ and $\hat{\tilde{U}}_{f}^{Sn'}$ thus represent the values of the averaged signal obtained from the set of functionalized cantilevers at a given revolution, respectively, before and after the

exposure to a sample. These values are used when continuous flow measurements are performed, i.e. when the values obtained from different revolutions are not averaged. The standard deviations of the measured deflection values at a given revolution n can be simply calculated as:

$$\hat{\sigma}_{Vf}^{Sn} = \sqrt{\frac{1}{K_f}\sum_{k=1}^{K_f}\left(\hat{\hat{V}}_{l,k}^{Sn} - \hat{\hat{V}}_{f}^{Sn}\right)^2} \qquad \hat{\sigma}_{Vr}^{Sn} = \sqrt{\frac{1}{K_r}\sum_{k=1}^{K_r}\left(\hat{\hat{V}}_{l,k}^{Sn} - \hat{\hat{V}}_{r}^{Sn}\right)^2} \tag{5.28}$$

$$\hat{\sigma}_{Uf}^{Sn'} = \sqrt{\frac{1}{K_f}\sum_{k=1}^{K_f}\left(\hat{\hat{U}}_{l,k}^{Sn'} - \hat{\hat{U}}_{f}^{Sn'}\right)^2} \qquad \hat{\sigma}_{Ur}^{Sn'} = \sqrt{\frac{1}{K_r}\sum_{k=1}^{K_r}\left(\hat{\hat{U}}_{l,k}^{Sn'} - \hat{\hat{U}}_{r}^{Sn'}\right)^2} \tag{5.29}$$

Eqs. 5.25, 5.27, 5.28 and 5.29 fully define the statistical behavior of the cantilever employed in continuous flow measurements.
Figure 5.4 illustrates how the computed variables are plotted in the deflection Vs revolutions graph.

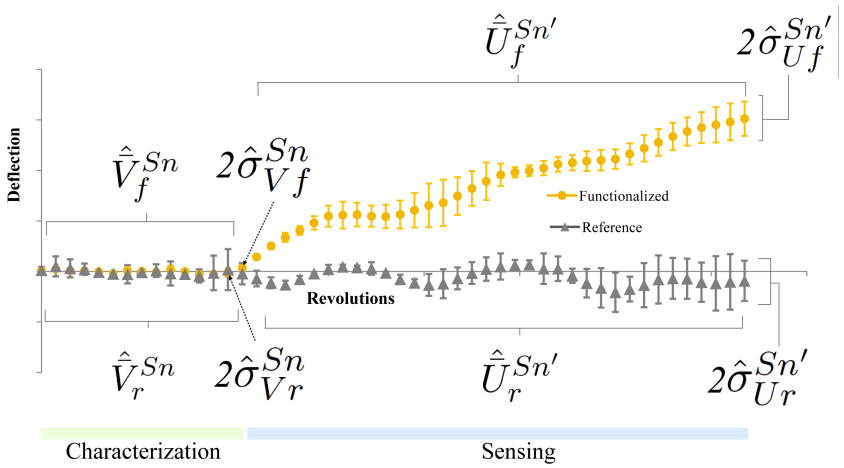

Figure 5.4: Illustration of the data plotting for continuous flow measurements.

Bending analysis - Wet & Dry

When performing measurements in wet & dry, cantilever profiles are monitored for a specific interval of time. Within this interval, moving averages are continuously calculated. At a given revolution $\hat{n}$, these variables store the averages evaluated over the last $\hat{n}$ revolutions. In formulas:

$$\hat{\hat{V}}_f^{S\hat{n}} = \frac{1}{\hat{n}}\sum_{n=1}^{\hat{n}}\hat{\hat{V}}_f^{Sn}\,|_{\hat{n}<N} \qquad \hat{\hat{V}}_r^{S\hat{n}} = \frac{1}{\hat{n}}\sum_{n=1}^{\hat{n}}\hat{\hat{V}}_r^{Sn}\,|_{\hat{n}<N} \tag{5.30}$$

$$\hat{\hat{U}}_f^{S\hat{n}'} = \frac{1}{\hat{n}'}\sum_{n'=1}^{\hat{n}'}\hat{\hat{U}}_f^{Sn'}\,|_{\hat{n}'<N'} \qquad \hat{\hat{U}}_r^{S\hat{n}'} = \frac{1}{\hat{n}'}\sum_{n'=1}^{\hat{n}'}\hat{\hat{V}}_r^{Sn'}\,|_{\hat{n}'<N'} \tag{5.31}$$

These moving averages are evaluated during every revolution ($\hat{n}$ for characterization and $\hat{n}'$ for sensing), and they converge to the values obtained when averaging over the complete set of disc revolutions (N for characterization and N' for sensing):

$$\hat{\bar{V}}_f^S = \hat{\bar{V}}_f^{S\hat{n}} \mid \hat{n} = N; \qquad \hat{\bar{V}}_r^S = \hat{\bar{V}}_r^{S\hat{n}} \mid \hat{n} = N; \tag{5.32}$$

$$\hat{\bar{U}}_f^S = \hat{\bar{U}}_f^{S\hat{n}'} \mid \hat{n}' = N'; \qquad \hat{\bar{U}}_r^S = \hat{\bar{U}}_r^{S\hat{n}'} \mid \hat{n}' = N' \tag{5.33}$$

The two variables expressed in Eqs. 5.32 contain the values of averaged deflection of the set of cantilevers of the same type, evaluated over N characterization revolutions. Eqs. 5.33 on the other hand expresses the values of averaged deflections after the cantilevers have been exposed to the sample, analyzed over N' revolutions.
According to Eqs. 5.28, 5.29, 5.30 and 5.31, the corresponding standard deviation values computed at intermediate revolutions are:

$$\hat{\sigma}_{Vf}^{S\hat{n}} = \sqrt{\frac{1}{K_f \hat{n}} \sum_{k=1}^{K_f} \sum_{n=1}^{\hat{n}} \left(\hat{\bar{V}}_{l,k}^{Sn} - \hat{\bar{V}}_f^{S\hat{n}} \right)^2} \mid_{\hat{n}<N} \tag{5.34}$$

$$\hat{\sigma}_{Vr}^{S\hat{n}} = \sqrt{\frac{1}{K_r \hat{n}} \sum_{k=1}^{K_r} \sum_{n=1}^{\hat{n}} \left(\hat{\bar{V}}_{l,k}^{Sn} - \hat{\bar{V}}_r^{S\hat{n}} \right)^2} \mid_{\hat{n}<N} \tag{5.35}$$

$$\hat{\sigma}_{Uf}^{S\hat{n}'} = \sqrt{\frac{1}{K_f \hat{n}'} \sum_{k=1}^{K_f} \sum_{n'=1}^{\hat{n}'} \left(\hat{\bar{U}}_{l,k}^{Sn'} - \hat{\bar{U}}_f^{S\hat{n}'} \right)^2} \mid_{\hat{n}'<N'} \tag{5.36}$$

$$\hat{\sigma}_{Ur}^{S\hat{n}'} = \sqrt{\frac{1}{K_r \hat{n}'} \sum_{k=1}^{K_r} \sum_{n'=1}^{\hat{n}'} \left(\hat{\bar{U}}_{l,k}^{Sn'} - \hat{\bar{U}}_r^{S\hat{n}'} \right)^2} \mid_{\hat{n}'<N'} \tag{5.37}$$

While according to Eqs. 5.32 and 5.33, the standard deviation values corresponding to the last characterization and sensing revolutions are:

$$\hat{\sigma}_{Vf}^S = \hat{\sigma}_{Vf}^{S\hat{n}} \mid \hat{n} = N \qquad \hat{\sigma}_{Vr}^S = \hat{\sigma}_{Vr}^{S\hat{n}} \mid \hat{n} = N; \tag{5.38}$$

$$\hat{\sigma}_{Uf}^S = \hat{\sigma}_{Uf}^{S\hat{n}'} \mid \hat{n}' = N' \qquad \hat{\sigma}_{Ur}^S = \hat{\sigma}_{Ur}^{S\hat{n}'} \mid \hat{n}' = N'; \tag{5.39}$$

These standard deviations indicate the level of homogeneity of the bending distribution along the $L_f K_f + L_r K_r$ analyzed cantilevers. Subtracting the sensing and characterization values, information about the average change of deflection of the specific set of cantilevers are obtained:

$$\Delta\hat{\bar{U}}_f^S = \hat{\bar{U}}_f^S - \hat{\bar{V}}_f^S \qquad \Delta\hat{\bar{U}}_r^S = \hat{\bar{U}}_r^S - \hat{\bar{V}}_r^S \tag{5.40}$$

The difference in behavior between functionalized and reference cantilevers can then easily be obtained as

$$\Delta\hat{\bar{U}}^S = \Delta\hat{\bar{U}}_f^S - \Delta\hat{\bar{U}}_r^S \tag{5.41}$$

Eqs. 1.30-1.41 fully define the behavior of the analyzed cantilevers in wet & dry mode. Figure 5.5 illustrates how the different variables are plotted in the output graph.

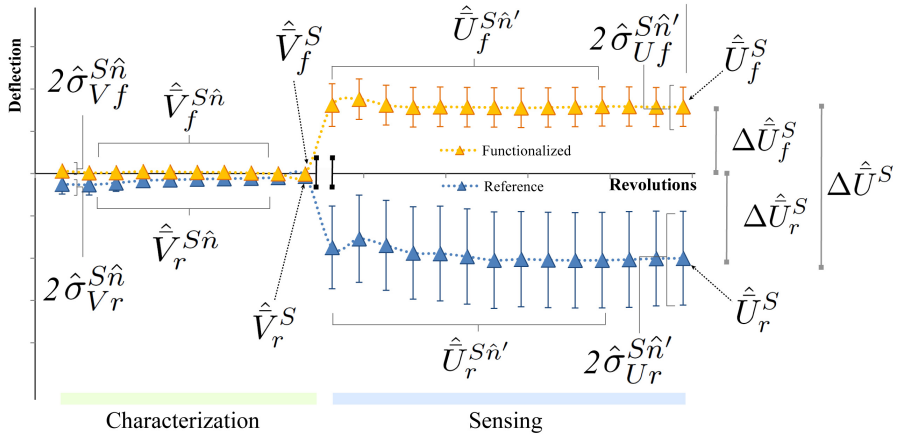

Figure 5.5: Data plotting for Wet % Dry analysis

Surface roughness analysis

The statistical analysis of surface roughness is similar to the bending protocol described in the previous paragraph.
Assuming that the variable expressed by Eq. 1.9 is a good indicator of the topography of the surface of a cantilever, the "roughness" variable of a given profile, $R^n_V(l,k)$ is then defined as:

$$R^n_V(l,k) = \hat{\sigma}^n_{\hat{V}(l,k)} \tag{5.42}$$

The values of $R^n_V(l,k)$ are computed for different values of x (the radial position along the cantilever length). For simplicity of the mathematical expressions the value of x is ignored in the following analysis.

Similarly to the case of the bending analysis, the averaged roughness of a set of equally treated cantilevers at a given revolution can be computed as:

$$R^n_{Vf} = \frac{1}{L_f K_f}\sum_{l=1}^{L_f}\sum_{k=1}^{K_f} R^n_V(l,k) \qquad R^n_{Vr} = \frac{1}{L_r K_r}\sum_{l=1}^{L_r}\sum_{k=1}^{K_r} R^n_V(l,k) \tag{5.43}$$

$$R^{n'}_{Uf} = \frac{1}{L_f K_f}\sum_{l=1}^{L_f}\sum_{k=1}^{K_f} R^{n'}_U(l,k) \qquad R^{n'}_{Ur} = \frac{1}{L_r K_r}\sum_{l=1}^{L_r}\sum_{k=1}^{K_r} R^{n'}_U(l,k) \tag{5.44}$$

While the averaged values over a set of revolutions in the interval $(1,\hat{n})$ are given, according to Eqs. 5.30 and 5.31 by

$$R^{\hat{n}'}_{Uf} = \frac{1}{\hat{n}'}\sum_{n'=1}^{\hat{n}'} R^{n'}_{Uf}\,|_{\hat{n}'<N'} \qquad R^{\hat{n}'}_{Ur} = \frac{1}{\hat{n}'}\sum_{n'=1}^{\hat{n}'} R^{n'}_{Ur}\,|_{\hat{n}'<N'} \tag{5.45}$$

$$R^{\hat{n}'}_{Uf} = \frac{1}{\hat{n}'}\sum_{n'=1}^{\hat{n}'} R^{n'}_{Uf}\,|_{\hat{n}'<N'} \qquad R^{\hat{n}'}_{Ur} = \frac{1}{\hat{n}'}\sum_{n'=1}^{\hat{n}'} R^{n'}_{Ur}\,|_{\hat{n}'<N'} \tag{5.46}$$

And the averaged values along the entire revolutions of the experiment are calculated from

$$R_{Vf} = R^{\hat{n}}_{Vf} \mid \hat{n} = N \qquad R_{Ur} = R^{\hat{n}}_{Vr} \mid \hat{n} = N \tag{5.47}$$

$$R_{Uf} = R_{Uf}^{\hat{n}'} \mid \hat{n}' = N' \qquad R_{Ur} = R_{Ur}^{\hat{n}'} \mid \hat{n}' = N' \tag{5.48}$$

The variables computed through Eqs. 5.43 and 5.44 are used for data plotting of continuous flow measurements, while the values obtained with Eqs. 1.45-1.48 describe roughness values for wet & dry experiments. Standard deviations computed by formulas similar to Eqs. 5.28,5.29 and 5.34-5.37 can be plotted, respectively, in continuous flow and wet & dry graphs.

It is often useful to plot the three-dimensional profiles of the cantilevers (or their averages) to have further information on the topography of the sensor surfaces.

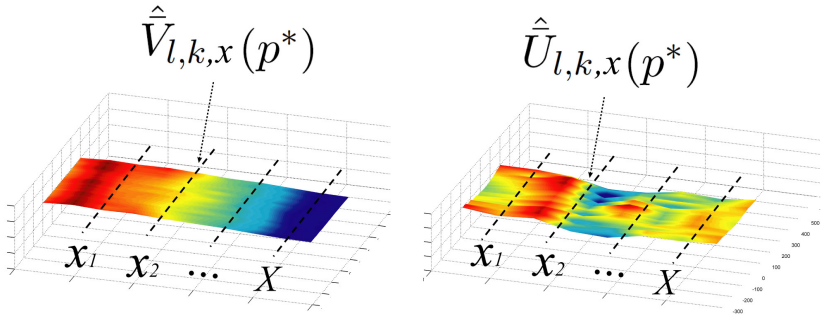

Figure 5.6: Three-dimensional surface reconstruction of cantilevers before and after exposure to sample.

Figure 5.6 illustrates the graphical output of 3D surfaces acquired in Block 1 and in Block 2. The filtered point averages corresponding to different values of x ($\hat{\bar{V}}_{l,k,x}(p^*)$ are plotted into a three-dimensional graph.

Resonance frequency analysis

The thermal noise statistical post-processing is much simpler than the one for the bending presented in the previous paragraphs. This is due to the fact that the stored variables, $T_{l,k}^{n}$ for characterization and $J_{l,k}^{n'}$ for sensing, are composed by single value of resonance frequency (in some cases, by frequency and Q factor). The average resonance frequencies for a given set of cantilevers, before ($\bar{T}_f$, $\bar{T}_r$) and after ($\bar{J}_f$ and $\bar{J}_r$) the exposure to a sample, can be easily calculated as

$$\bar{T}_f = \frac{1}{LK_f \sum_{l=1}^{L}} \sum_{k=1}^{K_f} T_{l,k} \qquad \bar{T}_r = \frac{1}{LK_r} \sum_{l=1}^{L} \sum_{k=1}^{K_r} T_{l,k} \tag{5.49}$$

$$\bar{J}_f = \frac{1}{LK_f} \sum_{l=1}^{L} \sum_{k=1}^{K_f} J_{l,k} \qquad \bar{J}_r = \frac{1}{LK_r} \sum_{l=1}^{L} \sum_{k=1}^{K_r} J_{l,k} \tag{5.50}$$

The variables expressed by Eqs. 5.49 and 5.50 are used to evaluate the change in resonance frequency after the exposure to a sample:

$$\Delta J_f = \bar{J}_f - \bar{T}_f \qquad \Delta J_r = \bar{J}_r - \bar{T}_r \tag{5.51}$$

Where $\bar{T}_f$ and $\bar{J}_f$ are averaged over K_f and $\bar{T}_r$ and $\bar{J}_r$ are averaged over K_r. These values are typically plotted in histograms. The standard deviations are then computed

$$\sigma_{T_f} = \sqrt{\frac{1}{LK_f}\left(\sum_{l=1}^{L}\sum_{k=1}^{K_f} T_{l,k} - \bar{T}_f\right)^2} \quad \sigma_{T_r} = \sqrt{\frac{1}{LK_r}\left(\sum_{l=1}^{L}\sum_{k=1}^{K_r} T_{l,k} - \bar{T}_r\right)^2} \tag{5.52}$$

$$\sigma_{J_f} = \sqrt{\frac{1}{LK_f}\left(\sum_{l=1}^{L}\sum_{k=1}^{K_f} J_{l,k} - \bar{T}_f\right)^2} \quad \sigma_{J_r} = \sqrt{\frac{1}{LK_r}\left(\sum_{l=1}^{L}\sum_{k=1}^{K_r} J_{l,k} - \bar{T}_r\right)^2} \tag{5.53}$$

Using Eqs. 5.52 and 5.53, combined standard deviations are calculated as

$$\Delta\sigma_{J_f} = \sqrt{\sigma_{J_f}^2 + \sigma_{T_f}^2} \qquad \Delta\sigma_{J_r} = \sqrt{\sigma_{J_r}^2 + \sigma_{T_r}^2} \tag{5.54}$$

and presented in the plot in the form of error bars. The difference between the values calculated from Eq. 5.51 is then used to quantify the difference in frequency shift between sets of functionalized and reference cantilevers.

$$\Delta J = \Delta J_f - \Delta J_r \tag{5.55}$$

Figure 5.7 shows the histogram of the variables computed through Eqs. 5.51, 5.54 and 5.55. The same approach can be implemented on sets of Q factor measurements.

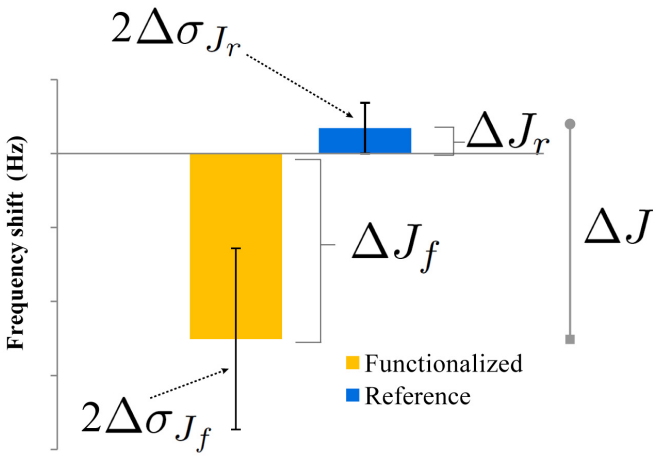

Figure 5.7: Histogram graphical representation of the resonance frequency shift for the sets of functionalized and reference cantilevers.

5.2 Software Interface

This Section briefly describes the working principle of the software interfacing the platform with the PC. The software functionalities presented here corresponds to the last generation of *System V*3. Several intermediate versions have been tested during the project, and the overall performance of the program was highly improved during the years.
The functions were designed in collaboration with IPAS, and implemented in Labview by a software engineer, Mr. C.H. Chen.

Figure 5.8 schematically illustrates the working principle of the Labview interfacing program.
The digital data transmitted to the PC from the motor controller and the DAQ card are acquired and read from interface functions embedded in Labview. The computer control is driven by a modulized program, which displays multiple panels for operating the different system functions. This program allow the access to the parameters of the individual system components: (i) Motor, (ii) X- and Z- coils of the VCM, (iii) FES acquisition, (iv) microfluidic pump (in wet & dry mode), (v) cantilever separation function, (vi) pre-processing panel, (vii) post-processing functions and (viii) data plotting window.

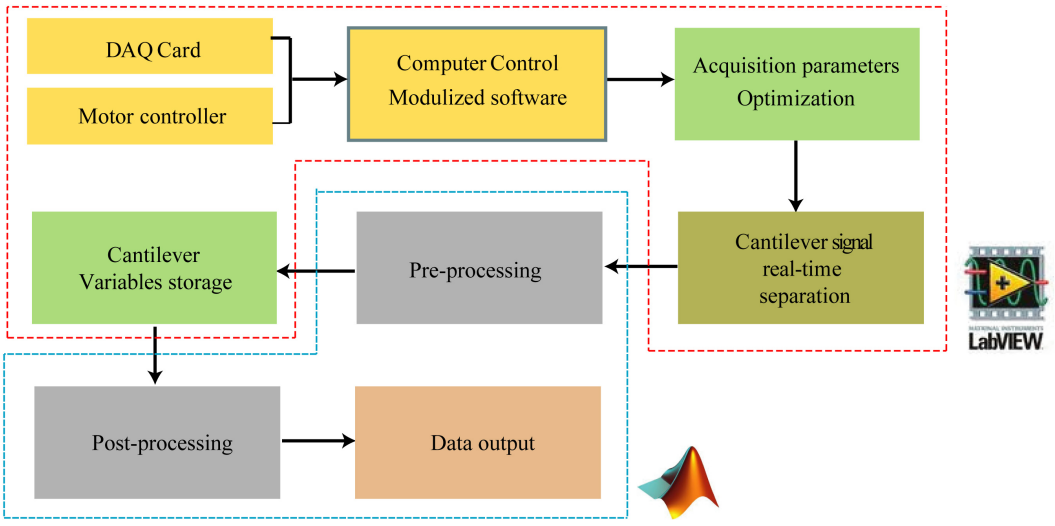

Figure 5.8: Block scheme for the program which interface the system with the PC. The Labview program controls the mechanical and electronic components, and it runs pre-processing and post-processing matlab codes. A window for output visualization is also embedded.

The overall software functions are obtained through integration of matlab codes into Labview blocks (see Figure 5.8).

5.2.1 Profiles separation

One of the most critical functions implemented in the program is the automatic cantilever separation. This function allows the real-time sectioning of the chip profile into eight individual cantilever profiles ($V^n_{l,k,x}(p)$). This operation is fundamental for the whole data analysis presented in this chapter. The cantilever separation algorithm has been optimized by Mr. Chen during the whole course of the project, resulting in a robust function which separates the profiles very fast and very accurately.

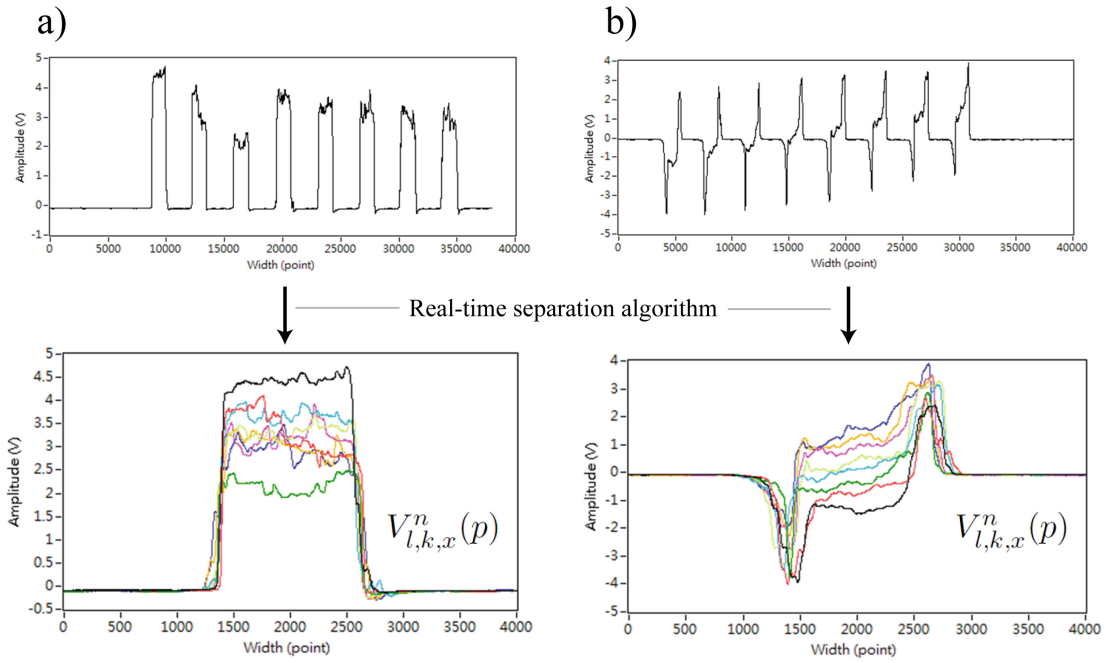

Figure 5.9: Automated cantilever separation function for a) positive FES values and b) FES values close to zero. The cantilevers measured close to the center of the FES are slightly tilted.

The separation algorithm faces the challenge of separating very diverse types of signal. This algorithm provides the raw data which are pre-processed by the method described in the previous section. The robustness of the separation algorithm is then closely connected to the overall quality of the measurement.
If chip profiles are cut wrongly, the variables computed during the pre-processing step would contain corrupted values. The whole data analysis would then be run on meaningless measurements. The robustness of the separation functions has thus been a high priority during software development.
Figure 5.9 illustrates the result of real-time separation function when the FES is positive (upper part of the S-curve, see Figure 2.3) and when the FES is near the center of the linear range. The bottom panels show eight separated cantilever profiles.
The robustness of the algorithm was tested measuring cantilevers with very noisy profiles (e.g. used cantilevers). Tilted cantilevers were also used to evaluate the ability of the program to withstand high-noise signals. Figure 5.10 illustrates the separation result

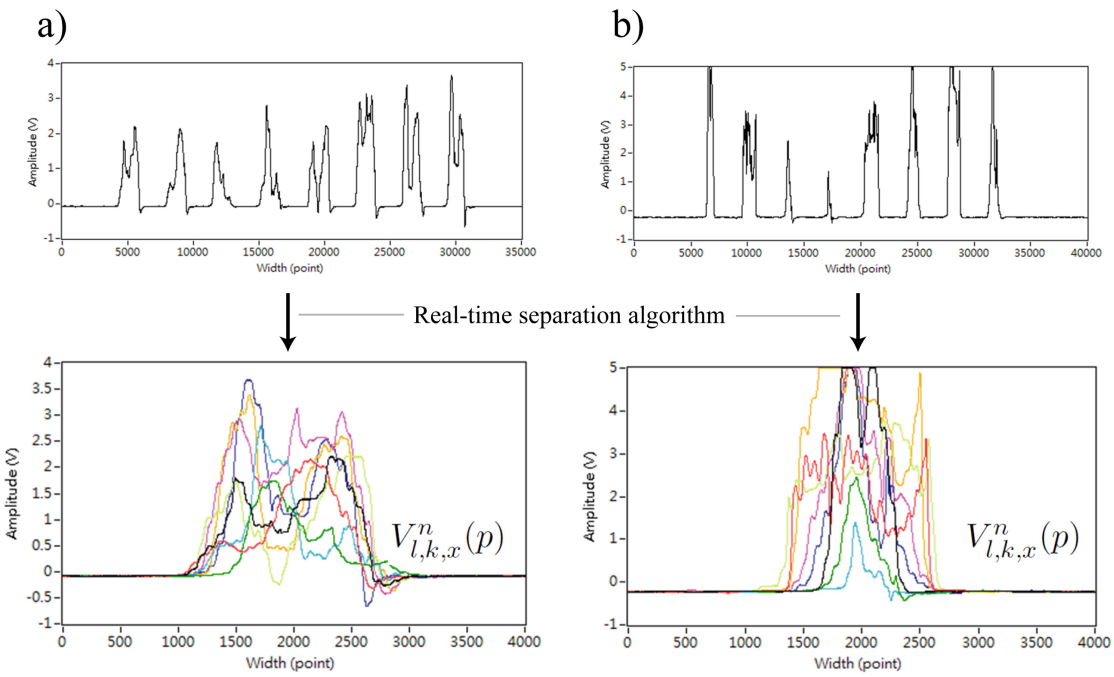

Figure 5.10: Separation of high-noise signal acquired from damaged cantilevers. The program recognizes and saves the individual cantilever profiles.

when very noisy signal is acquired by the DAQ card. Even if the the signal quality is very poor, the program correctly separates the individual cantilever profiles.

The automation performance of the system has been continuously improved. Several issues however still need to be addressed. Among them, a numerical characterization of the profiles that can automatically identify outliers and remove them before preprocessing needs to be developed.
Libraries of system settings should be created in order to precisely reproduce sensing experiments under the same conditions. Furthermore, centrifugal microfluidic automation still needs to be implemented, and X- and Z-direction auto-tracking need further development in order to be applied in real sensing experiments.

Chapter 6

Sensing Results

6.1 Introduction

In this chapter the experimental results obtained with the technology developed during the three years of the project are presented. Several samples were tested, starting with well established assays, like biotin-streptavidin, to less tested areas, like aptamer-based assays for low concentration detection of cancer markers (PAI-1).
The experimental investigation was an extremely important tool for the technological development of the sensing platform. In fact, the experience earned during the experimental tests was extensively used for technology improvements.
Several preliminary tests were performed before real sensing could be achieved. The first proper sensing experiment (biotin-streptavidin, presented in Section 6.2) was carried out around 1 year after the beginning of the platform design and fabrication.

Experiment		System			Disc					
Assay	method	$V1$	$V2$	$V3$	$V1$-B	$V2$-A	$V2$-B	$V2$-C	$V3$-A	$V3$-B
Biotin - Streptavidin	wet & dry	x			x					
BAM - Anti-BAM	wet & dry	x			x	x				
TTF - DNT (liquid)	wet & dry		x				x	x		
TTF - DNT (vapor)	gas flow		x				x	x		
TTF - DNT (liquid)	Continuous flow		x						x	
Aptamers - PDGF	Continuous flow		x	x					x	x
Aptamers - PAI-1	Continuous flow		x	x					x	
TTF - DNT (vapor)	Thermal evaporation	Vibrometer								

Table 6.1: Working method and system/disc versions summary for the different sensing experiments.

Furthermore, the system capabilities were constantly improved during the 3 years of technology development, leaving some experiments to be carried out under different conditions than others. For example, some tests were performed with earlier generation

systems and discs, while others were measured using more advanced technological tools.

Experiment		Cantilevers		
Assay	Method	IBM500	MMT500	MMT750
Biotin - Streptavidin	wet & dry	x		
BAM - Anti-BAM	wet & dry	x		
TTF - DNT (liquid)	wet & dry		x	
TTF - DNT (vapor)	gas flow		x	x
TTF - DNT (liquid)	Continuous flow		x	
Aptamers - PDGF	Continuous flow		x	
Aptamers - PAI-1	Continuous flow		x	
TTF - DNT (vapor)	Thermal evaporation			x

Table 6.2: Cantilever chips employed in different sensing experiments.

The same is valid for the software acquisition systems described in Chapter 5, which substantially improved the resolution of the platform during the system development.
Even the cantilevers have changed during the three years period. Experiments with SU-8 and TOPAS chips fabricated in our Danchip facilities were initially performed. Commercial chips purchased by Concentris (IBM500) and Micromotive (MMT500 and MMT750) were later used in the sensing experiments. IBM500 and MMT500 chips embed cantilevers with identical geometry: 500 μm long, 100 μm wide and 1 μm thick, coated with 4 nm Ti + 20 nm Au. The MMT750 cantilevers are 750 μm long, 100 μm wide and 1 μm thick (same metal coating).
Different working modes were investigated: wet & dry measurements, continuous liquid flow detection, gas flow analysis and thermal evaporation measurements.

It is difficult to think that all the changes in the experimental conditions did not affect the coherence of the results. It is thus quite difficult to compare results obtained with different assays, since they were typically obtained with different technological tools. In general, the experiments were carried out in a "chronologically improving" environment, thus a monotonic increase in the quality of the results presented in this chapter is also observed. This fact makes also quite difficult to perform theoretical analyses of the data, being the output itself constantly affected by the technology improvement.
This chapter is meant to give the reader an idea of how the technology of the device was developed according to the obtained sensing results. Further experiments should be done in steady conditions (same platform, same disc, same software, same chips, same assay) in order to generate more data for a deeper understanding of the theoretical aspects of cantilever-based biosensing.
During the project, detection of the following compounds have been tested with the various versions of platforms, disc, software and chips:

- Streptavidin proteins
- 2,6-Dichlorobenzamide (BAM) antibodies
- 2,4-Dinitrotoluene (DNT) molecules
- Plateret Derivative Growth Factor proteins (PDGF)
- PAI-1 proteins

In order to reduce confusion generated by the different conditions of the experiments, in Tables 6.1 and 6.2 are listed the system and disc versions employed in each sensing test, as well as the types of cantilevers.

6.2 Streptavidin detection

The well established binding properties between biotin and streptavidin [140] were chosen for initial tests of the performance of the system when investigating molecular binding. Due to robust binding between the protein (streptavidin) and the B-complex vitamin (biotin), this assay has been widely investigated in microcantilever based sensing experiments [141–145]. This assay was used as a first demonstration of wet & dry measurements using the DVD-ROM based platform [146].

6.2.1 Materials and methods

Several chips were functionalized with a thiolated biotin layer. Next, streptavidin was bound to the cantilever surfaces. The presence of streptavidin on the cantilever surfaces was confirmed by fluorescence microscopy. For fluorescence studies the streptavidin was labeled with Cy3 fluorochromes.

Materials

The following materials and chemicals have been used in the biotin functionalization and in the streptavidin solutions preparation:

- EZ-link Biotin-HPDP, Pierce prod. nr. 21341 (mol. weight: 539.78 g/mol)
- Streptavidin Cy3 labeled (mol. weight: 52.8 kDa)
- Dimethylsulfoxide (DMSO) or Dimethylformamide (DMF)
- PBS buffer (100 mM)
- Absolute ethanol and Milli-Q water
- Piranha solution (98% H_2SO_4, 30% H_2O_2)

IBM500 chips (see Figure 2.10a) were used. The chips were functionalized by dipping them into the biotin solution.

Piranha cleaning

The first step to be performed was the cleaning of the Au coated cantilever surfaces. For this purpose a strong chemical cleaning process was adopted.
Piranha mix was prepared in a 25 ml container: 2.5 ml of 30% H_2O_2 was carefully added to 7.5 ml 98 % H_2SO_4 (the mixture rapidily heats up due to the reaction). To prevent dangerous overheating the beakers were placed iside bigger glasses filled with water.
The cantilever chips were placed in the piranha solution and left for 10 minutes. Then they were transfered to four serial Milli-Q water beakers, washed and left 1-2 minutes in each of them. At the end, the chips were washed in absolute ethanol or isopropanol. The high hydrophilicity induced by the piranha treatment makes the surface conditions optimal for functionalization.
The surfaces were functionalization immediately after the chemical cleaning.

Biotin-HPDP coating

Biotin-HPDP is a pyridyldithiol-activated, sulfhydryl-reactive biotinylation reagent that conjugates via a reversible disulfide bond, see Figure 6.1 [147]. For immobilization of

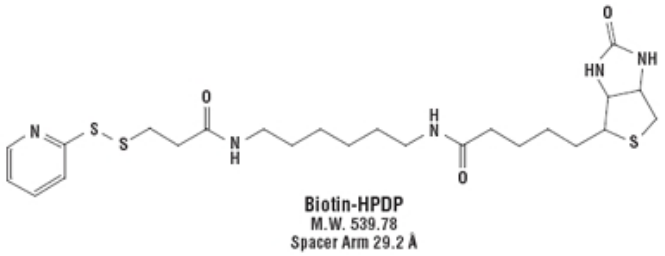

Figure 6.1: Biotin-HPDP structure.

biotin on the surface, a solution of 1 mM EZ-link Biotin-HPDP in Dimethylsulfoxide (DMSO) or Dimethylformamide (DMF) was prepared. The stock solution (10 mM) was divided in 10 x 100 μl aliquots, to be used for individual chip functionalization.
The preparation of the vials for the individual dipping of chips was carried out dissolving 50 μl of 10 mM EZ-link Biotin-HPDP Stock solution with 950 μl absolute ethanol into a 1.5 ml eppendorf tube.
The cantilever chips were placed into individual 1.5 ml eppendorfs and placed on a low shaking table for 24 hours at room temperature. The chips were then transfered into another vial filled with pure ethanol and left for 10 min. Chip were then dried and loaded on the rotating platform.

Streptavidin preparation

Relatively high concentration of streptavidin-Cy3 (1.6 μM) was used for initial testing of the capabilities of the sensing platform.
The stock streptavidin solution was 1 mg/ml: 10 μl of 1 mg/ml stock streptavidin-Cy3

was then diluted in 90 μl of 10 mM PBS buffer. During sensing experiments, variable amounts between 5 to 10 μl were delivered to the cantilever chips and left to incubate for 10 min.

6.2.2 Experimental results

The biotin-streptavidin experiments were performed, as listed in Table 6.1, using *System V*1 and *Discs V*1. The chosen sensing methodology was wet & dry.
Eight cantilevers were functionalized with thiolated biotin and eight untreated cantilevers were used for reference measurements. The chips were inserted into reservoirs in *Disc V*1-*B* and a buffer solution containing streptavidin was injected into the reservoirs. After 10 min of exposure to streptavidin, all cantilevers were washed in buffer and subsequently water. The water was left to evaporate. The cantilever responses were measured continuously before and after incubation with streptavidin. During incubation and washing the disc rotation was halted and data were not acquired.
Cantilever bending and surface roughness were recorded. Functionalized cantilevers were compared with reference cantilevers.

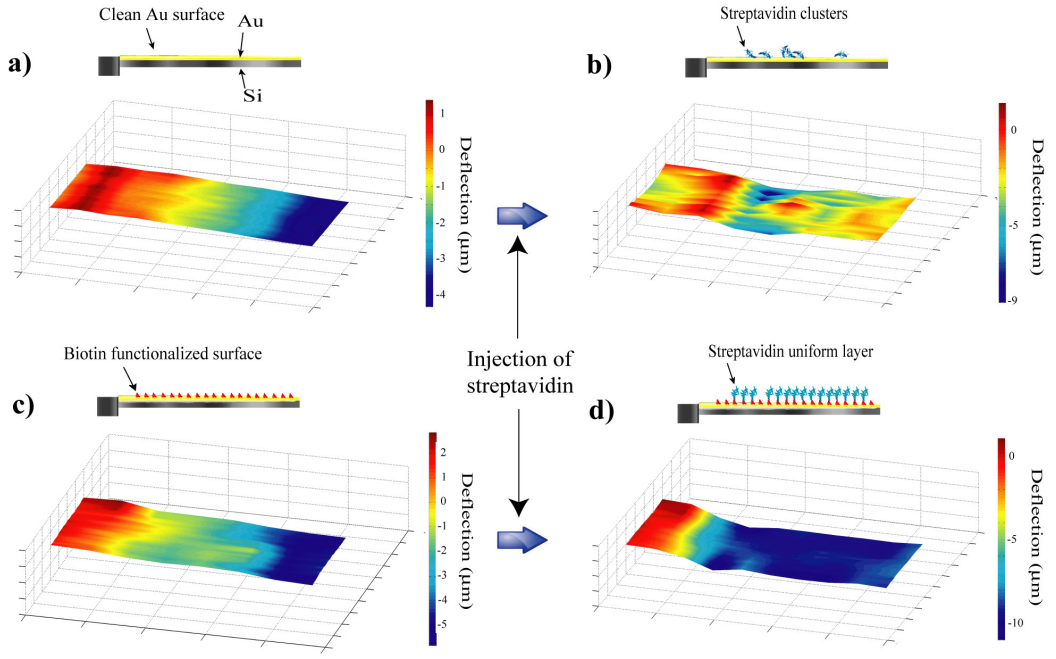

Figure 6.2: Detection of biotin-streptavidin binding. a) Surface reconstruction of clean cantilever. b) The same cantilever after exposure to streptavidin solution showing increased roughness. c) Surface reconstruction of biotin functionalized cantilever and d), of the same cantilever after reaction with streptavidin.

Figure 6.2a shows the averaged 3D surface reconstruction of the gold coated side of 8 untreated reference cantilevers, measured before the injection of streptavidin. These

surfaces have a roughness of a few nm, indicating that the gold layer is clean. The measured initial end point deflection of the untreated cantilevers was around 5 μm.
After injection of streptavidin (incubation time about 10 minutes) and washing of the cantilevers, the same cantilevers show a high increase in surface roughness, suggesting that an inhomogeneous layer has formed (Figure 6.2b). This indicates that streptavidin has bound unspecifically to the untreated cantilever surfaces as schematically illustrated in Figure 6.2b.
The cantilevers functionalized with biotin are initially bent 5-6 μm at the cantilever apex and the surface appears optically smooth, see Figure 6.2c. This reflects that the biotin functionalization had created a monolayer on the gold surface of the cantilevers.
After the biotin-streptavidin binding occurred, the observed change in cantilever bending is approximately 3 μm and the roughness of the surface appears unchanged, indicating that streptavidin has been uniformly bound to the biotin layer (see Figure 6.2d).
Figure 6.3 compares data from the untreated and the biotin functionalized cantilevers. Each data point corresponds to the averaged value from 8 cantilevers.
It can be noticed that after the incubation with streptavidin the bending of the untreated cantilevers decreases, reaching an asymptotic value after around 15 disc revolutions (approximately 5 minutes), as shown in Figure 6.3a.

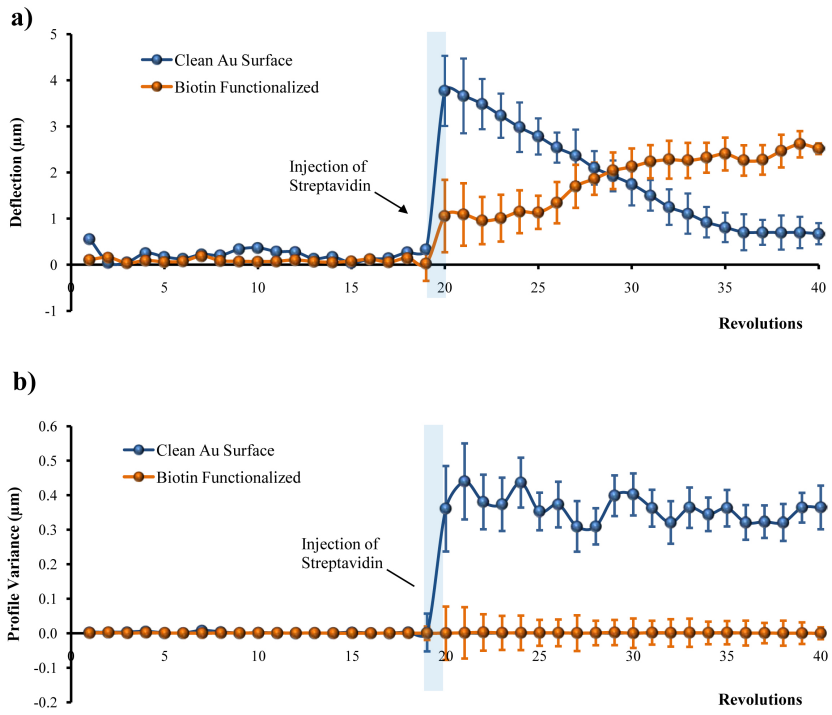

Figure 6.3: Averaged change in cantilever bending a) and surface roughness b) for an untreated surface (average value of 8 cantilevers) and a biotin functionalized surface (average value of 8 cantilevers). At revolution 19 the cantilevers are incubated for 10 minutes in streptavidin.

At this stage the water has fully evaporated from the reservoir and stable measurement

conditions can be obtained. Similar behavior (but opposite direction) is observed for the biotin functionalized cantilevers. These cantilevers show an averaged change in deflection which is approximately 2 μm larger than for the untreated reference cantilevers when the measurements have stabilized.
The averaged change in surface roughness (Figure 6.3b) is significant for the untreated cantilevers compared with the functionalized ones, suggesting that an irregular streptavidin layer is formed on the untreated cantilever whereas a uniform layer, as expected, is formed on the biotin-coated surface.
Thus, the specific binding of streptavidin results in significant differential changes (biotin functionalized minus untreated cantilever) in cantilever deflection and surface roughness.

6.3 Antibody detection

Similar experiments were run for detection of the pesticide derivative dichlorobenzamide (BAM) antibodies [148–150]. The used protocol was originally developed for a competitive assay, which implies that the sensing cantilevers were initially coated with a layer of BAM, while the target analyte was its specific antibody [47].

6.3.1 Materials and methods

In these set of experiments, the selected working mode was wet & dry, and the measurements have been performed using *System V*1 and *Disc V*1. IBM500 cantilevers were used.
To coat the cantilever and subsequently monitor the surface effects of the binding BAM antibody to BAM pesticide, the gold surfaces of the cantilevers were coated with BAM haptens immersed in a ovalbumin (OVA) matrix. The BAM antibody binding could be confirmed with a fluorescence microscope via Cy3 fluorochrome attached to the BAM antibody.

Solutions preparation

The chips were chemically cleaned before the functionalization in a similar way to the biotin coating described in Section 6.2.1. Ten minutes of Piranha cleaning was followed by multiple rinses in Milli-Q water and isopropanol. The chips were then let to dry before being inserted in a microspotting machine (CantiTMSpot, Cantion, DK). The microspotting machine is a platform consisting of an inkjet printer head, a PC interface camera, a lightning system and a manual X-Y stage. The system is mounted with a piezo electric controlled pin head (Sub-micro-liter Piezoelectric Dispenser A010-006 SPIP, Gesim, DE) and capable of delivering 0.1 nl drops to each cantilever surface while being monitored via a camera on a PC.
The OVA preparation, the OVA-BAM coatings and the BAM antibody solution preparation details are summarized in the following points:

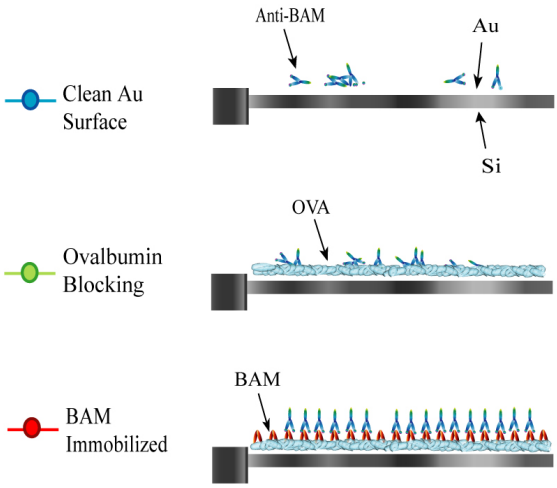

Figure 6.4: Schematics of the cantilever coatings employed in the BAM- Anti-BAM experiments. Blank Au coated cantilevers (top) and OVA blocked cantilevers (center) were used as reference sensors to the specifically coated BAM-OVA ones (bottom).

- Cy3 BAM Antibody: Made from mouse serum at Statens Serum Institut, HYB 273-01, Batch no. 03102P01/071008. Marking was done with Amersham Cy3 Dye Antibody monofuctional Labeling Kit for 1 mg antibody. Solution was diluted to 0.1 mg/ml prior to use.
- BAM hapten EQ0031 conjugated to Ovalbumin: 1.68 g natrium hydrogen carbonate was dissolved in 200 ml Milli-Q water. BAM haptens were first activated by taking 35.3 μmol EQ0031 and 35.3 μmol BOP (Benzotriazol-1-yloxy-tris (dimethylamino) phosphonium hexafluorophosphate) and dissolving it in 1.5 ml dry DMSO (Dimethyl sulfoxide). Subsequently 18.5 μl DIEA (N-Ethyldiisopropylamine) was added. 5 μl of activated EQ0031 was then added to 1 ml (1 mg/ml) solution of freeze-dried OVA dissolved in conjugation buffer and shaken 2 hours in darkness. The solution was divided into aliquots and kept at 4°C. The BAM-ovalbumin conjugate was tested positive by a BAM ELISA.
- OVA solution: the OVA solution was made from freeze dried ovalbumin dissolved in Milli-Q Water. A stock solution of 1 mg/ml was then made; the solution was distributed in 100 μl PCR tubes and kept in a freezer until use.

Cantilevers microspotting

Several chips were prepared for the measurements. Figure 6.4 shows the three types of cantilever surfaces employed in these experiments. The functionalization of individual

cantilevers was performed using a micro-spotter with a sub-microliter piezoelectric dispenser head (A010-006, Gesim Inc, DE) in a XYZ stage monitored via CCD camera.

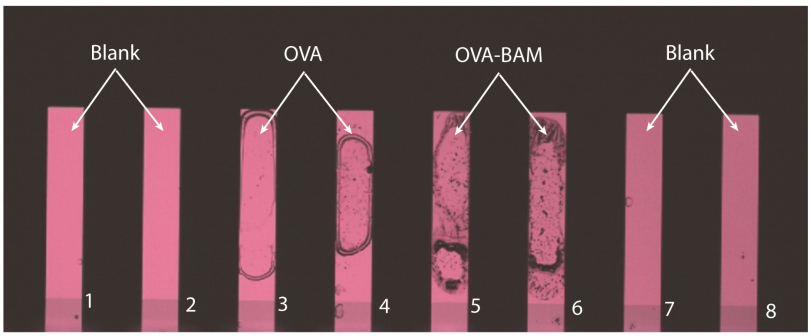

Figure 6.5: IBM500 chip functionalized with microspotter. the 4 external cantilevers are left blank, while the 4 central are, respectively, coated with OVA blocking layer (left) and OVA-BAM layer (right).

BAM immobilized cantilevers were prepared through microspotting an OVA matrix with BAM molecules. Blank Au-coated cantilevers were used as control sensors, together with a set of cantilevers coated with OVA matrix, without BAM molecules immobilized. It is believed that the OVA layer without BAM molecules could provide a better reference layer than the untreated surfaces.
Each chip contained two cantilevers functionalized with BAM, two cantilevers with an OVA blocking layer and four untreated cantilevers.
Figure 6.5 shows an example of a cantilever chip functionalized with microspotter. The material distribution of the spotting is clearly inhomogeneous. This is an intrinsic drawback of the microspotting process, clearly visible looking at the OVA blocking layer cantilevers. It is in fact difficult to control precisely the amount of material to be deposited on the cantilevers, sometimes resulting in inhomogeneous coverage of the surfaces.
Statistical measurements over several chips is believed to reduce sensing artifacts due to imprecisions of the functionalization process.

6.3.2 Experimental results

The initial bending of the cantilevers was measured as described in Section 6.2. Specific antibodies against BAM were then injected into the reservoirs followed by a rinse in water and subsequent water evaporation. Figure 6.6a shows the induced averaged bending of the differently functionalized cantilevers.
The BAM-functionalized cantilevers deflect approximately 10 μm compared with 3-5 μm for the untreated and OVA coated cantilevers. Probably, the antibodies bind strongly to the BAM functionalized surfaces causing a large change in surface stress whereas they bind unspecifically to the other cantilevers, as illustrated in Figure 6.6b.
Cantilever profiles reveal that the untreated cantilevers become significantly rough, while

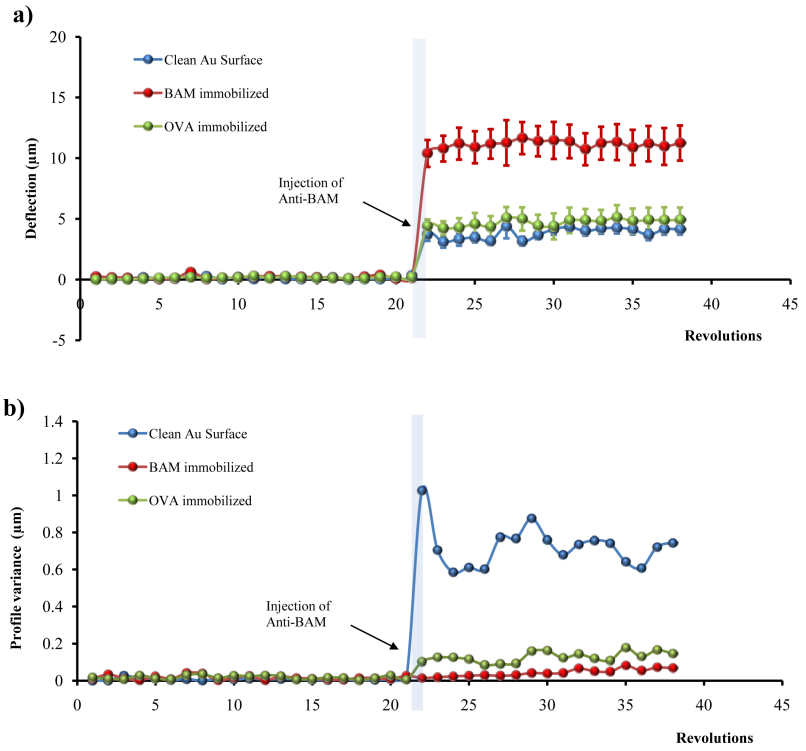

Figure 6.6: Detection results of anti-BAM antibodies. a) Averaged changes in cantilever deflections when exposed to BAM antibodies. All data points represent averaged values from either 4 (OVA and BAM coated) or 8 (untreated gold-coated) cantilevers. b) Averaged changes in surface roughness after exposure to BAM antibodies. At revolution 21 the cantilevers are incubated for 10 minutes in the anti-BAM solution.

the BAM and OVA coated ones are unaffected by the introduction of antibodies. The OVA coated cantilevers were initially rough reflecting the nature of the coating (see Figure 6.6c). It is believed that this is once again an indication that specific binding results in ordered uniform layers whereas the unspecific binding results in a random and rough surface. The specific binding of BAM antibodies is thus detectable due to large differential signals in both deflection and surface roughness.
In the BAM experiments, the capability of the system to measure changes in the resonant frequency was tested. Figure 6.7a shows the change in resonant frequency for the 16 monitored cantilevers after reaction with antibodies has taken place and the washing solution has evaporated.
The BAM functionalized cantilevers had the highest change in resonant frequency (approximately 10%). Compared to that, minor changes are observed for the OVA blocked and the untreated cantilevers (1-2%), which can be attributed to unspecific binding of antibodies as well as solidification of salt present in the buffer solution.

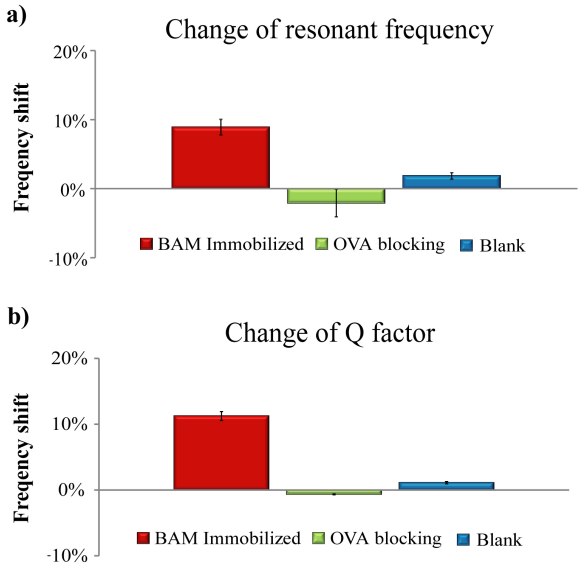

Figure 6.7: Detection of BAM antibodies. a) Measured averaged changes in resonant frequency and b) Q-factor. The significant change for the BAM coated cantilevers indicates binding of the anti-BAM antibodies on the cantilevers surfaces.

The observed frequency changes for the BAM functionalized cantilevers were positive, which was probably a result of changes in surface stress, or of a combination between surface effects and added mass [30].
The corresponding Q-factors extracted from the resonant curves (Fig. 6.7b) generally follow the changes in resonant frequency, suggesting that an increase in stiffness of the cantilevers due to addition of a surface layer has occurred. Uniformly added mass on the cantilevers could have increased the stored energy of the resonator to produce the increase of the Q-factor. However, the relationship between surface stress change and the stiffness of the cantilever is still under theoretical debate [151].

6.4 Explosive sensing

In this Section the capability of the DVD-ROM based readout to detect DNT in water and gas phase through colorimetric functionalization of the cantilevers is presented.
The silicon cantilevers were functionalized with a layer of TTF-calix[4]pyrrole molecules (TTF), specifically designed to bind nitro-aromatic compounds, such TNB, DNT and TNT.

6.4.1 Introduction

Detecting low concentrations of TNT or its derivative, DNT, is a critical issue in demining processes, where clearance of fields still have major challenges in terms of costs, time and reliability.
At present, hundreds of fields are still uncleared in several parts of the world, and only from 1999-2008, Landmine Monitor recorded at least 73.576 casualties of landmines, explosive remnants of war, and Improvised Explosive Devices [152]. These casualties were spread over 119 countries and areas.
Furthermore, large quantities of explosives have been dumped on military bases, both as consumed ammunition and as waste from military manufactures, making the cleanup job extremely labor intensive and potentially dangerous. Any new technology that can improve the process of detecting low concentrations of explosive contaminants will have a significant impact on personal involved in clearance as well as the surrounding communities.

Design of miniaturized sensors and synthesis of biochemical compounds devoted to detection of low concentration of explosive molecules is therefore an increasing field of interest for both humanitarian and military applications [153, 154]. Explosive detection is a rapidly growing field of application for Micro- and NanoElectroMechanicalSystems since these have the potential to provide portable and sensitive solutions.
Ideally, a sensor for explosives should be able to operate in both vapor and liquid phase. DNT at room temperature has a high vapor pressure (around 1 Pa) [155] and the presence of explosives can thus be spotted by 'sniffing' the surrounding air - much like a sniffing dog. However, often water supplies are contaminated by explosives. In order to secure water quality and to spot buried land mines the underground water is therefore analyzed for traces of explosives [156].

In general, many different biochemical receptors have been employed for selective detection of TNT and its derivatives on a variety of surfaces: Specific antibodies [157, 158] and peptides [159] are the most extensively used coatings for TNT and DNT detection. Recently, the synthesis of molecular receptors that can function as colorimetric chemosensors for nitroaromatic explosives has been investigated. Within this context, compounds that detect nitroaromatic analyte via color changes, have been attracting particular interest [160–163].
Their ease of use and their ability to function in the absence of readout instrumentation could make them applicable in situations where a qualitative indication about the presence of explosive molecules is needed. Recent publications investigated the use of colorimetric receptors for TNT as chemical receptors on cantilevers for gas detection of TNB vapors [164].

6.4.2 TTF-calix[4]pyrrole receptors

TTF-calix[4]pyrrole receptors were used for functionalization of the cantilevers [160]. These molecules have been synthesized to specifically bind nitroaromatic compounds. Two binding sites are present in these chiral molecules, as shown in Figure 6.8.
Employing TTF as sensing molecules, the effect of conformational change is expected to generate a high signal in static mode. In dynamic mode a small shift in resonance frequency is expected due to the low added mass.

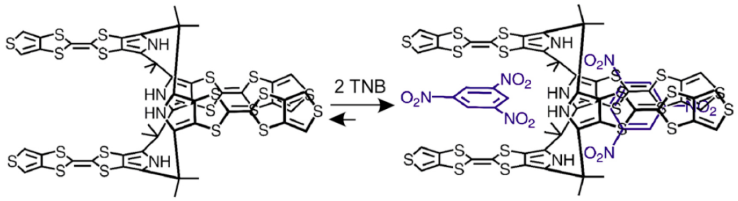

Figure 6.8: TTF receptor chiral structure. Two binding sites are available for chemical absorption of nitroarmatic host molecules.

It is also believed that the small explosive molecules in vapor phase will tend to stick on even untreated surfaces (reference cantilevers coated with blocking layers), generating higher probabilities of unspecific mass change. On the other hand, conformational changes are not expected in cantilevers not specifically treated.

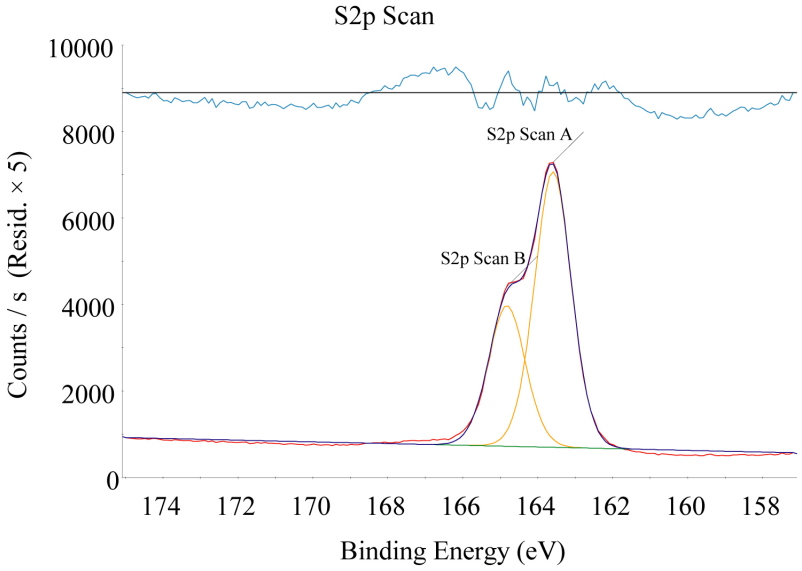

Figure 6.9: S2p scanning from TTF-calix[4]pyrrole receptors immobilized on Au surface. No peaks indicating the bond between S and Au are visible.

The Au layers of the cantilevers were chemically treated with TTF molecules, expected to bind strongly on the surface through S-Au bonds. The TTF layers on the cantilever surfaces have been characterized through XPS analysis. In Figures 6.9 and 6.10 the results of the XPS scans are shown. Fig. 6.9 shows the S_{2p} peak scan. The sharp sulfur peak suggests the presence of the molecules on the surface, confirmed also by the the peaks C_{1s}, O_{1s} and N_{1s}.

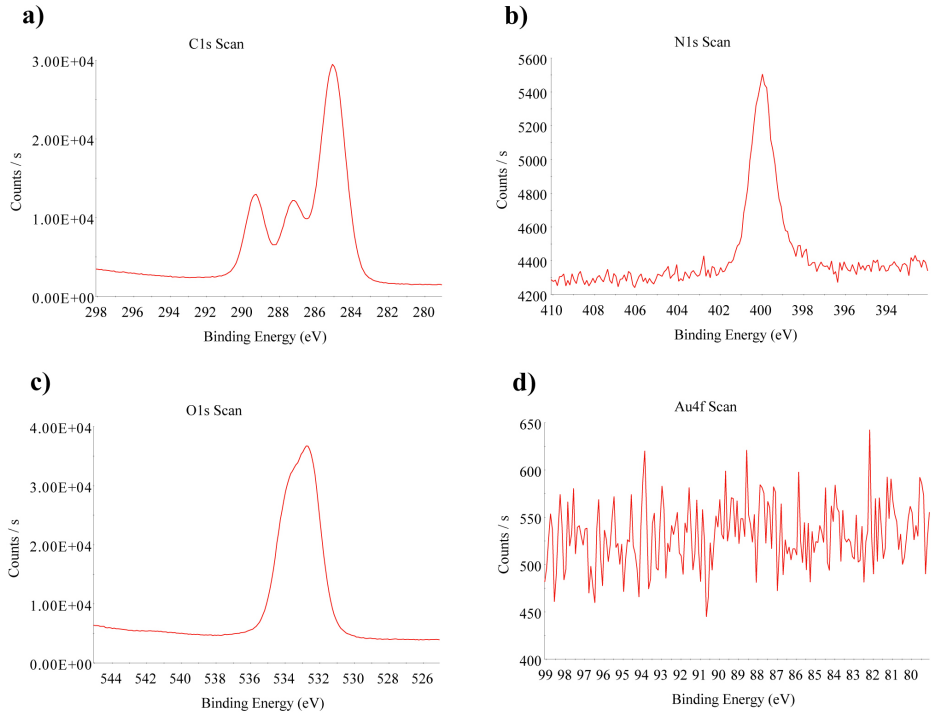

Figure 6.10: a) C_{1s}, b) O_{1s}, c) N_{1s} and d) Au_{4f} scans from TTF receptors immobilized on Au surface. All the three peaks are visible indicating the presence of the elements on the Au coated surface.

However it is not visible any peak on the low binding energy side of the S_{2p} peak. This lower energy peak indicates the bond between S and Au [165]. Furthermore, no signal is visible from the Au either. Probably, the TTF molecular layer is too thick to give signal from the first monolayer. Therefore it is impossible to determine if there is a chemical bond between the first monolayer of the TTF molecule and the Au surface.

6.4.3 Material and methods

For the gas-phase DNT sensing experiments Si cantilevers with dimensions of 750 μm x 100 μm x 1 μm, coated with 20 nm of Au, were used. Same types of cantilevers have been used to test the water/DNT vapor mixture as sensing target. For liquid phase sensing we employ cantilevers of 500 μm x 100 μm x 1 μm. *System V2* was used in connection with *Discs V2-B*, *V2-C* and *V3-A*.

Prior to TTF immobilization the cantilever chips were cleaned in Piranha solution similarly to the way described in Section 6.2.1, and then treated in UV-ozone oven (UVP PR-100, power 1,5 mW/cm^2) for 30 min to render the Au surface hydrophilic and to remove possible organic contaminants. The chips were then placed in PCR tubes with 1 mg/ml TTF in Dichloromethane (DCM).
The solution was incubated at 5°C in darkness overnight (or for a minimum of 12 hours). The chips were then rinsed in 5 ml DCM for 5 minutes to remove excess TTF from the surface. The chips were then allowed to dry before being inserted in the sensing platform and exposed to DNT sample.

During experiments the deflection and resonant frequency shift of TTF functionalized cantilevers were compared with reference cantilevers. The presence of reference cantilevers is crucial in determining if specific binding of molecules occurs on the surface of the TTF treated cantilevers.
In order to minimize artifacts due to intrinsic differences in surface properties, the reference cantilevers were left blank or treated with thiolated biotin to mimic the treatment of the TTF functionalized cantilevers. Biotin was immobilized on the surface using the protocol described in Section 6.2.1.

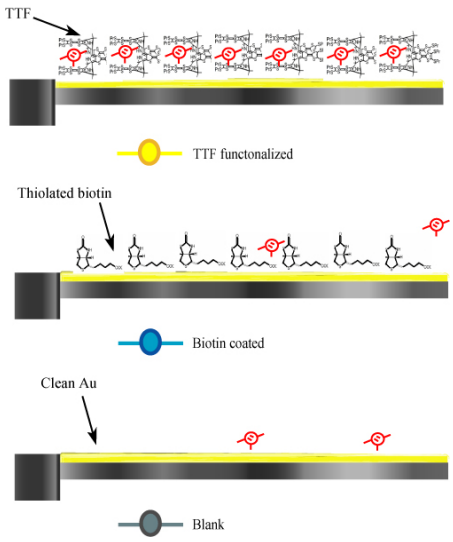

Figure 6.11: Schematics of the three functionalization layers used for DNT detection experiments. Two reference types of cantilevers are used as control sensors, the clean Au surfaces (bottom) and biotin coated ones (center). The functionalization of the biotin layer has been done following the protocols described in Section 6.2.1.

Functionalization was always carried out on entire cantilever chips (8 cantilevers). This avoided cumbersome and inhomogeneous (see Figure 6.5) functionalization of closely spaced cantilevers on the individual chips and allowed the use of classical 'beaker-based' chemistry. Typical experiments involved the use of 16-32 TTF functionalized cantilevers (2-3 chips) and 8-16 reference cantilevers (1-2 chips).

6.4.4 DNT detection in gas phase

Initially, gas-phase experiments were performed. A crystal of DNT was heated to 65°C in a vial connected to a nitrogen pressure pump. While the DVD-ROM scanning was performed, the sensing chamber was exposed to 40 μl/min of continuous nitrogen flow, and then switched to DNT saturated gas mixture. As reference, cantilevers coated with a thiolated biotin layer were used.
The cantilever baseline was recorded during 10 minutes (under N2 flow). After the injection of DNT sample, the cantilever signals were read for approximately 20 min. Mixture

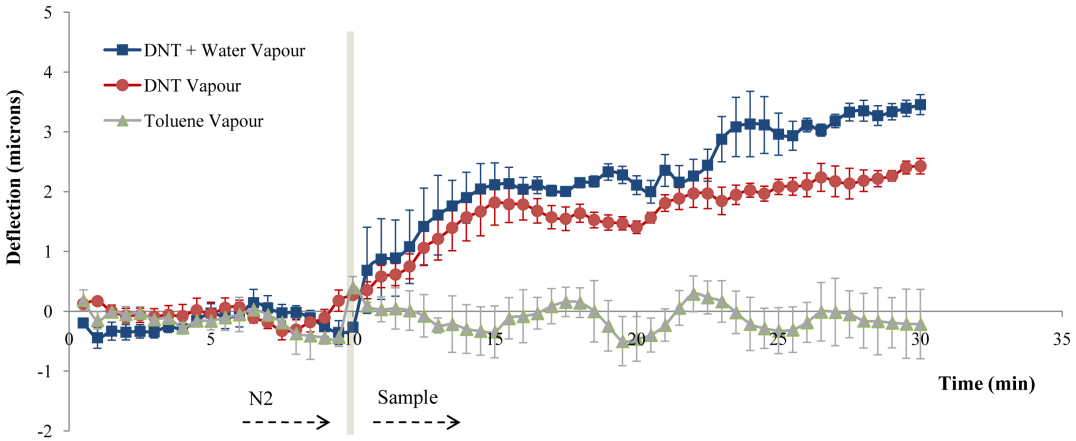

Figure 6.12: Gas phase detection of DNT. Each curve reports the averaged differential signal between a set of TTF treated cantilevers (16) and a blank ones (8). Toluene has been tested as control analyte, which is shown to not generate visible signal.

of DNT gas and water vapor was tested to evaluate the influence of the water content on the activity of the TTF layer.
The gas from a 10 g crystal of DNT and 2 ml of Milli-Q water heated to 65°C was then added using a nitrogen gas pressure pump. A separate round of experiments was performed to test for unspecific signal. With same experimental protocol of pure DNT vapor and DNT/water mixture, reaction to solution of 200 μl of pure toluene was monitored.
In Figure 6.12 the results obtained by monitoring the deflection of 72 cantilever sensors for 30 minutes are plotted. Each curve is obtained by subtracting the signal averaged over 16 TTF functionalized cantilevers and over 8 reference cantilevers. About 10% of the original cantilever data was lost in the acquisition process (see Section 5.1.5). The curves thus actually report the deflection averages over 65 independent sensors.
It can be noticed that after 2 min, in case of DNT vapor or DNT-water mixture, it is

already possible to identify a change in the cantilevers' averaged deflection. However, after 5-10 min the responses become more pronounced, reaching asymptotic differential deflection values of 2.5 μm and 3.5 μm, for respectively DNT vapor and DNT-water mixture.

In order to evaluate the performance on cantilever-based detection of DNT in gas phase compared with other techniques, a set of experiments of thermal evaporation of DNT crystals on the cantilever surfaces was performed. These experiments were done simultaneously on four Xsense sensors: calorimetric, SERS, colorimetric cantilevers [1–3]. The methods and results obtained on cantilever thermal evaporation of DNT are presented in Appendix C. For this set of experiments the MSA-500 Polytec Scanning Vibrometer[1] was used.

6.4.5 DNT detection in liquid phase

*System V*2 was used also for measurements of DNT detection in liquid phase. Measurements in continuous liquid flow, where the deflection is continuously monitored in liquid, and in wet & dry, where the cantilever are measured in air before and after exposure to liquid samples, were tested.

Continuous flow

In the continuous flow mode, the reaction chamber was filled with Milli-Q water with a 20 μl/min flow. While the cantilever signals were recorded, a valve switched to a Milli-Q water saturated DNT solution with a 20 μl/min flow for 10 min.
Figure 6.13 presents data acquired from eight TTF functionalized cantilevers and eight clean Au coated reference cantilevers.
After switching to DNT saturated water a response is clearly visible from the deflection of TTF treated cantilevers. The sensing response seems faster in liquid medium than vapor phase, and after less than one minute it is already possible to notice the deflection of the functionalized cantilevers.
On the other hand the reference cantilevers do not show any significant bending. The noise level is also smaller when performing experiments in liquid medium compared to gas phase. The signal to noise ratio ranges from 8 to 15. Intrinsic noise of the system (mostly syringe pump and electronics components) is believed to affect the variance of the signal.

Wet & dry

To measure cantilever deflection and resonance frequency in wet & dry mode, the chamber was filled with 200 μl of a Milli-q water saturated DNT solution using a nitrogen pressure pump and incubated for 10 min. The solution was removed by spinning the disc at high frequency and the cantilever signals were read again for approximately 10

[1] http://www.polytec.com/us/

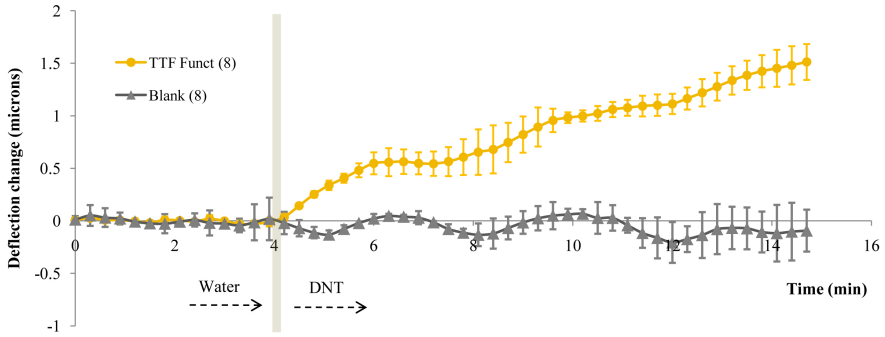

Figure 6.13: Liquid phase detection of DNT in continuous flow mode. The plots are obtained averaging signal obtained by one functionalized chip (8 cantilevers) and one reference blank (8 cantilevers).

minutes.
The cantilever profiles and their resonance frequencies were measured before and after the exposure to the sample.
In Figure 6.14 the measurements obtained in wet & dry mode over 2 set of experiments are shown, for a total of 32 analyzed cantilevers (16 TTF functionalized and 16 biotin blocked) in dry phase. The signal from 15% of the cantilevers was however lost in the measurement process. The data are thus averaged values from 27 cantilevers.
Figure 6.14a presents the averaged values of deflection change after the exposure to 10 min of DNT saturated water. The statistics is here performed over 14 cantilevers (6 TTF coated and 8 biotin blocked). Values of resonance frequency shifts for this experiment are reported in Figure 6.15. The results show a slight positive increase in the resonance frequency of the biotin blocked cantilevers, while the TTF functionalized reveal a negative value of the frequency change.
The change in resonance frequency is much more pronounced for the TTF functionalized cantilevers, probably due to larger mass absorbed on the surfaces of the cantilevers, compared to the biotin blocked cantilevers. The variance along the different measurements is however quite high, suggesting that the dynamic mode detection system is less robust than the static one. The data are anyway in quite agreement with the trend observed when measuring the thermal evaporation of DNT on the cantilevers (See Appendix C).
In Figure 6.14b similar results obtained repeating the experiments over a larger sample of sensors are shown. The conditions of the two experiments have been kept constant: sample solution and functionalization protocols were meticulously repeated, and the rotating disc and DVD-ROM optical head employed were the same for both experiments. Resonance frequency monitoring was however not performed for the second experiment. It is noticed that the TTF treated cantilevers show a quite uniform positive bending behavior (mean 804 nm, standard deviation 440 nm) in both experiments. The stress

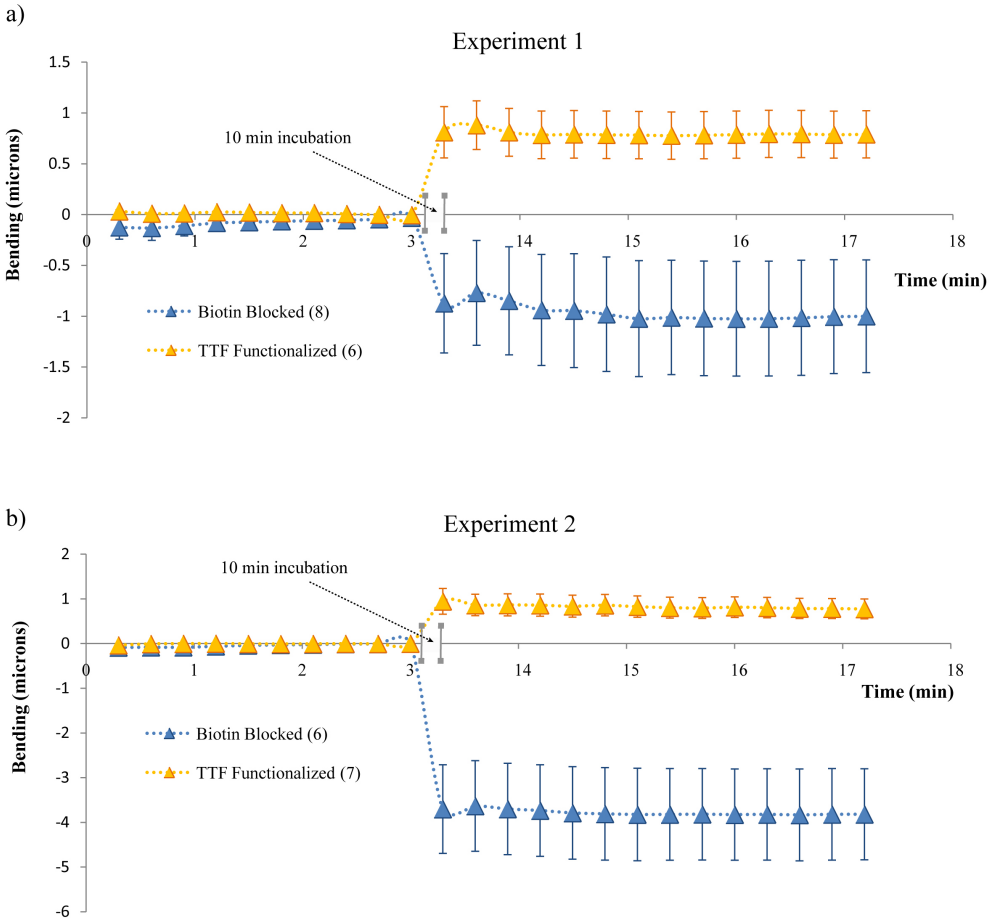

Figure 6.14: Two experiments of wet & dry measurements of DNT saturated water, performed under same conditions. a) 6 TTF treated and 8 biotin blocked cantilevers are exposed for 10 minutes to the liquid sample. After incubation the averaged measured change of deflection is positive (mean $\approx$ 0.8 μm) for TTF cantilevers and negative (mean $\approx$ -1.1 μm) for biotin coated cantilevers. b) 7 TTF treated cantilevers present positive averaged change of deflection (mean $\approx$ 0.7 μm), while 6 biotin blocked cantilevers deflect an averaged value of $\approx$ -3.9 μm.

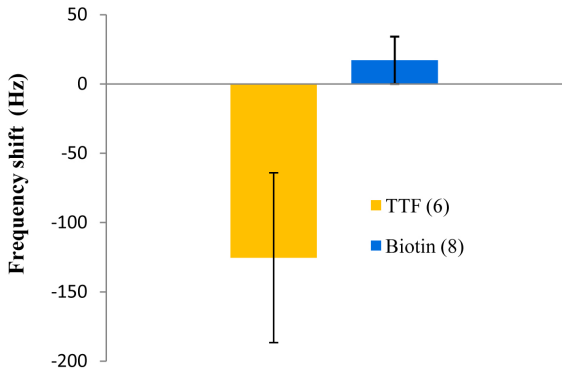

Figure 6.15: Change of resonance frequency after the exposure to 10 minutes of DNT saturated sample for the cantilevers measured in experiment 1 (Figure 6.14a).

induced by the binding of DNT molecules on the TTF layer is believed to reflect the conformational change properties of the molecule when its binding sites are occupied by nitro-aromatic molecules.

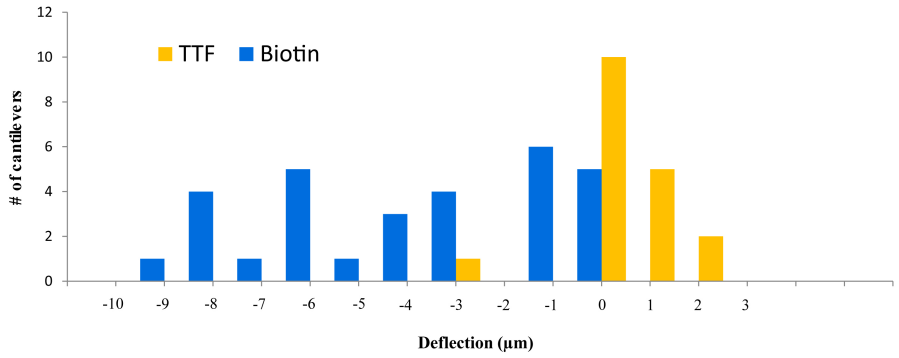

Figure 6.16: Statistical distribution of bending response to DNT saturated water of 4 different experiments performed under the same conditions. The total amount of cantilever measured is 48 (18 TTF functionalized and 30 biotin blocked).

The reference cantilevers coated with biotin exhibit a spread negative bending (mean -6.2 μm, standard deviation 4.5 μm). In Figure 6.16 the bending value distribution of 48 cantilevers (18 TTF and 30 biotin) exposed to the same experimental conditions as the data shown in Figure 6.14 is presented. The data were collected over 4 different experimental sessions, with a total of 25% of the cantilever data lost.
It is evident that the bending behavior of the biotin treated cantilevers differs from the bending of the TTF functionalized cantilevers. The bending distribution of the TTF cantilevers is centered around 0.8 μm, with 80% of the cantilevers bending between 0.3 μm and 1.6 μm. The biotin blocked cantilever distribution spans almost 10 μm of neg-

ative deflection.
It is seen that all biotin coated cantilevers have a negative bending. This behavior could be attributed to an opposite change in surface stress due to the higher adsorption of DNT on the silicon surface of the cantilever compared to the biotin blocked surface. The significant inhomogeneity of the bending distribution might be caused by random processes of DNT adhesion on the cantilever surfaces.

6.5 Aptamer-based biosensing

In this section the results obtained applying aptamer-based biochemistry to microcantilever sensors employing *System V2* and *System V3* are presented.
Section 6.5.1 introduces the aptamers and their application in biosensing.

6.5.1 Aptamers introduction

Aptamers are typically composed of RNA, single-stranded DNA or a combination of these with non-natural nucleotides. They range in size from approximately 6 to 40 kDa and have typically complex three-dimensional structures. They bind to their targets with concentrations in the low nanomolar range and they are highly selective.
Aptamers are isolated from extremely complex libraries of nucleic acids, generated by combinatorial chemistry, by an iterative process of adsorption, recovery and reamplification.
The selection of aptamers is an in vitro process called systematic evolution of ligands by exponential enrichment (SELEX) [166, 167]. During this process a large library of oligonucleotides are screened by repeated selection and amplification. During the SELEX selection process, a large number of RNA molecules are screened so that the chance of generating an aptamer for the target protein is very high. Since this is an in vitro process, the degree of control over the product is very high.

Aptamers are widely employed as biorecognition elements in biosensor applications. Aptasensors are biosensors that use aptamers as their biorecognition element. Aptasensors were first used in the ninetieth as selective components in an optical sensor application where they were part of a model system consisting of beads that interact with fluorescent-tagged aptamers [168]. Since then, extensive research has been done on fluorescently labeled aptamers for various sort of protein detection [169, 170].
In the past decade several label-free aptasensor papers have been published, using different types of transductors [171–174]. Aptamers have been used in many detection techniques: quartz crystal microbalance (QCM) [175, 176] and surface plasmon resonance (SPR) [177, 178] are two of the most employed techniques for transduction of non-labeled aptamers.
Still, only few papers however report the use of microcantilevers functionalized with aptamer layers for the detection of biomolecules [179, 180].

Comparison between RNA aptamers and antibodies

The main advantage of aptamers is their in vitro selection process, whereas the production of antibodies uses biological systems. To produce antibodies, the induction of an immune response is necessary. However, this procedure might discriminate target proteins that has similar structure to endogenous proteins or toxic compounds that would kill the antibody producing animal. By isolating aptamers in vitro, an aptamer can be produced for any target molecule.
Furthermore, a series of advantages compared to antibodies is increasing the interest in applying aptamers in biological detection processes. The main advantages are:

- **Specificity**: aptamers are capable of larger specificity and affinity than antibodies [181]. The labeling of antibodies can cause them to lose their affinity to their target molecules. However, the position of these labeling molecules on aptamers can be easily changed to positions where binding is not affected.
- **Detection capability**: by forming unique secondary and tertiary structures aptamers have very high degree of specificity to the target molecules. They are able to detect very small structural changes, such as the presence or absence of a methyl or hydroxy group.
- **Robustness**: aptamers are self-refolding, single-chain, and redox-insensitive. They also lack the large hydrophobic cores of proteins and thus do not aggregate. They tolerate (or recover from) pH and temperatures that proteins do not.
- **Stability**: aptamers are much more stable at ambient (and higher) temperature than antibodies, thus having a much higher shelf life. They can tolerate transportation without any special requirements for cooling, eliminating the need for a continuous cold storage.
- **Synthesis**: the SELEX selection process usually takes about 8 weeks for the development of an aptamer. An antibody selection takes approximatively 6 months. Therefore, this will save a large amount of time compared to the in vivo selection process for antibodies. This SELEX process can be automated, reducing the workload for the investigators.

6.5.2 PDGF detection

The first tests using cantilever aptasensors were performed detecting varying concentrations of platelet-derived growth factor proteins (PDGF). These proteins are large (25 kDa) and their binding properties with specific aptamers have been widely investigated [173].
Several detection methods have been applied to nM concentration detection of PDGF. The most widely published methods is electrochemical based [182–185]. Chemically treated gold nanoparticles have also been used for sensing of PDGF via specific aptamers [186–188].

At the moment, only one conference proceeding has stated the use of cantilevers for aptamer-based detection of PDGF. The work has been done at the BioMEMS laboratory[2] in Columbia University, NYC. Their microfluidic device features a parylene cantilever array within a microchamber formed by a PDMS spacer layer and a glass slide including a patterned ITO temperature sensor for the monitoring of the binding efficiency of aptamer-PDGF with respect to changes of temperature [189].
Through a research collaboration with the BioMEMS group, thiolated aptamers with high affinity to the PDGF were tested.

Material and methods

The functionalization protocol for PDGF specific aptamers was developed by optimizing recipes suggested from different collaborators (DTU Nanotech, Aarhus University and Columbia University) and combined with information available in literature [190]. MMT500 chips were used for the experiments.
The following chemicals have been identified as necessary for a uniform coating of the Au surface of the cantilevers:

- Water (DNA grade) from Sigma Aldrich (CAS Number: 7732-18-5)
- PBS buffer (100 mM)
- Stock HS-Aptamer solution (44.6 μM concentration)
- PDGF proteins powder (M.W. = 25 kDa)
- BSA proteins solution (M.W. = 67 kDa)
- HCl (M.W. = 36.5) (37%) (densiy = 1.2 g/mL)
- BSA proteins solution (M.W. = 67 kDa)
- UREA 98% (M.W. = 60.06)
- EDTA (M.W. = 292.24)

Employing the above chemicals, different solutions were prepared, both for the functionalization process and for the PDGF sample preparation.

- **PDGF sample**: 50 ml of 4mM protein buffer solution has been prepared diluting 16.4 μL of HCl (37%) in 50 mL of Milli-Q Water + 0.1% BSA. Stock PDGF solution at 600 nM was made adding 10 μg of PDGF in 650 μl of protein buffer. 100 μl of PDGF protein solution was then prepared at different concentrations. Initial tests were performed at 400 nM and 100 nM concentration. Further investigation involved samples at concentrations of 50 nM, 10 nM and 2 nM.

[2] http://biomems.me.columbia.edu/

- **Aptamer functionalization**: 600 μl of HS-aptamer functionalization solution at 5 μmol was made adding 50 μl of stock aptamer solution in 450 μl DNA-grade water. 3 ml of aptamer washing bath was then prepared mixing 4M Urea and 15 mM EDTA in Milli-Q water.

The aptamer immobilization was done on freshly deposited Au layers. If chips had to be reused, a chemical cleaning of the Au was performed (see Section. 6.2.1). The Au surfaces were then cleaned in distilled water, acetone and absolute ethanol, before being immediately immersed in a 100 μl vial solution of 5 μmol HS-aptamer overnight (or at least 10 h). Cantilever chips were then rinsed by 4M Urea +15 mM EDTA for 1 minute, and then washed in Milli-Q water. The washing step was always performed twice.

6.5.3 PDGF experimental results

The first sensing tests were performed with *System V*2 and *Disc V*3-*A*. The initially tested concentrations were chosen to be relatively high, in order to have preliminary indications of the detecting capability of the system combined with the aptasensors.
Candidate concentrations of 400 nM and 100 nM have been chosen. These concentrations are 20-80 times higher than the detection limit demonstrated by Wang et al. [189].

Before the sensing experiment started, microfluidics connectors, tubes, channels chambers were filled with 1% BSA solution in order to prevent unspecific binding of PDGF on the sidewalls of the microfluidic sytem. The BSA was flowing through the system (without the sensors) for half an hour at a flow rate of 20 μl/min.
Next, the cantilevers were placed in the sensing chamber and the buffer solution was injected in the system at 10 μl/min flow rate. The cantilever baselines were recorded during the first 5 minutes. While the cantilever signals were recorded continuously, a valve switched to the PDGF sample solution for 15 additional minutes.
In Figures 6.17a and 6.17b the results of these preliminary experiments are shown. 28 cantilevers were monitored (14 aptamer functionalized and 14 blank) for 20 minutes after the exposure to the PDGF sample flow. Figure 6.17a illustrates the averaged measurements of functionalized (dark and light blue) and reference (black and grey) cantilevers for 400 nM and 100 nM of PDGF concentration. It can be noticed that, while the reference cantilevers bend few hundreds of nm independently of the PDGF concentration, the functionalized cantilevers show higher bending at higher concentrations. In Figure 6.17b the differential signals are plotted. After these preliminary tests, responses to PDGF concentrations of 50 nM, 10 nM and 2 nM, were investigated. For this new set of experiments, *System V*3 in connection with *Disc V*3-*A* were used. Each chamber was loaded with two functionalized and one reference chip (24 cantilevers in total).
Figure 6.18 presents the results obtained at 50 nM. The functionalized cantilevers experience a change of bending clearly higher than the functionalized ones. The signal from the two functionalized chips are plotted separately (see Figure 6.18a) and they are seen to differ approximately 200 nm in the final average deflection. This could be due to functionalization processes or to small misalignments of the cantilever apexes on the

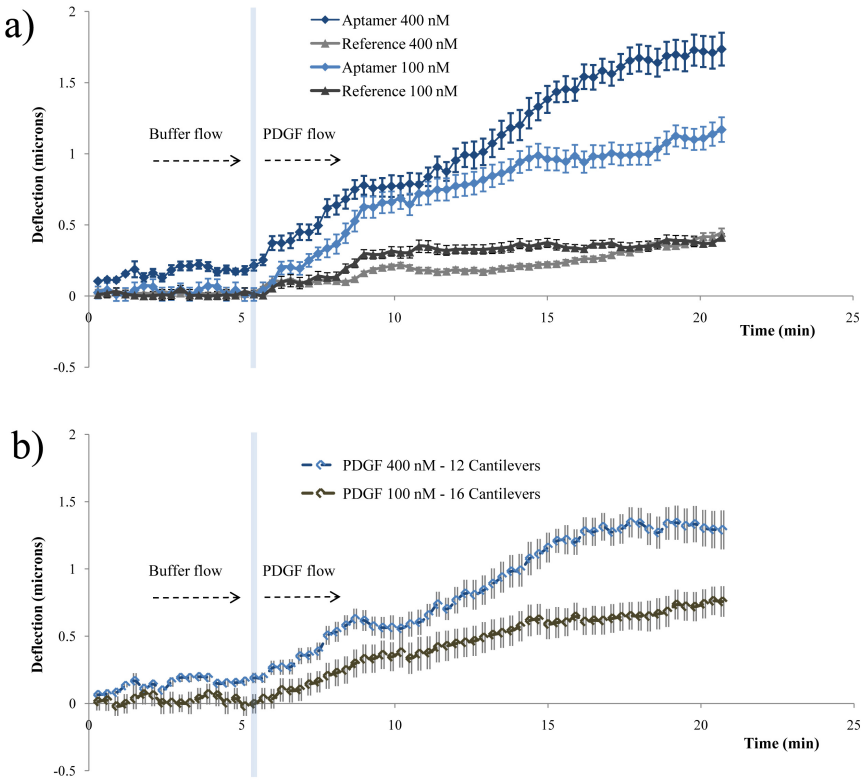

Figure 6.17: a) Bending results in continuous flow for functionalized and reference cantilevers under 100 nM and 400 nM of PDGF flow. b) differential signals obtained at 100 nM and 400 nM.

radial track (see Figure 3.1). The averaged differential signal is shown in Figure 6.18b. An average deflection of 510 nm ± 195 nm is obtained.
Figure 6.19 shows the result of the detection for 10 nM. Here 16 cantilevers have been monitored (8 aptamer functionalized and 8 blank) for 15 minutes after the exposure to the PDGF sample flow. The average change of bending for the functionalized cantilevers compared to the reference ones is significant and the average differential deflection is 280 nm.
The last experiment was performed with a 2 nM sample concentration. The results, reported in Figure 6.20, do not reveal significant deflection change of the functionalized of the reference cantilevers. The actual cantilever deflection probably falls below the noise level of the system.
Figure 6.21 shows data obtained from the 100 analyzed independent cantilevers (52 aptamer-functionalized, 48 reference) at different PDGF concentrations.
It is anyway difficult to compare the data placed on the left side of Figure 6.21 (obtained with *System V2*) and the ones on the right side (obtained with *System V2*). The two devices had in fact different characteristics, in terms of noise level, sensitivity, and more generally, in detection performances (see Sections 2.4 and 2.5). Within this context, even though the average deflection value of functionalized cantilevers was found to increase

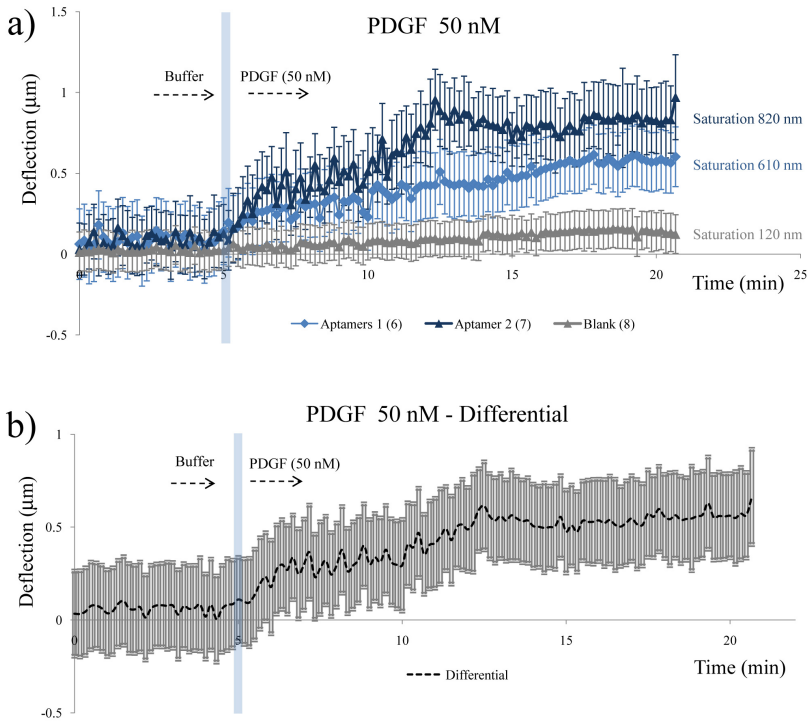

Figure 6.18: a) Bending results in continuous flow for 13 functionalized and 8 reference cantilevers at 50 nM PDGF flow. b) differential signal.

with the protein concentration, further experiments will be needed to fully validate the experimental results.

6.5.4 uPA detection

The last experiments performed during the PhD program were related to the detection of cancer marker proteins. Through a collaboration with Aarhus University (Prof. Jorgen Kjems), two sets of plasminogen activators (uPA and its activator inhibitor-1, PAI-1) which act as markers for tumoral presence in the body were available.
Urokinase, also called urokinase-type plasminogen activator (uPA), is a serine protease, i.e. an enzyme that cleaves peptide bonds in proteins [191].
uPA has an activity on the metastase formation from cancer tissue [192]. The activity of uPA is mainly inhibited by the serpin plasminogen activator inhibitor-1 (PAI-1) [193]. It has been demonstrated that cancer patients with low levels of uPA or PAI-1 have a significantly better prognosis than patients with high levels. The levels of uPA and PAI-1 in the blood are therefore considered strong markers for the presence of malignant cancer in the body [194].
As test experiments, detection of relatively low concentrations (∼10 nM) of PAI-1 was

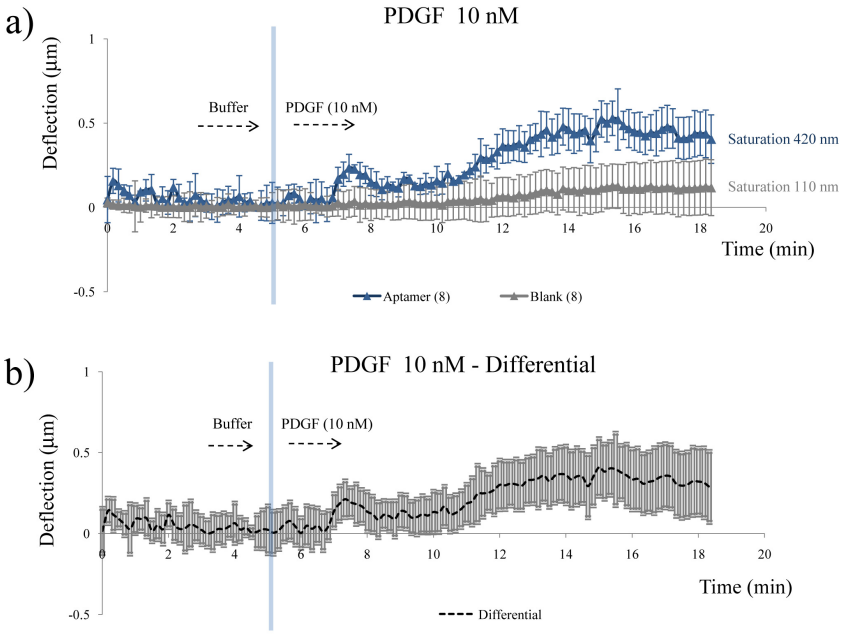

Figure 6.19: a) Bending results in continuous flow for 8 functionalized and 8 reference cantilevers at 10 nM PDGF flow. b) differential signal.

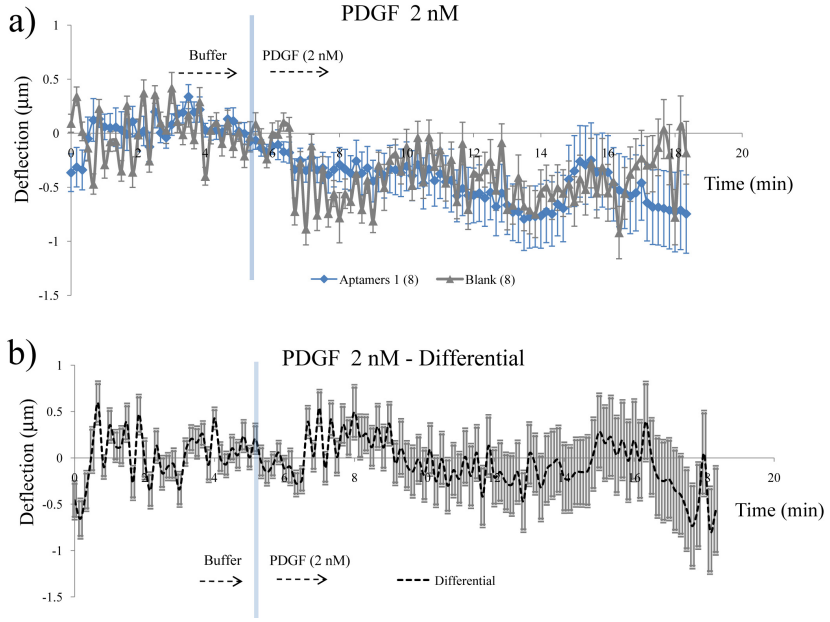

Figure 6.20: a) bending results in continuous flow for 8 functionalized and 8 reference cantilevers at 2 nM PDGF flow. b) differential signal.

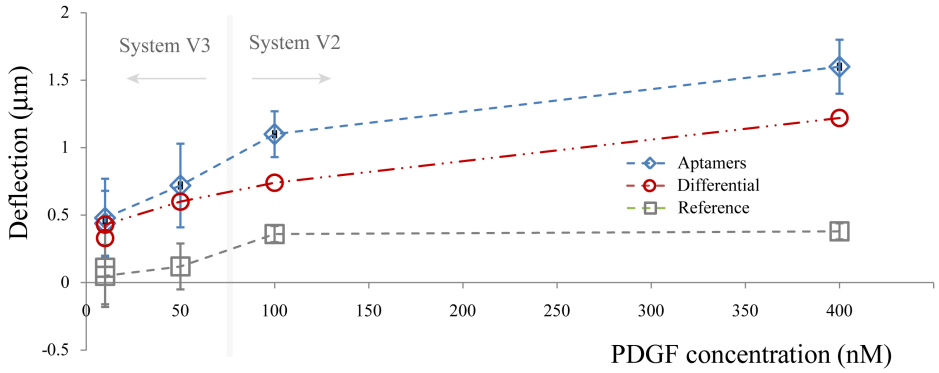

Figure 6.21: Statistical deflection Vs PDGF concentration measured over 52 cantilever aptasensors and 48 reference ones. The data are obtained from the plots presented in this Section, plus few more experiments not reported here.

performed under continuous flow, using *System V2* in combination with *Disc V3-A*.

Material and methods

The following biochemicals were used for the preparation of the protein detection:

- Recombinant active PAI-1 (Mol Weight: 50 kDa), stock solution at 0.643 mg/ml
- Anti-PAI-1 aptamers
- 10mM 4-(2-hydroxyethyl)-1-piperazineethanesulfonic acid (HEPES) buffer (Mol weight 238.3 g/mol)
- NaCl (mol weight 58.44 g/mol)
- 1% BSA Blocking buffer in 10 mM HEPES + 150 mM NaCl

The silicon chips were cleaned 3 times in acetone solution and incubated for 30 minutes in an UV ozone oven to enhance the hydrophilic properties of the gold layer.
100 μl of 2.5 μM aptamer (anti-PAI-1) mixed with 1 ml of HEPES buffer were place in PCR tubes. The chips were immersed in the PCR tubes and incubated overnight at room temperature. While some chips were functionalized with the aptamer layers, others were left blank to provide reference cantilevers.
The PAI-1 solution was prepared mixing 3 μl of 0.643 mg/ml PAI-1 with 3 ml HEPES buffer, resulting in 12.8 nM concentration.

In order to avoid unspecific binding, the system (without the cantilevers) was rinsed for 1 hour with a 1% solution of BSA (Bovine Serum Albumine) in 1x PBS buffer at

flow rate of 20 μl/min, using a syringe pump.
The BSA solution was then removed through HEPES buffer flushing (20 min at flow of 20 μl/min) followed by 10 minutes of Milli-Q rinsing (same flow rate) before the cantilever chips were inserted in the disc. This procedure removes the excess of BSA and avoids salt deposits.
The chips were then placed inside the disc chamber and flushed with HEPES buffer for 10 min, to remove excess aptamer solution and to obtain a stable baseline. The signal was then acquired for approx 10 minutes, before a microfluidic switch injected PAI-1 proteins inside the system. The flow rate used for measurements was set to 15 μl/min and kept constant.

6.5.5 uPA experimental results

Figure 6.22 shows the results obtained monitoring the deflection of one functionalized chip (blue curve) and one reference chip (grey curve). Only the signal from 5 out of 8 functionalized cantilevers and 7 out of 8 reference cantilevers could be recorded. It can be noticed that about 1 minute after the PAI-1 proteins were injected into the microchannels, the functionalized cantilevers started to bend. After approx. 10 minutes,

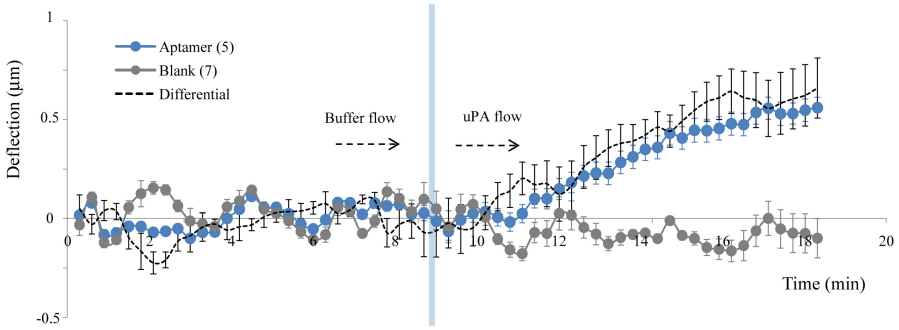

Figure 6.22: Average deflection change for 5 aptamers functionalized cantilevers (blue) and 7 blank cantilevers (grey). The black dashed line refers to the differential signal, whose value after 10 minutes reached around 550 nm.

the average deflection change reached the value of 550 nm. The reference cantilevers did not exhibit significant change of bending. The black dashed line illustrates the differential signal (560 nm $\pm$130 nm).
In Figure 6.23 the values evaluated over more cantilevers are reported. The experimental conditions were kept the same as before. This experiment was carried out to evaluate the reliability of the preliminary tests presented in Figure 6.22. 13 out of 16 aptamer functionalized cantilevers and 15 out of 16 reference cantilevers were monitored under the same flow rate and PAI-1 concentration as before. The average deflection change for aptamer coated sensors is higher than in the previous test (around 850 nm against 550 nm), with similar standard deviation. Furthermore, also the reference cantilevers exhibit a small deflection change, in the order of 180 nm.
The differential signal (dashed black line) reaches a value of 700 nm ($\pm$100 nm), slightly

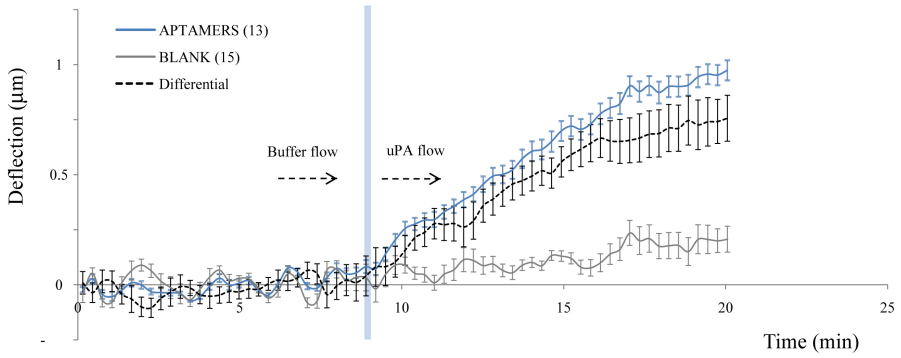

Figure 6.23: Average deflection change for 13 aptamers functionalized cantilevers (blue) and 15 blank cantilevers (grey). The black dashed line refers to the differential signal (700 nm ±100 nm).

higher than the differential value obtained with the previous experiment (560 nm ±130 nm).

6.6 Concluding remarks

Several assays have been tested during the platform development. Relatively high amount of statistical data were generated at each experiment, where typically 24-72 cantilevers were simultaneously monitored. Reaction of antibodies, proteins and explosives have been tested with the three different systems. The platform allows for simultaneous measurements of deflection, vibrational amplitude and surface roughness, increasing the amount of information to be obtained and consequently the reliability of data. The different system versions were successfully employed in measurements in gas phase and liquid phase.

Calibration issues

Typically, very high values of cantilever deflections are reported in this work. Compared to available literature, measured deflections are found to be, in some cases, up to one order of magnitude higher. Table 6.3 lists some examples of deflections measured optically by different groups on several assays and cantilever geometries. It is difficult to directly compare deflection measurements performed on different samples and cantilever types. Analyte concentrations and functionalization coatings are expected to significantly affect the overall bending of the cantilever. Typically, deflection values on the order of hundreds of nm are reported when, for example, sub-nanomolar concentrations of proteins are monitored.
In this thesis some inconsistencies of the absolute deflection values can be noticed. The experiments performed with *System V*1 (biotin-streptavidin and BAM-Anti-BAM) show high deflection value, up to several microns in magnitude. Sensing experiments on DNT, performed with *System V*2, exhibit deflections on the order of 1 μm. Aptamer-based experiments, run mainly on *System V*3, show deflection values of the functionalized

Material	Length (μm)	Width (μm)	Thickness (μm)	Assay	Deflection (nm)
SiN	200	20	0.5	DNA hybridization	10-40 [24]
SiN	200	20	0.5	Antibody-protein	20-150 [39]
SiN	200	20	0.5	Avidin-Neutravidin	5-20 [39]
Si	200	40	0.6	Antibody-DDT	5-20 [46]
SiN	200	40	0.7	pH detection	200-400 [50]
SiN	200	200	0.8	DNA hybridization	20-60 [61]
Si	500	100	0.45	DNA hybridization	20-200 [35]
SiN	500	100	0.5	DNS-proteins	50-100 [42]
Si	500	100	0.5	Antibody-protein	120-800 [40]
Si	500	100	0.9	pH detection	60-500 [26]
Si	500	100	1	DNA hybridization	20-600 [34]
Si	500	100	1	DNA hybridization	10-50 [195]

Table 6.3: Deflection values for different types of cantilevers and measured assays.

cantilevers on the order of hundreds of nm.
The many changes in experimental conditions (assays, chip type, system and disc version, lenses and FES magnifications) strongly affected the coherence of the absolute deflection conversion. The investigation on the capabilities of the setup was oriented towards analysis of the differential signal between functionalized and reference cantilevers. Probably not enough attention was given to the determination of the actual bending values. Y-axes in this chapter were then converted into deflection through calibrations performed mostly manually, causing an uncertainty on the absolute voltage/micron relation. The calibration of *System V3* was the first to be characterized in more details. The deflections measured with this system are comparable to deflections observed in literature for similar cantilevers and similar assays.

Chapter 7

Conclusions

The main goal of the project has been the development of a platform for high-throughput measurements of cantilever sensors. The DVD platform offers a number of advantages over traditional cantilever sensing. It readily supplies large amount of data for statistical analysis facilitating the onset of statistical cantilever based sensing. Also, the nanometer sized laser spot of the PUH facilitates measurements on mechanical sensors with sub-micrometer dimensions. Finally, the platform integrates a simple and well established method of controlling liquids by centrifugal forces.
During the project several technological features have been investigated and developed:

- **DVD-ROM based readout**: A DVD-ROM based readout approach has been implemented for high-throughput measurements. This optical readout allows precise measurements of cantilever deflection through the astigmatic method built-in to the PUH. Compared with optical lever technique, the astigmatic detection system has more advantages for high speed microcantilever deflection measurements, such as compact size, easy adjustment and high angular tolerance. With this method, different objective lenses can be employed for sub micrometer cantilevers and long distance measurement applications.

- **System design and assembly**: Three generations of systems have been assembled and tested. While the first one was mostly used for proof of concept (parallelized acquisition and biosensing), the following versions were built in order to address technological issues like stability, robustness and resolution of detection. *System V3* was specifically designed to reduce mechanical wobbling of the rotating stage and to run sensing experiments in continuous flow.

- **Disc-like sensing platform**: The integration of the DVD reader with the on-substrate DVD-like approach leads to a high throughput flexible platform with easy self-alignment and replacement of cantilever chips. With this new approach, hundreds of cantilevers can be placed on the disc and read sequentially. Several disc designs were fabricated and tested in different materials. These discs could hold up to 1000 cantilevers aligned along independent sensing tracks. While SU-8

based discs were useful for proof of concept, PMMA microfluidics was found to work better under steady flow conditions. Different open-close sealing methods were also implemented.

- **Optics characterization**: Different optics have been used in connection with the three generations of systems. Depending on the lens employed, different sensitivities were achieved. Depending on whether the measurements were to be performed in air or in liquid, specific setting configurations were optimized. Electronic and optical enhancement were combined in order to obtain optimal conditions for the specific applications

- **Data treatment**: A robust data analysis protocol has been developed and applied to cantilever sensing. The data are pre-processed before being saved on the PC hard drive, highly reducing the stored amount of data. The variables are then computed through a statistical analysis of the cantilever measurements.

- **System automation**: The system functionalities are controlled by a modulized program which interfaces the whole system (DAQ, motor, PUHs, data analysis code) with the PC. Auto-tracking methods have been proved and partially applied to the system.

- **Sensing results**: Several assays have been tested during the platform development. Detection of explosives, antibodies and proteins have been demonstrated. Statistical data were generated at each experiments, where typically 24-72 cantilevers were simultaneously monitored. The platform allows for simultaneous measurements of deflection, vibrational amplitude and surface roughness, increasing the amount of information to be achieved and consequently the reliability of data. The wet & dry sensing mode has been identified as a promising technique to increase the amount of data.

Several features still need further development. Among them, particular effort should be directed towards:

- **System**: Next generation system should rely on on-line wobbling compensation mechanisms. The mechanical-based wobbling compensation implemented in $System\ V3$ was an excellent approach for sensing tests, however it would probably be insufficient for out-of-the-lab sensing applications. Also, the optics need further characterization and optimization. Automation protocols have to be implemented, and effort has to be directed to further software development. Compactness also needs to be addressed. While the overall system dimensions are quite small, the platform still relies on power lines and computer interface. Batteries and embedded calculator are envisioned to provide a compact and fully portable device.

- **Disc**: Fully polymeric platforms (e.g. Polycarbonate) are targeted as next generation discs. These discs will be substantially cheaper than glass-based platforms, and their fabrication could be easily implemented in mass production technologies

(e.g. injection molding). Centripetal microfluidics needs to be further investigated, in order to provide full functionalities for on-the-spot sensing experiments. Among these, centrifugation, dilution and mixing of samples would highly increase the applicability of the platform to, for example, diagnostics and water monitoring.

- **Software**: The functions which drive the system need further development. Numerical characterization of the profiles that automatically screens outliers is believed to highly enhance the overall detection resolution of the system. Libraries of experimental settings need be created in order to perform sensing experiments under steady conditions.

- **Sensing**: New assays need to be tested. Aptamer-based functionalization is believed to offer great potentiality for real sensing applications. Assays for hormone detection in water samples are currently under development. In general, higher reproducibility of experimental conditions is required.

Our platform represents a new and powerful tool for analyzing biochemical reactions, where the reliability of the measurements is ensured by the statistical analysis and by the full parallel characterization of the cantilevers. We also envision that we in the future will be able to operate ultra-sensitive cantilevers for i.e. mass sensing. We hope that our concept will be of use for fundamental as well as more applied studies and we believe that it opens up for a wide range of experiments where reliability and statistical significance of data are of great importance (as in case of drug screening or medical diagnostic).

Bibliography

[1] Natalie Kostesha, M S Schmidt, F. G. Bosco, J K Olsen, Carsten Johnsen, K A Nielsen, J O Jeppesen, T S Alstrø m, Jan Larsen, and T Thundat. The Xsense Project: The Application of an Intelligent Sensor Array for High Sensitivity Handheld Explosives Detectors. *Scanning*, pages 11–15, 2010.

[2] Michael S Schmidt, Natalie Kostesha, F. G. Bosco, Jesper K Olsen, Carsten Johnsen, Kent A Nielsen, Jan O Jeppesen, Tommy S Alstrom, Jan Larsen, Mogens H Jakobsen, Thomas Thundat, and Anja Boisen. Xsense: using nanotechnology to combine detection methods for high sensitivity handheld explosives detectors. *Russell The Journal Of The Bertrand Russell Archives*, 7664:76641H–76641H–6, 2010.

[3] M S Schmidt, N Kostesha, F. G. Bosco, J K Olsen, C Johnsen, K A Nielsen, J O Jeppesen, T S Alstrom, J Larsen, T Thundat, M H Jakobsen, and A Boisen. Xsense - a miniaturised multi-sensor platform for explosives detection. In *Proceedings of SPIE*, page In press, 2011.

[4] a. Greve, J. Olsen, N. Privorotskaya, L. Senesac, T. Thundat, W.P. King, and a. Boisen. Micro-calorimetric sensor for vapor phase explosive detection with optimized heat profile. *Microelectronic Engineering*, 87(5-8):696–698, May 2010.

[5] Dechang Yi, Anders Greve, Jan H. Hales, Larry R. Senesac, Zachary J. Davis, Don M. Nicholson, Anja Boisen, and Thomas Thundat. Detection of adsorbed explosive molecules using thermal response of suspended microfabricated bridges. *Applied Physics Letters*, 93(15):154102, 2008.

[6] a. Greve, J. K. Olsen, a. Boisen, N. Privorotskaya, W. P. King, L. Senesac, and T. Thundat. Micro-calorimetric sensor for vapour phase explosive detection with optimized heat profile. *2009 IEEE Sensors*, pages 723–726, October 2009.

[7] Jesper K. Olsen, Anders Greve, N. Privorotskaya, L. Senesac, T. Thundat, W. P. King, and A. Boisen. Micro-calorimetric sensor for trace explosive particle detection. *SPIE conference proceeding*, 7679:767929–767929–10, 2010.

[8] Jesper Kenneth Olsen. Micro Calorimetric Sensor for Explosives Detection. *PhD thesis - DTU Nanotech*, 2011.

[9] Michael Stenbaek Schmidt, Anja Boisen, and Jorg Hubner. Towards easily reproducible nano-structured SERS substrates. *2009 IEEE Sensors*, pages 1763–1767, October 2009.

[10] Michael Stenbæ k Schmidt, Jesper Kenneth Olsen, and Anja Boisen. Nanostructured Surface Enhanced Raman Scattering Substrates for Explosives Detection. *IEEE Sensors Journal*, pages 2634–2637, 2010.

[11] J.K. Gimzewski, Ch. Gerber, E. Meyer, and R.R. Schlittler. Observation of a chemical reaction using a micromechanical sensor. *Chemical Physics Letters*, 217(5-6):589–594, January 1994.

[12] T. Thundat, R. J. Warmack, G. Y. Chen, and D. P. Allison. Thermal and ambient-induced deflections of scanning force microscope cantilevers. *Applied Physics Letters*, 64(21):2894, 1994.

[13] AM Moulin, SJ O'Shea, and ME Welland. Microcantilever-based biosensors. *Ultramicroscopy*, 82(1-4):23–31, February 2000.

[14] R Raiteri. Micromechanical cantilever-based biosensors. *Sensors and Actuators B: Chemical*, 79(2-3):115–126, October 2001.

[15] Christiane Ziegler. Cantilever-based biosensors. *Analytical and bioanalytical chemistry*, 379(7-8):946–59, August 2004.

[16] Philip S Waggoner and Harold G Craighead. Micro- and nanomechanical sensors for environmental, chemical, and biological detection. *Lab on a chip*, 7(10):1238–55, October 2007.

[17] Jürgen Fritz. Cantilever biosensors. *The Analyst*, 133(7):855–63, July 2008.

[18] Maria L. Sushko, John H. Harding, Alexander L. Shluger, Rachel A. McKendry, and Moyu Watari. Physics of Nanomechanical Biosensing on Cantilever Arrays. *Advanced Materials*, 20(20):3848–3853, October 2008.

[19] Ram Datar, Seonghwan Kim, Sangmin Jeon, Peter Hesketh, Scott Manalis, Anja Boisen, and Thomas Thundat. Cantilever Sensors : Nanomechanical Tools for Diagnostics. *MRS Bulletin*, 34(June):449–454, 2009.

[20] Anja Boisen, Soren Dohn, Stephan Sylvest Keller, Silvan Schmid, and Maria Tenje. Cantilever-like micromechanical sensors. *Reports on Progress in Physics*, 74(3):036101, March 2011.

[21] J L Arlett, E B Myers, and M L Roukes. Comparative advantages of mechanical biosensors. *Nature nanotechnology*, 6(4):203–15, April 2011.

[22] GY Chen, T Thundat, EA Wachter, and RJ Warmack. Adsorption-induced surface stress and its effects on resonance frequency of microcantilevers. *Journal of Applied Physics*, 77(8):3618–3622, 1995.

[23] R. Berger. Surface Stress in the Self-Assembly of Alkanethiols on Gold. *Science*, 276(5321):2021–2024, June 1997.

[24] G Wu, H Ji, K Hansen, T Thundat, R Datar, R Cote, M F Hagan, a K Chakraborty, and a Majumdar. Origin of nanomechanical cantilever motion generated from biomolecular interactions. *Proceedings of the National Academy of Sciences of the United States of America*, 98(4):1560–4, February 2001.

[25] Rodolphe Marie, Henriette Jensenius, Jacob Thaysen, Claus B Christensen, and Anja Boisen. Adsorption kinetics and mechanical properties of thiol-modified DNA-oligos on gold investigated by microcantilever sensors. *Ultramicroscopy*, 91(1-4):29–36, May 2002.

[26] Moyu Watari, Jane Galbraith, Hans-Peter Lang, Marilyne Sousa, Martin Hegner, Christoph Gerber, Mike a Horton, and Rachel a McKendry. Investigating the molecular mechanisms of in-plane mechanochemistry on cantilever arrays. *Journal of the American Chemical Society*, 129(3):601–9, January 2007.

[27] Michel Godin, Vincent Tabard-Cossa, Yoichi Miyahara, Tanya Monga, P J Williams, L Y Beaulieu, R Bruce Lennox, and Peter Grutter. Cantilever-based sensing: the origin of surface stress and optimization strategies. *Nanotechnology*, 21(7):75501, February 2010.

[28] Suman Cherian and Thomas Thundat. Determination of adsorption-induced variation in the spring constant of a microcantilever. *Applied Physics Letters*, 80(12):2219, 2002.

[29] Thomas Braun, Viola Barwich, Murali Ghatkesar, Adriaan Bredekamp, Christoph Gerber, Martin Hegner, and Hans Lang. Micromechanical mass sensors for biomolecular detection in a physiological environment. *Physical Review E*, 72(3):1–9, September 2005.

[30] Javier Tamayo, Daniel Ramos, Johan Mertens, and Montserrat Calleja. Effect of the adsorbate stiffness on the resonance response of microcantilever sensors. *Applied Physics Letters*, 89(22):224104, 2006.

[31] S Dohn, W Svendsen, A Boisen, and O Hansen. Mass and position determination of attached particles on cantilever based mass sensors. *Review of scientific instruments*, 78(10):103303, October 2007.

[32] S. Dohn and O. Hansen. Measurement of the resonant frequency of nano-scale cantilevers by hard contact readout. *Microelectronic Engineering*, 85(5-6):1390–1394, May 2008.

[33] B. Ilic, D. Czaplewski, M. Zalalutdinov, H. G. Craighead, P. Neuzil, C. Campagnolo, and C. Batt. Single cell detection with micromechanical oscillators. *Journal of Vacuum Science & Technology B: Microelectronics and Nanometer Structures*, 19(6):2825, 2001.

[34] Rachel McKendry, Jiayun Zhang, Youri Arntz, Torsten Strunz, Martin Hegner, Hans Peter Lang, Marko K Baller, Ulrich Certa, Ernst Meyer, Hans-Joachim Güntherodt, and Christoph Gerber. Multiple label-free biodetection and quantitative DNA-binding assays on a nanomechanical cantilever array. *Proceedings of the National Academy of Sciences of the United States of America*, 99(15):9783–8, July 2002.

[35] J Zhang, H P Lang, F Huber, a Bietsch, W Grange, U Certa, R McKendry, H-J Güntherodt, M Hegner, and Ch Gerber. Rapid and label-free nanomechanical detection of biomarker transcripts in human RNA. *Nature nanotechnology*, 1(3):214–20, December 2006.

[36] Jing Zhang and Hai-Feng Ji. An anti E. coli O157:H7 antibody-immobilized microcantilever for the detection of Escherichia coli (E. coli). *Analytical sciences : the international journal of the Japan Society for Analytical Chemistry*, 20(4):585–7, April 2004.

[37] Karin Y Gfeller, Natalia Nugaeva, and Martin Hegner. Micromechanical oscillators as rapid biosensor for the detection of active growth of Escherichia coli. *Biosensors & bioelectronics*, 21(3):528–33, September 2005.

[38] K.Y. Gfeller, Natalia Nugaeva, and Martin Hegner. Rapid biosensor for detection of antibiotic-selective growth of Escherichia coli. *Applied and environmental microbiology*, 71(5):2626, 2005.

[39] G Wu, R H Datar, K M Hansen, T Thundat, R J Cote, and a Majumdar. Bioassay of prostate-specific antigen (PSA) using microcantilevers. *Nature biotechnology*, 19(9):856–60, September 2001.

[40] Y Arntz, JD Seelig, HP Lang, J Zhang, P Hunziker, JP Ramseyer, E Meyer, M Hegner, and Ch Gerber. Label-free protein assay based on a nanomechanical cantilever array. *Nanotechnology*, 14(1):86, January 2003.

[41] Natalija Backmann, Christian Zahnd, Francois Huber, Alexander Bietsch, Andreas Plückthun, Hans-Peter Lang, Hans-Joachim Güntherodt, Martin Hegner, and Christoph Gerber. A label-free immunosensor array using single-chain antibody fragments. *Proceedings of the National Academy of Sciences of the United States of America*, 102(41):14587–92, October 2005.

[42] François Huber, Martin Hegner, Christoph Gerber, Hans-Joachim Güntherodt, and Hans Peter Lang. Label free analysis of transcription factors using microcantilever arrays. *Biosensors & bioelectronics*, 21(8):1599–605, February 2006.

[43] Vita Dauksaite, Martin Lorentzen, Flemming Besenbacher, and Jø rgen Kjems. Antibody-based protein detection using piezoresistive cantilever arrays. *Nanotechnology*, 18(12):125503, March 2007.

[44] Min Yue, JC Stachowiak, Henry Lin, Ram Datar, and Richard Cote. Label-free protein recognition two-dimensional array using nanomechanical sensors. *Nano letters*, 8(2):520–4, February 2008.

[45] A. Subramanian, P. I. Oden, S. J. Kennel, K. B. Jacobson, R. J. Warmack, T. Thundat, and M. J. Doktycz. Glucose biosensing using an enzyme-coated microcantilever. *Applied Physics Letters*, 81(2):385, 2002.

[46] Mar Alvarez, Ana Calle, Javier Tamayo, Laura M Lechuga, Antonio Abad, and Angel Montoya. Development of nanomechanical biosensors for detection of the pesticide DDT. *Biosensors and Bioelectronics*, 18(5-6):649–653, May 2003.

[47] Michael Bache, Rafael Taboryski, Silvan Schmid, Jens Aamand, and Mogens Havsteen Jakobsen. Investigations on antibody binding to a micro-cantilever coated with a BAM pesticide residue. *Nanoscale research letters*, 6(1):386, January 2011.

[48] S Cherian. Detection of heavy metal ions using protein-functionalized microcantilever sensors. *Biosensors and Bioelectronics*, 19(5):411–416, December 2003.

[49] B. Rogers, L. Manning, M. Jones, T. Sulchek, K. Murray, B. Beneschott, J. D. Adams, Z. Hu, T. Thundat, H. Cavazos, and S. C. Minne. Mercury vapor detection with a self-sensing, resonating piezoelectric cantilever. *Review of Scientific Instruments*, 74(11):4899, 2003.

[50] H Ji. Detection of pH variation using modified microcantilever sensors. *Sensors and Actuators B: Chemical*, 72(3):233–238, February 2001.

[51] T Thundat, GY Chen, RJ Warmack, DP Allison, and EA Wachter. Vapor detection using resonating microcantilevers. *Analytical Chemistry*, 67(3):519–521, 1995.

[52] HP Lang, R Berger, F Battiston, J.P. Ramseyer, E Meyer, C Andreoli, J Brugger, P Vettiger, M Despont, T Mezzacasa, and Others. A chemical sensor based on a micromechanical cantilever array for the identification of gases and vapors. *Applied Physics A: Materials Science & Processing*, 66:61–64, 1998.

[53] a Boisen, J Thaysen, H Jensenius, and O Hansen. Environmental sensors based on micromachined cantilevers with integrated read-out. *Ultramicroscopy*, 82(1-4):11–6, February 2000.

[54] Heniette Jensenius, Jacob Thaysen, A. Annette Rasmussen, LH Veje, Ole Hansen, and A Boisen. A microcantilever-based alcohol vapor sensor-application and response model. *Applied Physics Letters*, 76(18):2615–2617, 2000.

[55] A Greve, S Keller, S Dohn, A Kristensen, M Cerruti, A Majumdar, and A Boisen. Effects of Surface Structured Polymer Cantilever Fabricated by Nanoimprint Lithography. In *International Workshop on Nonmechanical Cantilever Sensors*, pages 2–3, 2009.

[56] PG Datskos, NV Lavrik, and MJ Sepaniak. Detection of explosive compounds with the use of microcantilevers with nanoporous coatings. *Sensors Letters*, 1(1):25–32, 2003.

[57] LA Pinnaduwage, A. Gehl, DL Hedden, G. Muralidharan, T. Thundat, RT Lareau, T. Sulchek, L. Manning, B. Rogers, M. Jones, and Others. A microsensor for trinitrotoluene vapour. *Nature*, 425(6957):474, 2003.

[58] L. a. Pinnaduwage. Detection of trinitrotoluene via deflagration on a microcantilever. *Journal of Applied Physics*, 95(10):5871, 2004.

[59] L.a Pinnaduwage, T Thundat, J.E Hawk, D.L Hedden, P.F Britt, E.J Houser, S Stepnowski, R.a McGill, and D Bubb. Detection of 2,4-dinitrotoluene using microcantilever sensors. *Sensors and Actuators B: Chemical*, 99(2-3):223–229, May 2004.

[60] Alexander Bietsch, Jiayun Zhang, Martin Hegner, Hans Peter Lang, and Christoph Gerber. Rapid functionalization of cantilever array sensors by inkjet printing. *Nanotechnology*, 15(8):873–880, August 2004.

[61] M Alvarez, L G Carrascosa, M Moreno, a Calle, a Zaballos, L M Lechuga, C Martínez-A, and J Tamayo. Nanomechanics of the formation of DNA self-assembled monolayers and hybridization on microcantilevers. *Langmuir : the ACS journal of surfaces and colloids*, 20(22):9663–8, October 2004.

[62] MP De Boer, J.a Knapp, T.a Michalske, U Srinivasan, and R Maboudian. Adhesion hysteresis of silane coated microcantilevers. *Acta materialia*, 48(18-19):4531–4541, December 2000.

[63] G Blagoi, S Keller, a Johansson, a Boisen, and M Dufva. Functionalization of SU-8 photoresist surfaces with IgG proteins. *Applied Surface Science*, 255(5):2896–2902, December 2008.

[64] Cantion (DK) Microspotter. http://www.cantion.com/CantiSpot.htm.

[65] Concentris (CH). http://www.concentris.ch/.

[66] G Meyer and N M Amer. Novel optical approach to atomic force microscopy. *Applied Physics Letters*, 53(12):1045, 1988.

[67] G Binnig, C F Quate, and C Gerber. Atomic Force Microscope. *Physical Review Letters*, 56(9):930–933, 1986.

[68] H P Lang, R Berger, C Andreoli, J Brugger, M Despont, P Vettiger, C Gerber, J K Gimzewski, J P Ramseyer, E Meyer, and H J Guntherodt. Sequential position readout from arrays of micromechanical cantilever sensors. *Applied Physics Letters*, 72(3):383, 1998.

[69] J. Mertens, M. Alvarez, and J. Tamayo. Real-time profile of microcantilevers for sensing applications. *Applied Physics Letters*, 87(23):234102, 2005.

[70] S Lim, D Raorane, S Satyanarayana, and A Majumdar. Nano-chemo-mechanical sensor array platform for high-throughput chemical analysis. *Sensors and Actuators B: Chemical*, 119(2):466–474, 2006.

[71] Genki Yoshikawa, Hans-Peter Lang, Terunobu Akiyama, Laure Aeschimann, Urs Staufer, Peter Vettiger, Masakazu Aono, Toshio Sakurai, and Christoph Gerber. Sub-ppm detection of vapors using piezoresistive microcantilever array sensors. *Nanotechnology*, 20(1):015501, 2009.

[72] Jeong W. Yi, Wan Y. Shih, R. Mutharasan, and Wei-Heng Shih. In situ cell detection using piezoelectric lead zirconate titanate-stainless steel cantilevers. *Journal of Applied Physics*, 93(1):619, 2003.

[73] Jeong Hoon Lee, Kyo Seon Hwang, Jaebum Park, Ki Hyun Yoon, Dae Sung Yoon, and Tae Song Kim. Immunoassay of prostate-specific antigen (PSA) using resonant frequency shift of piezoelectric nanomechanical microcantilever. *Biosensors & bioelectronics*, 20(10):2157–62, April 2005.

[74] Gajendra Shekhawat, Soo-Hyun Tark, and Vinayak P Dravid. MOSFET-Embedded microcantilevers for measuring deflection in biomolecular sensors. *Science (New York, N.Y.)*, 311(5767):1592–5, March 2006.

[75] Soo-Hyun Tark, Arvind Srivastava, Stanley Chou, Gajendra Shekhawat, and Vinayak P. Dravid. Nanomechanoelectronic signal transduction scheme with metal-oxide-semiconductor field-effect transistor-embedded microcantilevers. *Applied Physics Letters*, 94(10):104101, 2009.

[76] Veeco (US). http://www.veeco.com/.

[77] Mecwins (ES). http://www.mecwins.com/.

[78] Uni Basel (CH). http://www.cantileversensors.unibas.ch/CLA/Welcome.html.

[79] Nanonord/Cantion (DK). http://www.nanonord.dk/.

[80] Seiko Instruments (JP). http://www.sii.co.jp/info/eg/mems2.html.

[81] Intelligent Microsystem Center (KR). http://www.microsystem.re.kr/.

[82] Régis Peytavi, Frédéric R Raymond, Dominic Gagné, François J Picard, Guangyao Jia, Jim Zoval, Marc Madou, Karel Boissinot, Maurice Boissinot, Luc Bissonnette, Marc Ouellette, and Michel G Bergeron. Microfluidic device for rapid (¡15 min) automated microarray hybridization. *Clinical chemistry*, 51(10):1836–44, October 2005.

[83] Marc Madou, Jim Zoval, Guangyao Jia, Horacio Kido, Jitae Kim, and Nahui Kim. Lab on a CD. *Annual review of biomedical engineering*, 8:601–28, January 2006.

[84] Robert Gorkin, Jiwoon Park, Jonathan Siegrist, Mary Amasia, Beom Seok Lee, Jong-Myeon Park, Jintae Kim, Hanshin Kim, Marc Madou, and Yoon-Kyoung Cho. Centrifugal microfluidics for biomedical applications. *Lab on a chip*, 10(14):1758–73, July 2010.

[85] R D Johnson, I H Badr, G Barrett, S Lai, Y Lu, M J Madou, and L G Bachas. Development of a fully integrated analysis system for ions based on ion-selective optodes and centrifugal microfluidics. *Analytical chemistry*, 73(16):3940–6, August 2001.

[86] Libby G Puckett, Emre Dikici, Siyi Lai, Marc Madou, Leonidas G Bachas, and Sylvia Daunert. Investigation into the applicability of the centrifugal microfluidics platform for the development of protein-ligand binding assays incorporating enhanced green fluorescent protein as a fluorescent reporter. *Analytical chemistry*, 76(24):7263–8, December 2004.

[87] T Leu and Pey-Yu Chang. Pressure barrier of capillary stop valves in micro sample separators. *Sensors and Actuators A: Physical*, 115(2-3):508–515, September 2004.

[88] Jerry M. Chen, Po-Chun Huang, and Mou-Gee Lin. Analysis and experiment of capillary valves for microfluidics on a rotating disk. *Microfluidics and Nanofluidics*, 4(5):427–437, July 2007.

[89] Debapriya Chakraborty, Robert Gorkin, Marc Madou, Lawrence Kulinsky, and Suman Chakraborty. Capillary filling in centrifugally actuated microfluidic devices with dynamically evolving contact line motion. *Journal of Applied Physics*, 105(8):084904, 2009.

[90] Hansang Cho, HY Kim, JY Kang, and Tae Song Kim. Capillary passive valve in microfluidic system. *Technical Proc. of the 2004 NSTI*, 1(3):263–266, 2004.

[91] Hansang Cho, Ho-Young Kim, Ji Yoon Kang, and Tae Song Kim. How the capillary burst microvalve works. *Journal of colloid and interface science*, 306(2):379–85, February 2007.

[92] Eishin Mori, Yoshiaki Komma, Katsuhiko Yasuda, Naoya Hotta, Osamu Imafuji, Atsuo Kikuchi, and Tatsuo Itoh. Digital Versatile Disc Read-Only Disc, Rewritable Disc and Compact Disc Compatible Optical Pickup with a Two-Wavelength Laser Diode Unit. *Japanese Journal of Applied Physics*, 41(Part 1, No. 7B):4845–4849, July 2002.

[93] E.-T. Hwu, S.-K. Hung, C.-W. Yang, I.-S. Hwang, and K.-Y. Huang. Simultaneous detection of translational and angular displacements of micromachined elements. *Applied Physics Letters*, 91(22):221908, 2007.

[94] B Hnilicka, a Voda, and H Schroder. Modelling the characteristics of a photodetector in a DVD player. *Sensors and Actuators A: Physical*, 120(2):494–506, May 2005.

[95] Yi-Cheng Liu, Kuang-Chao Fan, Chih-Liang Chu, Christian Andreas Werner, and Gerd Jäger. Development of an optical accelerometer for low-frequency vibration using the voice coil on a DVD pickup head. *Measurement Science and Technology*, 19(8):084012, August 2008.

[96] Kuang-Chao Fan, Chih-Liang Chu, and Jong-I Mou. Development of a low-cost autofocusing probe for profile measurement. *Measurement Science and Technology*, 12(12):2137–2146, December 2001.

[97] Kuang-Chao Fan, Chih-Liang Chu, Jarn-Lien Liao, and Jong-I Mou. Development of a high-precision straightness measuring system with DVD pick-up head. *Measurement Science and Technology*, 14(1):47–54, January 2003.

[98] N Scuor, P Gallina, O Sbaizero, H V Panchawagh, and R L Mahajan. Dynamic characterization of MEMS cantilevers in liquid environment using a low-cost optical system. *Measurement Science and Technology*, 17(1):173–180, January 2006.

[99] C. During, S. Andersson, and J. Wilkander. Non-contact absolute position measurement using a compact disc player optical pick-up. *Sensors and Actuators A: Physical*, 32(1-3):575–581, April 1992.

[100] Jos Benschop and Gerard Van Rosmalen. Confocal compact scanning optical microscope based on compact disc technology. *Applied optics*, 30(10):1179–1184, 1991.

[101] a Bartoli, P Poggi, F Quercioli, and B Tiribilli. Fast one-dimensional profilometer with a compact disc pickup. *Applied optics*, 40(7):1044–8, March 2001.

[102] Klaus Ehrmann, Arthur Ho, and Klaus Schindhelm. A 3D optical profilometer using a compact disc reading head. *Measurement Science and Technology*, 9(8):1259–1265, August 1998.

[103] S. Kostner and M. J. Vellekoop. DVD pickup heads for optical measurement applications. *Elektrotechnik & Informationstechnik*, 125(3):98–101, March 2008.

[104] F. Quercioli, B. Tiribilli, C. Ascoli, P. Baschieri, and C. Frediani. Monitoring of an atomic force microscope cantilever with a compact disk pickup. *Review of Scientific Instruments*, 70(9):3620, 1999.

[105] En-Te Hwu. Design and Development of a Multiaxial Astigmatic Displacement Measuring System. *PhD Thesis - Institute of Mechanical Engineering National Taiwan University*, 2004.

[106] En-Te Hwu, Kuang-Yuh Huang, Shao-Kang Hung, and Ing-Shouh Hwang. Measurement of Cantilever Displacement Using a Compact Disk/Digital Versatile Disk Pickup Head. *Japanese Journal of Applied Physics*, 45(No. 3B):2368–2371, March 2006.

[107] Kuang-Yuh Huang, En-Te Hwu, and Chow Hsin-Yi. Develpment of an optical pickup system for measuring the displacement of the micro cantilever in scanning probe microscope. *Proceeding of International conference on Mechatronics*, pages 695–698, 2005.

[108] En-Te Hwu, Hsien-Shun Liao, Filippo G. Bosco, Ching-Hsiu Chen, Stephan Sylvest Keller, Anja Boisen, and Kuang-Yuh Huang. An Astigmatic Detection System for Polymeric Cantilever-Based Sensors. *Journal of Sensors*, 2012:1–7, 2012.

[109] Stephan Keller, Gabriela Blagoi, Michael Lillemose, Daniel Haefliger, and Anja Boisen. Processing of thin SU-8 films. *Journal of Micromechanics and Microengineering*, 18(12):125020, December 2008.

[110] Stephan Keller, Daniel Haefliger, and Anja Boisen. Fabrication of thin SU-8 cantilevers: initial bending, release and time stability. *Journal of Micromechanics and Microengineering*, 20(4):045024, April 2010.

[111] H. Lorenz, M. Despont, N. Fahrni, N. LaBianca, P. Renaud, and P. Vettiger. SU-8: a low-cost negative resist for MEMS. *Journal of Micromechanics and Microengineering*, 7:121, 1997.

[112] Gabriela Voskerician, Matthew S. Shive, Rebecca S. Shawgo, Horst Von Recum, James M. Anderson, Michael J. Cima, and Robert Langer. Biocompatibility and biofouling of MEMS drug delivery devices. *Biomaterials*, 24(11):1959–1967, May 2003.

[113] R.J. Jackman, T.M. Floyd, R. Ghodssi, M.A. Schmidt, and K.F. Jensen. Microfluidic systems with on-line UV detection fabricated in photodefinable epoxy. *Journal of Micromechanics and microengineering*, 11:263, 2001.

[114] W. Hu, B. Yang, C. Peng, and S. W. Pang. Three-dimensional SU-8 structures by reversal UV imprint. *Journal of Vacuum Science & Technology B: Microelectronics and Nanometer Structures*, 24(5):2225, 2006.

[115] Alvaro Mata, Aaron J Fleischman, and Shuvo Roy. Characterization of polydimethylsiloxane (PDMS) properties for biomedical micro/nanosystems. *Biomedical microdevices*, 7(4):281–93, December 2005.

[116] G M Whitesides, E Ostuni, S Takayama, X Jiang, and D E Ingber. Soft lithography in biology and biochemistry. *Annual review of biomedical engineering*, 3:335–73, January 2001.

[117] J.C. McDonald, D.C. Duffy, J.R. Anderson, D.T. Chiu, H. Wu, O.J.A. Schueller, and G.M. Whitesides. Fabrication of microfluidic systems in poly (dimethylsiloxane). *Electrophoresis*, 21(1):27–40, 2000.

[118] John F Ashley, Neil B Cramer, Robert H Davis, and Christopher N Bowman. Soft-lithography fabrication of microfluidic features using thiol-ene formulations. *Lab on a chip*, 11(16):2772–8, August 2011.

[119] Xiao-Mei Zhao, Younan Xia, and George M. Whitesides. Soft lithographic methods for nano-fabrication. *Journal of Materials Chemistry*, 7(7):1069–1074, 1997.

[120] Holger Becker and Laurie E Locascio. Polymer microfluidic devices. *Talanta*, 56(2):267–87, February 2002.

[121] G. M. Davis, M. C. Gower, C. Fotakis, T. Efthimiopoulos, and P. Argyrakis. Spectroscopic studies of ArF laser photoablation of PMMA. *Applied Physics A Solids and Surfaces*, 36(1):27–30, January 1985.

[122] Ji-Yen Cheng, Cheng-Wey Wei, Kai-Hsiung Hsu, and Tai-Horng Young. Direct-write laser micromachining and universal surface modification of PMMA for device development. *Sensors and Actuators B: Chemical*, 99(1):186–196, April 2004.

[123] C Friedrich. Micromilling development and applications for microfabrication. *Microelectronic Engineering*, 35(1-4):367–372, February 1997.

[124] Stephan S. Keller. Fabrication of an autonomous surface stress sensor with the polymer SU-8. *PhD Thesis*, 2008.

[125] W Petasch, K. Baumgartner, E. Rauchle, and M Walker. Influence of plasma surface treatment on the adhesion of thin films on metals. *Surface and Coatings Technology*, 59(1-3):301–305, 1993.

[126] P Leech. Reactive ion etching of quartz and silica-based glasses in CF4/CHF3 plasmas. *Vacuum*, 55(3-4):191–196, December 1999.

[127] R. Maboudian. Surface processes in MEMS technology. *Surface Science Reports*, 30(6-8):207–269, 1998.

[128] Han-Hyoung Kim, Se-Geun Park, El-Hang Lee, Seung-Gol Lee, and Beom-Hoan O. Durability of nitrided fluorocarbon polymer films for nanoimprint lithography. *Thin Solid Films*, 519(16):5490–5493, June 2011.

[129] R. M. Ahmed. Optical Study on Poly(methyl methacrylate)/Poly(vinyl acetate) Blends. *International Journal of Photoenergy*, 2009:1–7, 2009.

[130] R Srinivasan. Ablation of polymethyl methacrylate films by pulsed (ns) ultraviolet and infrared (9.17 mm) lasers: A comparative study by ultrafast imaging. *Journal of applied physics*, 73(6):2743–2750, 1993.

[131] Henning Klank, Jorg P Kutter, and Oliver Geschke. CO(2)-laser micromachining and back-end processing for rapid production of PMMA-based microfluidic systems. *Lab on a chip*, 2(4):242–6, November 2002.

[132] H Becker and U. Heim. Hot embossing as a method for the fabrication of polymer high aspect ratio structures. *Sensors and Actuators A: Physical*, 83(1-3):130–135, May 2000.

[133] Holger Becker, Wolfram Dietz, and Peter Dannberg. Microfluidic manifolds by polymer hot embossing for mTAS applications. In *Micro total analysis systems' 98: proceedings of the [Mu] TAS'98 Workshop, held in Banff, Canada, 13-16 October 1998*, page 253. Kluwer Academic Publishers, 1998.

[134] Xavi Illa, Olga Ordeig, Detlef Snakenborg, Albert Romano-Rodríguez, Richard G Compton, and Jörg P Kutter. A cyclo olefin polymer microfluidic chip with integrated gold microelectrodes for aqueous and non-aqueous electrochemistry. *Lab on a chip*, 10(10):1254–61, May 2010.

[135] Pedro S. Nunes, Pelle D. Ohlsson, Olga Ordeig, and Jörg P. Kutter. Cyclic olefin polymers: emerging materials for lab-on-a-chip applications. *Microfluidics and Nanofluidics*, 9(2-3):145–161, April 2010.

[136] J Mecomber, D Hurd, and P Limbach. Enhanced machining of micron-scale features in microchip molding masters by CNC milling. *International Journal of Machine Tools and Manufacture*, 45(12-13):1542–1550, October 2005.

[137] Holger Becker and Claudia Gärtner. Polymer microfabrication technologies for microfluidic systems. *Analytical and bioanalytical chemistry*, 390(1):89–111, January 2008.

[138] D Snakenborg, G Perozziello, H Klank, O Geschke, and J P Kutter. Direct milling and casting of polymer-based optical waveguides for improved transparency in the visible range. *Journal of Micromechanics and Microengineering*, 16(2):375–381, February 2006.

[139] V. S. Sooraj and Jose Mathew. An experimental investigation on the machining characteristics of microscale end milling. *The International Journal of Advanced Manufacturing Technology*, 56(9-12):951–958, March 2011.

[140] M González, L a Bagatolli, I Echabe, J L Arrondo, C E Argaraña, C R Cantor, and G D Fidelio. Interaction of biotin with streptavidin. Thermostability and conformational changes upon binding. *The Journal of biological chemistry*, 272(17):11288–94, April 1997.

[141] Hao Zhang, Wei Pang, Mong S. Marma, Chuang-Yuan Lee, Sanat Kamal-Bahl, Eun Sok Kim, and Charles E. McKenna. Label-free detection of protein-ligand interactions in real time using micromachined bulk acoustic resonators. *Applied Physics Letters*, 96(12):123702, 2010.

[142] Montserrat Calleja, Javier Tamayo, Maria Nordstrom, and Anja Boisen. Low-noise polymeric nanomechanical biosensors. *Applied Physics Letters*, 88(11):113901, 2006.

[143] H Butt. A Sensitive Method to Measure Changes in the Surface Stress of Solids. *Journal of Colloid and Interface Science*, 180(1):251–260, June 1996.

[144] B.Y. Shew, Y.C. Cheng, and Y.H. Tsai. Monolithic SU-8 micro-interferometer for biochemical detections. *Sensors and Actuators A: Physical*, 141(2):299–306, February 2008.

[145] Wenmiao Shu, Ernest D Laue, and Ashwin a Seshia. Investigation of biotin-streptavidin binding interactions using microcantilever sensors. *Biosensors and Bioelectronics*, 22(9-10):2003–9, April 2007.

[146] F. G. Bosco, En-Te Hwu, Ching-Hsiu Chen, Stephan Keller, Michael Bache, Mogens H Jakobsen, Ing-Shouh Hwang, and Anja Boisen. High throughput label-free platform for statistical bio-molecular sensing. *Lab on a chip*, 11(14):2411–2416, May 2011.

[147] B Ghebrehiwet, S Bossone, a Erdei, and K B Reid. Reversible biotinylation of C1q with a cleavable biotinyl derivative. Application in C1q receptor (C1qR) purification. *Journal of immunological methods*, 110(2):251–60, June 1988.

[148] Erland Björklund, Gitte Gotholdt Anskjæ r, Martin Hansen, Bjarne Styrishave, and Bent Halling-Sø rensen. Analysis and environmental concentrations of the herbicide dichlobenil and its main metabolite 2,6-dichlorobenzamide (BAM): a review. *The Science of the total environment*, 409(12):2343–56, May 2011.

[149] Liselotte Clausen, Flemming Larsen, and Hans-Jø rgen Albrechtsen. Sorption of the herbicide dichlobenil and the metabolite 2,6-dichlorobenzamide on soils and aquifer sediments. *Environmental science & technology*, 38(17):4510–8, September 2004.

[150] L Bruun, C Koch, B Pedersen, M H Jakobsen, and J Aamand. A quantitative enzyme-linked immunoassay for the detection of 2, 6-dichlorobenzamide (BAM), a degradation product of the herbicide dichlobenil. *Journal of immunological methods*, 240(1-2):133–42, June 2000.

[151] Michael Lachut and John Sader. Effect of Surface Stress on the Stiffness of Cantilever Plates. *Physical Review Letters*, 99(20):1–4, November 2007.

[152] Landmine. Landmine monitor report. In *Human Rights*, number March. Human Rights Watch, 2009.

[153] Yoni Engel, Roey Elnathan, Alexander Pevzner, Guy Davidi, Eli Flaxer, and Fernando Patolsky. Supersensitive detection of explosives by silicon nanowire arrays. *Angewandte Chemie (International ed. in English)*, 49(38):6830–5, September 2010.

[154] L.a. Pinnaduwage and T. Thundat. Moore's law in homeland defense: an integrated sensor platform based on silicon microcantilevers. *IEEE Sensors Journal*, 5(4):774–785, August 2005.

[155] Andrew Freedman, Paul L Kebabian, Ziman Li, Wade a Robinson, and Joda C Wormhoudt. Apparatus for determination of vapor pressures at ambient temperatures employing a Knudsen effusion cell and quartz crystal microbalance. *Measurement Science and Technology*, 19(12):125102, December 2008.

[156] G.W. Watson and D. McGuire. Detection of Explosives in Soil and Water with an Electronic Nose. In *Proceedings of the American Chemical Society Meeting, Ontario, CA October*, pages 5–7, 1999.

[157] Dhesingh Ravi Shankaran, Kiyoshi Matsumoto, Kiyoshi Toko, and Norio Miura. Development and comparison of two immunoassays for the detection of 2,4,6-trinitrotoluene (TNT) based on surface plasmon resonance. *Sensors and Actuators B: Chemical*, 114(1):71–79, March 2006.

[158] Anderson Lin and Eun Sok Kim. Selectivity and Long-Term Reliability of Resonant Explosive-Vapor-Trace Detection based on Antigen-Antibody Binding. *IEEE 22nd International Conference on Micro Electro Mechanical Systems*, pages 316–319, January 2009.

[159] E Goldman. Selection of phage displayed peptides for the detection of 2,4,6-trinitrotoluene in seawater. *Analytica Chimica Acta*, 457(1):13–19, April 2002.

[160] Jung Su Park, Franck Le Derf, Christopher M Bejger, Vincent M Lynch, Jonathan L Sessler, Kent a Nielsen, Carsten Johnsen, and Jan O Jeppesen. Positive homotropic allosteric receptors for neutral guests: annulated tetrathiafulvalene-calix[4]pyrroles as colorimetric chemosensors for nitroaromatic explosives. *Chemistry*, 16(3):848–54, January 2010.

[161] Erol Erça, Ayem Uzer, and Reat Apak. Selective spectrophotometric determination of TNT using a dicyclohexylamine-based colorimetric sensor. *Talanta*, 78(3):772–80, May 2009.

[162] N V Kostesha, T S Alstrom, C Johnsen, K A Nilesen, J O Jeppesen, J Larsen, M H Jakobsen, and A Boisen. Development of the colorimetric sensor array for detection of explosives and volatile organic compounds in air. In *SPIE conference proceeding - Methods*, volume 7673, pages 76730I–76730I–9, 2010.

[163] Ying Jiang, Hong Zhao, Ningning Zhu, Yuqing Lin, Ping Yu, and Lanqun Mao. A simple assay for direct colorimetric visualization of trinitrotoluene at picomolar levels using gold nanoparticles. *Angewandte Chemie*, 47(45):8601–4, January 2008.

[164] Weibin Zhu, Jung Su Park, Jonathan L. Sessler, and Angelo Gaitas. A colorimetric receptor combined with a microcantilever sensor for explosive vapor detection. *Applied Physics Letters*, 98(12):123501, 2011.

[165] S Berner, S Biela, G Ledung, a Gogoll, J Backvall, C Puglia, and S Oscarsson. Activity boost of a biomimetic oxidation catalyst by immobilization onto a gold surface. *Journal of Catalysis*, 244(1):86–91, November 2006.

[166] D.L. Robertson and G.F. Joyce. Selection in vitro of an RNA enzyme that specifically cleaves single-stranded DNA. *Nature*, 344(6265):467–468, 1990.

[167] AD Ellington. Selection in vitro of single-stranded DNA molecules that fold into specific ligand-binding structures. *Nature*, 355:850–852, 1992.

[168] Craig Tuerk. Systematic evolution of ligands by exponential enrichment: RNA ligands to bacteriophage T4 DNA polymerase. *Science*, 249(4968):505–510, 1990.

[169] Thomas G McCauley, Nobuko Hamaguchi, and Martin Stanton. Aptamer-based biosensor arrays for detection and quantification of biological macromolecules. *Analytical Biochemistry*, 319(2):244–250, August 2003.

[170] M Lee and D R Walt. A fiber-optic microarray biosensor using aptamers as receptors. *Analytical biochemistry*, 282(1):142–6, June 2000.

[171] ThaiHuu Nguyen, John P. Hilton, and Qiao Lin. Emerging applications of aptamers to micro- and nanoscale biosensing. *Microfluidics and Nanofluidics*, 6(3):347–362, January 2009.

[172] Kun Han, Zhiqiang Liang, and Nandi Zhou. Design Strategies for Aptamer-Based Biosensors. *Sensors*, 10(5):4541–4557, May 2010.

[173] Shiping Song, Lihua Wang, Jiang Li, Chunhai Fan, and Jianlong Zhao. Aptamer-based biosensors. *Trends in Analytical Chemistry*, 27(2):108–117, February 2008.

[174] Beate Strehlitz, Nadia Nikolaus, and Regina Stoltenburg. Protein Detection with Aptamer Biosensors. *Sensors*, 8(7):4296–4307, July 2008.

[175] M Minunni, S Tombelli, A Gullotto, E Luzi, and M Mascini. Development of biosensors with aptamers as bio-recognition element: the case of HIV-1 Tat protein. *Biosensors and bioelectronics*, 20(6):1149–56, December 2004.

[176] Michael Liss, Birgit Petersen, Hans Wolf, and Elke Prohaska. An aptamer-based quartz crystal protein biosensor. *Analytical chemistry*, 74(17):4488–95, September 2002.

[177] Zhuangzhi Wang, Thomas Wilkop, Danke Xu, Yi Dong, Guangyu Ma, and Quan Cheng. Surface plasmon resonance imaging for affinity analysis of aptamer-protein interactions with PDMS microfluidic chips. *Analytical and bioanalytical chemistry*, 389(3):819–25, October 2007.

[178] S Tombelli, M Minunni, E Luzi, and M Mascini. Aptamer-based biosensors for the detection of HIV-1 Tat protein. *Bioelectrochemistry*, 67(2):135–41, October 2005.

[179] Cagri a Savran, Scott M Knudsen, Andrew D Ellington, and Scott R Manalis. Micromechanical detection of proteins using aptamer-based receptor molecules. *Analytical chemistry*, 76(11):3194–8, June 2004.

[180] Sang-myung Lee, Jun Hwan Choi, Kyo Seon Hwang, and Sang Kyung Kim. Microcantilever-based thrombin detection using a structure-switching aptamer as the receptor molecule. *Thirteenth International Conference on Miniaturized Systems for Chemistry and Life Sciences*, 1:1374–1376, 2009.

[181] S.D. Jayasena. Aptamers: an emerging class of molecules that rival antibodies in diagnostics. *Clinical Chemistry*, 45(9):1628, September 1999.

[182] R.Y. Lai, K.W. Plaxco, and A.J. Heeger. Aptamer-based electrochemical detection of picomolar platelet-derived growth factor directly in blood serum. *Analytical chemistry*, 79(1):229–233, 2007.

[183] Yong Huang, Xin-Min Nie, Shao-Long Gan, Jian-Hui Jiang, Guo-Li Shen, and Ru-Qin Yu. Electrochemical immunosensor of platelet-derived growth factor with aptamer-primed polymerase amplification. *Analytical biochemistry*, 382(1):16–22, November 2008.

[184] Wei Liao and Xinyan Tracy Cui. Reagentless aptamer based impedance biosensor for monitoring a neuro-inflammatory cytokine PDGF. *Biosensors and Bioelectronics*, 23(2):218–24, September 2007.

[185] a Rahim Ruslinda, Shinya Tajima, Yoko Ishii, Yuichiro Ishiyama, Robert Edgington, and Hiroshi Kawarada. Aptamer-based biosensor for sensitive PDGF detection using diamond transistor. *Biosensors and Bioelectronics*, 26(4):1599–604, December 2010.

[186] Shih-Ju Chen, Chih-Ching Huang, and Huan-Tsung Chang. Enrichment and fluorescence enhancement of adenosine using aptamer-gold nanoparticles, PDGF aptamer, and Oligreen. *Talanta*, 81(1-2):493–8, April 2010.

[187] Jing Wang, Wenying Meng, Xiaofeng Zheng, Shanli Liu, and Genxi Li. Combination of aptamer with gold nanoparticles for electrochemical signal amplification: application to sensitive detection of platelet-derived growth factor. *Biosensors and Bioelectronics*, 24(6):1598–602, February 2009.

[188] Chih-Ching Huang, Sheng-Hsien Chiu, Yu-Fen Huang, and Huan-Tsung Chang. Aptamer-functionalized gold nanoparticles for turn-on light switch detection of platelet-derived growth factor. *Analytical chemistry*, 79(13):4798–804, July 2007.

[189] B Wang, F Huang, and TH Nguyen. Microcantilever-based label-free thermal characterization of biomolecular affinity binding. *IEEE MEMS Micro Electro Mechanical Systems*, (8):20–20, 2010.

[190] Subramanian Balamurugan, Anne Obubuafo, Steven a Soper, and David a Spivak. Surface immobilization methods for aptamer diagnostic applications. *Analytical and bioanalytical chemistry*, 390(4):1009–21, February 2008.

[191] Lizbeth Hedstrom. Serine protease mechanism and specificity. *Chemical reviews*, 102(12):4501–24, December 2002.

[192] Nadia Harbeck, Ronald E Kates, Katja Gauger, Amina Willems, Marion Kiechle, Viktor Magdolen, and Manfred Schmitt. Urokinase-type plasminogen activator (uPA) and its inhibitor PAI-I: novel tumor-derived factors with a high prognostic and predictive impact in breast cancer. *Thrombosis and haemostasis*, 91(3):450–6, March 2004.

[193] Daniel Miotto Dupont, Jeppe Buur Madsen, Roland Karl Hartmann, Bertrand Tavitian, Frédéric Ducongé, Jø rgen Kjems, and Peter André Andreasen. Serum-stable RNA aptamers to urokinase-type plasminogen activator blocking receptor binding. *RNA (New York, N.Y.)*, 16(12):2360–9, December 2010.

[194] Bernd R Binder, Günter Christ, Florian Gruber, Nelly Grubic, Peter Hufnagl, Michael Krebs, Judit Mihaly, and Gerald W Prager. Plasminogen activator inhibitor 1: physiological and pathophysiological roles. *News in physiological sciences*, 17:56–61, April 2002.

[195] J. Fritz. Translating Biomolecular Recognition into Nanomechanics. *Science*, 288(5464):316–318, April 2000.

Appendix A

List of Publications

Refereed Journal Articles

- F. G. Bosco, M. Bache, E.-T. Hwu, C.H. Chen, K. A. Nielsen, S. S. Keller, J. O. Jeppesen , I.-S. Hwang and A. Boisen, *Statistical detection of the explosives DNT using functionalized microcantilever sensors*, **Sensors and Actuators: B**, SUBMITTED

- E.-T. Hwu, H.-S. Liao, F. G. Bosco, C.-H. Chen, S. S. Keller, A. Boisen and K.-Y. Huang, *An Astigmatic Detection System for Polymeric Cantilever-Based Sensors*, **Journal of Sensors** 2012, 1-7 (2012)

- F. G. Bosco, E.-T. Hwu, C.-H. Chen, S. Keller, M. Bache, M. H. Jakobsen, I.-S. Hwang and A. Boisen, *High throughput label-free platform for statistical biomolecular sensing*, **Lab Chip** 11 (14), 2411-2416 (2011)

- F. G. Bosco, H.-T. Hwu, S. Keller, A. Greve and A. Boisen, *Self aligned cantilever positioning for on-substrate measurements using DVD pickup head*, **Microelectronics Engineering** 87, 708-711 (2010)

Conference Proceedings

- F. G. Bosco, J. Yang, C. H. Chen, E.-T. Hwu, S. S. Keller, M. Bache, Q. Lin and A. Boisen, 36th IEEE MEMS conference, *Micromechanical aptasensor-based proteins detection using a compact-disc format microfluidics system*, **36th IEEE MEMS conference**, (2012)

- F. G. Bosco, C. H. Chen, E.-T. Hwu, M. Bache, S. Keller and A. Boisen, *High-throughput automated system for statistical biosensing employing microcantilever arrays*, **35th IEEE MEMS conference**, 877-880 (2011)

- M. S. Schmidt, N. Kostesha, F. G. Bosco, J. K. Olsen, J. C. Nielsen, J. O. Jeppesen, T. S. Alstrom, J. Larsen, T. Thundat, M. H. Jakobsen and A. Boisen, *Xsense* -

a miniaturised multi-sensor platform for explosives detection, **SPIE Micro- and Nanotechnology Sensors, Systems, and Applications III**, 8031, (2011)

- F. G. Bosco, E.-T. Hwu and A Boisen, *High throughput readout system for cantilever-based sensing of explosive compounds*, **SPIE Micro- and Nanotechnology Sensors, Systems, and Applications II** 7679, 767925 (2010)

- M. S. Schmidt, N. Kostesha, F. G. Bosco, J. Olesen, J. Carsten, K. A. Nielsen, J. O. Jeppesen, J. Oskar, T. S. Sonne, J. Larsen, M. H. Jakobsen, T. Thundat, A. Boisen, *Xsense: Using nanotechnology to combine detection methods for high sensitivity handheld explosives detectors*, **SPIE Detection and Sensing of Mines, Explosive Objects and Obscure Targets XV** 7664, 76641H (2010)

Conference Contributions

- F. G. Bosco, C. H. Chen, E.-T. Hwu, M. Bache, S. Keller and A. Boisen, *Rotating microcantilever array platform for high-throughput statistical biosensing*, **International Workshop on Nanomechanical Sensing 2011**, Dublin, IE (Talk)

- F. G. Bosco, C. H. Chen, E.-T. Hwu, M. Bache, S. Keller and A. Boisen, *High-throughput automated system for statistical biosensing employing microcantilever arrays*, **IEEE MEMS 2011**, Cancun, MX (Poster)

- F. G. Bosco, E.-T. Hwu, C. H. Chen, S. Keller and A. Boisen, *Fully automated readout system for parallel characterization of microcantilever arrays using DVD-ROM pickup heads*, **Micro-Nano Engineering 2010**, Genova, IT (Talk).

- F. G. Bosco, E.-T. Hwu and A. Boisen, *High-throughput readout system for cantilever-based sensing of explosive compounds*, **SPIE Defense, Security, and Sensing: Materials, Systems, and Devices 2010**, Orlando, FL, US (Poster).

- F. G. Bosco, E.-T. Hwu, S. Keller and A. Boisen, *Self aligned cantilever positioning for on-substrate measurements using DVD optical pickup head*, **Micro-Nano Engineering 2009**, Ghent, BE (Poster).

- F. G. Bosco, J. Kennet Olsen, M Schmidt, N. Kosheka and A. Boisen, *Integrating nanotechnology for explosive detection*, **Danish Physical Society 2009**, Copenhagen, DK (Talk).

- J. Kennet Olsen, F. G. Bosco, M Schmidt, N. Kosheka, A. Boisen, *The Xsense project*, **COMS 2009**, Copenhagen, DK (Best poster award).

Appendix B

SU-8 Discs cleanroom processes

Disc V1-A

Step	Description	Equipment	Program/Parameters	Remarks
1	WAFER PRE-CLEANING			
1.1	Stock out			
1.2	Pyrex cleaning		See remark	
2	SU-8 FIRST LAYER SPINNING			
2.1	SU-8 spin-coating	Z3/KS Spinner	1000rpm, 30s, 100rpm/s; 2500 rpm, 60s, 100rpm/s	SU-8 2075; 6s; 42psi; Gyrset
2.2	SU-8 soft-bake	Z3/Hotplate	4h, 50ºC, 2ºC/min	
3	SU-8 FIRST LAYER PHOTOLITHOGRAPHY			
3.1	SU-8 exposure	Z3/KS Aligner	2x250 mJ/cm2; soft contact	
3.2	Post-exposure bake	Z3/Hotplate	6h, 50ºC, 2ºC/min	
4	SU-8 SECOND LAYER SPINNING			
4.1	SU-8 spin-coating	Z3/KS Spinner	500rpm, 30s, 100rpm/s; 1250rpm, 60s, 100rpm/s	SU-8 2150; 40s; 42psi; Gyrset
4.2	SU-8 soft-bake	Z3/Hotplate	14h, 50ºC, 2ºC/min	over night
5	SU-8 SECOND LAYER PHOTOLITHOGRAPHY			
5.1	SU-8 exposure	Z3/KS Aligner	4x250mJ/cm2, sub 900µm, al 150µm, exp 100µm	GlobalWEC, Prox;
5.2	Post-exposure bake	Z3/Hotplate2	12h, 50ºC, 2ºC/min	over night
6	SU-8 DEVELOPEMENT			
6.1	SU-8 development	Z3/Developer	20min FIRST, 20min FINAL	PGMEA
6.2	Rinse	Z3/Developer	Isopropanol, Air	
7	THICKNESS INSPECTION			
7.1	Thickness	Z9/Dektak		
7.2	SEM inspection	SEM-JEOL	tilt 35º, voltage 1kV	

Disc V1-B

Step	Description	Equipment	Program/Parameters	Remarks
1	GETTING STARTED			
1.1	wafer	quartz wafer		Fused silica wafer 0.5 mm
1.2	wafer preprocess	HDMS	standard recipe	
2	CALIBRATION PATTERN LITHOGRAPHY			
2.1	Spinning	Track1	1.5_bake	
2.2	Exposure	KS aligner	1x70 mJ/cm2; hard contact	10 s exp. BackSide Microscope
2.3	Development	AZ devloper	100 s	
2.4	SIO2 etch	RIE1	fibo_ox - 22 min	
2.5	AZ removal	Plasma asher	10 min	
3	METAL LAYER LITHOGRAPHY			
3.1	First Exposure	KS aligner	1x35 mJ/cm2; hard contact	5 s exp. BackSide Microscope
3.2	Post-exposure bake	120 C hotplate	110 s	
3.3	Flood exposure	KS Aligner	1x210 mJ/cm2	30 s maskless exposure
3.4	Development	AZ devloper	100 s	Shaking
3.5	Metal deposition	Wordentec	dep rate = 10 A/s	
3.6	Liftoff	Liftoff bath	15 min with U-sound	1s pulse - 20s break
4	SU-8 LITHOGRAPHY			
4.1	SU-8 spin-coating	Z3/KS Spinner	1000rpm, 30s, 100rpm/s; 2500 rpm, 60s, 100rpm/s	SU-8 2075; 6s; 42psi; Gyrset
4.2	SU-8 soft-bake	Z3/Hotplate	4h, 50ºC, 2ºC/min	
4.3	SU-8 exposure	Z3/KS Aligner	2x250 mJ/cm2; soft contact	
4.4	Post-exposure bake	Z3/Hotplate	6h, 50ºC, 2ºC/min	
4.5	SU-8 spin-coating	KS Spinner	500rpm, 30s, 100rpm/s; 1250rpm, 60s, 100rpm/s	SU-8 2150; 40s; 42psi; Gyrset
4.6	SU-8 soft-bake	Hotplate	14h, 50ºC, 2ºC/min	over night
4.7	SU-8 exposure	KS Aligner	4x250mJ/cm2, sub 1100µm, al 150µm, exp 100µm	GlobalWEC, Prox;
4.8	Post-exposure bake	Hotplate2	12h, 50ºC, 2ºC/min	over night
4.9	SU-8 development	Z3/Developer	40min FIRST, 40min FINAL	
4.1	Rinse	Z3/Developer	Isopropanol, Air	
5	INSPECTION			
5.1	Thickness	Z9/Dektak		

Disc V2-A

Step	Description	Equipment	Program/Parameters	Remarks
1	WAFER PRE-CLEANING			
1.1	Stock out			
1.2	Pyrex cleaning		See remark	dehydratation bake at 250 C - 5 h
2	SU-8 FIRST LAYER SPINNING			
2.1	SU-8 spin-coating	Z3/KS Spinner	1000rpm, 30s, 100rpm/s; 2500 rpm, 60s, 100rpm/s	SU-8 2075; 6s; 42psi; Gyrset
2.2	SU-8 soft-bake	Z3/Hotplate	4h, 50ºC, 2ºC/min	
3	SU-8 FIRST LAYER PHOTOLITHOGRAPHY			
3.1	SU-8 exposure	Z3/KS Aligner	2x250 mJ/cm2; soft contact	
3.2	Post-exposure bake	Z3/Hotplate	6h, 50ºC, 2ºC/min	
4	SU-8 SECOND LAYER SPINNING			
4.1	SU-8 spin-coating	Z3/KS Spinner	500rpm, 30s, 100rpm/s; 1250rpm, 60s, 100rpm/s	SU-8 2150; 40s; 42psi; Gyrset
4.2	SU-8 soft-bake	Z3/Hotplate	14h, 50ºC, 2ºC/min	over night
5	SU-8 SECOND LAYER PHOTOLITHOGRAPHY			
5.1	SU-8 exposure	Z3/KS Aligner	4x250mJ/cm2, sub 900µm, al 150µm, exp 100µm	GlobalWEC, Prox;
5.2	Post-exposure bake	Z3/Hotplate2	12h, 50ºC, 2ºC/min	over night
6	SU-8 THIRD LAYER SPINNING			
6.1	SU-8 spin-coating	Z3/KS Spinner	500rpm, 30s, 100rpm/s; 1250rpm, 60s, 100rpm/s	SU-8 2150; 40s; 42psi; Gyrset
6.2	SU-8 soft-bake	Z3/Hotplate	12h, 50ºC, 2ºC/min	over night
7	SU-8 THIRD LAYER PHOTOLITHOGRAPHY			
7.1	SU-8 exposure	Z3/KS Aligner	4x250mJ/cm2, sub 1200µm, al 150µm, exp 100µm	GlobalWEC, Prox;
7.2	Post-exposure bake	Z3/Hotplate2	10h, 50ºC, 2ºC/min	over night
8	SU-8 DEVELOPEMENT			

Disc V2-B

Step	Description	Equipment	Program/Parameters	Remarks
1	WAFER PRE-CLEANING			
1.2	Pyrex cleaning		250 Oven	dehydratation bake at 250 C - 5 h
1.2	wafer preprocess	HDMS	standard recipe	
2	METAL LAYER LITHOGRAPHY			
2.1	Spinning	Track1	PR2_2	
2.2	First Exposure	KS aligner	1x70 mJ/cm2; hard contact - 10 s	10 s exp backside microscope
2.3	Development	AZ devloper	100 s	new developer
2.4	Metal deposition	Wordentec	dep rate = 10 A/s	
2.5	Liftoff	Liftoff bath	ultrasound 15 min	Pulsed - rotate wafers every 5 min
3	SU-8 FIRST LAYER PHOTOLITHOGRAPHY			
3.1	SU-8 spin-coating	Z3/KS Spinner	1000rpm, 30s, 100rpm/s; 2500 rpm, 60s, 100rpm/s	SU-8 2075; 6s; 42psi; Gyrset
3.2	SU-8 soft-bake	Z3/Hotplate	4h, 50ºC, 2ºC/min	
3.3	SU-8 exposure	Z3/KS Aligner	2x250 mJ/cm2; soft contact	
3.4	Post-exposure bake	Z3/Hotplate	6h, 50ºC, 2ºC/min	
4	SU-8 SECOND LAYER PHOTOLITHOGRAPHY			
4.1	SU-8 spin-coating	Z3/KS Spinner	500rpm, 30s, 100rpm/s; 1250rpm, 60s, 100rpm/s	SU-8 2150; 40s; 42psi; Gyrset
4.2	SU-8 soft-bake	Z3/Hotplate	14h, 50ºC, 2ºC/min	over night
4.3	SU-8 exposure	Z3/KS Aligner	4x250mJ/cm2, sub 900µm, al 150µm, exp 100µm	GlobalWEC, Prox;
4.4	Post-exposure bake	Z3/Hotplate2	12h, 50ºC, 2ºC/min	over night
5	SU-8 THIRD LAYER PHOTOLITHOGRAPHY			
5.1	SU-8 spin-coating	Z3/KS Spinner	500rpm, 30s, 100rpm/s; 1250rpm, 60s, 100rpm/s	SU-8 2150; 40s; 42psi; Gyrset
5.2	SU-8 soft-bake	Z3/Hotplate	12h, 50ºC, 2ºC/min	over night
5.3	SU-8 exposure	Z3/KS Aligner	4x250mJ/cm2, sub 1200µm, al 150µm, exp 100µm	GlobalWEC, Prox;
5.4	Post-exposure bake	Z3/Hotplate2	10h, 50ºC, 2ºC/min	over night
6	SU-8 DEVELOPEMENT			

Disc V2-C

Step	Description	Equipment	Program/Parameters	Remarks
1	GETTING STARTED			
1.1a	wafer	botrofloat 0.5mm		
1.2	wafer preprocess	HDMS	standard recipe	
2	METAL LAYER LITHOGRAPHY			
2.1	Spinning	Track1	PR2_2	
2.2	First Exposure	KS aligner	1x70 mJ/cm2; hard contact - 10 s	10 s exp backside microscope
2.3	Development	AZ devloper	100 s	new developer
2.4	Metal deposition	Wordentec	dep rate = 10 A/s	scratch in one wafer
2.5	Liftoff	Liftoff bath	ultrasound 15 min	Pulsed - rotate wafers 1h
3	THICK SU-8 LITHOGRAPHY - FOOTPRINT			
3.1	SU-8 spin-coating	KS Spinner	500rpm, 30s, 100rpm/s; 1130rpm, 60s, 100rpm/s	SU-8 2150; 40s; 42psi; NO Gyrset
3.2	SU-8 soft-bake	Hotplate	14h, 50ºC, 2ºC/min	over night
3.3	SU-8 exposure	KS Aligner	4x250mJ/cm2, sub 850µm, al 150µm, exp 100µm	GlobalWEC, Prox;
3.4	Post-exposure bake	Hotplate2	12h, 50ºC, 2ºC/min	over night
4	THICK SU-8 LITHOGRAPHY - CHANNELS			
4.1	SU-8 spin-coating	KS Spinner	500rpm, 30s, 100rpm/s; 1130rpm, 60s, 100rpm/s	SU-8 2150; 40s; 42psi; NO Gyrset
4.2	SU-8 soft-bake	Hotplate	12h, 50ºC, 2ºC/min	
4.3	SU-8 exposure	KS Aligner	4x250mJ/cm2, sub 1150µm, al 150µm, exp 100µm	GlobalWEC, Prox;
4.4	Post-exposure bake	Hotplate2	12h, 50ºC, 2ºC/min	over night
4.5	SU-8 development	Z3/Developer	30min FIRST, 30min FINAL	PGMEA
4.6	Rinse	Z3/Developer	Isopropanol, Air	
5	INSPECTION			
5.1	Thickness	Z9/Dektak		channels-footprints depth

Appendix C

DNT thermal evaporation - dynamic measurements

The chips were placed over a 1 mm large nozzle acting as exhaust for thermally evaporated DNT flow. The cantilevers where oriented with the Au surface facing the nozzle. Three control materials were also evaporated and tested on the sensors: 2,4-Diaminotoluene (DAT), Ammonium nitrate (NH_4NO_3) and Diesel were employed as control sample for testing the performance of the 4 detection principles.
In Figures 7.1 and 7.2 are reported the measured resonance frequency shifts measured over the four samples. 24 TTF functionalized cantilevers and 24 blank ones were measured for each sample, for a total of 192 thermal noise measurements. The measurements were carried out in batch of 48 cantilever per time, three times per day, for four days. Evaporation conditions and exposure time to the gas flow were carefully maintained constant along the 12 experiments.
The chips were exposed to the gas flow for 2 minutes, placed at 1 mm distance from the evaporation nozzle.
In Table 7.1 are reported the 172 resonance frequency shifts measured in the set of thermal evaporation experiments. According to the averaged values listed in Table 7.1, it seems that the evaporation of DAT and ammonium nitrate on the cantilevers do not induce any significant signal. In fact the averaged differential frequency shift between TTF treated and blank cantilevers is of the order of few tens of Hz. Looking at Figure 7.1 is seems clear that no specific trend in the frequency shift is observable.
On the other hand in Figure 7.2 the data show a more evident behavior: the TTF treated cantilevers exposed to DNT gas flow exhibit a strong decrease in the resonance frequency (about 300 Hz), while the blank ones maintain almost unchanged their vibrational properties. This is probably due to a strong binding of DNT molecules on the TTF chemically treated surface.
When exposed to diesel flow however the TTF cantilevers exhibit a very small negative change (about 20 Hz), while the blank ones shift their resonance frequency of an averaged value of 150 Hz, leading to a positive differential averaged shift of 135 Hz. This strange behavior could be attributed to the higher sticking coefficient of diesel particles on the clean Au surface, with respect to the chemically treated TTF coated surfaces.

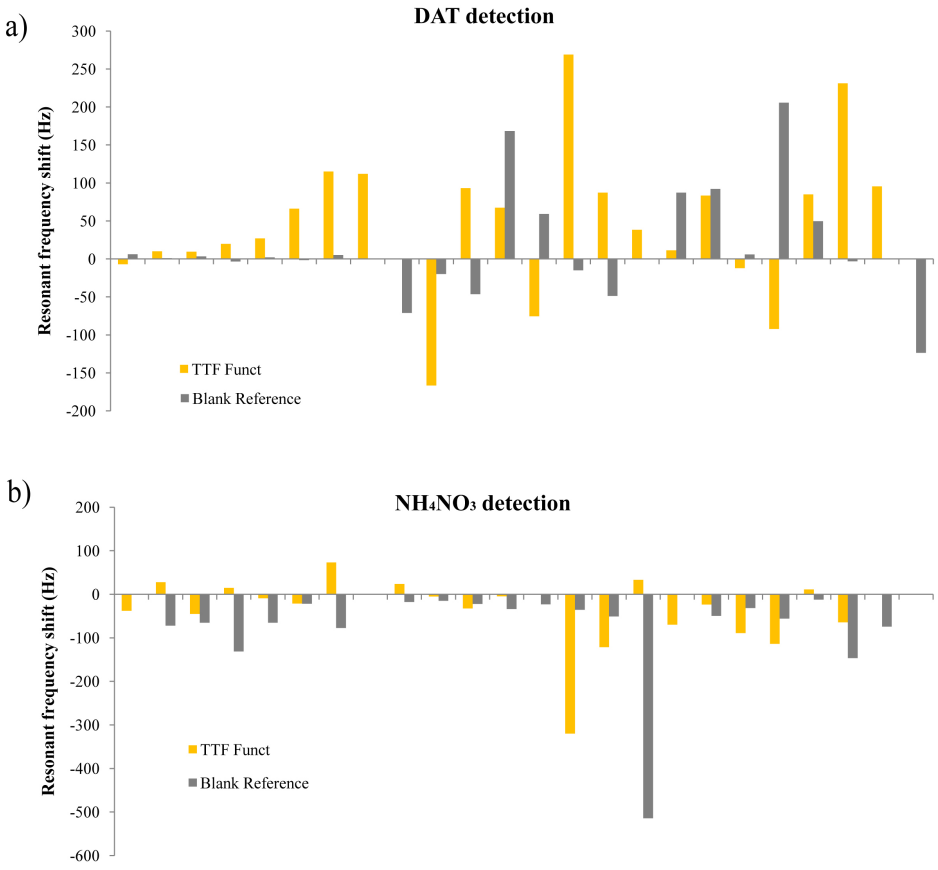

Figure 7.1: Resonance frequency shift for 24 measured TTF coated cantilevers and 24 blank cantilevers after thermal evaporation of a) DAT and b) ammonium nitride. About 8% of the cantilevers could not be measured after the exposure to the gas flow.

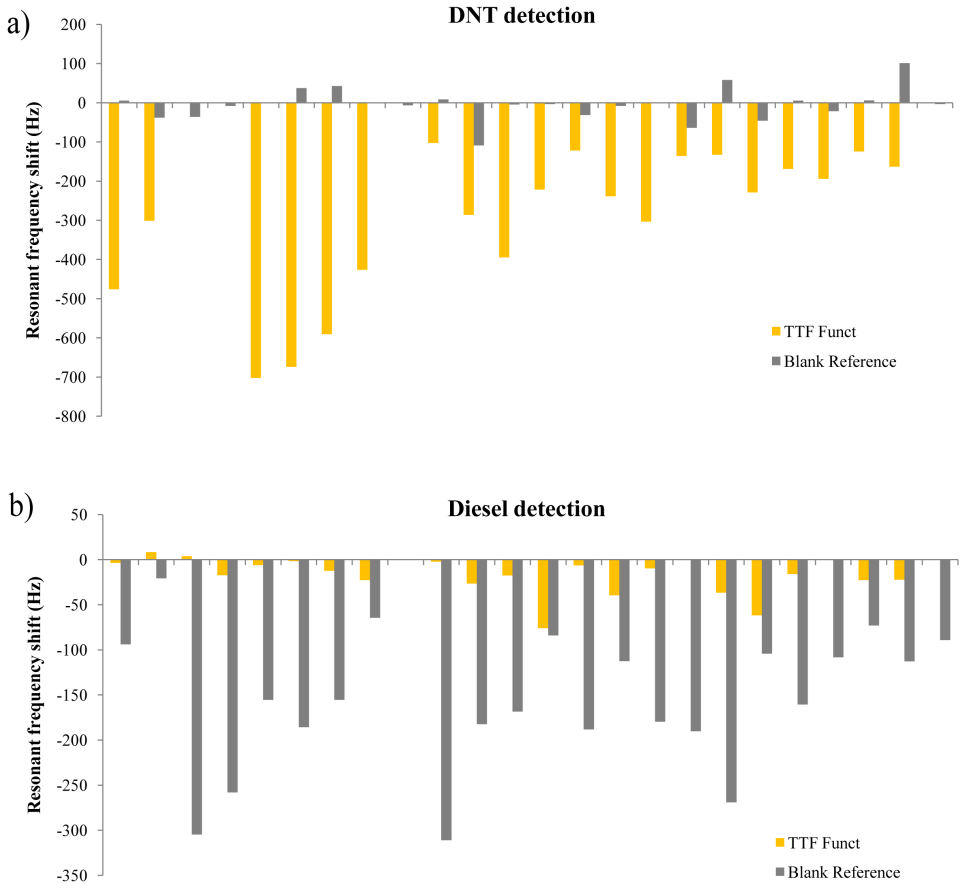

Figure 7.2: Resonance frequency shift for 24 measured TTF coated cantilevers and 24 blank after thermal evaporation of a) DNT and b) diesel. About 15% of the cantilevers could not be measured after the exposure to the gas flow.

Compound	**DAT**		**DNT**		**NH_4NO_3**		**DIESEL**	
Functionalization	TTF	Blank	TTF	Blank	TTF	Blank	TTF	Blank
Frequency shift	(Hz)	(Hz)	(Hz)	(Hz)	(Hz)	(Hz)	(Hz)	(Hz)
Measurement 1	-7.0	6.1	-475.7	5.7	-37.9	n.a.	-3.6	-93.7
Measurement 2	10.2	1.1	-300.9	-37.7	27.7	-72.0	8.3	-20.5
Measurement 3	9.6	3.3	n.a.	-35.9	-44.9	-65.1	3.8	-304.7
Measurement 4	19.9	-3.3	n.a.	-7.7	15.0	-131.3	-17.1	-257.9
Measurement 5	27.2	2.0	-702.0	-1.4	-9.1	-65.3	-5.9	-155.3
Measurement 6	66.2	-1.4	-673.5	37.7	-20.9	-21.4	-1.5	-185.7
Measurement 7	115.1	5.3	-590.7	42.6	73.4	-77.0	-12.3	-155.4
Measurement 8	112.0	-0.1	-426.3	n.a.	n.a.	n.a.	-22.6	-64.4
Measurement 9	n.a.	-71.0	n.a.	-6.5	23.9	-17.3	n.a.	n.a.
Measurement 10	-166.4	-19.9	-102.3	8.8	-4.9	-14.6	-2.2	-311.0
Measurement 11	93.3	-46.3	-285.8	-108.7	-32.5	-21.8	-26.3	-182.3
Measurement 12	67.4	168.5	-394.8	-4.3	-4.4	-33.5	-17.5	-168.3
Measurement 13	-75.3	59.2	-221.2	-3.2	1.0	-22.7	-75.8	-84.0
Measurement 14	269.0	-15.0	-121.9	-31.1	-319.6	-35.3	-6.2	-188.1
Measurement 15	87.2	-48.5	-238.7	-7.9	-121.3	-50.6	-39.5	-112.4
Measurement 16	38.3	0.8	-303.2	n.a.	33.3	-514.1	-9.6	-179.5
Measurement 17	11.5	87.4	-135.5	-63.9	-69.6	n.a.	n.a.	-190.1
Measurement 18	83.4	92.1	-132.4	58.2	-23.3	-49.6	-36.6	-268.9
Measurement 19	-12.0	6.0	-228.7	-45.7	-89.0	-31.2	-61.7	-104.2
Measurement 20	-92.0	205.7	-168.9	5.5	-113.6	-55.5	-15.9	-160.4
Measurement 21	84.9	49.7	-194.1	-21.6	11.4	-12.2	n.a.	-108.1
Measurement 22	231.1	-3.1	-124.4	6.1	-64.1	-146.4	-22.6	-72.9
Measurement 23	95.6	0.7	-162.9	101.3	n.a.	-74.2	-22.2	-112.6
Measurement 24	n.a.	-123.6	n.a.	-3.2	n.a.	n.a.	n.a.	-89.1
AVERAGES	48.6	14.8	-299.2	-5.1	-36.6	-75.6	-19.4	-155.2
DIFFERENTIAL	**33.8 Hz**		**−294.1 Hz**		**38.9 Hz**		**135.8 Hz**	

Table 7.1: Resonance frequency measurement for cantilevers exposed to DAT, DNT, Ammonium nitrate (NH_4NO_3) and Diesel. Results are averaged over 24 measurements performed under the same gas flow conditions.

List of Figures

List of Tables

The future is already here,
it's just unevenly distributed

William Gibson